Influence of steel composition and plastic deformation on the surface properties induced by low-temperature thermochemical processing

PhD Thesis

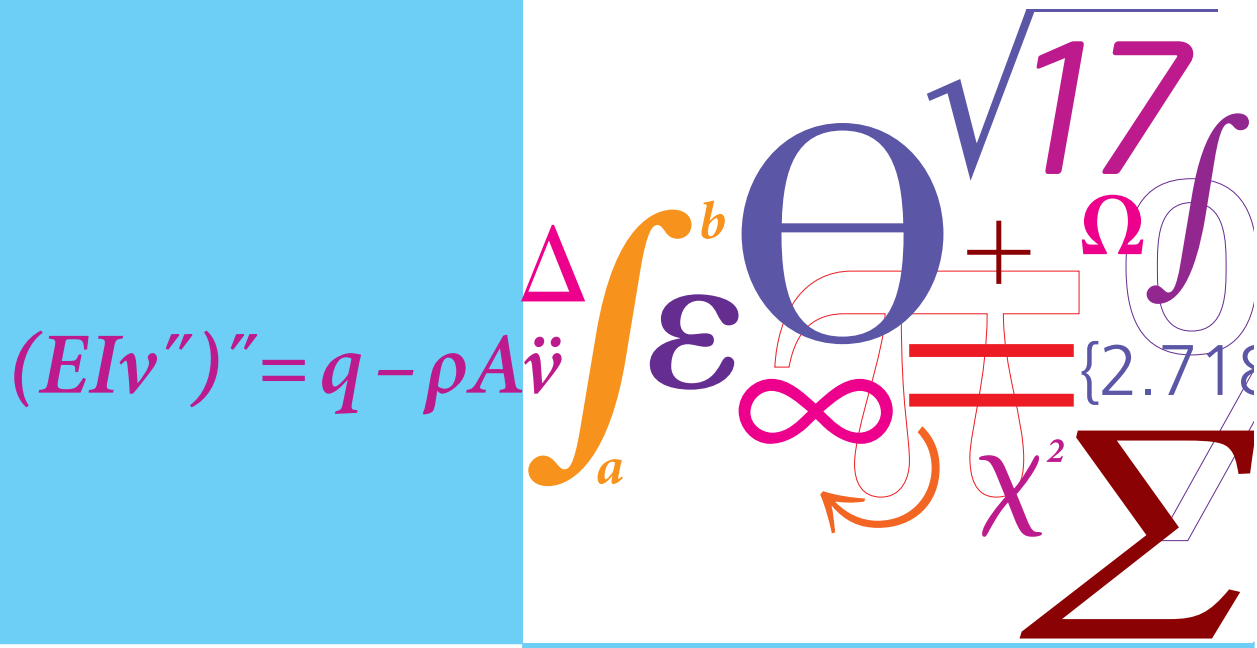

Federico Bottoli
December 2015

DTU Mechanical Engineering
Department of Mechanical Engineering

Technical University of Denmark

Department of Mechanical Engineering

Section of Materials and Surface Engineering

Influence of steel composition and plastic deformation on the surface properties induced by low-temperature thermochemical processing

Ph.D. Thesis

December 2015

Federico Bottoli

Supervisors:

Grethe Winther

Thomas L. Christiansen

Marcel A.J. Somers

Preface

The present Ph.D. thesis is submitted in candidacy for a Ph.D. degree from the Technical University of Denmark (DTU). The work presented in this thesis was carried out during the period November 2012 to December 2015 at the Department of Mechanical Engineering – Section for Materials and Surface Engineering under the supervision of Associate Professor Grethe Winther, Senior Researcher Thomas L. Christiansen and Professor Marcel A.J. Somers.

The project was part of the "PressPerfect" project and partly financed by the "Research Fund for Coal and Steel". The main goal of the "PressPerfect" project was to create a methodology to predict the performance of high quality stainless steels after forming and finishing treatments.

The different tasks in the projected were divided among the different project partners. In particular Sandvik materials technology and CENIM were involved in the material's characterization and study of the precipitation and transformation kinetics; M2i, Philips, University of Twente and Luleå university carried out a study on the simulation of the forming operations and prediction of the material properties and DTU was involved in the study of low-temperature thermochemical processing of various stainless steel classes after forming and finishing operations.

Kgs. Lyngby, December 2015

Federico Bottoli

Abstract

Low-temperature thermochemical surface hardening by nitriding, carburizing and nitrocarburizing is used to improve the performance of stainless steels with respect to wear, fatigue and corrosion resistance.
The dissolution of nitrogen and/or carbon atoms in the materials surface leads to the formation of a supersaturated solid solution known as expanded austenite, or S-Phase.
Expanded austenite is characterized by high hardness, up to 1400 Vickers, and high compressive stresses in the surface region, which result in improved wear and fatigue resistance of the components.
Along with the improvement of these properties, the corrosion resistance of the stainless steel is fully maintained or even enhanced.
Despite low-temperature thermochemical processing of austenitic stainless steels has been widely studied in literature, other stainless steel classes and the influence of steel´s initial condition, such as phase composition and/or plastic deformation, have not received the same attention.
The topic of this Ph.D. thesis is the study of the influence of the material's initial phase composition and the presence of plastic deformation on the properties of the surface layers obtained through low-temperature thermochemical processes of austenitic, precipitation hardening and martensitic stainless steels.
Parts of the work presented in this Ph.D. project were implemented in the European project ""PressPerfect", wherein several industrial and university partners were involved. The main goal of the "PressPerfect" Project was to create a methodology to predict the performance of high quality stainless steels after forming and finishing treatments.
The Ph.D. Project focused on the optimization of low-temperature thermochemical processes on several stainless steel classes used for the surface treatment of industrial products.
The activities carried out encompass the study and the characterization of the following aspects:

- Influence of plastic deformation prior to the low-temperature thermochemical process
- Influence of initial phase composition on the properties and morphology of the nitrided/nitrocarburized surface layer
- Influence of interstitial alloying on the mechanical properties of stainless steels
- Study of the corrosion performance of expanded austenite layer.
- Study of compressive residual stresses in expanded austenite and the influence of the material condition prior to nitriding/nitrocarburizing on the stress distribution.

The experimental techniques applied entail X-ray diffraction (XRD), Glow Discharge Optical Emission Spectroscopy (GD-OES), Scanning electron microscopy (SEM), light optical microscopy (LOM) and hardness measurement.

Resumé

Lav-temperatur termokemisk overfladehærdning i form af nitrering, karburering og nitrokarburering anvendes til at forbedre egenskaberne af rustfri ståltyper mht. slid, udmattelse og korrosionsbeskyttelse.
Opløsning af nitrogen- og/eller karbonatomer i materialets overflade fører til dannelse af en overmættet fast opløsning kaldet expanderet austenit eller S-fase.
Expanderet austenit er kendetegnet ved stor hårdhed, optil 1400 Vickers, og høje trykspændinger i overfladen, som resulterer i øget modstandsdygtighed mod slid og udmattelse.
Samtidigt med forbedringen af disse egenskaber bibeholdes eller forbedres korrosionsbeskyttelsen af det rustfri stål.
På trods af at lav-temperatur termokemiske processer på austenitiske rustfri ståltyper er rigt beskrevet i litteraturen, har andre klasser af rustfrit stål og betydningen af materialets begyndelsestilstand, som f.eks. fasesammensætningen og/eller plastisk deformation ikke fået samme opmærksomhed.
Emnet for denne Ph.D afhandling er at studere betydningen af materialets initiale fasesammensætning og plastiske deformationstilstand for egenskaberne af overfladelag opnået gennem lav-temperatur termokemiske processer.
Dele af dette Ph.D. projekt er udført i forbindelse med det europæiske projekt "PressPerfect", hvori adskillige industrielle og universitetspartnere er involveret. Hovedformålet med "PressPerfect" projektet var at finde en metode til at forudsige effektiviteten af høj-kvalitets rustfri ståltyper efter formgivnings- og færdigbehandlingsprocesser. Ph.D. projektet fokuserer på optimering af lav-temperatur termokemiske processer for adskillige klasser af rustfrit stål som anvendes i industriel produktion.
De udførte aktiviteter omfatter undersøgelser og karakterisering af følgende aspekter:

- Betydningen af plastisk deformation forud for lav-temperatur termokemiske processer
- Betydningen af materialets initiale fasesammensætning for egenskaberne og morfologien af det nitrerede/nitrokarburerede overfladelag
- Betydningen af legering med indskudsatomer på de mekaniske egenskaber af rustfrit stål
- Undersøge korrosionsegenskaberne af lag af ekspanderet austenit
- Undersøge residuale trykspændinger i ekspanderet austenit og effekten af materialets tilstand forud for nitrering/nitrokarburering på spændingsfordelingen

De anvendte eksperimentelle teknikker omfatter Røntgendiffraktion (XRD), Glow Discharge optisk emissions spektroskopi (GD-OES), skanning elektron mikroskopi (SEM), lysoptisk mikroskopi (LOM) og hårdhedsmålinger.

Acknowledgements

Firstly I would like to thank my supervisors Grethe Winther, Thomas L. Christiansen and Marcel A.J. Somers for their incredible support and valuable constructive criticism throughout my Ph.D. project. I am extremely thankful for their continuous contribution which has been a source of great inspiration and motivation for these past three years.

I would like to extent my gratitude to all the partners of the "PressPerfect" project Sandvik Materials Technology, Philips, CENIM, M2i – Materials Innovation Institute, the University of Twente and Luleå University for their collaboration, inspiring scientific and technical discussions and for providing an excellent working environment.

Special thanks go to all my colleagues for proving an excellent working atmosphere, for sharing their experience and for supporting me with helpful advices; in particular, Flemming Bjerg Grumsen and Steffen Sonne Munch are gratefully acknowledged for their precious help and valuable advices during the experimental activity.

I would also like to thank Sandvik materials technology for providing the materials necessary for the experimental work and the "Research Fund for Coal and Steel" for the financial support to the project.

Finally, I would like to thank my friends and my family, in particular my parents, for their constant support and encouragement.

List of Publications

I. F. Bottoli, G. Winther, T.L. Christiansen, and M.A.J. Somers: "Influence of Plastic Deformation on Low Temperature Surface Hardening of Austenitic Stainless Steel by Gaseous Nitriding" Metall. Mater. Trans. A, 2015, vol. 46, pp. 2579–90.

II. F. Bottoli, G. Winther, T.L. Christiansen, and M.A.J. Somers: "Influence of microstructure and process conditions on simultaneous low-temperature surface hardening and bulk precipitation hardening of Nanoflex®" , Metall. Mater. Trans. A, 2015, vol. 46, pp. 5201–16.

III. F. Bottoli, G. Winther, T.L. Christiansen, C. Vinter Dahl, and M.A.J. Somers: "Low-temperature nitriding of deformed austenitic stainless steels with various nitrogen contents obtained by prior high temperature solution nitriding", Submitted to Metall. Mater. Trans. A, 26th November 2015

IV. F. Bottoli, M. S. Jellesen, T.L. Christiansen, G. Winther, and M.A.J. Somers: "Electrochemical characterization and crevice corrosion performance of high temperature solid-solution nitrided and low-temperature nitrided austenitic stainless steel" Submitted to

V. F. Bottoli, G. Winther, T.L. Christiansen, and M.A.J. Somers: "Effect of plastic pre-straining on residual stress and composition profiles in low-temperature surface hardened austenitic stainless steel" Submitted to Metall. Mater. Trans. A, 26th November 2015

Conference contributions not included in the thesis

1. F. Bottoli, G. Winther, T.L Christiansen, and M.A.J. Somers: "Influence of Plastic Deformation on Low Temperature Surface Hardening of Austenitic Stainless Steel by Gaseous Nitriding", in Proceedings of the Twenty Eighth International Conference on Surface Modification Technologies – SMT28, ed. T.S. Sudarshan; P. Vuoristo; H. Koivuluoto, VALARDOCS, 2015, pp. 211-222. (not included).

2. F. Bottoli, G. Winther, T.L. Christiansen, and M.A.J. Somers: "Influence of Plastic Deformation on Low Temperature Surface Hardening of Austenitic and Precipitation Hardening Stainless Steels by Gaseous Nitriding", HTM – Journal of Heat Treatment and Materials, 2015, vol. 5, pp. 228-238. (not included).

3. F. Bottoli, G. Winther, T.L. Christiansen, and M.A.J. Somers: "Influence of plastic deformation on low temperature surface hardening of stainless steel by gaseous nitriding", in "Heat Treating 2015: Proceedings of the 28th ASM Heat Treating Society Conference", ASM International, Detroit, 2015, pp. 612-619.

Guidelines for the Reader

The thesis consists of three chapters (1-3) outlining the background and existing literature relevant to the Ph.D. project. The main methods and results of the project are summarized in chapters 4-5. The results are reported in detail in a number of publications included as chapters 6-10. The main conclusions of the Ph.D. project are given in chapter 11.

Background

- *Chapter 1*: background knowledge for low-temperature thermochemical processing and the state of the art over the expanded austenite and its main features.
- *Chapter 2:* Description of the main features of high nitrogen steels and nitrogen alloying. Production routes for "High-Nitrogen Steels".
- *Chapter 3:* Theoretical background for stress analysis with X-ray diffraction, measuring techniques, grain interaction models and material´s X-ray diffraction elastic constant.

Summary of methods and results

- *Chapter 4:* Materials, experimental procedure and characterization techniques used in the experimental activity
- *Chapter 5:* Overview of the results and summary of the main findings in the experimental campaign.

Publications

- *Chapter 6-10:* Results presented in paper form.

Conclusions

- *Chapter 11:* Conclusions and future work

Contents

1 Low-Temperature Surface Hardening of Steels

Low-Temperature Surface Hardening of Steels

Low-Temperature Surface Hardening of Steels

1.1 Introduction

Nitriding and/or nitrocarburizing have been, and still are, widely used technique for surface hardening of iron alloys and steels. The processes are carried out at a temperature usually lower than 590°C and lead to the formation of a compound layer of ε-$Fe_2(N/C)_{1-z}$ and γ'-Fe_4N_{1-x} at the materials surface followed by a diffusion zone underneath it [1].

However, these processes, when applied to austenitic stainless steels lead to the formation of nitrides and /or carbides due to the presence of Cr, which significantly impair the corrosion resistance of these classes of materials.

In the middle of the 1980s, low-temperature thermochemical processes demonstrated that it was possible to improve surface properties of stainless steels, with respect to wear and hardness, without impairing their corrosion resistance [2–4]. Low-temperature nitriding and/or carburizing allow the formation of a metastable, precipitate-free, supersaturated solid solution at the materials surface.

XRD characterization carried out after low-temperature thermochemical process revealed the formation of peaks which could not be associated to any material listed in the ASTM index, therefore Ichii et al. [5] named these peaks S1-S5 and used the term S-Phase to describe the layer created at the materials surface.

Since then, low-temperature thermochemical treatments have received great scientific interest and extensive research has been carried out in order to characterize and understand the nature of this "new phase".

1.2 Structure of Expanded Austenite

Expanded austenite is not a "new phase", as the name S-phase would suggest. It's merely a metastable supersaturated solid solution of nitrogen or carbon in which the precipitation of nitrides and/or carbides is avoided if the processing temperature is lower than 450°C (723K) for nitriding and 550°C (823K) for carburizing. Depending on the interstitial element dissolved in the metal matrix, it is possible to distinguish two different kinds of expanded austenite: nitrogen expanded austenite (γ_N) and carbon expanded austenite (γ_C).

The nitrogen and carbon atoms dissolved in the stainless steel matrix are accommodated in the octahedral sites of the f.c.c. stainless steel crystal structure and provoke an expansion of the lattice parameter which is a function of the concentration and type of interstitial atom. Nitrogen expanded austenite has a higher concentration of interstitials , typically in the range of 20-38 at% [6–10] while concentrations ranging from 5% to 12 at% are usually found for carbon expanded austenite [6,11–13]. These concentrations are

significantly higher than the maximum solid solubility [14,15] and lead to a substantial increase in the stainless steel lattice parameter (Fig. 1.1)

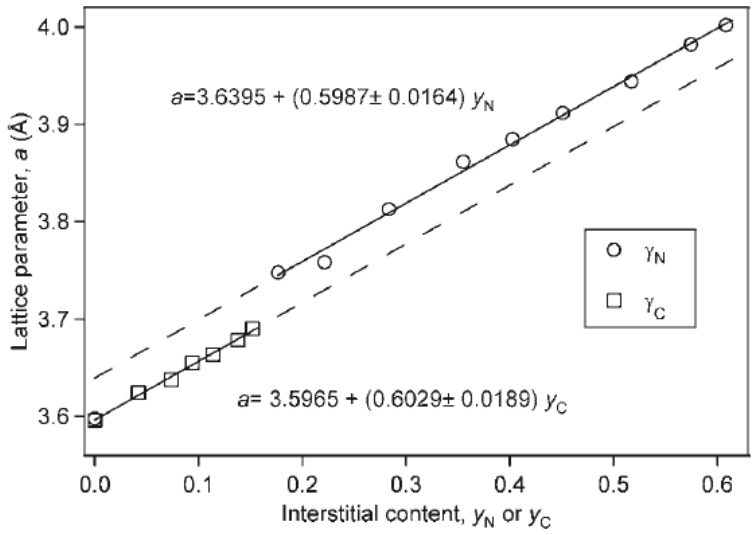

Figure 1.1: Lattice parameter expansion as function of the interstitial atoms dissolved during low-temperature thermochemical processes [16]

1.2.1 Crystallography of expanded austenite

The early XRD diffractograms collected on expanded austenite revealed the formation of peaks which were not be listed in any ASTM standard, leading to the hypothesis of the formation of a new phase, from which the name S-Phase. However, the diffraction pattern produced, resembled the one of an f.c.c. crystal structure although all the identified peaks were boarder and shifted to lower angles compared to a conventional f.c.c. crystal structure [10,13,17–19].

Initially the crystal structure of expanded austenite was defined as a compound layer having a M_4N (M=Fe, Cr, Ni) structure [5] or as a combination of austenite and γ' [$(Fe,Cr,Ni)_4M$] [2]. Later observations suggested that the shift in the peak position was connected to the lattice expansion and the characteristic diffraction lines could originate from an f.c.c. type structure [20] or from a face centred tetragonal structure, analogous to the one of martensite, called M-Phase [21].

The controversial interpretation on the crystal structure of expanded austenite was mainly due to the peak position, which is dependent on the lattice expansion and due to the fact that the a_{111}/a_{200} ratio shifts from the one of a perfect f.c.c. structure [22–24].

Further studies [13] revealed that this anomalous behaviour in the hkl-dependent shift and peak shape could be largely attributed to the presence of staking faults and residual stresses in the investigated layer which are accountable for a significant hkl-dependent shift from the expected lattice parameter (a_0). By taking into account these influences, it was possible to calculate theoretically with the Warren´s theory the expected peak shift for the various hkl reflections in expanded austenite.

However, the theoretically calculated peak position and the experimentally measured lattice parameters showed a significant scatter thereby leading to the conclusion that the crystal structure of expanded austenite could not be an ideal f.c.c..

This wrong interpretation can be essentially attributed to the investigation of inhomogeneous expanded austenite layers in which steep concentration profiles and high residual compressive stresses are present.

In this respect, Christiansen and Somers [19] succeeded in the synthesis of samples of homogenous expanded austenite powder in which the effects of gradients in the composition profile and residual stresses were minimized. For these homogeneous stress free powders it was possible to observe the excellent agreement between the theoretical peak shift due to the presence of stacking faults and the experimental peak position (Fig. 1.2).

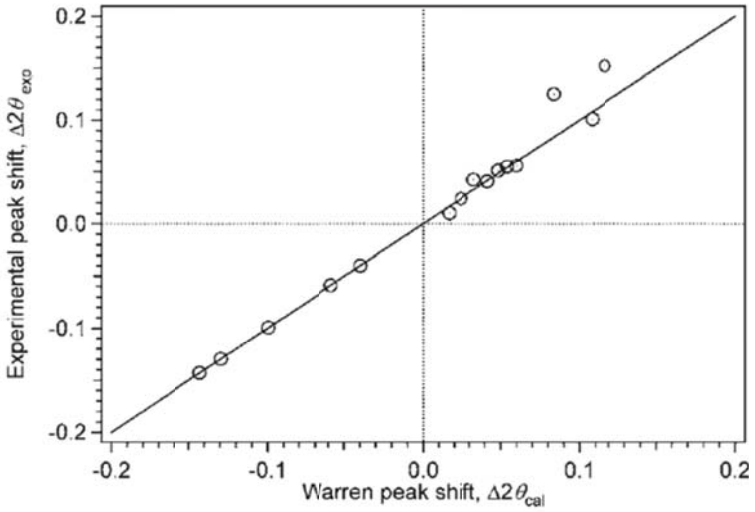

Figure 1.2: Comparison of experimental and predicted peak shift from an ideal f.c.c. structure due to presence of stacking faults [25].

These results explained the nature of the systematic shift of the reflection peaks from the ideal f.c.c. structure and clearly proved that expanded austenite has a face centred cubic structure. However, it has to be taken into account that the description of Warren is an oversimplification and that only the 111, 200 and 220 reflections were considered. Recent experiments have demonstrated that the crystal structure of expanded austenite is still not fully understood [26].

1.2.2 Structure of expanded austenite

Expanded austenite consists of a precipitate-free, metastable supersaturated solid solution of nitrogen and/or carbon and it appears as a bright featureless layer at the material´s surface after optical microscopy investigation (Fig. 1.3).

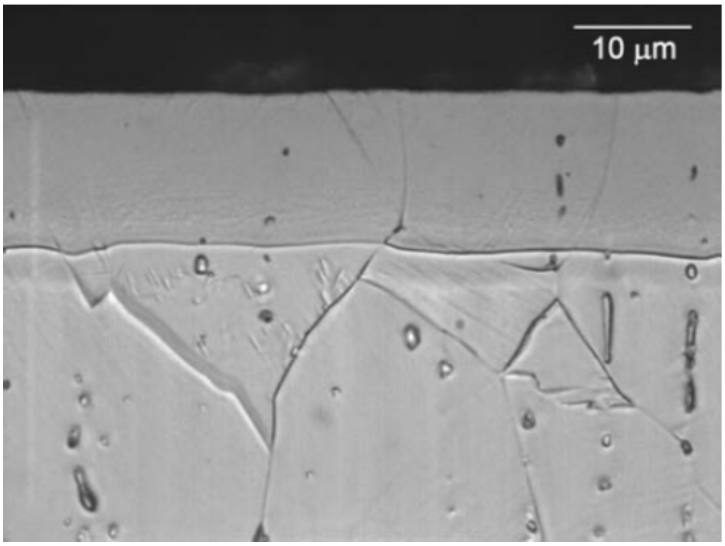

Figure1.3: Light-optical micrograph of low-temperature gas nitrided AISI 316; Nitriding conditions: T=445°C, t=22h, k_N=2.49Bar^{-1} [25].

The layer morphology is mainly related to the steep compositional gradient and the response to the etching agent differs from the one of the underlying substrate due to the increased corrosion potential after the thermochemical low-temperature treatment [27,28].

It is possible to observe that the grain boundaries, clearly visible in the substrate, continue into the expanded austenite zone hereby confirming that the formation of expanded austenite is purely a diffusion process and doesn't involve any nucleation and growth of a new phase. Therefore the size and shape of the grains of expanded austenite are the same as the untreated material.

Scanning and transmission electron microscopy investigation at high magnification revealed other interesting features in the expanded austenite layer [29]. It was in fact possible to identify parallel micro-twins (Fig 1.4a.), slip bands and dislocations (Fig 1.4b.) suggesting that plastic deformation may have occurred during the low-temperature thermochemical process.

Upon nitriding nitrogen dissolution results in the introduction of huge lattice strains corresponding to very large compressive stresses. Initially these strains are accommodated elastically and, along with an increase in interstitial content, the (expanded) austenite is strengthened.

Above a certain interstitial content, the lattice expansion cannot be accommodated elastically any further and leads to a residual stress increase that exceeds the additional yield strength. The stresses above the yield strength (which is composition dependent) results in plastic deformation occurring by slip.

Such plastic deformation has been observed for nitriding in the form of a nitrogen dissolution-induced lattice rotation, depending on the initial grain orientation [30–32]. The crystal rotation effect produced upon nitriding has many similarities [32] with the grain orientation dependent lattice rotations of individual bulk grains measured in monotonic tensile tests in a number of materials [33–35].

The plasticity and damage found in the expanded austenite layer is a direct consequence of the enormous expansion of the crystal lattice as a result of the supersaturation of N and/or C interstitial atoms [36,37]. The plastic deformation results in a roughening of the surface and a lattice rotation which is function of the

initial crystallographic texture of the material and the amount of interstitial dissolved during the low-temperature nitriding process [30–32]

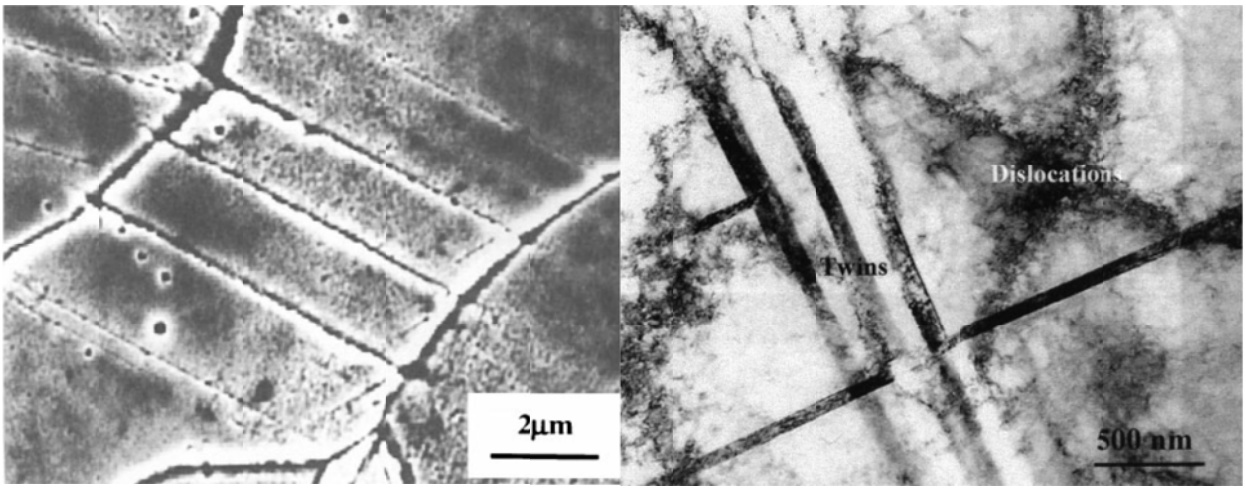

a. b.

Figure 1.4: Defects in expanded austenite (a.) SEM images showing the presence of twins; (b.) TEM images showing the presence of microtwins and dislocations in expanded austenite [38]

1.3 Types of expanded austenite

The properties and morphology of the expanded austenite layer depend significantly on the type of interstitial dissolved (N and/or C), the technique and the process parameters used. The techniques most commonly used for the formation of an expanded austenite surface layer are gas processes, plasma processes and ion implantation technologies.

Diffusion of nitrogen in the stainless steel matrix leads to the formation of nitrogen expanded austenite (γ_N). The lattice expansion due to N incorporation in nitrogen expanded austenite ranges from 6% to11% [7,10,19,39]; it depends strongly on the processing condition and it is a function of the depth, meaning that the lattice parameter is not constant but decreases with the decreasing N concentration with increasing layer depth. At the interface between the layer and the substrate it is possible to observe a sharp transition due to the locally steep diffusion profile of nitrogen (cf. Fig. 1.3). The hardness profile obtained for γ_N is strongly dependent on the processing condition and thus on the amount of interstitial dissolved in the stainless steel matrix; however, in all cases it´s possible to identify a plateau like region, characterized by high hardness, followed by a sharp drop in transition region (Fig. 1.5)

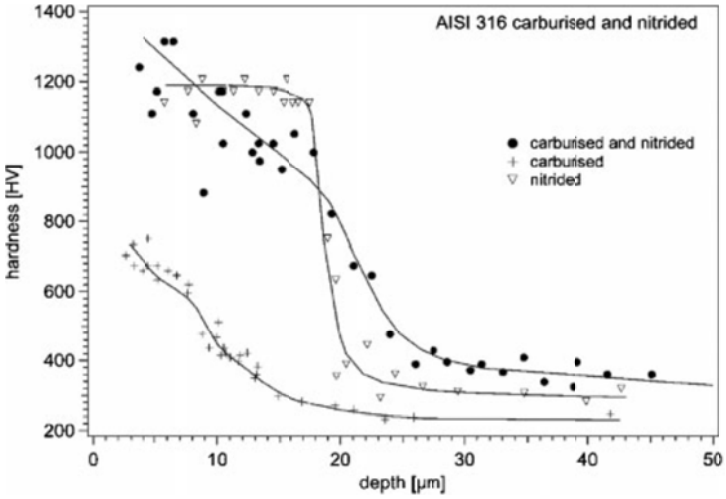

Figure 1.5: Hardness depth profiles after low-temperature gas nitriding, carburizing and a combined process (carburizing and nitriding). [6]

The significant lattice expansion due to N dissolution in γ_N is constrained by the austenite substrate, therefore very high residual stresses, in the order of GPa, have been reported in nitrogen expanded austenite [16,40,41]. The real magnitude of the compressive residual stresses is however still debated [42]. Carbon expanded austenite (γ_C) is formed when alloying with carbon through carburizing or through C ion implantation (Fig. 1.6).

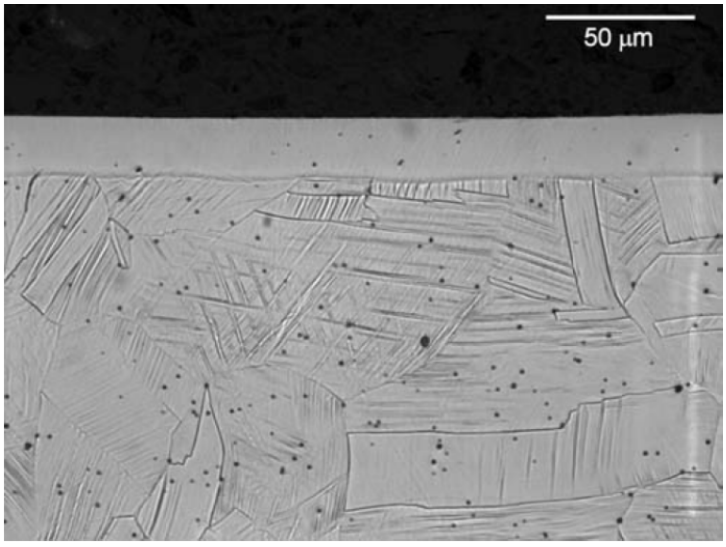

Figure 1.6: Light optical micrograph of carburized AISI 316 at 420ºC (693K) for 67h in a 48%C_2H_2-48%H_2-4%N_2 atmosphere [25].

The maximum content of interstitial carbon in expanded austenite is significantly lower than for nitrogen [43–46] and therefore a smaller lattice expansion (1.4-3%) is found for γ_C [7,11,13,19,47,48]; however, a thicker case can be obtained through low-temperature carburizing compared to low-temperature nitriding. Even in this case the hardness profile obtained is strongly dependent on the

processing parameters, but, compared to the one of γ_N, a maximum hardness value is reached at the surface and then it progressively decreases with the increasing layer depth until the substrate is reached (Fig. 1.5)
The lattice expansion provoked by the carbon dissolution is not as significant as for nitrogen, however, even in the γ_C, the austenite substrate constrains the expansion thus generating high compressive residual stresses in the low-temperature surface treated layer.
Eventually, it was shown for the first time by Leyland et al [20], that is possible to obtain simultaneous dissolution of nitrogen and carbon thereby forming a dual layer characterized by nitrogen expanded austenite in the outermost region followed by carbon expanded austenite in the inner zone [8,9] (Fig. 1.7).

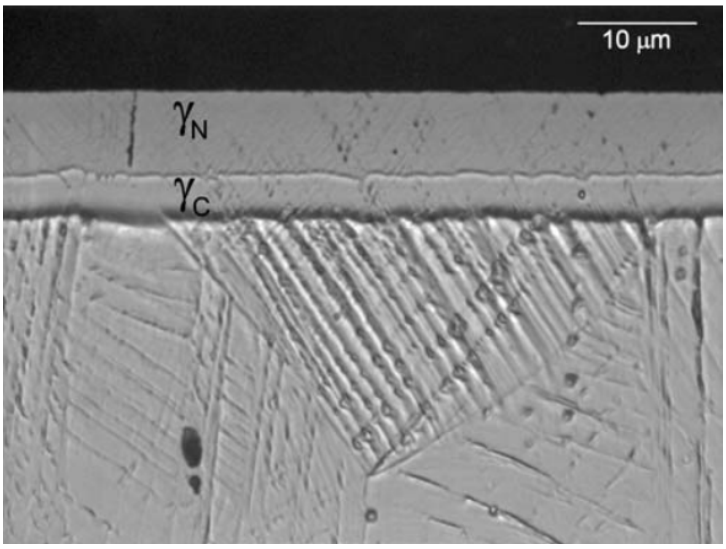

Figure 1.7: Light optical micrograph of AISI 304 gas nitrocarburized in an atmosphere 14%C_3H_6-54%NH_3-22%H_2-10%Ar at 420°C for 19h [25].

The properties of this layer are a combination of the two types of expanded austenite. The hardness profile obtained for nitrocarburized stainless steels is in fact characterized by a high hardness at the surface, due to γ_N, and a smooth transition in the γ_C region to the bulk hardness value.
As for the hardness profiles, the residual stress profile is a superposition of the γ_N and γ_C profiles. The high residual stresses in the nitrogen expanded region are followed by lower magnitude residual stresses in the inner carbon expanded region, thus a smoother transition of the stress profile is obtained for this case.
Due to the combination of the interesting properties of both types of the expanded austenite, nitrocarburizing is receiving a great interest in research and industrial applications [9,25,38,49].

1.4 Thermal stability of expanded austenite

Due to its supersaturated nature, expanded austenite is metastable and therefore it decomposes into stable phases if it is exposed to temperatures above a certain value [50–52]. The thermal stability of expanded austenite depends strongly on the type and amount of interstitials (N or C) as well as on the chemical composition of the stainless steel (substitutional elements) [38,52].

Since decomposition of expanded austenite is a diffusion controlled process, the incubation time is temperature dependent and, in particular, it decreases for higher temperatures [50,52].

Li et al. studied the decomposition of γ_N and γ_C in AISI 316 upon isothermal annealing, in a range of temperatures from 300ºC to 600ºC [50]. They showed that decomposition of the expanded phase occurs above a certain temperature, under which the expanded phase is stable. This threshold temperature was found to be 400 ºC for γ_C and 350 ºC for γ_N. In that study it was found that AISI 316 decomposes into CrN and austenite or CrN and ferrite depending on the annealing temperature. Above 500 ºC ferrite is formed, below this temperature austenite forms (Fig. 1.8). The formation of CrN starts as precipitation of very disperse laminar particles spaced few nanometres to each other and coherent with the expanded austenite structure. In later stages of the precipitation, the coherency is lost and the nitrogen content in the "former" expanded austenite drops to its nominal maximum concentration in austenite [50].

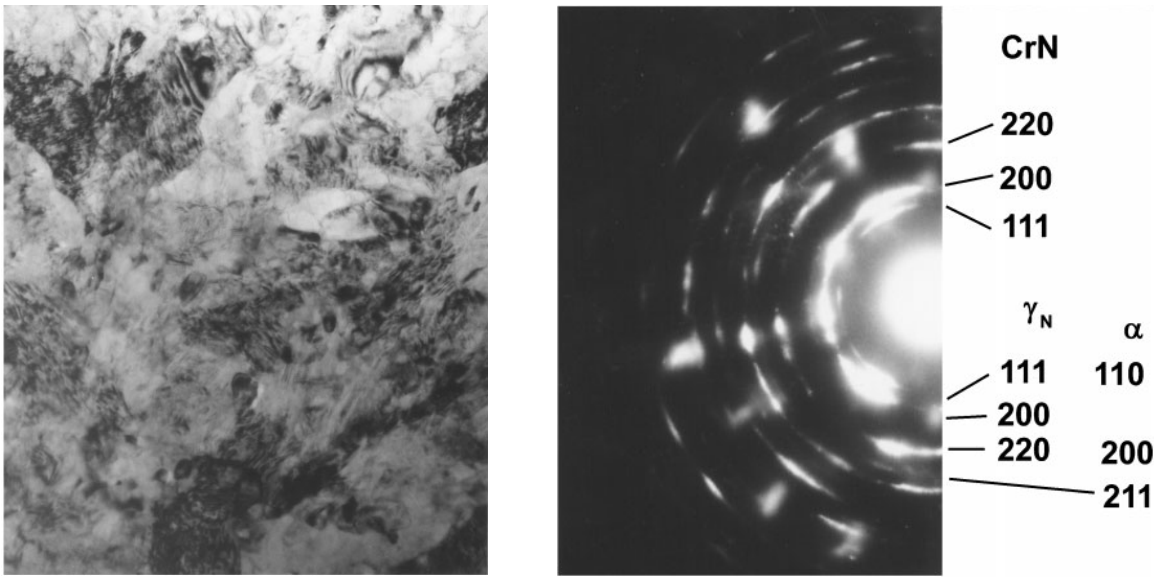

a. b.

Figure 1.8: a. TEM microstructure of decomposed expanded austenite, b. selected area diffraction pattern revealing the presence of CrN and ferrite.

Christiansen et al. [52] investigated the decomposition of nitrogen expanded austenite in AISI 316L and AISI 304L by isothermal annealing and found a marked difference between the two studied alloys. The X-ray diffraction analysis on the decomposition product revealed the formation of CrN and austenite for AISI 316L and CrN and ferrite for AISI 304L. The thermogravimetric analysis on the decomposition kinetics of these two alloys revealed a significant difference which could be directly related to the mechanism of the formation of the decomposition products. The activation energy for the process was in fact lower for AISI 304L (128±9.9 kJ·mol^{-1}) than for 316L (187±17.7 kJ·mol^{-1}). In AISI 304L the precipitation of CrN and ferrite occurs simultaneously and the more favourable orientation relationship existing between b.c.c. iron and chromium nitride, $\{001\}_{b.c.c.}//\{001\}_{CrN}$ and $<100>_{b.c.c.}//<001>_{CrN}$, is responsible for lowering the activation energy. While the mechanism of decomposition in AISI 316L was explained as a discontinuous process, thus requiring a higher energy for its activation.

Decomposition upon annealing of carbon expanded austenite has not received the same attention as nitrogen expanded austenite. Ernst et al. [53,54] reported the presence of M_5C_2 and M_7C_3 χ–carbides at the surface of the treated material after carburizing for 44h and TEM investigation suggested the presence of preferential orientation relationship between the carbide and austenite, lowering the energy barrier for nucleation and growth [54].

However, studies on isochronal annealing of γ_C powders supported by thermodynamic equilibrium predictions [25], reported that in expanded austenite with a high carbon content (4 wt%) M_7C_3 is formed while in low-carbon γ_C (1 wt%) $M_{23}C_6$ develops.

Precipitation of nitrides and carbides in expanded austenite has to be avoided because, despite it doesn't compromise the hardness in the layer, it significantly impairs its corrosion resistance because of the Cr depletion in the stainless steel matrix.

1.5 Diffusion coefficient

The diffusivity of interstitials in austenite and expanded austenite has been widely studied in literature and plays a major role on the morphology and thickness of the expanded austenite layers produced [55–60].

It has been shown that the diffusion coefficient of the interstitial species is strongly dependent on the chemical composition, nitrogen concentration and the presence of large residual stresses at the surface.

In particular, the diffusion coefficient is strongly affected by the strong interaction of the interstitial atoms (especially N) with the Cr present in the steel matrix (trapping model), therefore the interstitial will contribute in a different extent to the layer growth [61].

Early models for the determination of the diffusion coefficient of nitrogen in expanded austenite were calculated based on the concentration-depth profiles measured with GD-OES techniques [57,58] without taking into account the effect of the trapping of nitrogen atoms by the chromium and molybdenum present in the alloy. Furthermore these models have been determined for layers produced with plasma or implantation based techniques in which a certain unknown degree of sputtering at the surface occurs and therefore no direct correlation between the concentration and the diffusion coefficient can be extracted.

Christiansen and Somers [59] studied the diffusion coefficients of nitrogen in expanded austenite from stepwise denitriding experiments from fully nitrided samples and showed clearly that the diffusion coefficient is strongly depending on the nitrogen concentration in γ_N (Fig. 1.9).

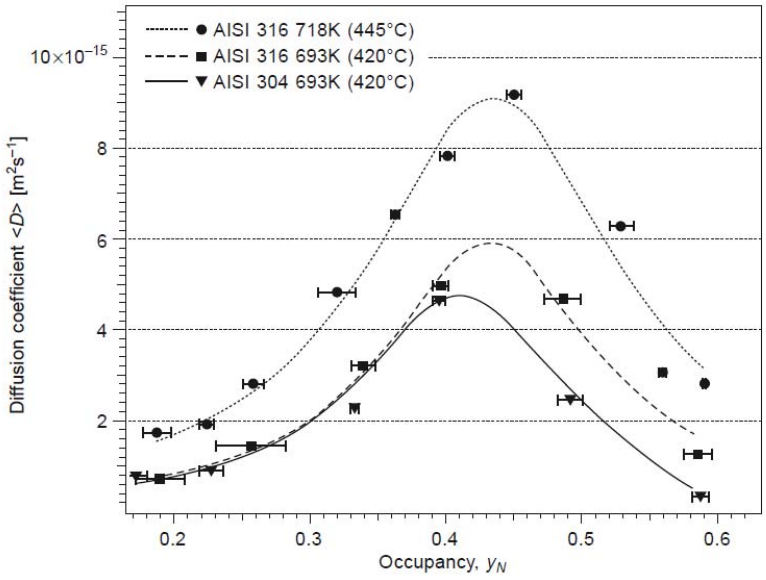

Figure 1.9: Diffusion coefficient of N in expanded austenite as function of the nitrogen content in the steel matrix for two nitriding conditions 420°C (AISI 304-AISI 316) and 445°C (AISI 316) [25].

The diffusion coefficient in expanded austenite, as depicted in Fig. 1.9 increases with the nitrogen content up to a maximum value after which a decrease is observed.

The trend of the diffusion coefficient was explained as follows: the nitrogen atoms diffused in the metal matrix are accommodated preferentially in the octahedral sites of the f.c.c structure and provoke an expansion of the crystal lattice. The dilatation of the crystal lattice will increase the size of the octahedral and tetrahedral interstices, thus lowering the activation energy for diffusion of the incoming nitrogen.

This behaviour is responsible for the increase in diffusion coefficient with the increasing nitrogen content in expanded austenite up to a point where the probability of finding an empty octahedral or tetrahedral interstice is low. At this point, after a maximum value is obtained, the diffusion coefficient decreases until maximum occupancy is reached.

However in this model, the huge compressive stresses building up at the surface [62], and their effect on the diffusion coefficient are not taken into account. Recent work in fact has shown that, together with the composition gradient, the presence of compressive stresses has a non-negligible effect on the diffusion kinetics [63].

So far, no systematic study of the diffusion coefficient of carbon in austenite or nitrogen in other phases (ferrite and martensite) has been carried out; however, it has been shown that the activation energy for carbon diffusion in austenite decreases as the carbon content in austenite increases [64].

Eventually, it was observed that the thickness of the nitrided layer was not homogenous but it changed in the different grains according to their specific crystallographic orientation. In particular it was observed that N diffuses deeper into 200 oriented grains than into 111 oriented grains [60,65–69].

Initially this behaviour was interpreted as different orientation dependent diffusion coefficients [66], however the different in diffusivity in the different crystallographic direction is believed to be related to the

different elastic residual stress for the specific crystal orientations [60]. The elastic young modulus changes according to the different crystallographic direction, therefore it will be easier for nitrogen to be accommodated along weakest direction. Since residual elastic stresses influences greatly the diffusion coefficient of nitrogen in expanded austenite, the different degree of expansion due to different nitrogen accommodation along the different crystallographic directions is held responsible for the different diffusivity [60].

1.6 Properties of expanded austenite

As mentioned above, expanded austenite possesses a series of extremely attractive properties which make low-temperature surface treated components suitable in many industrial applications where wear, corrosion and fatigue resistance are issues.

1.6.1 Hardness and wear resistance

Expanded austenite is characterized by an extremely high hardness. The maximum hardness achieved in an expanded austenite layer depends significantly on the processing parameters and the type and amount of interstitials dissolved in the surface. Typical ranges of hardness are reported as 1300-1500HV for γ_N and 700-1000HV for γ_C [70].

This difference can be related to the different amounts of dissolved interstitials and the different degree of lattice expansion in the stainless steel matrix. The N interstitial content is ranging from 20 to 38 at% [6–10] while C concentrations ranging from 5% to 12 at% are usually found for carbon expanded austenite [6,11–13].

The hardness profile measured over the cross section in the N and C expanded austenite is also different. Nitrogen expanded austenite is characterized by a plateau with very high hardness followed by a sharp drop in the bulk hardness value. This drop occurs within few μm in the γ_N-γ transition region (cf. Fig. 1.4).

The hardness profile measured over the cross section in γ_C is significantly different, with the highest hardness at the material´s surface and a gradual decrease to the bulk hardness value over the whole thickness of the treated layer (cf. Fig. 1.4).

The extreme hardness of expanded austenite and the compressive residual stresses parallel to the surface, are responsible for the excellent wear resistance of low-temperature surface treated steels [24,27,28,71–74]. Extensive research on the wear behaviour of low-temperature nitrided steels, proved an improvement of the wear properties and a considerable reduction of the weight loss during the tests compared to an untreated material [71,73] (Fig. 1.10).

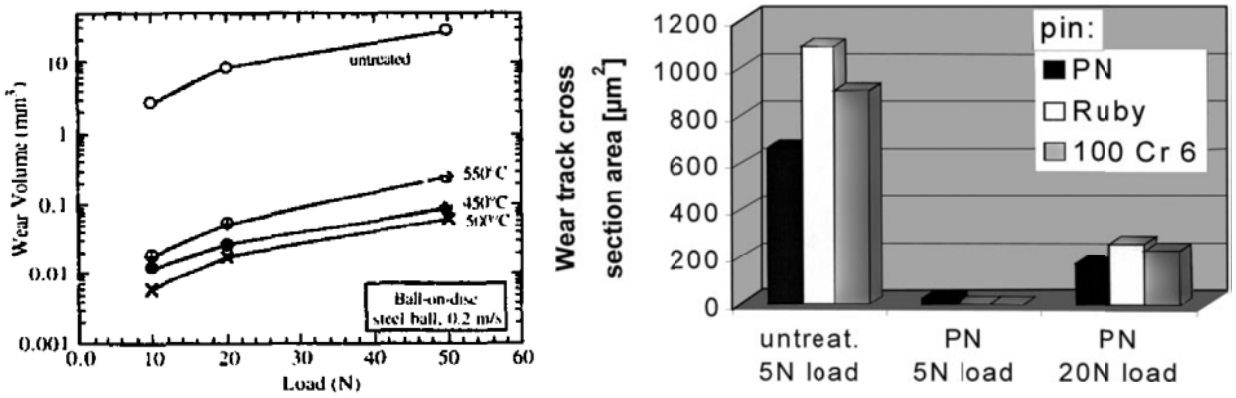

a. b.

Figure 1.10: a. Wear volume as function of the load for various treated steels in a ball-on-disc wear test (1200m sliding distance) [71]; b. Wear track cross-section area of untreated and plasma nitrided (PN, 5 h, 450°C) austenitic stainless steel discs obtained with various loads and pin materials [73].

Furthermore it was demonstrated that nitrided AISI 304 has a much lower friction coefficient against different substrates compared to the unnitrided material (Fig. 1.11) [73,74] and the main wear regime that dominates for a nitrided material was identified as abrasive wear [28,73,74].

There is still no agreement on the effect of nitrogen on the tribo-chemical reaction occurring during the wear tests; some research shows that the presence of nitrogen at the surface is responsible for the inhibition of tribo-chemical reactions [74] while other research show, that despite the wear rate is greatly reduced, the presence of nitrogen has no influence on these reactions [28].

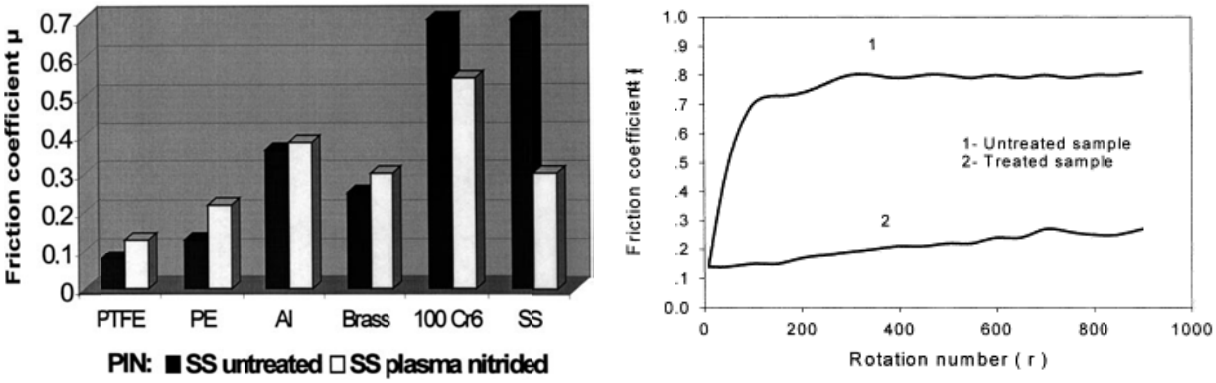

a. b.

Figure 1.11: a. Friction coefficient of plasma nitrided (PN, 5 h, 450°C) AISI 304 against different substrates [73]; b. Friction coefficients of the treated and untreated AISI304 samples vs. the number of rotations [74].

1.6.2 Residual stresses and fatigue resistance

The crystal lattice expansion in the case, due to the incorporation of the interstitial N and C, is (partially) constrained by the underlying austenite substrate and results in residual compressive stresses of several GPa at the material´s surface. The magnitude of the residual stresses created after the low-temperature surface engineering process is a function of the expansion of the crystal lattice and therefore is dependent on the type of interstitial and on the processing conditions.

The evaluation of residual stresses in expanded austenite has been mainly carried out with X-ray diffraction techniques [16,41,42,75,76] using the so-called $\sin^2\psi$ method [77,78]. Due to the presence of stress and compositional gradients, dedicated evaluation procedures have to be adopted in order to avoid erroneous results and limit the occurrence of so-called ghost stresses [42,76].

A detailed description of the residuals stress measurement with XRD and the evaluation method for expanded austenite will be given in Chapter 3.

Figure 1.12 depicts the stress profiles obtained for samples after gas carburizing and gas nitriding with different gas compositions [79]. The graphs clearly show how, in both cases, the processing parameters influence the obtained distribution of the residual stresses. Higher processing temperatures result in a higher dissolution of interstitial atoms and therefore in stresses of a higher magnitude. These findings confirm that the residual compressive stresses in expanded austenite are largely composition induced [62].

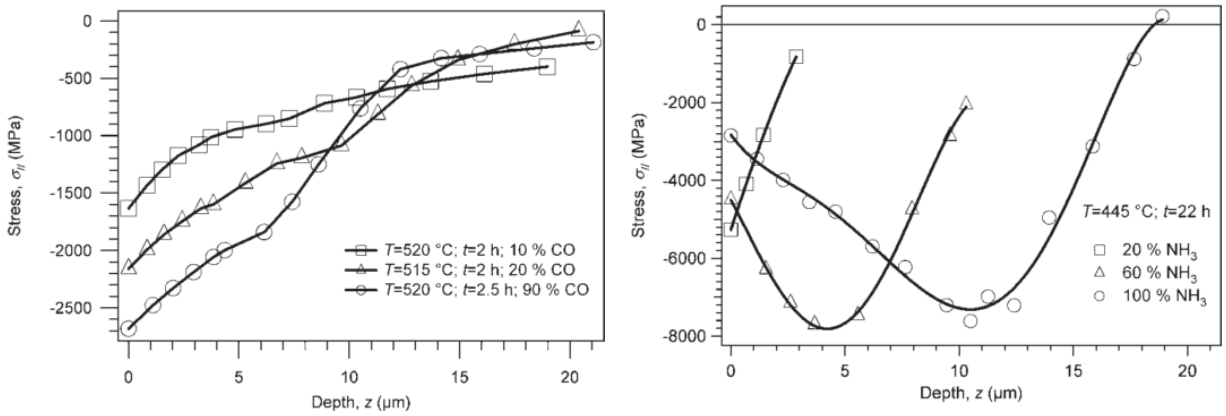

a. b.

Figure 1.12: Stress profiles for AISI 316 low-temperature gas carburized (a.) and nitrided (b.) [79]

However some differences can be found in the carbon and nitrogen expanded austenite residual stress profiles. In γ_C the maximum compressive stresses are significantly lower than in γ_N and they can be found at the material surface while in γ_N, the highest compressive stresses are found few µm below the surface.

The first effect is due to the lower expansion of the crystal lattice caused by carbon insertion compared to nitrogen, while the second one is believed to be due to stress relaxation at the material surface as a consequence of plastic deformation induced by the huge compressive stresses [62,79].

In addition to this, a sharp transition of the stresses from γ_N to γ can be found in nitrogen expanded austenite layers. This is due to the steeper composition gradients observed in nitrogen expanded austenite layer compared to carbon expanded austenite.

The residual stress profile obtained for nitrocarburizing is depicted in Fig. 1.13. As it could be observed in the hardness profile of a nitrocarburized sample, the residual stress profile is a superposition of the profiles obtained during nitriding and carburizing. The nitrocarburized layer is characterized by high residual stresses in the nitrogen expanded region and lower entity stresses in the carbon expanded austenite, and as a result of this, no sharp drop in the compressive stresses is observed when approaching the untreated substrate.

Carbon expanded austenite in a nitrocarburized layer allows a smoother transition to the untreated core and it allows to bridge more effectively the lattice parameter mismatch between γ_N and γ.

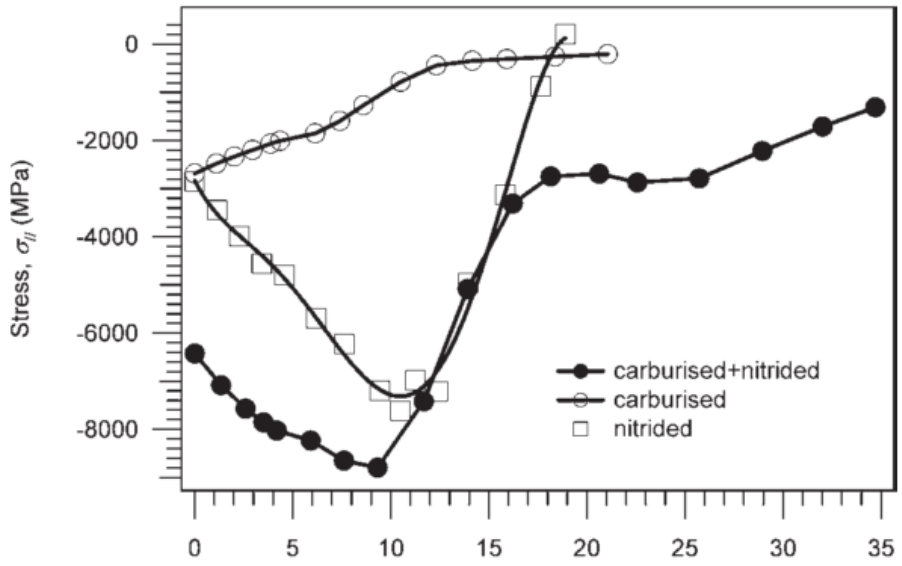

Figure 1.13: Stress profile for nitrided, carburized and carburized+nitrided samples [79]

The high residual stresses developed as a consequence of low-temperature surface engineered stainless steels have a positive effect on the fatigue behaviour of treated components [73,80–82].

Menthe et al. [73] studied the fatigue life of nitrided components in a cyclic fatigue test and proved that a significant improvement of the fatigue life is observed for the high cycle range (low cyclic loads) but no significant difference could be noticed in the low cycle range (high cyclic loads) (Fig. 1.14). They attributed this behaviour to the fact that at high cycles most of the fatigue life is associated with the crack initiation process, while at low cycles the crack growth in the bulk, unaffected by the treatment, controls the fatigue life.

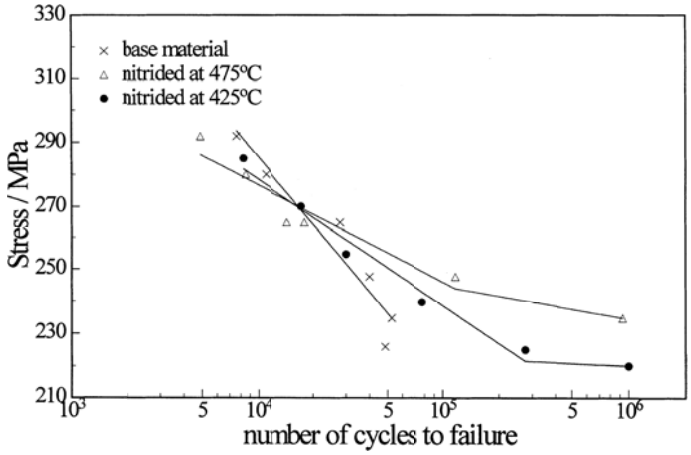

Figure 1.14: Number of cycles to failure for different stress amplitudes of untreated and plasma nitrided austenitic stainless [73].

Results of bending test on low-temperature nitrided [80] and low-temperature carburized [81] AISI 316 showed that the plain fatigue limit could be augmented by several MPa compared to untreated components.

Improvement of the fatigue properties were also observed by Tokaji et al. [82] during a bending fatigue test in air and in 3%NaCl solution in order to simulate the effect of environmental condition on carburized samples.

1.6.3 Corrosion properties

Austenitic stainless steels are well known for their excellent corrosion resistance due to the formation of a dense chromium oxide layer at the material surface. This passive film however, is susceptible to localized breakdown, especially in chloride containing solutions, thus causing localized corrosion such as pitting and crevice corrosion [83]. In addition to that, this class of materials suffers from poor wear resistance, in particular galling.

Major improvements of the wear resistance of stainless steels, along with an improvement of the corrosion properties can be obtained through low-temperature nitriding [17]. If the processing condition avoids the precipitation of CrN, the pitting and corrosion properties of the component are significantly improved compared to an untreated stainless steel.

Electrochemical behaviour of plasma nitrided AISI 304 [28] and AISI 316 [84,85] was studied in a 3.5% NaCl water solution. In these studies, as a consequence of dissolution of colossal amounts of N at the surface, the corrosion potential was shifted towards higher values and the current density was significantly reduced (Fig. 1.15). Furthermore no abrupt increase in the anodic current was recorded (pitting), suggesting that the corrosion mechanism taking place is more likely to be in a general corrosion form [84].

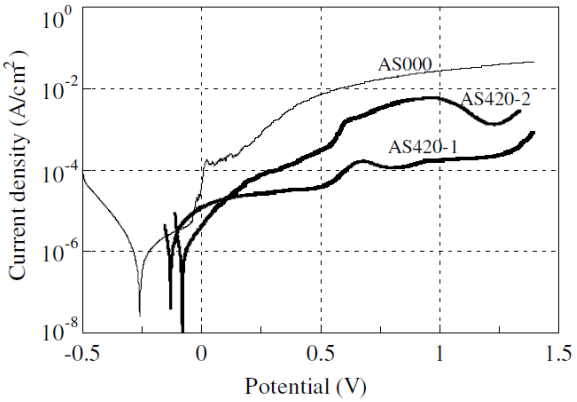

Figure 1.15: Comparison of polarisation curves of the low temperature AS plasma nitrided (AS420 series) and untreated 316 steel in 3.5% NaCl water solution. [84]

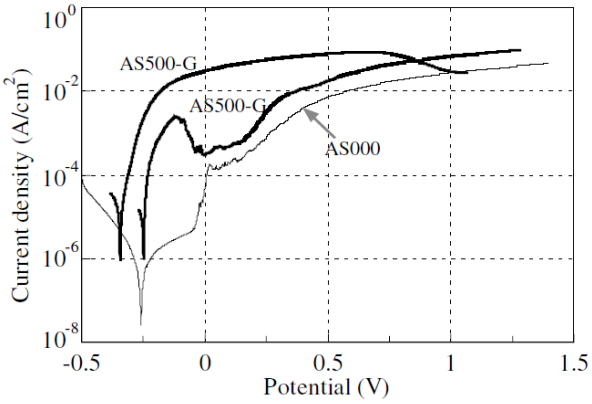

Figure 1.16: Polarisation curves for the untreated and 500°C AS plasma nitrided 316 steels. [65]

In the same study [84], it was shown how the precipitation of nitrides during the process, leads to a significant increase of the corrosion rate of the sample compared to an untreated stainless steel (Fig. 1.16).

The beneficial effect of dissolved nitrogen on the corrosion behaviour was subject of extensive literature study in both high nitrogen steels and expanded austenite layers [86–92] and proved that nitrogen influences the mechanism of repassivation kinetic. The improvement in pitting corrosion was attributed to the nitrogen dissolving during the process which consumes the acid in the pit and leads to a more alkaline solution, thus stopping the pit growth rate [84,93–96].

Normand et al. [92] found high concentration of NH_3 and NH_4^+ at the surface of the passive film through XPS investigation and they related the improvement of corrosion resistance to the breakdown of the CrN bond which leaves more Cr available for the oxide formation and more N for the protonation of NH_3 and NH_4^+.

Despite an improvement of the corrosion performance in chloride containing solutions, a reduction of the corrosion resistance was observed in acid environments. Lei at al. [97], carried out a study of the properties of nitrided layer in Ringer´s solution at different pH and observed occurrence of pitting at pH = 3.5.

A deterioration of the corrosion properties of nitrided steels in acid environments was also observed by Gontijo et al. [98] who showed the occurrence of localized corrosion in H_2SO_4 solution at pH 3.

The reduction of the corrosion resistance in acid environments is attributed to the presence of a high concentration of defects, such as slip bands, stacking faults and micro-twins in expanded austenite, which act as more favourable sites for the nucleation of precipitates [99].

Carbon expanded austenite was also reported not to be sensitive to pitting corrosion [13,100] but the mechanism of protection is still under investigation.

1.7 Role of alloying elements

The chemical composition of the alloy treated by low-temperature thermochemical processes has a substantial influence on the properties and morphology of the expanded austenite layer formed.
In particular, many researchers have pointed out that the presence of strong nitrides forming elements such as Mo, Cr, Ti, V, Nb and Mg is necessary for the formation of and stabilization of expanded austenite. These elements increase the diffusivity and solubility of the interstitial N and C, hence contributing to the supersaturation of the austenite matrix [101–106].
The absence of Cr [106,107] and Mo [103] in Ni-based alloys leads to very low interstitial concentration (1%) or no expansion of the f.c.c. crystal lattice and instead causes the precipitation of nitrides or carbides.
It is reported that low-temperature surface engineering of Fe-Ni and Fe-Mn alloys doesn't allow the formation of any expanded phase [108]. This effect is due to the very low solubility of the interstitial N and C in Ni and Mn and confirms how the presence of nitride-forming elements is a necessary prerequisite for the formation of expanded austenite. On the other hand, presence of Ni and Mn in stainless steel doesn't have a negative influence on the formation of expanded austenite.

1.8 Techniques

The first indication of the synthesis of expanded austenite can be tracked back to the early 1960s where a thin carbon saturated layer was formed as a "corrosion product" in stainless steels used in nuclear power production. Stainless steel was used to manufacture liquid-metal fast-breeder reactors (LMFBR) and the carbon impurities contained in the liquid sodium, used a cooling agent, were responsible for the unwanted carburizing reaction [1].
The first indication of nitrogen expanded austenite as a very thin transition zone between a chromium nitride zone and austenite was reported by Lebrun et al [109] in 1972 as the a results of plasma nitriding at temperatures above 500 °C.
After this, Zhang and Bell succeeded in the synthesis of a 20μm thick layer through plasma processes [2].
In the following decades several other processing techniques, such as gas processes, magnetron sputtering, ion implantation and liquid thermochemical treatments proved to be successful methods for the formation of expanded austenite.
In the following sections, a brief description of the most used processes will be given.

1.8.1 Plasma process

Plasma processes are widely used since the mid-1980s for the formation of expanded austenite [2,4,5]. Among the processes most frequently used for low-temperature thermochemical engineering, it is possible to find direct current plasma (DC) [110], pulsed plasma [73,98] and radio frequency plasma [111–113].

The main advantage of plasma processes is related to the sputtering effect, which removes the passive oxide layer present at the surface of stainless steel and allows the insertion of the active interstitial N and/or C [114].

Direct current plasma is the most used of the plasma processes; however, there are some limitations to its widespread industrial application mainly related to the non-uniform temperature distribution in the chamber and non-uniform electric discharge which then results in an inhomogeneous expanded austenite layer [113].

The treatment of complex geometries is also an issue in DC plasma processes; in fact, due to the inhomogeneous temperature and glow discharge it is possible to reach temperatures higher than the processing temperature in proximity of sharp edges, thus provoking precipitation of nitrides and/or carbides which impair the corrosion resistance of the component [115,116]

More recent plasma techniques such as pulsed DC, Plasma RF and in particular active screen plasma thanks to the use of an applied cathodic potential in the metallic mesh, hollow cathodes and cathodic heaters, allows to limit plasma disturbances and temperature gradients, thus producing a more homogenous surface layer [84,117] (Fig. 1.17).

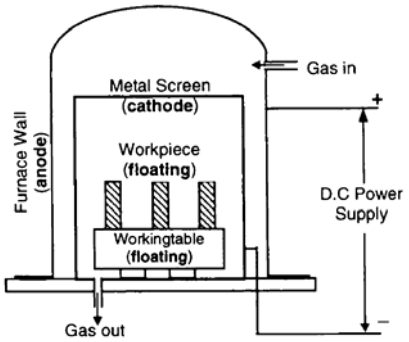

Figure 1.17: schematic of active plasma unit [38].

1.8.2 Ion implantation

Ion implantation technologies have been used for the production of expanded austenite layers at the surface of stainless steels, however the maximum thickness obtained with this processes is limited compared to plasma and gas processes.

In this technology, used from the 1970s, high-energy ions are implanted below the materials' surface [118,119]. The energy of the ions is significantly higher than the one used in the plasma processes and ranges from tens of KeV to several hundreds of KeV depending on the process used [38].

Conventional ion implantation processes on stainless steels allow the formation of a layer of expanded austenite with a thickness of 100-200 nm only [120]; whilst if the process is carried out at higher temperatures (400°C), the interstitial atom diffusivity is increased and a thicker expanded austenite layer is obtained [106].

A combination of ion implantation and plasma thermochemical alloys proved to increase the effectiveness of the ion implantation technology [27,121,122] but the thickness of the layer is still very limited compared to other processes.

1.8.3 Gas process

Gaseous nitriding carburizing and nitrocarburizing have been extensively used for low-temperature surface engineering of stainless steels and proved to offer several advantages compared to plasma and ion-implantation techniques in particular with respect to process control, materials handling and geometrical constraints.

Gaseous processes do not introduce additional surface defects such as, self-interstitials, vacancies and redisposition of sputtered atoms and, by controlling the nitriding potential, it is possible to control the amount of interstitials dissolved at the material´s surface (Fig. 1.18).

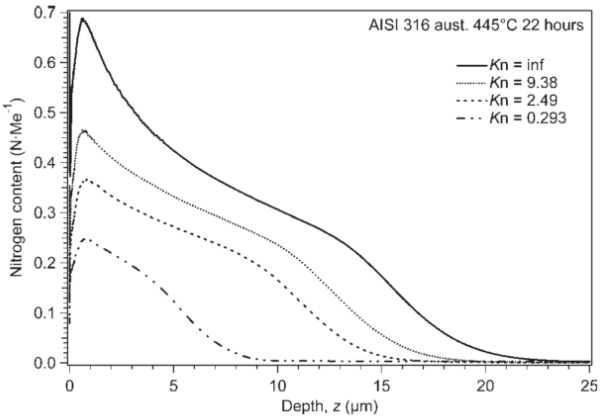

Figure 1.18: GDOES profiles on nitrided AISI 316 at different nitriding potentials [25].

The gas mixtures commonly used for the low-temperature gaseous processes are NH_3/H_2 for nitriding and $CO/H_2(/H_2O)$ or C_2H_2/H_2 for carburizing. The gas partial pressures, which are directly connected to the gas activities, define the so-called nitriding and carburizing potentials. These potentials are expressed as $K_N = p_{NH_3}/p_{H_2}^{3/2}$ for nitriding and $K_C = p_{CO} \cdot p_{H_2}/p_{H_2O}$ or $K_C = \sqrt{p_{C_2H_2}/p_{H_2}}$ for carburizing.

So far, the major limitation to the application of these gasses processes is related to the presence of a passive oxide layer at the material´s surface which hiders the dissociation of the gasses and prevents the insertion of the active species; therefore a pretreatment to remove this passive layer and activate the stainless steel surface is necessary prior to gas nitriding and/or carburizing.

Several methods have been developed for surface activation of stainless steels including pretreatment in halogen containing atmospheres [123,124], HCl gas at 250°C [125] and Plasma sputtering [126].

In 1999 Somers et al. developed a method for surface activation which involves chemical (Wood´s Ni-bath) or electrochemical ($NiCl_2$ electrolyte bath) stripping of the passive film and the subsequent

electrodeposition of a thin (20nm) layer of nickel. The electrodeposited nickel layer prevents the formation of the passive chromium oxide and catalyzes the dissociation of the gas into active species.
Subsequently Somers and Christiansen developed and patented a method for simultaneous activation and low-temperature carburizing through the use of unsaturated hydrocarbons and hydrogen (C_2H_2/ H_2) [127]. This method proved extremely efficient in the removal and breakdown of the oxide layer present at the material´s surface thanks to the formation of radicals. By controlling the gas mixtures it was possible to control the carburizing potential ($K_C = \sqrt{p_{C_2H_2/\mathrm{H2}}}$) and therefore activate the surface of the material; this allows to tailor the properties of the resulting case in one operating step.
More recently, they developed a method for in situ-surface activation also for nitriding processes; these proprietary procedures, owned by Expanite A/S, allow simultaneous activation and surface treatment with no need for any material pre-treatment.

1.9 Low-temperature surface engineering of different stainless steel classes

The excellent results and properties obtained through low-temperature nitriding of austenitic stainless steels had encouraged the scientific community in investigating the formation of an expanded phase in other steel classes such as precipitation hardening, martensitic and duplex stainless steels. In particular precipitation hardening stainless steels offer the possibility of simultaneous bulk and surface hardening because of the precipitation of hard phases occurring during the nitriding process [128].
However, no extensive research in the field has been carried out so far and the nature of the expanded phases formed after the thermochemical process is still under discussion.
Kochmanski et al. [129,130] observed the development of ε and γ' nitrides in PH 17-4 stainless steel after gaseous nitriding at 410°C whereas Kim at al. [111] recorded the formation of an expanded phase after nitriding a martensitic AISI 420 stainless steel for 4 hours at 400°C. The XRD analysis revealed a peak shift to lower angles but the absence of the 200 peak suggested that this phase could not be expanded austenite but rather expanded martensite formed during the process.
Light optical microscopy analysis revealed the formation of a layer with a significantly higher thickness than the layer created in a conventional austenitic stainless steel (AISI 304) treated with the same processing parameters; this effect is ascribed to the higher diffusion coefficient of nitrogen in martensite than in austenite [46].
Dong et al. [131] performed a SEM and TEM investigation of the layer produced in PH 17-4 SS after nitriding at various temperatures and their results show that the composition and properties of the nitrided layer is highly dependent on the processing temperature. For temperatures lower that 420°C they recorded the formation of a layer of both expanded martensite and expanded austenite. The expanded austenite present in the layer is generated from the retained austenite present in the steel matrix prior to low-temperature nitriding.

For temperatures higher than 420°C, γ'-Fe_4N was found at the surface of the material together with CrN and ferrite, sign of the decomposition of the expanded phase.

XRD characterization of the nitrided layer on Sandvik Nanoflex, a martensitic precipitation hardening stainless steel, was performed by Frandsen et al. [128]. They observed that depending on the nitriding potential applied a different expanded phase was formed, and in particular expanded martensite was observed for lower nitriding potentials whereas expanded austenite was formed at infinite nitriding potentials. The strong austenite stabilizing effect of nitrogen was accounted responsible for the transformation of martensite into austenite and thus expanded austenite.

This observation and interpretation were claimed to be inaccurate in [38] because, as shown in a previous research activity [132], it was deduced from XRD patterns where a significant degree of peak overlapping was observed.

However, in a recent work, Fernandes et al. [133] performed XRD grazing incidence investigation on PH 17-4 combined with successive layer removal. This procedure allowed avoiding peak overlapping due to the shallow penetration of the x-rays in grazing incidence geometry and confirmed that different layer compositions could be found at different depths depending on the nitrogen content (Fig. 1.19).

From the X-ray diffractograms it was possible to observe that at the material surface the layer consists mainly of epsilon nitrides $(Fe,Cr)_2N_{1-z}$ and expanded austenite. Deeper in the layer only expanded austenite was found and for higher depths γ_N disappeared and (lower nitrogen contents) expanded martensite was formed.

A schematic representation of layer composition after low temperature nitriding of a martensitic stainless steel is given in Fig. 1.20.

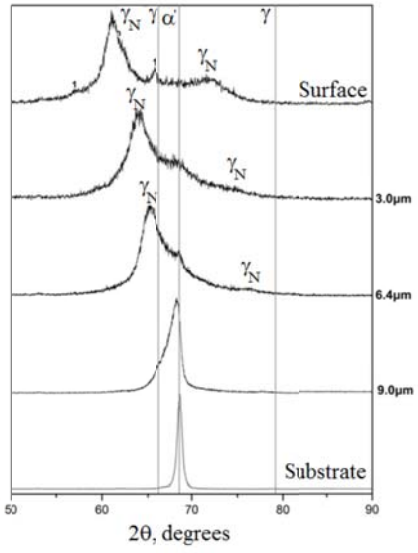

Figure 1.19: X-ray diffraction patterns after consecutive removal steps of the specimen gas nitrided at 420°C for 4h. 1-$(Fe,Cr)_2N_{1-z}$ [133].

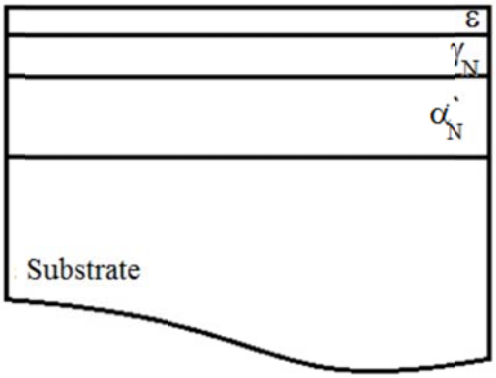

Figure 1.20: Schematic representation of the layer composition formed during low-temperature nitriding of a martensitic stainless steel at maximum nitriding potential [133].

1.10 Influence of plastic deformation and residual stress state on the nitriding process

It is recognized that in industrial practice the nitriding of components with plastic deformation in the surface region is the rule rather than the exception. As frequently observed in industrial practice, (severe) plastic deformation leads to early development of CrN during nitriding (and, analogously, Cr-carbides during carburizing); however, until now, no systematic study on the influence of plastic deformation and residual stresses on low-temperature nitriding have been carried out.

To the current authors knowledge the influence of plastic deformation at the materials' surface was only studied by Thiriet et al. [67]. In this investigation it was shown that plasma nitriding at 350°C for 8 hours on Inconel and AISI 316L leads to a significant increase in the layer thickness if severe plastic deformation by ultrasonic shot peening is applied to the material surface prior to nitriding. The reported thickness increase as consequence of shot peening prior to nitriding was from 1.7µm to 4µm for the AISI316L and from 1.3 to 3.1 for Inconel. However, no explanation has been given for the observed phenomenon.

Furthermore no presence of CrN was detected for these nitriding conditions by XRD phase analysis.

Li et al. [134] investigated the influence of elastic tensile stresses on plasma carburizing on AISI 316 in a range of temperatures form 400°C to 450°C. The tensile strain applied in situ during the carburizing process was demonstrated to have a measurable influence on the layer thickness and properties, in particular, an increasing thickness with the increasing applied load was observed for the carburized samples.

However, the authors calculated the activation energy through Fick's second law, assuming a constant diffusion coefficient throughout the layer and without taking into account the effect of stresses and trapping, and found that it decreases with increasing applied tensile load.

The external uniaxial tensile stresses applied to the samples during the carburizing process are believed to be responsible for cancelling partially the compressive residual stresses introduced in the crystal lattice as a consequence of the carbon dissolution and thus accelerating the diffusion kinetic of the interstadials in the alloy.

However, they also observed that beyond a certain value of tensile stress, precipitation of CrC and $M_{23}C_6$ type carbides occurs in the carbon expanded austenite and grain boundaries, respectively. This effect is ascribed to the activation energy for precipitation which is inversely proportional to the diffusion coefficient.

References

[1] E.J. Mittemeijer and M.A.J. Somers: *Thermochemical Surface Engineering of Steels: Improving Materials Performance*, Woodhead Publishing Ltd, Cambridge, 2014.

[2] Z.I. Zhang and T. Bell: *Surf. Eng.*, 1985, vol. 1, pp. 131–36.

[3] B.H. Kolster: *VDI. Ber.*, 1983, vol. 506, p. 107.

[4] E. Rolinski: *Surf. Eng.*, 1987, vol. 3, pp. 35–40.

[5] K. Ichii, K. Fujimura, and T. Takase: *Technol. Rep. Kansai Univ.*, 1986, vol. 27, pp. 135–44.

[6] T.L. Christiansen and M.A.J. Somers: *Surf. Interface Anal.*, 2005, vol. 21, pp. 445–55.

[7] T.L. Christiansen and M.A.J Somers: *Metall. Mater. Trans. A*, 2006, vol. 37, pp. 675–82.

[8] C. Blawert, H. Kalvelage, B.L. Mordike, G.A. Collins, K.T. Short, Y. Jirásková, and O. Schneeweiss: *Surf. Coatings Technol.*, 2001, vol. 136, pp. 181–87.

[9] Z. Cheng, C.X. Li, H. Dong, and T. Bell: *Surf. Coatings Technol.*, 2005, vol. 191, pp. 195–200.

[10] J. Buhagiar, H. Dong, and T. Bell: *Surf. Eng.*, 2007, vol. 23, pp. 313–17.

[11] T.S. Hummelshøj, T.L. Christiansen, and M.A.J Somers: *Scr. Mater.*, 2010, vol. 63, pp. 761–63.

[12] C. Blawert, B.L. Mordike, G.A. Collins, K.T. Short, Y. Jiraskova, O. Schneeweiss, and V. Perina: *Surf. Coatings Technol.*, 2000, vol. 128-129, pp. 219–25.

[13] Y. Sun, X. Li, and T. Bell: *Mater. Sci. Technol.*, 1999, vol. 15, pp. 1171–78.

[14] Y. Cao, F. Ernst, and G.M. Michal: *Acta Mater.*, 2003, vol. 51, pp. 4171–81.

[15] K. H. Jack: *Acta Crystallogr.*, 1952, vol. 5, pp. 404–11.

[16] T.L. Christiansen, T.S. Hummelshøj, and M.A.J. Somers: *Surf. Eng.*, 2010, vol. 26, pp. 242–47.

[17] Y. Sun, T. Bell, Z. Kolosvary, and J. Flis: *Met. Sci. Heat Treat.*, 1999, vol. 26, p. 9.

[18] K. Aoki and K. Kitano: *Surf. Eng.*, 2002, vol. 18, pp. 462–63.

[19] T.L. Christiansen and M.A.J. Somers: *Scr. Mater.*, 2004, vol. 50, pp. 35–37.

[20] A. Leyland, D.B. Lewis, P.R. Stevenson, and A. Matthews: *Surf. Coatings Technol.*, 1993, vol. 62, pp. 608–17.

[21] K. Marcher, C.V. Cooper, J.T. Blucher, and B.C. Giessen: *Surf. Coatings Technol.*, 1997, vol. 99, pp. 225–28.

[22] Y. Sun, X. Y. Li, and T. Bell: in *Stainl. Steel 2000 Thermochem. Surf. Eng. Stainl. Steel*, Osaka, Japan, 2000, pp. 263–73.

[23] X.Y. Li: *Surf. Eng.*, 2001, vol. 17, pp. 147–52.

[24] E. Menthe and K.T. Rie: *Surf. Coatings Technol.*, 1999, vol. 116-119, pp. 199–204.

[25] T.L. Christiansen and M.A.J Somers: *Int. J. Mater. Res. Former. Zeitschrift Fuer Met.*, 2009, vol. 100, pp. 1361–77.

[26] B. Brink: *Ph.D. Thesis - Synthesis and characterization of homogeneous interstitial solutions of nitrogen and carbon in iron-based lattices*, DTU - Technical University of Denmark, Lyngby, Denmark, 2015.

[27] M.K. Lei and X.M. Zhu: *Surf. Coatings Technol.*, 2005, vol. 193, pp. 22–28.

[28] W. Liang, X. Bin, Y. Zhiwei, and S. Yaqin: *Surf. Coatings Technol.*, 2000, vol. 130, pp. 304–8.

[29] X.Y. Li: *Ph.D. Thesis - Characterization of S-Phase*, University of Birmingham, Birmingham, UK, 1999.

[30] J.C. Stinville, P. Villechaise, C. Templier, J.P. Rivière, and M. Drouet: *Acta Mater.*, 2010, vol. 58, pp. 2814–21.

[31] C. Templier, J.C. Stinville, P. Villechaise, P.O. Renault, G. Abrasonis, J.P. Rivière, A. Martinavičius, and M. Drouet: *Surf. Coatings Technol.*, 2010, vol. 204, pp. 2551–58.

[32] J.C. Stinville, J. Cormier, C. Templier, and P. Villechaise: *Acta Mater.*, 2015, vol. 83, pp. 10–16.

[33] G. Winther, L. Margulies, S. Schmidt, and H.F. Poulsen: *Acta Mater.*, 2004, vol. 52, pp. 2863–72.
[34] H.F. Poulsen, L. Margulies, S. Schmidt, and G. Winther: *Acta Mater.*, 2003, vol. 51, pp. 3821–30.
[35] R. Pokharel, J. Lind, A.K. Kanjarla, R.A. Lebensohn, S.F. Li, P. Kenesei, R.M. Suter, and A.D. Rollett: *Annu. Rev. Condens. Matter Phys.*, 2014, vol. 5, pp. 317–46.
[36] C. Blawert, B.L. Mordike, Y. Jirásková, and O. Schneeweiss: *Surf. Coatings Technol.*, 1999, vol. 116-119, pp. 189–98.
[37] S. Mändl and B. Rauschenbach: *J. Appl. Phys.*, 2000, vol. 88, p. 3323.
[38] H. Dong: *Int. Mater. Rev.*, 2010, vol. 55, p. 34.
[39] T.L. Christiansen, T.S. Hummelshøj, and M.A.J. Somers: WO2012 146254-A1, 2012.
[40] C. Genzel, S. Krahmer, M. Klaus, and I.A. Denks: *J. Appl. Crystallogr.*, 2010, vol. 44, pp. 1–12.
[41] S. Jegou, T.L. Christiansen, M. Klaus, C. Genzel, and M.A.J. Somers: *Thin Solid Films*, 2013, vol. 530, pp. 71–76.
[42] F.A.P. Fernandes, T.L. Christiansen, Grethe Winther, and M.A.J. Somers: *Acta Mater.*, 2015, vol. 94, pp. 271–80.
[43] K. Frisk M. Kikuchi, M. Kajihara: *HNS 88 Lille (France)*, The insitute of Metals, London, 1989, p. 63.
[44] H. Okamoto: *J. Phase Equilibria*, 1992, vol. 13, pp. 543–65.
[45] K. H. Jack: *R. Soc.*, 1948, vol. 195.
[46] J.R.G. Da Silva and R.B. McLellan: *Mater. Sci. Eng.*, 1976, vol. 26, pp. 83–87.
[47] K. Farrell, E.D. Specht, J. Pang, L.R. Walker, A. Rar, and J.R. Mayotte: *J. Nucl. Mater.*, 2005, vol. 343, pp. 123–33.
[48] Y. Ueda, N. Kanayama, K. Ichii, T. Oishi, and H. Miyake: *Surf. Coatings Technol.*, 2005, vol. 193, pp. 50–54.
[49] T. Bell: *Key Eng. Mater.*, 2008, vol. 373-374, pp. 289–95.
[50] X. Y. Li, Y. Sun, and T. Bell: *Zeitschrift Für Met.*, 1999, vol. 90, pp. 901–7.
[51] X. Y. Li, S. Thaiwatthana, H. Dong, and T. Bell: *Surf. Eng.*, 2002, vol. 18, pp. 448–51.
[52] T.L. Christiansen and M.A.J Somers: *Zeitschrift Fur Met.*, 2006, vol. 97, pp. 79–88.
[53] F. Ernst, Y. Cao, and G.M. Michal: *Acta Mater.*, 2004, vol. 52, pp. 1469–77.
[54] F. Ernst, Y. Cao, G.M. Michal, and A.H. Heuer: *Acta Mater.*, 2007, vol. 55, pp. 1895–1906.
[55] S. Parascandola, W. Möller, and D.L. Williamson: *Appl. Phys. Lett.*, 2000, vol. 76, p. 2194.
[56] S. Parascandola, R. Günzel, R. Grötzschel, E. Richter, and W. Möller: *Nucl. and Meth. in Phys. Res. B,* 1998, vol. 136-138, pp. 1281-85.
[57] S. Mändl, F. Scholze, H. Neumann, and B. Rauschenbach: *Surf. Coatings Technol.*, 2003, vol. 174–175, pp. 1191–95.
[58] S. Mändl and B. Rauschenbach: *J. Appl. Phys.*, 2002, vol. 91, p. 9737.
[59] T.L. Christiansen, K.V. Dahl, and M.A.J. Somers: *Mater. Sci. Technol.*, 2008, vol. 24, pp. 159–67.
[60] T.L. Christiansen and M.A.J. Somers: *Defect Diffus. Forum*, 2006, vol. 258-260, pp. 384–89.
[61] R.E. Schacherl, P.C.J. Graat, and E.J. Mittemeijer: *Metall. Mater. Trans. A*, 2004, vol. 35, pp. 3387–98.
[62] T.L. Christiansen and M.A.J. Somers: *Metall. Mater. Trans. A*, 2008, vol. 40, pp. 1791–98.
[63] F.N. Jespersen, J.H. Hattel, and Marcel A.J. Somers: *ASM Heat Treat. 2015*, Detroit, USA, 2015, p. in press.
[64] C. Wells, W. Batz, and R.F. Mehl: *Trans. AIME*, 1950, vol. 188, p. 553.
[65] O. Öztürk and D.L. Williamson: *J. Appl. Phys.*, 1995, vol. 77, p. 3839.
[66] A. Martinavičius, G. Abrasonis, W. Möller, C. Templier, J.P. Rivière, A. Declémy, and Y. Chumlyakov: *J. Appl. Phys.*, 2009, vol. 105, p. 093502.
[67] T. Thiriet, T. Czerwiec, D. Hertz, G. Marcos, T. Toll-Duchanoy, S. Migot, B. Brugier, M. Foucault, and T. Belmonte: *Defect Diffus. Forum*, 2012, vol. 323-325, pp. 471–76.

[68] T. Czerwiec, H. He, G. Marcos, T. Thiriet, S. Weber, and H. Michel: *Plasma Process. Polym.*, 2009, vol. 6, pp. 401–9.
[69] H. He, T. Czerwiec, C. Dong, and H. Michel: *Surf. Coatings Technol.*, 2003, vol. 163-164, pp. 331–38.
[70] S. Thaiwatthana, X. Y. Li, H. Dong, and T. Bell: *Surf. Eng.*, 2002, vol. 18, pp. 433–37.
[71] Y. Sun and T. Bell: *Wear*, 1998, vol. 218, pp. 34–42.
[72] S Mändl, R. Günzel, E. Richter, and W. Möller: *Surf. Coatings Technol.*, 1998, vol. 100-101, pp. 372–76.
[73] E. Menthe, A. Bulak, J. Olfe, A. Zimmermann, and K.T. Rie: *Surf. Coatings Technol.*, 2000, vol. 133-134, pp. 259–63.
[74] X.B. Tian, Z.M. Zeng, B.Y. Tang, T.K. Kwok, and P.K.U. Chu: *Surf. Coatings Technol.*, 2000, vol. 128-129, pp. 226–30.
[75] T.L. Christiansen and M.A.J. Somers: *Mater. Sci. Forum*, 2004, vol. 443-444, pp. 91–94.
[76] T.L. Christiansen and M.A.J Somers: *Mater. Sci. Eng. A*, 2006, vol. 424, pp. 181–89.
[77] V. Hauk: *Structural and Residual Stress Analysis by Nondestructive Methods*, Elsevier, 1997.
[78] U. Welzel, J. Ligot, P. Lamparter, A.C. Vermeulen, and E.J. Mittemeijer: *J. Appl. Crystallogr.*, 2005, vol. 38, pp. 1–29.
[79] T.L. Christiansen: Ph.D. Thesis - Low Temperature surface hardening of stainless steels, DTU - Technical University of Denmark, Lyngby, Denmark, 2004.
[80] C. Allen, C.X. Li, T. Bell, and Y. Sun: *Wear*, 2003, vol. 254, pp. 1106–12.
[81] L. Ceschini and G. Minak: *Surf. Coatings Technol.*, 2008, vol. 202, pp. 1778–84.
[82] K. Tokaji, K. Kohyama, and M. Akita: *Int. J. Fatigue*, 2004, vol. 26, pp. 543–51.
[83] L.L. Shreir, R.A. Jarman, and G.T. Burstein: *Materials and Corrosion*, 3rd ed., Butterworth-Heinemann, Oxford, 1994.
[84] C.X. Li and T. Bell: *Corros. Sci.*, 2004, vol. 46, pp. 1527–47.
[85] E. Camps, F. Becerril, S. Muhl, O. Alvarez-Fregoso, and M. Villagrán: *Thin Solid Films*, 2000, vol. 373, pp. 293–98.
[86] H. Baba, T. Kodama, and Y. Katada: *Corros. Sci.*, 2002, vol. 44, pp. 2393–2407.
[87] A. Srinivasan, B. Reynerds, and J. Grabke: *Steel Res.*, 1995, vol. 66, pp. 439–43.
[88] T.H. de Keijser, J.I. Langford, E.J. Mittemeijer, and A.B.P. Vogels: *J. Appl. Crystallogr.*, 1982, vol. 15, pp. 308–14.
[89] I. Olefjord and L. Wegrelius: *Corros. Sci.*, 1996, vol. 38, pp. 1203–20.
[90] C.O.A. Olsson: *Corros. Sci.*, 1995, vol. 37, pp. 467–79.
[91] Y.C. Lu, R. Bandy, C.R. Clayton, and R.C. Newman: *J. Electrochem. Soc.*, 1983, vol. 130, p. 8.
[92] B. Normand, A. Pierre, and J. Pagetti: *Corros. Sci.*, 1995, vol. 37, pp. 1537–49.
[93] K. Osozawa: *Japan Soc. Heat Treat.*, 1985, vol. 36, pp. 206–12.
[94] K. Osozawa, N. Okato, Y. Fukase, and K. Yokota: *Boshoku Gjtutsu (Corros. Eng.)*, 1975, vol. 24, p. 1.
[95] X.Y. Li and H. Dong: *Mater. Sci. Technol.*, 2003, vol. 19, pp. 1427–34.
[96] X. Tian and P.K. Chu: *Scr. Mater.*, 2000, vol. 43, pp. 417–22.
[97] M.K. Lei and X.M. Zhu: *Biomaterials*, 2001, vol. 22, pp. 641–47.
[98] L.C. Gontijo, R. Machado, S.E. Kuri, L.C. Casteletti, and P.A.P. Nascente: *Thin Solid Films*, 2006, vol. 515, pp. 1093–96.
[99] M. Kuczynska-Wydorska and J. Flis: *Corros. Sci.*, 2008, vol. 50, pp. 523–33.
[100] Y. Sun: *Trans. Mater. Heat Treat.*, 2004, vol. 25, pp. 307–10.
[101] T. Makishi and K. Nakata: *Metall. Mater. Trans. A*, 2004, vol. 35, pp. 227–38.
[102] O. Öztürk and D.L. Williamson: *Surf. Coatings Technol.*, 2002, vol. 158-159, pp. 288–94.
[103] S. Mändl, R. Günzel, and E. Richter: *Surf. Coatings Technol.*, 2000, vol. 128-129, pp. 423–28.
[104] G. Michal, F. Ernst, H. Kahn, Y. Cao, F. Oba, N. Agarwal, and A. Heuer: *Acta Mater.*, 2006, vol. 54, pp. 1597–1606.

[105] M. Tsujikawa, S. Noguchi, N. Yamauchi, N. Ueda, and T. Sone: *Surf. Coatings Technol.*, 2007, vol. 201, pp. 5102–7.
[106] D.L. Williamson, O. Ozturk, R. Wei, and P.J. Wilbur: *Surf. Coatings Technol.*, 1994, vol. 65, pp. 15–23.
[107] F. Pedraza, C. Savall, G. Abrasonis, J.P. Rivière, J.F. Dinhut, and J.L. Grosseau-Poussard: *Thin Solid Films*, 2007, vol. 515, pp. 3661–69.
[108] E. Menthe, K.-T. Rie, J.W. Schultze, and S. Simson: *Surf. Coatings Technol.*, 1995, vol. 74-75, pp. 412–16.
[109] J.P. Lebrun, Michel. H., and M. Gantois: *Mém. Sci. Rev. Met.*, 1972, vol. 10, p. 727.
[110] T. Bell and Y. Sun: *Stainless Steel 2000: Thermochemical Surface Engineering of Stainless Steel*, The Institute of Materials, London, 2001.
[111] S.K. Kim, J.S. Yoo, J.M. Priest, and M.P. Fewell: *Surf. Coatings Technol.*, 2003, vol. 163-164, pp. 380–85.
[112] M.P. Fewell, D.R.G. Mitchell, J.M. Priest, K.T. Short, and G.A. Collins: *Surf. Coatings Technol.*, 2000, vol. 131, pp. 300–306.
[113] S. Leigh, M. Samandi, G.A. Collins, K.T. Shortb, P. Martin, and L. Wielunski: *Surf. Coatings Technol.*, 1996, vol. 85, pp. 37–43.
[114] V.I. Dimitrov, J. D'Haen, G. Knuyt, C. Quaeyhaegens, and L.M. Stats: *Surf. Coatings Technol.*, 1998, vol. 99, pp. 234–41.
[115] C. Jr. Alves, E.F. da Silva, and A.E. Martinelli: *Surf. Coatings Technol.*, 2001, vol. 139, pp. 2–6.
[116] A.R.P de Ataíde, C. Jr. Alves, V. Hajek, and J.P. Leite: *Surf. Coatings Technol.*, 2003, vol. 167, pp. 52–58.
[117] K.T. Rie: *Surf. Coatings Technol.*, 1999, vol. 112, pp. 56–62.
[118] H. Dong and T. Bell: *Surf. Coatings Technol.*, 1999, vol. 111, pp. 29–40.
[119] P. Sioshansi: *Thin Solid Films*, 1984, vol. 118, pp. 61–72.
[120] S. Fayeulle: *Defect Diffus. Forum*, 1988, vol. 57-58, pp. 327–58.
[121] J.R. Conrad: *Mater. Sci. Eng. A*, 1989, vol. 116, pp. 197–203.
[122] J.R. Conrad, R.A. Dodd, F.J. Worzala, and X. Qiu: *Surf. Coatings Technol.*, 1988, vol. 36, pp. 927–37.
[123] K. Aoki, T. Shirahata, M. Tahara, and K. Kitano: *Stainless Steel 2000: Thermochemical Surface Engineering of Stainless Steel*, The Institute of Materials, London, 2001.
[124] M. Tahara, H. Senbokuya, K. Kitano, T. Hayashida, and T. Minato: Patent no. EP 0588458B1, 1996.
[125] P. C. Williams and S. V. Mark: Patent no. 6547888B1, 2003.
[126] J. Baranowska: *Surf. Coatings Technol.*, 2004, vol. 180-181, pp. 145–49.
[127] M.A.J. Somers and T.L. Christiansen: Patent no. WO 2006136166_A1, 2006.
[128] R.B. Frandsen, T.L. Christiansen, and M.A.J. Somers: *Surf. Coatings Technol.*, 2006, vol. 200, pp. 5160–69.
[129] P. Kochmanski and J. Nowacki: *Surf. Coatings Technol.*, 2008, vol. 202, pp. 4834–38.
[130] P. Kochmański and J. Nowacki: *Surf. Coatings Technol.*, 2006, vol. 200, pp. 6558–62.
[131] H. Dong, M. Esfandiari, and X.Y. Li: *Surf. Coatings Technol.*, 2008, vol. 202, pp. 2969–75.
[132] Y. Sun and T. Bell: *Surf. Eng.*, 2003, vol. 19, pp. 331–36.
[133] F.A.P. Fernandes, T.L. Christiansen, and M.A.J. Somers: *Proc. 28th Int. Conf. Surf. Modif. Technol.*, Valardocs, Tampere, Finland, 2014, pp. 223–33.
[134] W. Li, X. Li, and H. Dong: *Acta Mater.*, 2011, vol. 59, pp. 5765–74.

2 High Nitrogen Steels

High Nitrogen Steels

2.1 Introduction

Austenitic stainless steels are widely used in several industrial applications due to their excellent mechanical and corrosion properties [1-3].The stability of the austenite phase is strongly dependent on the material´s chemical composition.

The alloying elements used in stainless steels have specific influences on the final microstructure and phase composition [3]. Depending on their effect, the various alloying elements are grouped into two main categories: austenite stabilizing elements and ferrite stabilizing elements. The former is usually expressed in terms of Ni-equivalent and the latter is described by a Cr-equivalent. Hence, by knowing the exact chemical composition, it is possible to predict the final phase composition of the stainless steel (Fig. 2.1).

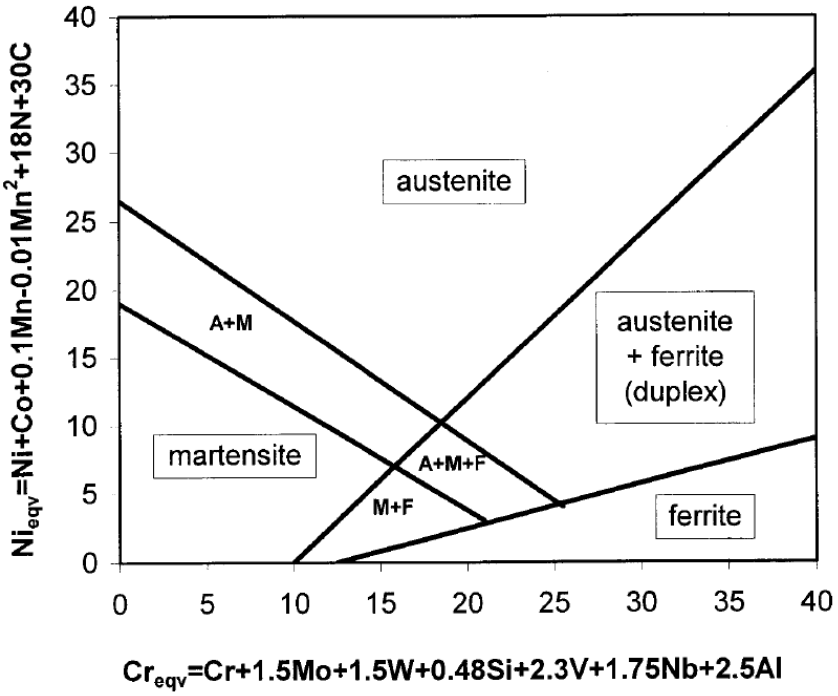

Figure 2.1: Modified Schaeffler diagram for high chromium steels. The diagram allows the predition of the phase composition as fucntion of the Cr and Ni equivalent for stainless steels [4].

Ni is extensively used for the production of austenitic stainless steels, but in the past decades, due to its high price, a general tendency for its substitution with other, less expensive, austenite stabilizers has been recorded [5–7]. In this respect, it can be mentioned that nitrogen is a very potent austenite stabilizer and its addition to the melt could lead to an important reduction of nickel content required for the production of austenitic stainless steels [8].

The effects of nitrogen as alloying element in stainless steel have been studied since the beginning of the 20th century [9] and, especially in the past decades, attempts were made to replace the expensive nickel-based stainless steels with high nitrogen steels [10,11].

Nitrogen decreases the tendency for the formation of martensite upon cooling and strain-induced martensite upon deformation [12] and offers many unique advantages compared to other alloying elements in terms of mechanical properties and corrosion resistance. Nitrogen is a stronger solid-solution strengthener than carbon or boron and enhances grain size strengthening [7,13]. Its addition in solid solution allows a remarkable increase of the yield and tensile strength, up to 350% in the annealed condition, compared to stainless steels of the AISI 200 and 300 series [12,14–16]. From a corrosion point of view, it has been shown that nitrogen brings about an improvement of the pitting and corrosion resistance [17,18].

Because of the above-mentioned favourable properties of nitrogen alloying, high nitrogen steels are becoming an important class of engineering materials and are considered as suitable substitute for Ni-based stainless steel in various industries where corrosion resistance and good mechanical properties are required [10,11,19].

However, the main limitation to their use in industry is related to their production. The solubility of nitrogen in liquid Fe and Fe-based alloys is extremely low at atmospheric pressure and therefore it is difficult to obtain high nitrogen concentrations in the melt and maintain them in solution during solidification [20,21].

Because of the challenges of nitrogen alloying, high melting pressure or powder metallurgy technologies are often used for the production of high nitrogen steels (HSN).

In the following sections an overview of the properties of HNS and the most common production routes for their production will be given.

2.2 Solubility of nitrogen

Solubility of gaseous nitrogen in liquid iron and iron-based alloys is the main obstacle for the production of high nitrogen steels [14]. In general the nitrogen solubility is a function of the temperature and pressure of the melt, and the alloy composition [20,22].

The solubility of nitrogen in liquid iron is 0.045% at 1600°C at atmospheric pressure, but it increases at higher pressure [20] (Figs. 2.2-2.3).

At low pressures, the nitrogen solubility follows Sievert's law; i.e. the solubility is proportional to the square root of the pressure. For high-pressures, there is a deviation from Sievert's law, and the solubility increases with the increasing pressure with a power less than ½ [20,22–24] (Fig. 2.3).

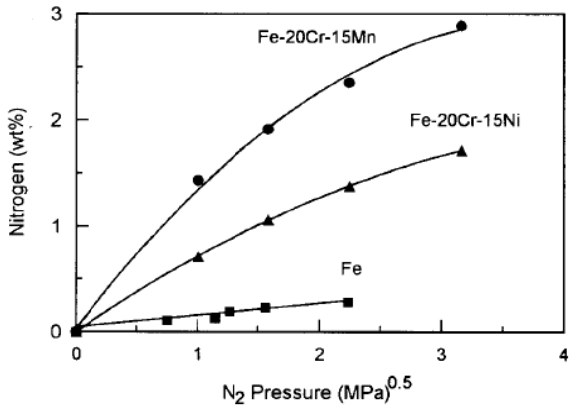

Figure 2.2: Influence of the pressure on solubilty of nitrogen in liquid iron and stainless steel alloys at 1600°C [20].

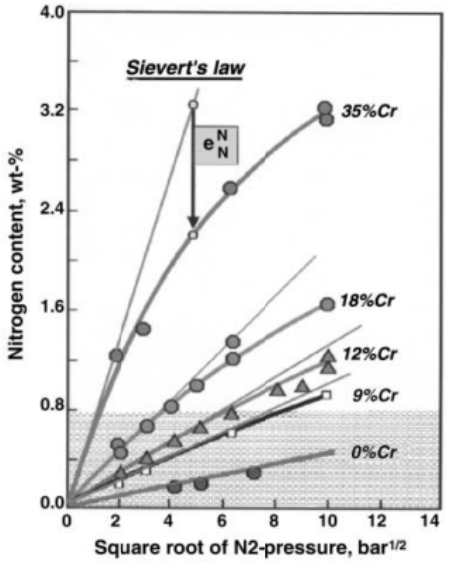

Figure 2.3: Influence of pressure and chemical composition at 1600°C on the solubilty of nitrogen; deviation from the Siviert´s law for higher pressure [10].

Alloying elements have a strong influence on the nitrogen solubility; in general nitride-forming elements such as Ti, Zr, V, Nb and Cr, in order of strength, lower the activity of nitrogen in the melt, and thus increase its solubility, whereas elements such as Ni or Al lower it (Fig. 2.4) [21,24].

Fig. 4 depicts the effect of various alloying elements on the nitrogen solubility normalized to the effect of Cr. It is possible to observe that apart from the strong effect of nitride-forming elements, also Mn, which is an austenite stabilizer element, enhances the solubility on nitrogen in the melt.

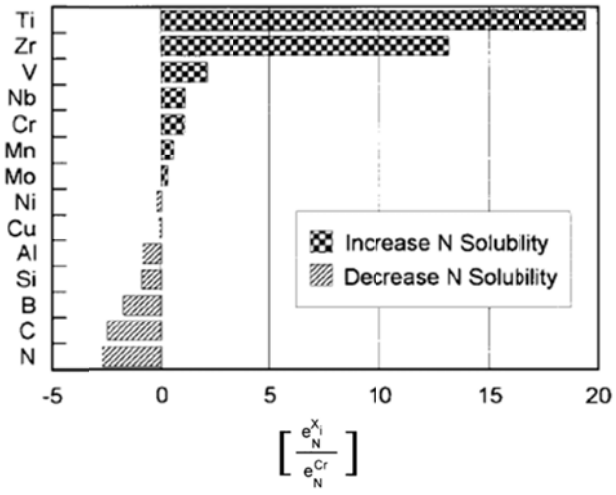

Figure 2.4: Effect of the various alloying elements on the nitrogen solubility in liquid iron, normalized to the effect of Cr [20]

It is reported that at 1600°C and 10 MPa, 3 wt% of N can be dissolved in molten Fe-20Cr-15Mn alloy while only 1wt% can be attained in Fe-20Cr-Ni alloys [12].

An equation (Eq. 2.1) for the prediction on nitrogen solubility in wt%, as a function of the composition was found by Speidel [5], showing excellent agreement with experimental data and empirical equation.

$$\%N = 0.067\%Cr + 0.02\%Mn + 0.04\%Mo - 0.01Ni - 1 \qquad \text{Equation 2.1}$$

The addition of strong nitride-forming elements to the melt to increase the solubility of nitrogen, results in a high-risk for precipitation of nitrides upon solidification. Chromium, abundantly present in the stainless steel composition, shows a less pronounced tendency for nitride formation compared to elements such as Ti, Zr, V and Nb but Cr_2N grain boundary precipitation was observed in Fe-Cr-Ni and Fe-Cr-Mn alloys during cooling or when the material is exposed to temperatures between 600°C and 1050 °C [8,25–27] . However, in a Fe-Cr-Mn alloy, the precipitation kinetics of this type of nitrides is approximately ten times slower compared to Ni-containing alloys. This effect is mainly related to the fact that nickel decreases nitrogen solubility whereas manganese increases it [21]. For this reason, Ni is usually partially or entirely replaced by manganese for the production of high nitrogen steel alloys.

The precipitation of secondary phases is highly undesirable as it impairs the mechanical and corrosion properties of the steel, therefore it should be avoided or minimized. To this end rapid quenching is usually employed during production of HNS in order to avoid precipitation of second phases.

Hence, the knowledge of the thermodynamics of the multicomponent system and the transformation kinetics for the various chemical compositions of the alloys are a necessary prerequisite for the production of high nitrogen steels.

2.3 Production techniques

2.3.1 High-pressure melting

The solubility of nitrogen can be increased by increasing the pressure of the melt and controlling the alloy´s chemical composition. Nitrogen is usually inserted in the liquid melt in two different ways: (1) decomposition of N_2 gas at the gas-liquid interface and dissolution of atomic N or (2) addition and remelting of stable nitrides to the melt.

Various high-pressure melting techniques have been developed through the years operating according to these different mechanisms [10,19,28,29].

Hot-isostatic pressure (HIP) and pressurized induction furnace operate according to the first mechanism. Through the reaction of nitrogen gas at the gas-liquid interface, atomic nitrogen is dissolved in the melt and the maximum concentration obtained in the liquid alloy is a function of the operating pressure above the melt. Because of the high concern for safety related to the very high operating pressure (up to 200MPa), other techniques operating at lower pressures are usually preferred in industrial production.

Pressurized electro-slag remelting (PESR) is usually the most used technique for industrial production of HNS. Nitrogen is dissolved in the melt by adding high-nitrogen additives such as FeCrN, CrN and Si_3N_4

into the slag. It operates at lower pressures (42 MPa) compared to other processes and in this case the pressure above the melt serves exclusively to keep the nitrogen in solution in the molten metal.

2.3.2 Powder metallurgy

Through powder metallurgy techniques it is possible to produce alloys with supersaturated levels of interstitial nitrogen. Because of the higher solubility of nitrogen in the solid state than in the liquid state, it is possible to obtain higher nitrogen levels compared to high pressure melting techniques [21]
The most common techniques for production of HNS with powder metallurgy methods are high-pressure-high-temperature diffusion and pressurized gas atomization [14].
In high-pressure-high-temperature diffusion processes a hot-isostatic pressure furnace is used for the diffusion of nitrogen in stainless steel powders. The amount of nitrogen dissolved is a function of the operating pressure and temperature as well as the time and chemical composition of the initial alloys. Stainless steel powders with a nitrogen level of 6wt% in solid solution were obtained through the use of this technique in a Fe-18Cr-18Ni stainless steel [30].
For the gas atomization process, nitrogen is used as backfilling gas in the melt chamber and it is possible to produce stainless steel powders with high nitrogen concentrations [14].

2.3.3 Solution nitriding

So far, high temperature solution nitriding is mainly used as a surface engineering process for the dissolution of high nitrogen contents at the surface of martensitic, ferritic and duplex stainless steels.
This allows the creation of a nitrogen martensite case which is characterized by high hardness and excellent wear resistance [19,31].
The dissolution of N through high temperature solution nitriding is also used for the thin-walled component for the conversion of commercially available stainless steels into high nitrogen steels and can be applied to several stainless steel classes.
As for the powder metallurgy process, the dissolution of nitrogen occurs in the solid state, where the solubility is higher.
The annealing procedure is performed in a nitrogen gas atmosphere and followed by inert gas quench to room temperature in order to maintain the dissolved nitrogen in solid solution and avoid formation of nitrides.
The amount of nitrogen that can be dissolved in the alloys is a function of several parameters including time, temperature, partial pressure of N_2 gas and chemical composition of the alloys.

2.4 Properties of HNS

2.4.1 Stabilization of austenite

Nitrogen is a very effective austenite stabilizer and it increases the austenite stability more effectively than other substitutional elements such as nickel or manganese. The effect of nitrogen on the formation of martensite upon cooling and deformation has been widely investigated in the literature [12].
In all the expressions to calculate the martensitic start temperature and the strain-induced martensite temperature, the nitrogen contribution is significantly higher than other alloying elements [5].
In this respect, the martensite start temperature is reported to decrease more than 1500°C while the strain-induced martensite temperature is also reduced about 250°C for nitrogen addition of 1 %wt [32].

2.4.2 Yield strength

The influence of substitutional elements on the yield strength (YS) of stainless steels is usually negligible or in some cases even negative (e.g. Ni). However the presence of interstitials such as C, B and in particular N allows a considerable increase of the yield strength [12].
Nitrogen is the most effective solid solution strenghtener of all the interstitial atoms used for stainless steel alloying [16] because it locks dislocations more efficiently than other interstitial elements, thus resulting into a greater obstacle for dislocation slip [33].
Its contribution to the marked increase in the flow stress is mainly due to two effects: solid-solution strengthening and grain-size strengthening.
The YS and ultimate tensile strength (UTS) at room temperature increase linearly with the increasing nitrogen content (Fig. 2.5) without compromising the steel ductility [15].

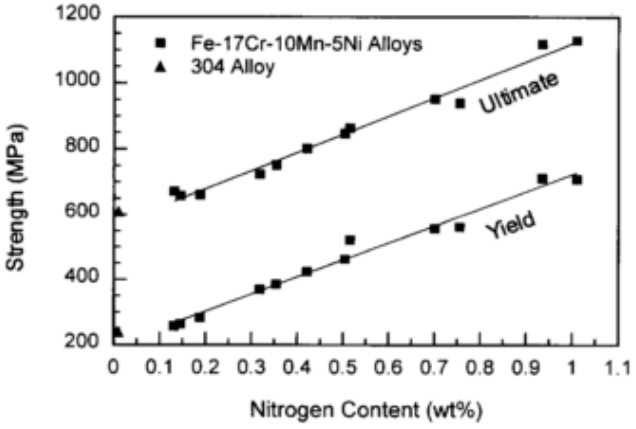

Figure 2.5: Increase of YS and UTS as function of the dissolved nitrogen [14]

In HNS the grain-size hardening effect (Hall-Petch slope) increases proportionally to the nitrogen content. Werner et al. [7] found that an increase of 400 MPa in the YS is obtained in a steel with 0.6 wt% N when

decreasing the grain size from 100μm to 10μm, whereas a much less pronounced increase (100Mpa) is found for 0.6 wt% C.

Because of the reasons listed above, the yield strength of HNS could be significantly augmented by cold deformation [34]. The presence of nitrogen increases the ability of austenite to be strengthened by deformation and it causes an increase of the strain hardening rate and strength coefficient, whereas no significant variation of the strain-hardening exponent was found [35].

Since heat-treatment cannot be applied in single phase materials, cold working is a very efficient way to obtain high YS materials and it is a widely used technique for hardening of HSN [14].

A marked increase in the yield strength with the increasing nitrogen content is also observed at cryogenic temperatures, however, if Mo and Ni are not present in the alloy, a significant embrittlement and thus a ductile-to-brittle transition is observed [36–38].

The strengthening effect of nitrogen is lost at higher temperatures; HNS in fact exhibits a decrease in the YS in the range of temperatures from 250°C to 600°C Fig. 2.6 [13].

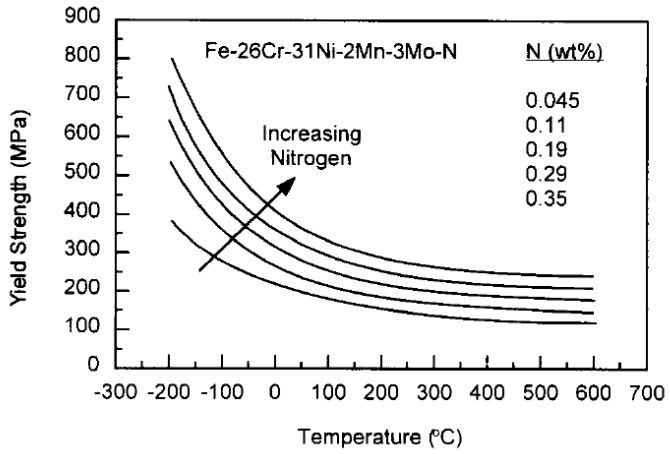

Figure 2.6: Dependence of the YS as function of temperature and nitrogen content [14].

The high strain hardening effect observed in HNS can be related to the dislocation structure produced upon plastic deformation. The dislocation structure created in high nitrogen steels differs greatly from the one observed in stainless steels not containing nitrogen. In the austenitic stainless steel of the 300 series a homogenous cellular dislocation structure as a result of plastic deformation is usually observed [39,40].

In HNS however, planar dislocation structures are observed [39,40]. This type of dislocation favours planar slip over cross-slip and thus leads to an enhanced strain hardening effect.

The preferential dislocation structure formed upon straining in HNS material is a direct consequence of: (1) lower stacking fault energy due to addition of nitrogen which reduces the tendency for cross-slip and climbing of dislocation and (2) short range atomic ordering occurring between Cr and N atoms [39–42].

In particular this second effect is due to the fact that the stronger Cr-N bond as compared to Fe-N and Ni-N bonds, therefore nitrogen resides preferentially in proximity of a Cr atom. Short range ordering increases the flow-stress due to the disruption of the local ordered structure.

2.4.3 Creep and fatigue

So far, the influence of nitrogen addition on the fatigue and creep resistance has been studied for nitrogen contents lower than 0.4 wt%; no data on HNS (N>0.4 wt%) could be found [14].
However, it has been demonstrated that even small nitrogen additions have a beneficial effect on both the creep behaviour and fatigue resistance [43–47].
For nitrogen-alloyed steels, it was possible to observe a decrease of the minimum creep rate and an increase of the rupture strength with increasing nitrogen contents even for high creep temperatures (1000 °C) [43].
At the investigated nitrogen concentrations, the increase of the creep resistance was attributed to the presence of nitrogen that inhibits carbide precipitation and favours planar slip. The suppression of cross-slip prevents subgrain formation, thus leading to a more homogeneous dislocation distribution.
Despite the results on stainless steel containing nitrogen up to 0.4wt% show the positive effect of nitrogen addition in creep resistance, the creep behaviour of HNS steels has not been investigated in detail. However, it is believed that the higher tendency for nitrides formation in HNS at the creep temperatures may affect the material´s performance. The stability of the alloy, and the effect of nitrides formation on the strength and flow properties will then determine the creep behaviour of the steel [14].
The more homogenous dislocation structure developed upon deformation is also believed to be responsible for the improved fatigue life compared to austenitic stainless steels not containing nitrogen [45].
The probability for strain localization and crack initiation is lowered. In addition greater slip reversibility is promoted, thus preventing the formation of persistent slip bands which will favour crack growth.

2.4.4 Corrosion properties

Austenitic stainless steels are well known for their excellent corrosion resistance due to the formation of a dense chromium oxide layer at the surface of the material [48]. However, it is sensitive for localized corrosion attacks such as pitting and crevice corrosion. In general the resistance of stainless steels to localized corrosion can be increased with the addition of elements such as Mo and N. In this respect, nitrogen is more efficient than the other substitutional elements and has been proven to increase significantly the resistance to localized attacks.
The steel resistance to localized attacks is usually measured with an index known as PREN (pitting resistance equivalent number). This index is a function of the weight % of the alloying elements present in the alloy and it expressed as follows:

$$\mathrm{PREN} = \%\mathrm{Cr} + 3.3\%\mathrm{Mo} + \mathrm{x}\%\mathrm{N} \qquad \text{Equation 2.2}$$

with x ranging from 13 to 30 [17,49]. In general the factor for nitrogen contribution is set to 16 and in the plot of the pitting potential as function of the PREN number, a plateau maximum is reached for PREN number higher than 33 [48,49].

Another index used for the prediction of resistance of stainless steels to localized corrosion is the MARC index; compared to the PREN number, the MARC index takes into account the influence of more alloying elements such as carbon, manganese and nickel [50–52]. The expression for the MARC number is the sum of the various contributions in weight % and is expressed as follows:

$$\mathrm{MARC} = \%\mathrm{Cr} + 3.3\%\mathrm{Mo} + 20\%\mathrm{N} + 20\%\mathrm{C} - 0.5\mathrm{Mn} - 0.25\mathrm{Ni} \qquad \text{Equation 2.3}$$

In both cases, it is possible to observe that nitrogen addition has a significant effect on the resistance to localized corrosion.

The influence of nitrogen addition on the corrosion properties of several stainless steel grades in various acidic and Cl^--containing solutions has been widely instigated in the literature [53–57].

The effect on the critical current density (i_{crit}) has not been fully understood since some researchers claim that nitrogen lowers the critical current density whereas others state that it has a negative or no effect.

However a systematic increase in the pitting potential has been observed with increasing nitrogen content in the alloy [53,58–64].

Speidel performed a series of tests on the critical pitting corrosion temperature in a 22wt% NaCl solution for various alloys [65]. The results of the potentiodynamic measurements confirmed that the critical temperature, defined as the temperature at which the localized attack is observed, increases with the increasing nitrogen content, thus confirming the strong effect of nitrogen on improving the steel´s pitting resistance (Fig. 2.7)

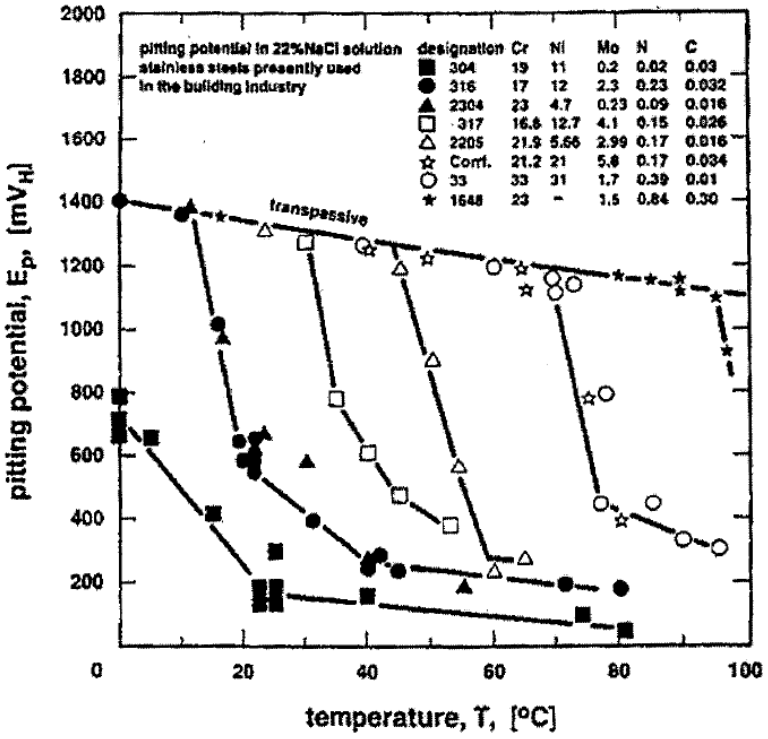

Figure 2.7: Critical pitting potential temperature for various alloys with increasing nitrogen content [66].

Furthermore, a study of the crevice corrosion behavior of HNS carried out with immersion tests at various temperatures in a 6% $FeCl_3$ solution showed an increase of the resistance to crevice corrosion with increasing nitrogen content in the alloy.

These experimental results enable the authors to find a good correlation between the MARC index and the critical pitting and corrosion temperatures (Fig. 2.8). The relationships for the calculation of these critical temperatures with the MARC index are expressed as follows:

$$T_{CCC} = 3.5 \cdot MARC - 65 \quad \text{in °C} \quad \text{Equation 2.4}$$

$$T_{CPC} = 3.5 \cdot MARC - 112 \quad \text{in °C} \quad \text{Equation 2.5}$$

Where T_{CCC} and T_{CPC} are respectively the crevice and pitting critical temperatures.

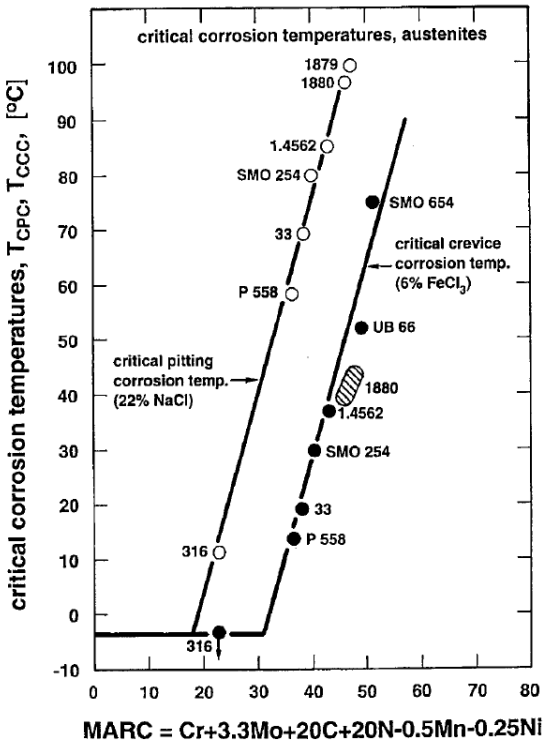

Figure 2.8: T_{CCC} and T_{CPC} for various stainless steels as function of the MARC index [66]

Several theories have been proposed to explain the increased resistance to localized corrosion: (1) Presence of high concentration of nitrogen at the steel/passive film surface stabilizing the passive film and suppressing dissolution [67–71]; (2) formation of NH_4^+ ions at the film/solution interface, neutralizing the acidity in the pit and thus promoting repassivation [54,72]; (3) formation of NO_3^- (nitrate) ions that allow an improvement in the pitting resistance [73]; (4) austenite-stabilizing effect of nitrogen [12,14].

XPS and AES measurements confirmed a high nitrogen concentration at the interface between the passivation film and the metal [67–69] and also the presence of NH_4^+ ions in the pits [74].

The research on the influence of nitrogen in stainless steels in non-pitting environments has not received the same attention. It has been reported that nitrogen addition does not have a significant effect on the material´s performance and corrosion rate.

Kearns et al. [75] found that nitrogen addition allows a slight decrease of the corrosion rate in various acidic solutions (nitric acid, phosphoric acid, acetic acid, formic acid, oxalic acid) but in sulfuric acid the corrosion attack is more pronounced as the nitrogen concentration in the steel increases.

However, Sakamoto et al. [76] investigated the corrosion behaviour of stainless steels containing 23-25%Cr-7-14%Ni-0.5-1.5%Mo with 0.1%N and 0.38%N and found that the corrosion rate in boiling sulfuric acid solution (5%) is reduced for higher nitrogen content.

References

[1] Z.I. Zhang and T. Bell: *Surf. Eng.*, 1985, vol. 1, pp. 131–36.

[2] T. Bell, K. Mao, and Y. Sun: *Surf. Coatings Technol.*, 1998, vol. 108-109, pp. 360–68.

[3] M.F. McGuire: *Stainless Steels for Design Engineers*, 1st ed., ASM International, Ohio, USA, 2008.

[4] M.O. Speidel and P. J. Uggowitzer: *Proc. of "High Manganese High Nitrogen Austenitic Steels - Cincinnati 1987*, Chicago, Illinois, USA, 1992.

[5] M.O. Speidel: *Materwiss. Werksttech.*, 2006, vol. 37, pp. 875–80.

[6] J. Johnson, B.K. Reck, T. Wang, and T.E. Graedel: *Energy Policy*, 2008, vol. 36, pp. 181–92.

[7] E. Werner: *Mater. Sci. Eng.*, 1988, vol. 101, pp. 93–98.

[8] E. Werner, P.J. Uggowitzer, and M.O. Speidel: *Mechanical Behavior of Materials -V*, Pergamon, New York, 1987, pp 419-27

[9] J.H. Andrew: *Carnagie Scholarsh. Mem.*, 1912, vol. III, p. 236.

[10] G. Stein and I. Hucklenbroich: *Mater. Manuf. Process.*, 2004, vol. 19, pp. 7–17.

[11] G. Stein, I. Hucklenbroich, and H. Feichtinger: *Mater. Sci. Forum*, 1999, vol. 318-320, pp. 151–60.

[12] R.P. Reed: *JOM*, 1989, vol. 41, pp. 16–21.

[13] M.L.G. Byrnes, M. Grujicic, and W.S. Owen: *Acta Metall.*, 1987, vol. 35, pp. 1853–62.

[14] J.W .Simmons: *Mater. Sci. Eng. A*, 1996, vol. 207, pp. 159–69.

[15] L.Å. Norström: *Met. Sci.*, 1977, vol. 11, pp. 208–12.

[16] K.J. Irvine, R.J. Llewellyn, and F.B. Pickering: *JISI*, 1961, vol. 199, p. 153.

[17] P. Gumpel and T. Tadwein: *HNS 88 Lille (France)*, The insitute of Metals, London, 1989, pp. 272–79.

[18] C.R. Clayton and K.G. Martin: *HNS 88 Lille (France)*, The insitute of Metals, London, 1989, pp. 256-60

[19] H. Berns: *ISIJ Int.*, 1996, vol. 36, pp. 909–14.

[20] A.H. Satir-Kolorz and H.K. Feichtinger: *Zeitschrift Fuer Met. Res. Adv. Tech.*, 1991, vol. 82, pp. 689–97.

[21] K. Frisk M. Kikuchi, M. Kajihara: *HNS 88 Lille (France)*, The insitute of Metals, London, 1989, p. 63.

[22] J. Rawers and M. Grujicic: *Mater. Sci. Eng. A*, 1996, vol. 207, pp. 188–94.

[23] H. Feichtinger, A.H. Satir-Kolorz, and Z. Xiao-Hong: *HNS 88 Lille (France)*, The insitute of Metals, London, 1989, p. 75.

[24] W.M. Small and R.D. Pehlke: *Trans. AIME*, 1968, vol. 242, pp. 2501–5.

[25] R. Presser and J.M. Silcock: *Met. Sci.*, 1983, vol. 17, p. 241.

[26] K. Frisk: *Calphad*, 1991, vol. 15, pp. 79–106.

[27] K. Frisk: *Metall. Trans. A*, 1990, vol. 21, pp. 2477–88.

[28] J. Menzel, G. Stein, and P. Dahlmann: *HNS 90 Aachen (Germany)*, Verlag Stahleisen GmbH, Dusseldorf, 1990, p. 365.

[29] J.W. Simmons, D.G. Atteridge, and J. Rawers: *J. Mater. Sci.*, 1992, vol. 27, p. 6105.

[30] J.W. Simmons, J. Rawers, J. Dunning, and R. Doan: *1st Int. Conf. on Processing Materials for Properties*, The Mineral, Metals and Materials Society, 1993, p. 659.

[31] H. Berns and S. Siebert: *ISIJ Int.*, 1996, vol. 36, pp. 927–31.

[32] R.P. Reed: *ASM Int. Alloy.*, 1988, pp. 225–56.

[33] V.G. Gavriljuk and H. Berns: *High Nitrogen Steels: Structure, Properties, Manufacture, Applications*, Springer - Verlag Berlin, Heidelberg, 1999.

[34] G. Stein, J. Menzel, and M. Wagner: *HNS 90 Aachen (Germany)*, Verlag Stahleisen GmbH,

Dusseldorf, 1990, p. 399.
[35] A. Soussan, S. Degallaix, and T. Magnin: *Mater. Sci. Eng. A*, 1991, vol. 142, pp. 169–76.
[36] T. Sakamoto: *Adv. Cryog. Eng.*, 1984, vol. 30, pp. 137–44.
[37] R.P. Reed and N.J. Simon: *HNS 88 Lille (France)*, The insitute of Metals, London, 1989, p. 180.
[38] S. Yamamoto, N. Yamagami, and C. Ouchi: *Adv. Cryog. Eng.*, 1986, vol. 32, pp. 57–64.
[39] M. Grujicic, J.O. Nilsson, W.S. Owen, and T. Thorvaldsson: *HNS 88 Lille (France)*, The insitute of Metals, London, 1989, p. 151.
[40] J. Sassen, A.J. Garratt-Reed, and W.S. Owen: i *HNS 88 Lille (France)*, The insitute of Metals, London, 1989, p. 159.
[41] P Müllner and C. Solenthaler: *Mater. Sci. Eng. A*, 1997, vol. 230, pp. 107–15.
[42] R. E. Stoltz and J.B. Vander Sande: *Metall. Trans. A*, 1980, vol. 11, pp. 1033–37.
[43] T. Matsuo, N. Morioka, S. Kaise, M. Kikuchi, and R. Tanaka: *HNS 88 Lille (France)*, The insitute of Metals, London, 1989, p. 213.
[44] R. Ebner, M. Panzebock, and H. Aigner: *HNS 90 Aachen (Germany)*, Verlag Stahleisen GmbH, Dusseldorf, 1990, p. 177.
[45] S. Degallaix, J. I. Dickson, and J. Foct: *HNS 88 Lille (France)*, The insitute of Metals, London, 1989, p. 380.
[46] Y. Kabawe, R. Nakagawa, and T. Makoyama: *Trans. Iron Steel Inst. Jap.*, 1968, vol. 8, pp. 353–62.
[47] P.D. Goodell, T.M. Cullen, and J.W. Freeman: *Basic Eng. (Trans. Amer. Soc. Met. E)*, 1967, vol. 89, pp. 517–24.
[48] L.L. Shreir, R.A. Jarman, and G.T. Burstein: *Materials and Corrosion*, 3rd ed., Butterworth-Heinemann, Oxford, 1994.
[49] J.E. Truman: *HNS 88 Lille (France)*, The insitute of Metals, London, 1989, p. 225
[50] M.O. Speidel and M. Zheng-Cui: *HSN 2003 Zürich (Switzerland)*, Hochschulverlag, Zürich, 2003, pp. 63–73.
[51] M.O. Speidel: *Trans. Ind. Inst. Met.*, 2003, vol. 56, p. 281.
[52] M.O. Speidel: *HNS 88 Lille (France)*, The insitute of Metals, London, 1989, p. 92.
[53] H. Baba, T. Kodama, and Y. Katada: *Corros. Sci.*, 2002, vol. 44, pp. 2393–2407.
[54] K. Osozawa, N. Okato, Y. Fukase, and K. Yokota: *Boshoku Gjtutsu (Corros. Eng.)*, 1975, vol. 24, p. 1.
[55] S.A. Vanini, J.P. Audouard, and P. Marcus: *Corros. Sci.*, 1994, vol. 36, pp. 1825–34.
[56] S.J. Pawel, E.E. Stansbury, and C.D. Lundin: *Corrosion*, 1989, vol. 45, p. 125.
[57] I. Olefjord: *J. Electrochem. Soc.*, 1985, vol. 132, p. 2854.
[58] J.J. Eckenrod and C.W. Kovach: *Properties of Austenitic Stainless Steels Their Weld Metals*, American Society for Testing and Materials (ASTM), Philadelphia, 1979, pp. 17–41.
[59] H. Yashiro, D. Hirayasu, and N. Kumagai: *ISIJ Int.*, 2002, vol. 42, pp. 1477–82.
[60] H. Yashiro, D. Takahashi, N. Kumagai, and K. Mabuchi: *Corros. Eng.*, 1998, vol. 47, p. 591.
[61] H. Ohno, H. Tanabe, A. Sakai, and T. Misawa: *Corros. Eng.*, 1998, vol. 47, p. 584.
[62] G.C. Palit, V. Kain, and H.S. Gadiyar: *Corrosion*, 1993, vol. 49, pp. 977–91.
[63] T. Komori and U. Nakada: in *39th Japan Corros. Conf. JSCE*, 1992, p. 353.
[64] M. Janik-Czachor, E. Lunarska, and Z. Szklarska-Smialowska: *Corrosion*, 1975, vol. 31, pp. 394–98.
[65] M.O. Speidel: in *Proc. Stainl. Steel World 2001 Conf.*, Hague, The Nederlands, 2001.
[66] P. Cobelli: *Ph.D. Thesis: Development of Ultrahigh Strength Austenitic Steels Alloyed with Nitrogen*, Swiss Federal Institue of Technology, Zurich, Switzerland, 2003.
[67] Y.C. Lu, R. Bandy, C.R. Clayton, and R.C. Newman: *J. Electrochem. Soc.*, 1983, vol. 130, p. 8.
[68] I. Olefjord and L. Wegrelius: *Corros. Sci.*, 1996, vol. 38, pp. 1203–20.
[69] C.O.A. Olsson: *Corros. Sci.*, 1995, vol. 37, pp. 467–79.
[70] A. Srinivasan, B. Reynders, and J. Grabke: *Steel Res.*, 1995., vol. 66, pp. 439–43.
[71] S. Ahila, B. Reynders, and H. J. Grabke: *Corros. Sci.*, 1996, vol. 38, pp. 1991–2005.

[72] K. Osozawa: *Japan Soc. Heat Treat.*, 1985, vol. 36, pp. 206–12.
[73] H.P. Leckie and H.H. Uhlig: *J. Electrochem. Soc.*, 1966, vol. 113, p. 1262.
[74] H. Baba and Y. Katada: *Corros. Sci.*, 2006, vol. 48, pp. 2510–24.
[75] J.R. Kearns and H.E. Deverell: *Mater. Perform.*, 1987, vol. 26, pp. 18–28.
[76] T. Sakamoto, H. Abo, T. Okazaki, H. Ogawa, and T. Zaizan: in *Conf. Alloy. 80s*, 1980.

3 Residual Stresses and Stress Analysis by X-Ray Diffraction

Residual Stresses and Stress Analysis by X-Ray Diffraction

3.1 Introduction on Residual Stresses

Residual stresses are defined as stresses present in a material independently from the outside forces and whose average, taken over the material´s cross section, is zero. These stresses are usually generated in a material as a consequence of elastic or plastic deformation due to incompatibilities in the state of deformation [1].

It is well established that residual stresses are present in every material component or structure, as a consequence of the various technological treatments and manufacturing processes [2,3]. These residual stresses can be deliberately introduced in the material, or can be a direct consequence of the material processing. Usually, their presence can have significant consequences on the behaviour of the final component.

Residual stress (RS) can be classified into three different families: stresses of 1st, 2nd and 3rd kind [1,4] (Fig. 3.1). RS of 1st kind are also referred as to as macrostresses (RS-macro) and stresses of 2nd and 3rd kind are denoted as microstresses (micro-RS).

RS of 1st kind (σ^{I}) are defined as nearly homogenous across large areas and in general can be in equilibrium over the total material volume (V). An alteration or release of the residual stresses of 1st kind can cause variations in the material geometry.

$$\sigma^{I} = \frac{1}{V}\int_{V} \sigma(x)dV \qquad \text{Equation 3.1}$$

RS of 2nd (σ^{II}) kind are homogenous over a microscopic area and can be defined as the mean deviation from the macro stress level. Its average values taken over all crystallites domain is zero.

$$\sigma^{II} = \frac{1}{V}\int_{\substack{Crystal \\ Volume\ V}} [\sigma(x) - \sigma^{I}]dV \qquad \text{Equation 3.2}$$

RS of 3rd (σ^{III}) are position dependent deviations from the average stress within a crystal and in general can be defined as inhomogeneous over sub-microscopic areas i.e. within a single grain. The average of σ^{III} over all the crystallites is zero.

$$\sigma^{III} = \sigma(x) - \sigma^{I} - \sigma^{II} \qquad \text{Equation 3.3}$$

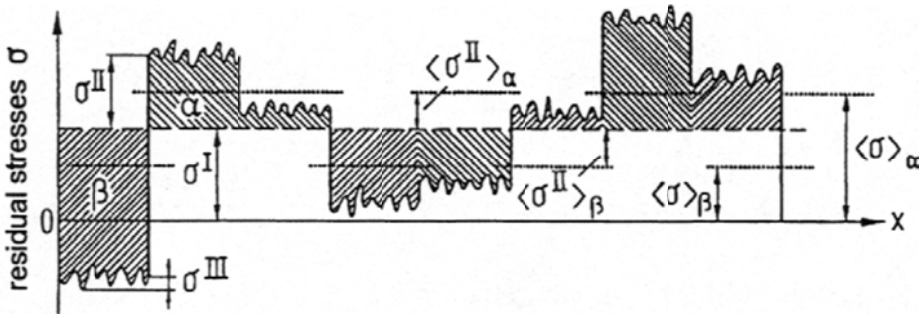

Figure 3.1: Classification of the three different types of residual stresses in a dual phase material with phases α and β [5]

Because of their influence on the material´s behaviour, the determination of all kind of stress state in all phases of the material is of fundamental importance. Over the years, several methods have been proposed for the measurement and determination of the materials stress state [6].

3.2 Determination of the stress state using the X-ray diffraction method

X-ray and neutron diffraction proved to be a successful method for the evaluation of residual macro and microstresses. This technique has been widely studied in literature and several relationships have been described for the interpretation of the experimental data [1,5,6,3]. X-ray stress evaluation is based on the diffraction of X-rays on the lattice of the crystal and the isotropic elasticity theory.
The stresses and strains in an isotropic material can be described with 2nd rank symmetrical matrix:

$$\sigma = \begin{pmatrix} \sigma_{11} & \sigma_{12} & \sigma_{13} \\ \sigma_{21} & \sigma_{22} & \sigma_{23} \\ \sigma_{31} & \sigma_{32} & \sigma_{33} \end{pmatrix} \qquad \varepsilon = \begin{pmatrix} \varepsilon_{11} & \varepsilon_{12} & \varepsilon_{13} \\ \varepsilon_{21} & \varepsilon_{22} & \varepsilon_{23} \\ \varepsilon_{31} & \varepsilon_{32} & \varepsilon_{33} \end{pmatrix} \qquad \text{Equation 3.4}$$

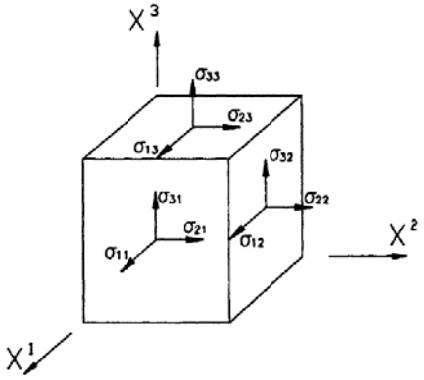

Figure 3.2: stress component definition [3].

The diagonal components, σ_{ii} and ε_{ii}, represents the normal stresses and strains respectively and they act perpendicularly to the faces. The non-diagonal components of the matrixes, σ_{ij} and ε_{ij}, where i≠j, act parallel to the face and are shear stresses and shear strains respectively. Because of the symmetry in a cubic system $\sigma_{ij}= \sigma_{ji}$ and $\varepsilon_{ij}= \varepsilon_{ji}$, only 6 of the 9 components are independent and therefore sufficient to describe the stress and strain at point in the material.
When certain stresses are applied to a material, the strains are a function of the material´s elastic properties. The total strain experienced by a material can be described as the sum of the elastic and plastic component

$$\varepsilon = \varepsilon_{pl} + \varepsilon_{el} \qquad \text{Equation 3.5}$$

From sufficiently small elastic stresses a linear dependence between stresses and strains can be found.

$$\varepsilon_{el} \sim \sigma \qquad \text{Equation 3.6}$$

This relationship is commonly described by the Hooke's law and in the one-dimensional case the proportionality factor is the Young´s modulus E. In general, the relationship between the stresses and strains matrix is described by a 4^{th} rank tensor of elastic stiffnesses. This matrix consists of 3^4=81 components c_{ikjl}.

$$\sigma_{ij} = c_{ijkl}\varepsilon_{kl} \qquad \text{Equation 3.7}$$

Because of several symmetry elements, the number of independent components in the stiffness matrix in an isotropic material in a cubic system is reduced from 81 to 3. The inversion of this equation (Eq. 3.7) yields the generalized Hooke's law in the form, where *s* is the elastic compliance tensor and is the inverse of the stiffness tensor.

$$\varepsilon_{ij} = s_{ijmn}\sigma_{mn} \qquad \text{Equation 3.8}$$

3.3 Elastically isotropic material

X-ray measurements allow the determination of lattice strains in a crystalline material by measuring the interplanar spacing in the different directions. In general, according to Bragg's law, it is possible to observe interferences in those directions where the scattering vector coincides with a vector of the reciprocal lattice [7].

$$2d(hkl)\sin\theta = n\lambda \qquad \text{Equation 3.9}$$

where d is the interplanar spacing; *hkl* the Miller´s indices; 2θ is the Bragg angle and n is the order of the interference, which is directly connected to the specific Miller´s indices. Therefore by measuring the d

spacing at the specific 2θ angle and by knowing the position of the stress-free lattice spacing, $d_{\varepsilon=0}$, it is possible to calculate the strain as:

$$\varepsilon = \frac{(d - d_{\varepsilon=0})}{d_{\varepsilon=0}} \qquad \text{Equation 3.10}$$

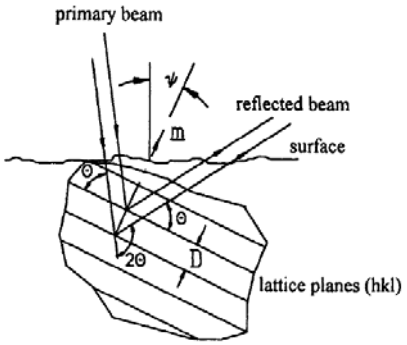

Figure 3.3: diffraction of the X-rays at the lattice plane of the crystallite [3].

In polycrystalline materials, several crystallites will contribute to the interference line depending on the specific *hkl* plane and only the crystallites whose orientation is perpendicular to the measurement direction will diffract. Furthermore the contribution of the crystallites to the interference line depends on their depth below the material´s surface: the crystallites closer to the surface have the stronger contribution while the ones deeper in the material will contribute to a lesser extent to the diffracted intensity.
Therefore, the position of the diffracting line is a function of the average d spacing value over a certain measurement volume.

$$d = \frac{\int_{VC} d(z) \exp\left(-\frac{z}{\tau}\right) dz}{\int_{VC} \exp\left(-\frac{z}{\tau}\right) dz} \qquad \text{Equation 3.11}$$

XRD measurements are commonly performed in the laboratory system (L_1, L_2, L_3) while the stresses are described in the specimen system. The transformation from one system to the other is described by a matrix with the direction cosines of the 2 angles (ψ,φ) between the axes of the new and old axes system.

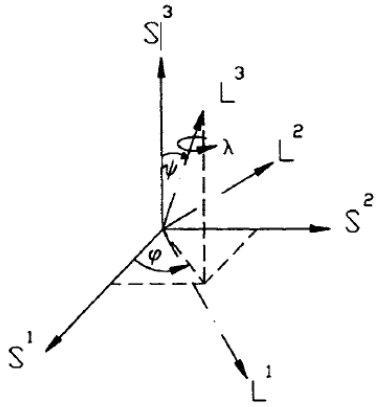

Figure 3.4: Position of the laboratory system relative to the specimen system [3].

Therefore, the strain measured in the direction *m* that in the specimen system is given by the two angles ψ and φ correspond to the ε'_{33} of the laboratory system.

$$\varepsilon_m = \varepsilon_{\varphi\psi} = \langle \varepsilon_{33}{}' \rangle^x = \frac{(d_{\varphi\psi} - d_{\varepsilon=0})}{d_{\varepsilon=0}} \qquad \text{Equation 3.12}$$

$\varepsilon_{\varphi\psi}$ can be expressed as the projection of the strain tensor in the measurement direction within the specimen system:

$$\begin{aligned} \varepsilon_{\varphi\psi} &= \langle \varepsilon_{ij} \rangle^x m_i m_j \\ &= \langle \varepsilon_{11} \rangle^x cos^2\varphi sin^2\psi + \langle \varepsilon_{22} \rangle^x sin^2\varphi sin^2\psi + \langle \varepsilon_{33} \rangle^x cos^2\psi \\ &+ \langle \varepsilon_{12} \rangle^x sin2\varphi sin^2\psi + \langle \varepsilon_{13} \rangle^x cos\varphi sin2\psi + \langle \varepsilon_{23} \rangle^x sin\varphi sin2\psi \end{aligned} \qquad \text{Equation 3.13}$$

$\langle \varepsilon_{ij} \rangle^x$ represents the average strain component of the different crystalline domains contributing to the specific hkl interference line. Assuming that the material is elastically isotropic and that the strain ε_{ij} is homogenous in the region of penetration of the x-rays, Hooke´s law can be applied:

$$E\varepsilon_{ij} = (1 + \upsilon)\sigma_{ij} - \nu\delta_{ij}(\sigma_{11} + \sigma_{22} + \sigma_{33}) \qquad \text{Equation 3.14}$$

where E is the Young´s modulus, ν is the Poisson's ration and δ_{ij} is the Kronecker delta $\delta_{ij} = \begin{cases} 1 \; if \; i = j \\ 0 \; if \; i \neq j \end{cases}$

The relationship between $\varepsilon_{\varphi\psi}$ and σ_{ij} can be now described as follows:

$$\begin{aligned} \varepsilon_{\varphi\psi} = {} & \tfrac{1}{2}S_2^m[\sigma_{11}cos^2\varphi sin^2\psi + \sigma_{22}sin^2\varphi sin^2\psi + \sigma_{33}cos^2\psi] + \\ & \tfrac{1}{2}S_2^m[\sigma_{12}sin2\varphi sin^2\psi + \sigma_{13}cos\varphi sin2\psi + \sigma_{23}sin\varphi sin2\psi] + S_1^m[\sigma_{11} + \sigma_{22} + \sigma_{33}] \end{aligned} \qquad \text{Equation 3.15}$$

With the macroscopic elastic constants, $\tfrac{1}{2}S_2^m$ and S_1^m, defined as:

$$\tfrac{1}{2}S_2^m = \frac{1+\nu}{E}, \qquad S_1^m = \frac{-\nu}{E} \qquad \text{Equation 3.16}$$

The equation defines the stress-strain relationship for an elastically isotropic body. However, as stated before in the section, the interference line is the result of the contribution of several crystalline domains. Therefore the elastic behaviour of the crystals, due to the anisotropy, may differ from the macroscopic elastic behaviour. The macroscopic elastic constants are replaced by x-ray elastic constants, depending on the specific {hkl} plane [8]. On these assumptions the equation becomes:

$$\varepsilon_{\varphi\psi} = \frac{(d_{\varphi\psi} - d_{\varepsilon=0})}{d_{\varepsilon=0}} = \tfrac{1}{2}S_2(hkl)[\sigma_{11}cos^2\varphi sin^2\psi + \sigma_{22}sin^2\varphi sin^2\psi + \sigma_{33}cos^2\psi] + \tfrac{1}{2}S_2(hkl)[\sigma_{12}sin2\varphi sin^2\psi + \sigma_{13}cos\varphi sin2\psi + \sigma_{23}sin\varphi sin2\psi] + S_1(hkl)[\sigma_{11} + \sigma_{22} + \sigma_{33}] \quad \text{Equation 3.17}$$

3.4 Biaxial Stress State

In the case of elastically isotropic surface engineered materials, it is common practice to assume a state as rotationally symmetric biaxial stress. Therefore the stress components normal to the surface can be assumed as zero [9].

$$\sigma_{13} = \sigma_{23} = \sigma_{33} = 0, \qquad \sigma_{11} = \sigma_{22} = \sigma_{//} \quad \text{Equation 3.18}$$

Under these conditions Equation 3.17 can be rewritten as follows:

$$\varepsilon_{\psi} = \frac{(d_{\psi} - d_{\varepsilon=0})}{d_{\varepsilon=0}} = \tfrac{1}{2}S_2(hkl)\sigma_{//}sin^2\psi + 2S_1(hkl)\sigma_{//} \quad \text{Equation 3.19}$$

Or, in terms of lattice spacings as:

$$d_{\psi} = d_{\varepsilon=0} + \tfrac{1}{2}S_2(hkl)\sigma_{//}d_{\varepsilon=0}sin^2\psi + 2S_1(hkl)\sigma_{//}d_{\varepsilon=0} \quad \text{Equation 3.20}$$

$d_{\varepsilon=0}$, the so called strain free lattice spacing is obtained by equating Equation 3.19 to zero. The lattice strain-free spacing is found in the direction $\psi_{\varepsilon=0}$ from:

$$sin^2\psi_{\varepsilon=0} = -\frac{2S_1(hkl)}{\tfrac{1}{2}S_2(hkl)} \quad \text{Equation 3.21}$$

For a rotationally symmetric biaxial stress state, it is possible to apply the $\sin^2\psi$ method and obtain the value of the residual stresses present in the material. By plotting the d-spacing d_ψ as function of different $\sin^2\psi$ angles (Equation 3.20), and by knowing the right X-ray elastic constants (XEC), it is possible to extrapolate the value of the stress from the slope of a linear dependence of d_ψ on $sin^2\psi$.

3.5 Information Depth

Thermochemical surface engineering processes for surface modification introduce residual surface stresses which are generally associated with the introduction of a stress and a composition gradient. The presence of gradients has to be taken into account in the stress quantification method else it will lead to a wrong estimation of the stress state.

In fact, the lattice spacing $\langle d_\psi \rangle$ determined with the x-ray diffraction experiments is the diffracted intensity-weighted average over a depth z

$$\langle d_\psi^{hkl} \rangle = \frac{\int_0^t d_\psi^{hkl}(z) exp\{-\mu(E)kz\}dz}{\int_0^t (z) exp\{-\mu(E)kz\}dz} \qquad \text{Equation 3.22}$$

where t is the layer thickness, μ(E) is the linear absorption coefficient and k is the absorption factor. The formula for the absorption factor K is dependent on the diffraction geometry, the Bragg angle 2θ and the tilt angle ψ.

Hence the lattice strain calculated over the diffracting volume is obtained as follows:

$$\langle \varepsilon_\psi^{hkl} \rangle = \frac{\langle d_\psi^{hkl} \rangle}{\langle d_{\varepsilon=0}^{hkl} \rangle} - 1 = \frac{\int_0^t d_\psi^{hkl}(z) exp\{-\mu(E)kz\}dz}{\int_0^t d_{\varepsilon=0}^{hkl}(z) exp\{-\mu(E)kz\}dz} - 1 \qquad \text{Equation 3.23}$$

This lattice strain, which is calculated from the strain and unstrained lattice spacing over a defined depth, is often attributed to apply at a certain depth[1], defined as:

$$\tau(E) = \langle z \rangle = \frac{\int_0^t z \cdot exp\{-\mu(E)kz\}dz}{\int_0^t exp\{-\mu(E)kz\}dz} = \frac{1}{\mu(E)k} - t\frac{exp\{-\mu(E)kt\}}{exp\{-\mu(E)kt\} - 1} \qquad \text{Equation 3.24}$$

This so-called information depth in a symmetric geometry configuration is strongly dependent on the Bragg angle θ and the tilt angle ψ. This significant variation in the presence of steep composition and/or stress gradients can lead to a wrong estimation of the real stress state over the investigated depth. However, by applying the grazing incidence mode (asymmetric geometry) it is possible to limit the penetration depth to a shallow region at the material´s surface and hence limit the mistake made.

The application of a fixed shallow grazing incidence angle limits significantly the information depth, while by tailored variation of the incidence angle with the tilt angle a constant information depth can in principle be achieved.

When applying grazing incidence mode, it has to be taken into account that the lattice planes are probed in a direction that is tilted with respect to the surface normal even for no actual χ tilt. The effective tilt angle ψ therefore is given by:

[1] Note that it does not generally hold that the absolute value of strain obtained in Eq. 3.24 exists at the information depth.

$$cos\psi = cos\chi \cos(\theta - \alpha)$$ Equation 3.25

Where χ is the tilt angle in the laboratory frame of reference. Hence, asymmetric geometry setup does not require correction procedures, which would have been the case for measurement in symmetric geometry mode, where gradients may strongly affect the obtained lattice spacings.

However, investigation of the ghost stresses in expanded austenite [10] proved that, even for this evaluation method and for this shallow penetration depths, ghost stresses can exceed 1GPa due to the presence of very steep concentration gradients.

3.6 X-Ray Elastic Constants

For any practical applications of diffraction stress analysis, the knowledge of the X-ray elastic constants is a prerequisite for the determination of the stress-state of the material. Generally the X-ray elastic constants (XEC) can be quantified by measuring in a diffractometer the lattice parameter variation with an applied known load stress. This technique provides a direct estimation of the X-ray elastic constant of the material, but due to the great difficulties in the experimental procedure it is rarely used. Generally the materials XEC can be extrapolated from a single-crystal elastic constant through the use of grain interaction models (GIM).

Several grain interaction models have been proposed in literature [11] . The Voigt [12] and Reuss [13] grain interaction models are considered the two extremes. The first one assumes that the strain distribution is homogenous in the specimen while the latter assumes that the stress tensor is equal for all crystallites. The two extreme cases of the grain interaction model in polycrystals were proven by Hill to set the upper and lower bounds for the mechanical elastic constants. The Neerfeld-Hill model [14,15] suggests that the arithmetic average of the Voigt and Reuss models is in better agreement with the experimental data.

The Vook-Witt and the inverse Vook-Witt models [16] include extreme grain interaction assumptions along the two considered principal directions. For special conditions at the free surface the Vook-Witt model assumes equal strains in the surface plane and zero stress perpendicular to the surface while the inverse Vook-Witt model assumes equal strain perpendicular to the surface and equal stresses in the surface plane.

Eventually in the Eshelby-Kröner model [17,18] the crystallites surrounding an individual crystallite are conceived as an elastically homogenous matrix with the elastic properties of the entire polycrystal.

The values of the single crystal elastic constants are therefore essential for the calculation of the X-ray elastic constants for polycrystals irrespective of the grain interaction model adopted.

3.6.1 XEC and GIM for Expanded austenite

So far, single crystal elastic constants have not been determined for expanded austenite; therefore, the elastic constants reported for stainless steel Fe-12%Cr-12%Ni are often used [10,19,20]. This limits significantly the accuracy of the residual stress state calculated in the expanded austenite case.

It has been proved that the presence and the amount of interstitial atoms in solid solution has an enormous influence on the X-ray elastic constants. In nitrogen free austenite $E_{200}<E_{111}$, while for nitrogen expanded austenite it has been found that the elastic modulus for the 200 reflection is higher than the one of the 111. Furthermore, the ratio between the elastic modulus of the different reflections (E_{200}/E_{111}) grows substantially with the growing content of dissolved atoms [10]. These results strongly indicate that the amount of interstitials has definitely a considerable influence on the material´s elastic constants.

In previous research activities [20–22] the XECs of stainless steel Fe-12%Cr-12%Ni calculated with the Elhelby-Kröner model were often used for the evaluation of the stress profiles in expanded austenite cases. However, the significant discrepancy in the stress distribution between the analysed peaks suggested that this method is not reliable for a correct determination of the residual stress profiles, since if the model is correct, a fair correspondence between the different reflections probed should be obtained.

More recent work [10] pointed out that among the different grain interaction models, the Reuss GIM gave a fair correspondence between the 111 and 200 reflections for both the stress profiles and the strain free lattice parameter.

In the present work, the X-ray elastic constants of Fe-12%Cr-12%Ni and γ'-Fe_4N (Table 1) were calculated using the Reuss grain interaction model and used for the evaluation of residual stresses in expanded austenite. The comparison between the two materials was performed because of similarity in the crystal structure of austenite and γ'-Fe_4N but the significant difference in elastic compliances due to the nitrogen content.

Moreover, the Reuss model was selected because of the good correspondence of the obtained stress profiles for the 111 and 200 family planes in previous research works [10].

3.7 Stacking Faults

The presence of residual plastic deformation and residual stresses in metal and alloys influences the peak broadening, but also the position of the diffracting lines [3]. The fundamental work on this subject, carried out by Warren [23], Paterson [24] and Wagner [25], confirms that the stacking fault type and stacking fault density may provoke a shift of the diffraction line, in particular in f.c.c. crystals.

Staking faults are considered as faults in the ideal sequence of close packed planes, which in the case of an f.c.c crystal is ABCABC (Fig. 3.5a). Plastic deformation and the resulting slip in the (111) plane generates a fault in the stacking sequence according to which that the B layer in the staking sequence becomes a C layer (Fig 3.5b). The shift of each layer sequence after the first faulted layer (Fig 3.5c) produces a twin fault.

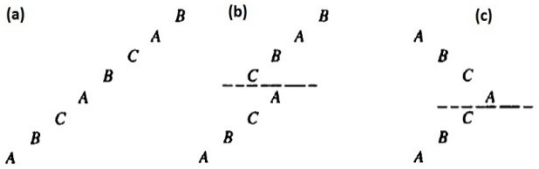

Figure 3.5: (a) Ideal sequence of closed pack layers in f.c.c. crystals, (b) deformation stacking fault, (c) twin fault [3]

The presence and type of faults in the stacking sequence has a considerable effect on the position and shape of diffraction peak. Deformation stacking faults cause a symmetric broadening and a shift of the diffraction line [24] while twin stacking faults are responsible for asymmetric line broadening but their effect on the shift of the diffraction line is negligible [23].

The shift in the peak for a polycrystal where all the interferences {hkl} are observed at the same time, is the average values of the shift for each single reflection and it is defined by:

$$\langle \Delta(2\theta) \rangle_{hkl} = \pm \frac{270}{\pi l_0} \beta \langle cos\phi \rangle_{hkl}\, j \tan\theta \qquad \text{Equation 3.26}$$

Where θ is the Bragg angle, β is the stacking fault probability, ϕ is the angle between the (hkl) plane and the (111) plane, $l_o=(h^2+ k^2+ l^2)^{½}$ and j is the fraction of faulted planes. The sign of the shift is defined by the relation:

$$|h + k + l| = 3N \pm 1 \qquad \text{Equation 3.27}$$

Because of this, according to the different hkl reflections, the shift could be towards lower or higher 2θ angles.

The peak shift associated to the presence of stacking faults is also responsible for the generation of fictitious strains [26] which are defined as :

$$\frac{da}{a} = \mp \frac{3}{4\pi l_0} \beta \langle cos\phi \rangle_{hkl}\, j \qquad \text{Equation 3.28}$$

where a is the lattice parameter.

Table 3.1 reports the values of the 2θ shift and the generated fictitious strains for several reflections.

Table 3.1: Peak shifts and fictitious strains for various hkl planes due to staking faults presence

hkl reflection	$\langle\Delta(2\boldsymbol{\theta})\rangle \cdot \boldsymbol{\beta^{-1}}$	$\frac{\boldsymbol{da}}{\boldsymbol{a}} \cdot \boldsymbol{\beta^{-1}}$
111	3.95·tanθ	$3.45 \cdot 10^{-2}$
200	-7.90·tanθ	$6.90 \cdot 10^{-2}$
220	3.95·tanθ	$-3.45 \cdot 10^{-2}$
311	-1.43·tanθ	$1.26 \cdot 10^{-2}$
222	-1.97·tanθ	$1.27 \cdot 10^{-2}$
400	3.95·tanθ	$-3.45 \cdot 10^{-2}$
331	0.83·tanθ	$-0.73 \cdot 10^{-2}$
420	-0.79·tanθ	$0.69 \cdot 10^{-2}$
420	0	0
511	-0.33·tanθ	$0.29 \cdot 10^{-2}$

The effect of stacking faults on the peak broadening is due to the reduction of the coherently diffracting domains in a polycrystal and provokes a symmetrical broadening for deformation stacking faults (α) or asymmetric broadening in case of twin stacking faults (β). The reduction of the coherently diffracting domains is calculated as:

$$\frac{1}{L_{eff}} = \frac{1}{L} + \frac{1.5\alpha + \beta}{D(111)} \langle cos\phi \rangle_{hkl}\, j \qquad \text{Equation 3.29}$$

where D(111) is the lattice spacing of the 111 planes and α and β are the stacking fault density for the deformation and twin stacking faults respectively.

The presence of peak shifts, fictitious strains and also peak broadening due to stacking faults is therefore an important parameter to take into account in the calculation of residual stresses. The misinterpretation of a peak shift due to stacking fault presence with a strain induced shift, might introduce a significant amount of ghost stresses which will then lead to a wrong interpretation of the residual stress state present in the material.

References

[1] E. Macherauch: *Residual Stress.*, 1987, vol. 4, pp. 1–36.
[2] A Simon: *Rev. Metall. D Informations Tech.*, 1997, vol. 94, p. 151.
[3] V. Hauk: *Structural and Residual Stress Analysis by Nondestructive Methods*, Elsevier, 1997.
[4] E. Macherauch, H. Wohlfahrt, and U. Wolfstieg: *HTM*, 1973, vol. 28, pp. 201–11.
[5] V. Hauk and H. J. Nikolin: *Textures and Microstuctures*, 1988, vols 8-9, pp. 693-716.
[6] V. Hauk, P. Höller, and E. Macherauch: *Residual Stress. Sci. Technoloy*, 1987, vol. 1, pp. 231–42.
[7] B.E. Warren: *X-Ray Diffraction*, Courier Dover Publications, New York, USA, 1969.
[8] J Stickforth: *Techn. Mitt. Krupp*, 1966, vol. 24, pp. 89–102.
[9] C. Genzel, S. Krahmer, M. Klaus, and I.A. Denks: *J. Appl. Crystallogr.*, 2010, vol. 44, pp. 1–12.
[10] F.A.P. Fernandes, T.L. Christiansen, G. Winther, and M.A.J. Somers: *Acta Mater.*, 2015, vol. 94, pp. 271–80.
[11] U. Welzel, J. Ligot, P. Lamparter, A.C. Vermeulen, and E.J. Mittemeijer: *J. Appl. Crystallogr.*, 2005, vol. 38, pp. 1–29.
[12] W. Voigt: *Lehrbuch Der Kristallphysik*, Teubner, Leipzig, 1910.
[13] A. Reuss: *Z. Angew. Math, Mech.*, 1929, vol. 9, p. 49.
[14] H. Neerfeld: *Mitt. K. Wilh. Inst. Eisenforschg.*, 1942, vol. 24, pp. 61–70.
[15] R. Hill: *Proc.Phys. Soc. London*, 1952, vol. 65, pp. 349–54.
[16] R.W. Wook and F. Witt: *J. Appl. Phys.*, 1965, vol. 7, pp. 2169–71.
[17] E. Kröner: *Z. Phys.*, 1958, vol. 151, pp. 504–18.
[18] J.D. Eshelby: *Proc. R. Soc. A.*, 1957, vol. 241, pp. 376–96.
[19] S. Jegou, T.L. Christiansen, M. Klaus, C. Genzel, and M.A.J. Somers: *Thin Solid Films*, 2013, vol. 530, pp. 71–76.
[20] T.L. Christiansen and M.A.J. Somers: *Metall. Mater. Trans. A*, 2008, vol. 40, pp. 1791–98.
[21] T.L. Christiansen and M.A.J. Somers: *Mater. Sci. Eng. A*, 2006, vol. 424, pp. 181–89.
[22] T.L. Christiansen and M.A.J. Somers: *Mater. Sci. Forum*, 2004, vol. 443-444, pp. 91–94.
[23] B.E Warren and E.P Warekois: *Acta Metall.*, 1955, vol. 3, pp. 473–79.
[24] M.S. Paterson: *J. Appl. Phys.*, 1952, vol. 23, pp. 805–11.
[25] C.N.J Wagner: *Acta Metall.*, 1957, vol. 5, pp. 427–34.
[26] R.I. Hartmann and E. Macherauch: *Zeitschrift Fur Met.*, 1963, vol. 54, pp. 282–86.

4 Overview of the Materials, Processes and Characterization Techniques

Overview of the Materials, Processes and Characterization Techniques

In this section a brief overview of the processes, materials and characterization technique used in the experimental activity will be given. Samples of the selected materials in the as-received of pre-treated conditions were subjected to low-temperature nitriding and/or low-temperature nitrocarburizing.

4.1 Materials

The chemical composition of all stainless steel grades tested during the experimental activity is given in the following table (Table 4.1).

Table 4.1: Chemical composition of the stainless steels used for the experimental activity as measured by the suppliers

	C	Si	Mn	Cr	Ni	Mo	N	Ti	Cu	Al
EN 1.4369	0.09	0.74	5.92	18.58	7.11	0.18	0.23	-	-	-
AISI 304	0.08	0.75	2.0	18.5	10.5	-	-	-	-	-
AISI 304L	0.03	0.32	1.78	18.28	8.08	-	-	-	-	-
AISI 316	0.07	0.4	1.6	17	10.55	2	0.05			
Sandvik Nanoflex®	0.008	0.26	0.34	11.72	8.8	3.82	-	0.86	1.88	0.35

The materials tested differ for chemical composition, mechanical properties and particularly, austenite stability.

The chemical composition of the EN 1.4369 SS resembles the one of AISI 201 and like the stainless steels of the 200 series, the content of expensive nickel is reduced compared to the alloys of the 300 series.

In order to obtain stable austenite in the alloy of the 200 series, manganese and nitrogen are used as alloying elements. In particular nitrogen, which is a strong austenite stabilizer, also prevents the formation of strain-induced martensite upon deformation.

AISI 304, 304L and 316 were used as reference materials because of their importance in several industrial applications and the extensive study carried out on their behaviour upon nitriding.

Sandvik Nanoflex is a metastable precipitation hardening stainless steel. It´s stability at room temperature is function of various parameters such as annealing conditions, temperature and applied mechanical load.

The martensite start temperature, defined as the temperature at which martensite forms instantaneously during cooling, is reported to be 83K. However the formation of isothermal martensite has been observed even at room temperature depending on the material processing conditions.
The precipitation hardening effect in Nanoflex is achieved through the precipitation of Cu-clusters, as well as the ordered intermetallic phases η–Ni_3(Ti,Al) and Ni_3Mo and Fe_2Mo (Laves phase) from the martensite matrix.

4.2 Pre-treatments

4.2.1 Annealing

Annealing treatments were performed on different steel grades in order to obtain specific phase compositions at room temperature and study their influence on the subsequent nitriding process.
In all cases, annealing experiments, including heating and cooling, were performed in a horizontal tube furnace with a protective argon atmosphere. Cooling was achieved by moving the sample to a cold part of the furnace. Treatment time and temperatures were adjusted according to the different samples tested.
The temperature during annealing was controlled throughout the entire process with a type K thermocouple, positioned in proximity to the samples.

4.2.2 High-Temperature Solution Nitriding

High-temperature solution nitriding was employed in order to create high nitrogen steels from commercially available stainless steel grades. This treatment is a commercial process provided by the company Expanite A/S [1,2]. Various samples were treated at a temperature of 1150°C for 4 hours in a N_2-gas atmosphere.
Three different N_2-gas pressures (0.3 bar, 0.6 bar, 0.9 bar) were used in order to produce samples with different nitrogen contents. At the end of the process, high-pressure gas quench was applied to avoid the formation of nitride precipitates during cooling.
Through this treatment it was possible to produce samples with uniform nitrogen content.

4.2.3 Plastic Deformation

In this experimental series, the materials were plastically deformed at various strain levels using different deformation techniques in order to study the influence of the degree and type of plastic deformation on the subsequent thermochemical process.
Tensile test were performed on an Instron ASM tensile test machine with a load capacity of 100kN and the tensile test specimens were cut from plate material in accordance with ASTM standard E 8M-04 [3]. The tensile loading direction was chosen parallel to the rolling direction of the plate and the deformation was obtained applying a strain rate of $6.67*10^{(-3)}$ s^{-1}.

Shear deformation tests were performed by M2i - University of Twente. The geometry of the shear samples is described in [4] and the shear direction was chosen perpendicular to the rolling direction in the plane of the plate.

Plane strain deformation mimicking the rolling process was performed reducing the thickness of a slab applying compression onto the metal slab with two dies. Plane strain compression was performed on specimens with standardized dimensions (40x100x5)mm^3 [5].

4.3 Surface treatments

Irrespective of the pre-treatment, the surfaces of all the samples subjected to nitriding was ground and polished until 3μm finish and subsequently electro-polished in order to remove the plastic deformation. The electro-polishing was carried out in a "Struers Polectrol" apparatus using a "Struers electrolyte A2" with an applied potential of 20-30V and a current density of 1-2A/cm^2.

4.3.1 Low-temperature thermochemical processes

Low-temperature nitriding and nitrocarburizing were performed on different steel classes in different processing conditions in order to investigate the influence of the material´s phase composition and the degree of applied plastic deformation on the case produced during the thermochemical treatments.

The experiments were performed in an industrial LAC annealing furnace model PKRC 55/09 retrofitted for gaseous nitriding under gas circulation.

All the nitriding experiments were performed in ammonia gas atmosphere at atmospheric pressure. In all cases the ammonia flow was set at a maximum and kept constant for the entire nitriding process through the use of a flowmeter. Due to a certain, unknown, degree of dissociation of the ammonia gas in the furnace, the exact nitriding potential was unknown

The nitrocarburizing experiments were performed in a propene/ammonia gas mixture. The gas flow was kept constant for the entire treatment time.

For both processes the temperature during the entire procedure, including in-situ activation and cooling, was monitored with a type K thermocouple, positioned very close to the samples.

The nitriding/nitrocarburizing temperatures and times were adjusted according to the different experiments performed.

4.4 Characterization

A brief description of the various techniques used for the characterization of the materials is given in the following sections.

4.4.1 Microscopy – LOM and SEM

The samples´ cross sections were analysed with light optical microscopy and scanning electron microscopy. The samples were ground and polished to 1μm diamond paste finish and, in order to reveal the materials microstructure, they were etched with Kalling's reagent no. 1 for 4-10s depending on the sample condition. Light optical micrographs were collected using an Olympus GX41 operating in bright field and a Neophot 30 operated bright field light with 100x oil immersion planapochromate objective for optimal resolution.
SEM investigation was performed on ground and polished (1μm) samples using an Inspect S, FEI microscope using an acceleration voltage of 15 keV and a beam spot size of 5 nm.

4.4.2 Hardness

The assessment of the hardness of the bulk and the nitrided case was carried out using a Future-Tech FM700 instrument. For the bulk hardness evaluation a load of 2N was selected; the assessment of the microhardness in the nitrided/nitrocarburized case, in order to measure the hardness profiles over the cross section, was carried out applying a load of 0.05N.

4.4.3 X-Ray Diffraction

X-ray diffraction was extensively used in order to characterize the materials in the as received condition and, after plastic deformation and thermochemical surface treatments.
All X-ray diffractograms were collected in a Bruker D8 AXS X-ray diffractometer equipped with Cr-anode operating at a voltage of 40kV and a current of 40mA.
Phase analysis was performed in Bragg-Brentano symmetric geometry mounting a Göbel mirror in the incident beam.
Grazing incidence at different angles (α=2.5°,5° and 7.5°) was applied in order to investigate the material composition in the near-surface region and at different depths.
In both cases the step size chosen was equal to 0.03° 2θ and the counting time was 4s per 2θ step.
The lattice spacing profiling for residual stress analysis over the thickness of the hardened surface was determined in grazing incidence geometry using point focus configuration and a vanadium window to remove Cr K_β.

The measurements were performed in a range of 55°-85° 2θ. This range was selected to include the 111 and 200 reflections of austenite and expanded austenite. The step size was 0.05° 2θ and the counting time was 6s per 2θ step.

The grazing incidence angle was kept fixed at a value α=2° for all the tilting angles χ. Line profiles were obtained for 5 values of χ angle (0°, 25°, 38°, 49°, 60°).

4.4.4 GD-OES

Composition-depth profiles of the nitrided and nitro-carburized cases was determined with Glow Discharge Optical Emission Spectroscopy (GD-OES), using a Horiba Jobin Yvon GD profiler 2. The plasma applied for controlled sputtering of the sample surface was 1000 Pa pressure and 40 W. Concentration profiles of substitutionally and interstitially dissolved components were obtained using a selection of stainless steel reference materials and γ'-Fe_4N on pure iron as a reference for nitrogen.

4.4.5 Corrosion Testing – Potentiodynamic Curves and Crevice Immersion Test

Corrosion properties were investigated with potentiodynamic polarization measured and crevice corrosion immersion tests.

Potentiodynamic polarization measurements were performed at room temperature using an ACM potentiostat (GillAC). A flat cell set-up with an exposed area of 0.95 cm^2 of the working electrode (sample) was used for the measurement. An Ag/AgCl electrode and Pt wire were employed as reference and counter electrode, respectively. The open circuit potential (OCP) was monitored for 30 min prior to conducting each polarization scan. The polarization scans were conducted in naturally aerated 0.1 M NaCl solution of pH 5.2 ± 0.3. The current was measured as a function of the applied potential, which was changed from -0.2 V Ag/AgCl below OCP to +1 V above OCP with a scan rate of 60mV/s.

The crevice corrosion performance of the materials was evaluated by immersion tests according to the ASTM standard G48-11 [6]. A hole of 6mm was drilled in the centre of the samples with dimensions 5x2cm^2. Two teflon crevice washers were applied on the two parallel flat surfaces of the sample and tightened with bolts. Immersion tests were carried out at room temperature for 168h (1week) in a 3 wt.% Fe_3Cl solution of pH~1.

References

[1] T. L. Christiansen, T. S. Hummelshøj, and Marcel A.J. Somers: WO2012 146254-A1, 2012.

[2] T. L. Christiansen, T. S. Hummelshøj, and M. A. J. Somers: WO2013159781-A1, 2013.

[3] ASTM International: Standard Test Methods for Tension Testing of Metallic Materials [Metric], USA, 2004, no. E 8M – 04..

[4] J. Post: *Report RFSR-CT-2012-00021*, Drachten / Netherlands, 2013.

[5] G.W. Rowe: *Elements of Metalworking Theory*, Hodder Arnold, London, 1979.

[6] ASTM International: Standard test methods for pitting and crevice corrosion resistance of stainless steels and related alloys by use of ferric Chloride solution, USA, 2003, no. G48 - 11.

5 Overview of the Results – List of Papers

5.1 Influence of plastic deformation on low-temperature surface hardening of austenitic stainless steel by gaseous nitriding.

This article was submitted September 10, 2014 and published on-line March 12, 2015 in Metallurgical and Materials Transactions A, Vol. 46, Issue 6, pp. 2579-2590

Conclusions

The influence of phase composition and plastic deformation on the performance during low-temperature nitriding of AISI 304 and EN 1.4369 were investigated (Table 5.1).

Plastic strain and deformation mode have negligible influence on the morphology and properties of the nitrided case for EN 1.4369 whereas the formation of strain-induced martensite in 304 significantly affects the properties of the layer created though low-temperature surface engineering.

It was found that the presence of strain-induced martensite prior to nitriding promotes a faster growth of the case and promotes the formation of CrN.

Table 5.1: Combinations of material, deformation mode and nitriding temperature applied in this article. In all cases nitriding was performed in ammonia at atmospheric pressure for 20h.

Material	**Deformation condition**	**Equivalent strain**	**Nitriding temperature [K (ºC)]**
AISI 304	Undeformed (annealed)	0	703(430) 728(455)
	Tension	0.15, 0.30, 0.45, 0.50	
EN 1.4369	Undeformed (annealed)	0	703(430)
	Tension	0.15, 0.30, 0.45, 0.50	
	Shear	0.15, 0.30, 0.45	
	Plane Strain Compression	0.3, 0.5, 0.7	
EN 1.4369	Undeformed (annealed)	0	743(470)
	Tension	0.15, 0.30, 0.45, 0.50	

5.2 Influence of microstructure and process conditions on simultaneous low-temperature surface hardening and bulk precipitation hardening of Nanoflex®

This article was submitted February 24, 2015 and published on-line August 18, 2015 in Metallurgical and Materials Transactions A, Vol. 46, Issue 11, pp. 2501-2516.

Conclusions

Nitriding and nitrocarburizing were performed on a precipitation hardening stainless steel, Sandvik Nanoflex®, in order to obtain simultaneous bulk and surface hardening. It was demonstrated how the morphology and properties of the surface layer as well as the bulk are highly affected by the material´s initial microstructure.

The coexistence of martensite and austenite prior to nitriding leads to the formation of a non-homogeneous case where both expanded austenite and expanded martensite are present. As the martensite content in the steel increases a more homogenous case, consisting of expanded martensite, is obtained. A more efficient precipitation hardening process is also observed as the martensite content in the steel is augmented, as martensite is the precipitation hardenable phase.

Furthermore, the presence of a martensitic substrate allows a faster diffusion and results in a thicker case compared to an austenitic substrate treated in the same conditions.

Indications of CrN precipitation are also observed in the outermost region of the case when a martensitic substrate was nitrided in these experimental conditions.

Table 5.2: Combinations of annealing, deformation and low-temperature surface hardening treatment applied on Nanoflex (LTN = low-temperature nitriding; LTNC= low-temperature nitrocarburizing).

Condition	Type	Initial Condition	Plastic Deformation /Cryogenic Treatment	Thermochemical Treatment	Temperature [K]	Time [hours]
A	A1	As Received	-	LTN	693	20
			-	LTNC	693	80
	A2	As Received	Plastic deformation (ε=0.05, 0.10, 0.15)	LTN	693	20
				LTNC	693	80
	A3	As Received	Plastic deformation (ε=0.15)	LTN	673	20
B	B1	Annealing (1223K, 1800s)	-	LTN	673	20
	B2	Annealing (1223K, 1800s)	Plastic deformation (ε=0.25)			
C	C1	Annealing (1423K, 900s)	-	LTN	693	20
	C2	Annealing (1423K, 900s)	Plastic deformation (ε=0.25)			
	C3	Annealing (1423K, 900s)	Cryogenic Treatment (233K, 24h)			

5.3 Low-temperature nitriding of deformed austenitic stainless steels with various nitrogen contents obtained by prior high temperature solution nitriding

This article was submitted to Metallurgical and Materials Transactions A on November 26th, 2015.

Conclusions

Three different commercially available stainless steel grades (AISI 304L, AISI 316 and EN 1.4369) were subjected to high-temperature solution nitriding (HTSN) to produce high nitrogen steels. The maximum nitrogen content dissolved during the process was a function of the initial chemical composition of the alloys. Nitrogen greatly influences the mechanical properties as both yield strength and hardness increase with the increasing nitrogen content.

The presence of the dissolved nitrogen, due to its strong austenite stabilizing effect, prevented the formation of strain-induced martensite upon deformation.

The HTSN samples, before and after plastic deformation, were subjected to low-temperature nitriding process in order to improve the surface properties. In all cases, a homogeneous layer of expanded austenite was formed and no presence of CrN was detected.

Table 5.3: Combinations of processes and experimental conditions used in the present investigation (HTSN=high temperature solution nitriding)

Material	Initial condition	Plastic deformation	LTN
AISI 304L AISI 316 EN 1.4369	HTNS1 (1423K, 4h,0.3Bar)	- ε=0.15, ε=0.30, ε=max.	703K, 20h
AISI 304L AISI 316 EN 1.4369	HTNS2 (1423K, 4h,0.3Bar)	- ε=0.15, ε=0.30, ε=max.	703K, 20h

5.4 Electrochemical characterization and crevice corrosion performance of high temperature solid-solution nitrided and low-temperature nitrided austenitic stainless steel

This article was submitted to Surface and Coatings Technology on December 4th, 2015

Conclusions

The corrosion properties of three commercially available alloys (AISI 304L, AISI 316 and EN 1.4369) after high temperature solution nitriding and low-temperature nitriding were tested and compared to the as-received materials in the annealed condition. The dissolution of nitrogen in the bulk (HTSN) or at the material surface (LTN) proved beneficial for the resistance to localized attacks (pitting corrosion).
A crevice corrosion immersion test was performed to investigate localized corrosion performance after various treatments and shows that no significant improvement could be obtained after HTSN for the aggressive environment chosen. However, the presence of expanded austenite at the material´s surface, allowed a significant decrease in the weight loss after the immersion test, thereby proving its outstanding crevice corrosion resistance even under extreme environments.

Table 5.4: Combinations of processes and experimental tests used in the present investigation (Annealed: 1323K, 300s; HTSN1: 1423K, 4h,0.3Bar; HTSN2: 1423K, 4h,0.6Bar, HTSN 3: 1423K, 4h,0.9Bar)

Material	Initial condition	Corrosion Testing	
AISI 316	• Annealed • HTNS1 • HTNS2 • HTSN3 • Annealed+LTN	Potentiodynamic polarization curves	Crevice corrosion immersion tests
AISI 304L	• Annealed • HTNS1 • HTNS2 • HTSN3 • Annealed+LTN	Potentiodynamic polarization curves	Crevice corrosion immersion tests
EN 1.4369	• Annealed • HTNS1 • HTNS2 • HTSN3 • Annealed+LTN	Potentiodynamic polarization curves	Crevice corrosion immersion tests

5.5 Effect of plastic pre-straining on residual stress and composition profiles in low-temperature surface hardened austenitic stainless steel

This article was submitted to Metallurgical and Materials Transactions A on November 26th, 2015.

Conclusions

Residual compressive stresses were measured with grazing incidence X-ray diffraction on nitrided and nitrocarburized austenitic stainless steel samples. The samples were plastically deformed prior to nitriding and/or nitrocarburizing in order to investigate the influence of the residual plastic deformation on the residual stress profile created as a consequence of the thermochemical surface engineering processes.

The results show that plastic deformation prior to nitriding or nitrocarburizing has a negligible influence on the nitrogen enriched zone of the nitrided and nitrocarburized case. This effect is believed to be due to the plastic deformation and lattice rotation induced by the nitrogen dissolved in solid solution during the process, which dominates the effect of prior plastic deformation.

However plastic deformation has a considerable influence on the carbon enriched zone of the nitrocarburized layer. In this case, it is not possible to observe any additional plastic deformation as a consequence of carbon dissolution, because of the lower amount of interstitials dissolved compared to nitrogen; therefore the dislocation density influences the residual stresses and composition profile in the carbon enriched zone.

Because the X-ray elastic constants (XECs) for expanded austenite at different interstitial concentration have not been calculated so far, the authors used the XECs of austenite and γ'-Fe_4N in order to find the residual stress profiles in the nitrided and nitrocarburized case.

It has been demonstrated that this method can be used only for a qualitative estimation of the magnitude of residual stresses present and cannot be used for the correct quantitative determination of the residual stresses present in the expanded case because of the great dependence of the XECs on the interstitial content

Table 5.5: Combination of materials, experimental conditions and low-temperature thermochemical processes used employed for the evaluation of residual stress profiles with grazing incidence X-ray diffraction

Material	Deformation condition	Equivalent strain	Low-temperature surface treatment
EN 1.4369	Undeformed (annealed)	0	LTN 703K, 20h
	Tension	0.50	
EN 1.4369	Undeformed (annealed)	0	LTNC 693K, 20h
	Tension	0.50	

6 Paper I: Influence of plastic deformation on low-temperature surface hardening of austenitic stainless steel by gaseous nitriding

Federico Bottoli, Grethe Winther, Thomas L. Christiansen, Marcel A.J. Somers

Technical University of Denmark, Department of Mechanical Engineering, Produktionstorvet b.425, 2800 Kgs. Lyngby, Denmark

Article published in Metallurgical and Materials Transactions A, Vol. 46, Issue 6, pp. 2579-2590

Influence of Plastic Deformation on Low-Temperature Surface Hardening of Austenitic Stainless Steel by Gaseous Nitriding

FEDERICO BOTTOLI, GRETHE WINTHER, THOMAS L. CHRISTIANSEN, and MARCEL A.J. SOMERS

This article addresses an investigation of the influence of plastic deformation on low-temperature surface hardening by gaseous nitriding of two commercial stainless steels: EN 1.4369 and AISI 304. The materials were plastically deformed to several levels of equivalent strain by conventional tensile straining, plane strain compression, and shear. Gaseous nitriding of the strained material was performed in ammonia gas at atmospheric pressure at various temperatures. Microstructural characterization of the as-deformed state and the nitrided case produced included X-ray diffraction analysis, reflected-light microscopy, and microhardness testing. The results demonstrate that a case of expanded austenite develops and that the presence of plastic deformation has a significant influence on the morphology of the nitrided case. The presence of strain-induced martensite favors the formation of CrN, while a high dislocation density in a fully austenitic structure does not lead to such premature nucleation of CrN.

DOI: 10.1007/s11661-015-2832-5

I. INTRODUCTION

STAINLESS steels are extensively used in structural applications where corrosion resistance is of crucial importance. Austenitic stainless steels of the Ni-containing 300 series are the most widely applied due to their excellent corrosion resistance, mechanical properties as well as formability and weldability.[1–3]

In recent years, an increasing interest in alloys of the 200 series has arisen, because of their improved mechanical properties[3] and lower cost,[4] as compared with the 300 series steels. In the stainless steels of the 200 series, the expensive nickel is replaced with other austenite stabilizing elements, in particular manganese and nitrogen.

Despite the wide use of the two classes of stainless steels due to their high mechanical properties and excellent corrosion resistance, the 200 and 300 series stainless steels suffer from poor wear resistance, particularly galling. Major improvement of the galling resistance can be achieved by dissolving high amounts of nitrogen and/or carbon in the austenite phase through low-temperature thermochemical processing, *e.g.*, nitriding, carburizing, or nitrocarburizing. Through the years, plasma and implantation technologies have provided the possibility of low-temperature surface hardening of stainless steels.[1,5–8] Plasma/Ion-based surface engineering removes the passive layer by sputtering and incorporates N and/or C interstitials in austenite, thus leading to the formation of expanded austenite,[9–11] also referred as to S-phase.[8] In the last 15 years, gaseous processes for nitriding and carburizing of stainless steel were developed, matured, and commercialized.[9,12] Gaseous processes provide a substantial advantage over plasma and implantation processes, in particular with respect to process control, materials handling, and geometrical constraints.

Expanded austenite is not a new phase, as S-phase would suggest, but is merely a supersaturated solid-solution of nitrogen/carbon in austenite. Its supersaturated nature implies that expanded austenite is metastable and is kinetically stabilized by choosing a process temperature that does not allow the precipitation of Cr-based nitrides and/or carbides during processing. The change in the surface hardness and the incorporation of composition-induced compressive residual stress, which both are associated with the dissolution of high contents of interstitials, are beneficial for the wear and fatigue performance of stainless steel, without affecting the resistance against general corrosion.[6,13–15] Furthermore, the incorporation of a high amount of nitrogen/carbon improves the resistance against localized corrosion, as it shifts the transpassive region to higher applied potentials.[16]

In practice, low-temperature surface hardening could be applied as a finishing step after a series of metal forming operations to shape the stainless product. Preliminary activities, however, suggested that plastic deformation and the presence of (elastic) residual stress have an influence on the resulting nitriding/carburizing behavior, for example, by causing early precipitation of Cr-nitrides or Cr-carbides, thereby impairing the corrosion resistance of the alloy. Severe plastic deformation as introduced by SMAT has been claimed to lead to faster development of a case during nitriding, particularly at low temperatures.[17–19]

FEDERICO BOTTOLI, Ph.D. Student, GRETHE WINTHER, Associate Professor, THOMAS L. CHRISTIANSEN, Senior Researcher, and MARCEL A.J. SOMERS, Section Head, Professor, are with the Technical University of Denmark, Department of Mechanical Engineering, Produktionstorvet b.425, 2800 Kgs. Lyngby, Denmark. Contact e-mail: febot@mek.dtu.dk; somers@mek.dtu.dk

Manuscript submitted September 10, 2014.

Article published online March 12, 2015

In the current study, the influence of plastic deformation up to an equivalent strain of 0.5 on different low-temperature nitriding parameters is studied for two commercially available alloys: EN 1.4369 and AISI 304.

II. EXPERIMENTAL

A. *Materials*

Compositions of the investigated alloys EN 1.4369* and AISI 304 are given in Table I. The materials were provided in the annealed condition as plates of 0.7 and 5 mm thickness for EN 1.4369 and 0.45 mm thickness for AISI 304. Microstructure analysis revealed a fully austenitic structure for both alloys. A hardness of 211 $HV_{2.0N}$ and average grain size of (29.5 ± 4.5) μm were found for EN 1.4369, while AISI 304 presented a hardness of 186 $HV_{2.0N}$ and an average grain size of (14.8 ± 1.2) μm.

*This alloy has no AISI equivalent, but in composition is close to AISI 201.

B. *Plastic Deformation of Plate Material*

Tensile test specimens were cut from the plate material in accordance with ASTM standard E 8M-04.[20] The tensile loading direction was chosen parallel to the rolling direction of the plate. Tensile straining was applied up to the following equivalent strains: 0.15, 0.30, 0.45, and 0.50 at a strain rate of $6.67 \times 10^{(-3)}$ s^{-1}.

Shear test specimens of EN 1.4369 were deformed to the following equivalent strains: 0.15, 0.30, and 0.45;[21] the shear direction was chosen perpendicular to the rolling direction in the plane of the plate.

Plain strain deformation mimicking the rolling process was performed reducing the thickness of a slab applying compression onto the metal slab with two dies. Plane strain compression was performed on EN 1.4369. To this end, specimens with standardized dimensions[22] of $(40 \times 100 \times 5)$ mm^3 were cut so that the elongation direction was parallel to the rolling direction. The thickness of the starting material was 5 mm, and the following equivalent strain levels were achieved: 0.3, 0.5, and 0.7.

C. *Low-Temperature Nitriding*

Prior to nitriding, the surfaces of the samples with dimension (15×12.5) mm^2 were ground and polished to a surface finish of 1 μm diamond. In order to remove the plastic deformation zone induced by grinding/polishing, the surface was subsequently electro-polished in a "Struers Polectrol" machine. The electro-polishing was carried out for 20 seconds in a "Struers Electrolyte A2" solution with an applied potential and current density of 20 V and 2.5 A, respectively. To enable low-temperature surface hardening, the sample surface was activated *in situ* by a proprietary procedure. The materials were nitrided in an industrial LAC annealing furnace model PKRC 55/09 retrofitted for gaseous nitriding under gas circulation. The temperature during the entire nitriding procedure, including *in situ* activation and cooling, was monitored with a type K thermocouple, positioned very close to the samples. Nitriding was performed in partly dissociated ammonia at atmospheric pressure; the degree of dissociation and, hence, the nitriding potential depended on the nitriding temperature and was not controlled. Nitriding temperatures of 703 K, 728 K, and 743 K (430 °C, 455 °C, and 470 °C) were applied. In all cases, the nitriding time, *i.e.*, the time that the samples were exposed to the nitriding time at the nitriding temperature was 20 hours. The combinations of stainless steel, straining, and nitriding temperature to be discussed in this work are collected in Table II.

D. *Microstructure Characterization*

The microstructures of all samples before and after low-temperature nitriding were investigated in cross sections with reflected-light microscopy. The samples were ground, polished, and etched with Kalling's reagent no. 1 for 5 to 8 seconds. Microhardness indentation measurements were performed on a Future-Tech FM700 instrument using a load of 2.0 N for the bulk hardness assessment; for the evaluation of the microhardness profile over the "case," a load of 0.05 N was applied.

X-ray diffractometry for phase identification was carried out with the Bragg–Brentano symmetric setting and with grazing incidence in a Bruker D8 AXS X-ray diffractometer equipped with Cr-anode and Göbel mirror in the incident beam. The step size was equal to 0.03 deg 2θ and a counting time of 4 seconds per 2θ step. To vary the information depth, several grazing incidence angles were applied. For characterization of the as-deformed states of stainless steel, Rietveld analysis was applied for estimating the phase fractions of austenite and martensite from X-ray diffractograms. Line-profile analysis was performed to determine microstrain and coherently diffracting domain size in the diffraction direction by applying pseudo-Voigt fitting of the line profiles.[23,24] Instrumental broadening was corrected for by subtracting the full width at half maximum (FWHM) for the (interpolated) Bragg angle

Table I. Chemical Composition AISI 304 and EN 1.4369 in Weight Percent as Determined by the Suppliers, Lemvigh Muller and Sandvik Materials Technology, Respectively

	C	Si	Mn	Cr	Ni	Mo	N
AISI 304	0.08	0.75	2.0	18.5	10.5	—	—
EN 1.4369	0.09	0.74	5.92	18.58	7.11	0.18	0.23

Table II. Combinations of Material, Deformation Mode, and Nitriding Temperature Applied in This Work

Material	Deformation Condition	Equivalent Strain	Nitriding Temperature [K (°C)]
AISI 304	undeformed (annealed)		703 (430)
	tension	0.15, 0.30, 0.45, 0.50	728 (455)
EN 1.4369	undeformed (annealed)		703 (430)
	tension	0.15, 0.30, 0.45, 0.50	
	shear	0.15, 0.30, 0.45	
	Plane strain compression	0.3, 0.5, 0.7	
EN 1.4369	undeformed (annealed)		743 (470)
	tension	0.15, 0.30, 0.45, 0.50	

In all cases, nitriding was performed in ammonia at atmospheric pressure for 20 h.

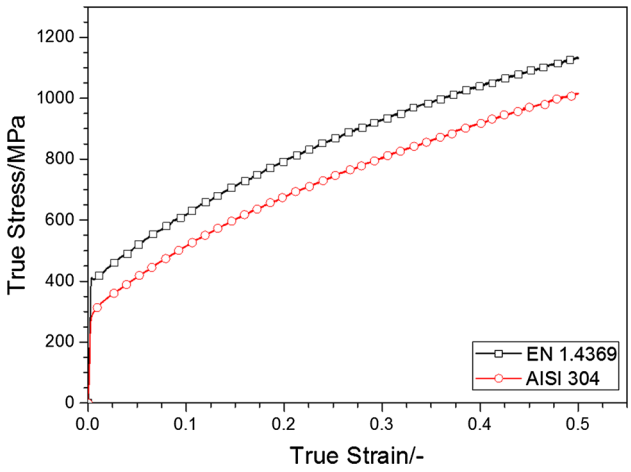

Fig. 1—True Stress–True Strain Curve for EN 1.4369 and AISI 304.

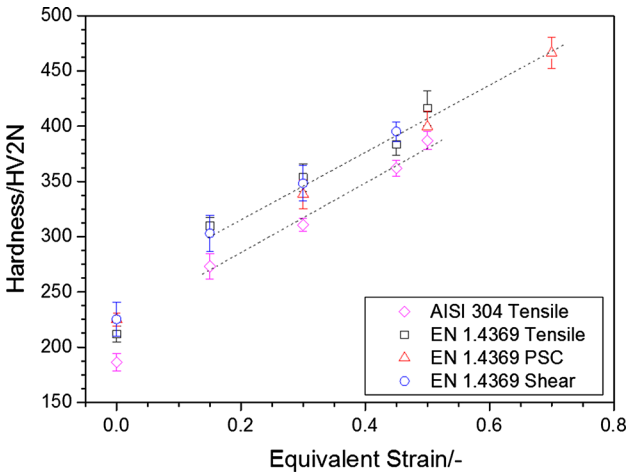

Fig. 2—Hardness evolution of the EN 1.4369 and AISI 304 alloys with the increasing equivalent deformation.

under consideration as measured for a LaB_6 reference powder.

III. RESULTS AND INTERPRETATION

A. *As-Deformed State of AISI 304 and EN 1.4369*

Stress–strain curves obtained in uniaxial tensile tests for both alloys are given in Figure 1. The yield strengths for EN 1.4369 and AISI 304 are 403 and 290 MPa, respectively. The difference in yield strength is largely attributed to the solid-solution strengthening effect of nitrogen in EN 1.4369.[3]

Graphs of the bulk hardness evolution with the increasing plastic deformation and X-ray diffractograms are given as a function of the equivalent strain in Figures 2 and 3, respectively, for both AISI 304 and EN 1.4369. Along with plastic straining, the bulk hardness increased for both alloys (Figure 2). As demonstrated for EN 1.4369, the hardness increased with equivalent plastic strain, irrespective of the mode of straining.

AISI 304 is fully austenitic in the annealed condition and develops strain-induced martensite on plastic straining. On the other hand, EN 1.4369 remained fully austenitic, irrespective of the mode of straining or the equivalent strain applied (Figure 3). Evidently, the austenite stabilizing elements in EN 1.4369, in particular

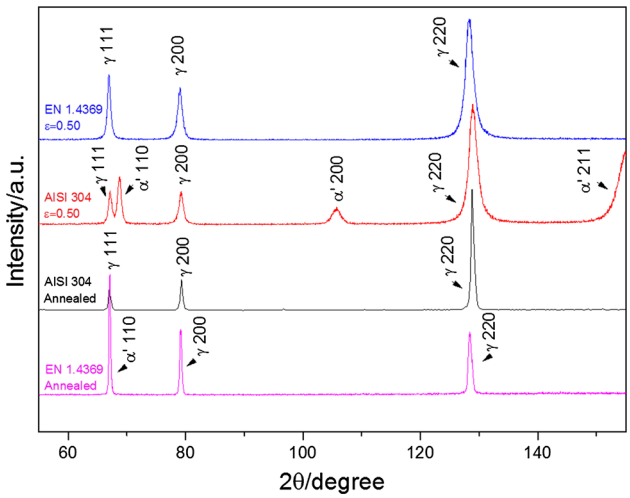

Fig. 3—XRD phase analysis of the maximum tensile plastic deformation ($\varepsilon = 0.5$) on EN 1.4369 and AISI 304.

nitrogen,[4] are more effective than nickel in AISI 304 and effectively prevent the development of strain-induced martensite.

Single-line method is a XRD method for the evaluation of microstrains and diffracting domain size, as

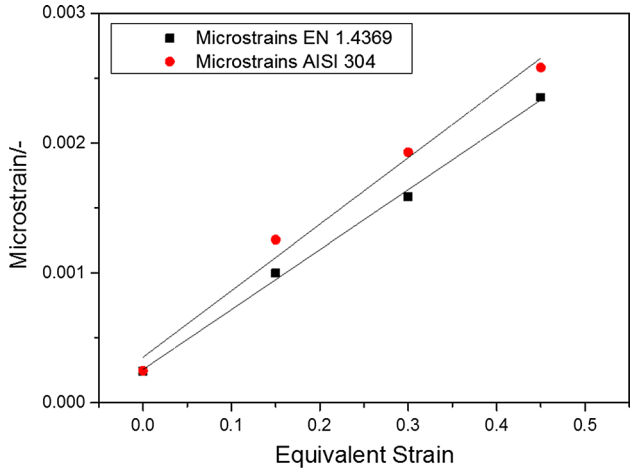

Fig. 4—Microstrains evolution with the increasing equivalent deformation for AISI 304 and EN 1.4369.

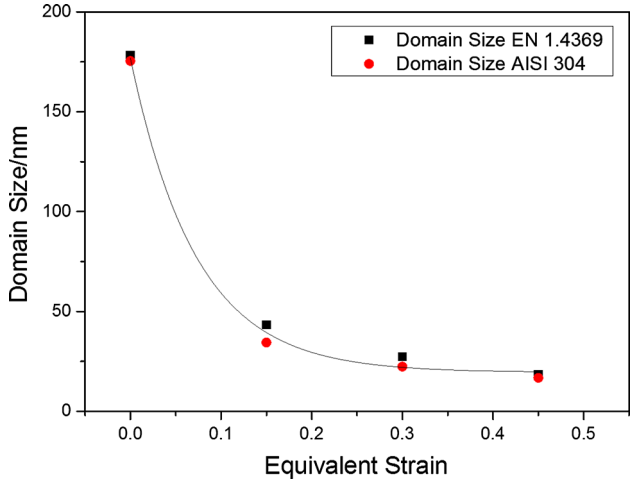

Fig. 5—Domain size evolution with the increasing equivalent deformation for AISI 304 and EN 1.4369.

reported in Reference 23. In AISI 304 higher microstrains developed upon plastic deformation as compared with the EN 1.4369 (Figure 4). This difference in microstrain is attributed to the local volume changes introduced by the formation of strain-induced martensite in AISI 304. The coherently diffracting domain size in austenite is practically the same for the two alloys (Figure 5).

B. *Nitriding Response of Deformed Austenitic Stainless Steel*

The nitriding response of the two investigated austenitic stainless steels will be discussed separately in the following.

1. *AISI 304*

a. LTN 703 K (430 °C), 20 hours. Cross-sectional micrographs of nitrided AISI 304 are given in Figure 6. From the micrographs, it is observed that nitriding of the annealed sample at 703 K (430 °C) produced a nitrided zone depth of approximately 12 μm. The expanded austenite zone appears featureless, while the austenite in the bulk *is* attacked by the etching agent. Ahead of the expanded austenite zone as marked by a line, a thin white zone is present parallel to this "separation" line. This is not considered to be an etching artifact and will be discussed in relation to EN 1.4369, where this feature is more clearly observed (*cf.* Figure 12). For higher equivalent strains, this thin white zone is more difficult to observe. From the difference in etching behavior between expanded austenite and the bulk, it follows that the corrosion potential is higher for expanded austenite than for the bulk. The occurrence of strain-induced martensite, introduced during the mechanical preparation of the cross section, can be observed in the bulk of the annealed and nitrided sample (Figure 6(a)). At equivalent strains larger than zero, dark-etched regions are observed in the nitrided zone, indicating reduced corrosion resistance in the applied etchant. The depth of the nitrided zone increases for the higher equivalent strains (Figure 6(d)).

The X-ray diffractograms for AISI 304 nitrided at 703 K (430 °C) show the formation of expanded austenite, γ_N, for all equivalent strains investigated (Figure 7). In the diffractograms, three peaks of expanded austenite are prominently present and corresponding reflections from austenite in the underlying steel are also observed, indicating that the information depth has been larger than the thickness of the nitrided zone. It is noted that in particular the 220 austenite reflection from the steel "substrate" is visible, because the information depth increases with scattering angle 2θ and because this reflection was dominant in the as-deformed state (*cf.* Figure 3). Despite the dominance of 220γ in the deformed substrate, the $220\gamma_N$ reflection is not prominent (even though it is rather broad), while $200\gamma_N$ (and to a lesser extent $111\gamma_N$) appear to dominate. These observations indicate that texture changes occur over the thickness of the expanded austenite zone, consistent with earlier observations and explained from lattice rotation as a consequence of plastic deformation induced by enormous composition-induced stresses in expanded austenite with a relatively high amount of nitrogen.[25]

Concerning the presence of appreciable amounts of strain-induced martensite in the as-deformed state, it is observed that a reduction of the diffracted intensity of martensite occurs on nitriding (see in particular absence of a clear $110\alpha'$ peak in nitrided deformed samples in Figure 7), suggesting that strain-induced martensite is converted to austenite upon nitriding.

Grazing incidence X-ray diffractograms at the lowest applied grazing incidence angle ($\alpha = 2.5$ deg) are given in Figure 8 for the annealed condition and for an equivalent strain of 0.5. Under these measurement conditions, the reflections from the austenite bulk are no longer visible, and it is possible to find significant differences between the samples in the different straining conditions. For the annealed sample, in addition to expanded austenite also (expanded) martensite, α', and ε-$(Fe,Cr)_2N_{1-z}$ are present close to the surface, albeit in small amounts. In principle, epsilon phase may be stabilized by a strain-induced martensitic transformation from f.c.c. to h.c.p. or by a high nitrogen content.[26] For grazing incidence diffractograms at larger

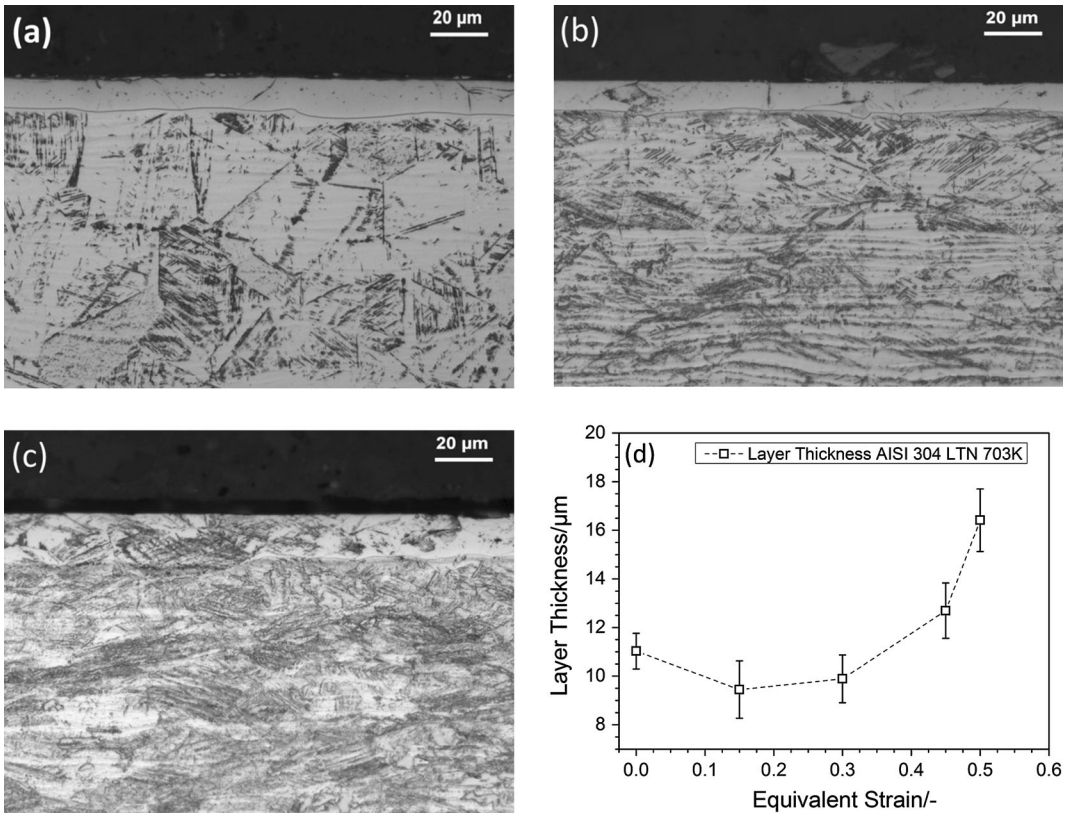

Fig. 6—Micrographs of nitrided AISI 304: (*a*) = Annealed, (*b*): $\varepsilon = 0.30$, (*c*): $\varepsilon = 0.50$, (*d*) depth of the nitrided zone *vs* equivalent strain (Nitriding conditions: $T = 703$ K (430 °C), 20 h, 100 pct NH_3).

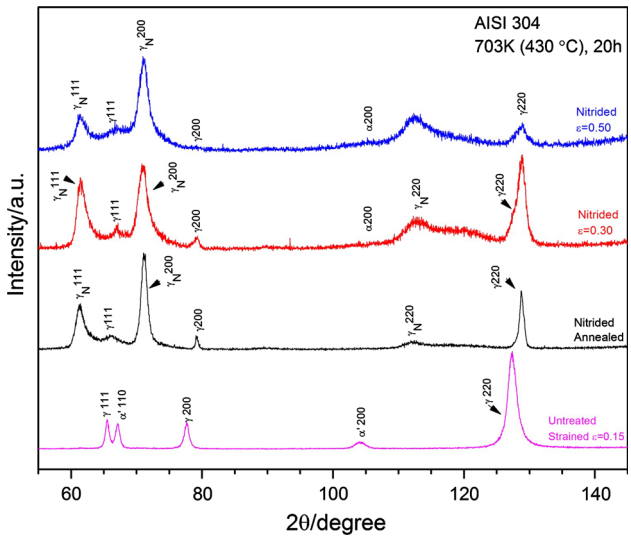

Fig. 7—X-ray diffractograms of nitrided AISI 304 [703 K (430 °C), 20 h].

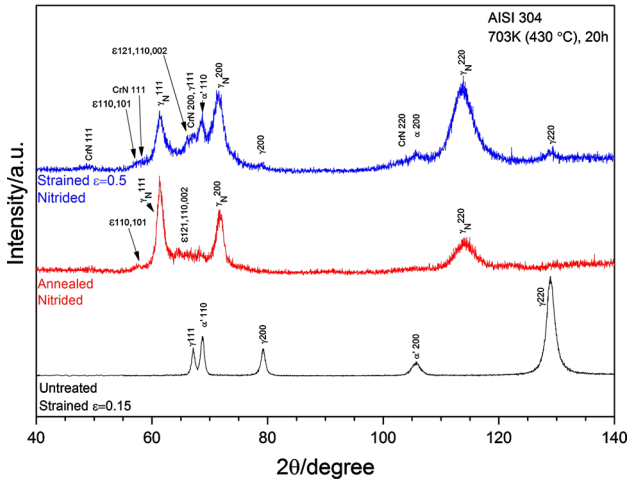

Fig. 8—GI X-ray diffractogram at $\alpha = 2.5$ deg of AISI 304 annealed and tensile strained.

incident angle, corresponding to averaging over a larger depth range, the relative intensity of epsilon phase was observed to be lower than for the one given in Figure 8, indicating that epsilon phase is only present at the very surface of the material, where the highest nitrogen content is expected. It is therefore concluded that, in particular, the high nitrogen content close to the surface, rather than strain-induced formation of epsilon martensite, is responsible for epsilon's presence. For the sample that was subjected to an equivalent strain of 0.5, in addition to expanded austenite, reflections of ferrite and CrN are observed in the surface region after nitriding at 703 K (430 °C) (Figure 8).

The hardness profiles of nitrided AISI 304 in annealed condition and deformed at the maximum equivalent strain are given in Figure 9. Apparently, the hardness in

the case is independent of the state of deformation, while that in the substrate clearly is. For both hardness profiles, a sharp drop is observed at the case–core transition. The bulk hardness remained unaffected by low-temperature nitriding.

b. LTN 728 K (455 °C), 20 hours. Nitriding at a temperature of 728 K (455 °C) led to a marked change in the morphology of the nitrided zone (Figure 10). For the annealed sample, a dark-etched region is present immediately underneath the surface, and only the part of the nitrided zone deepest in the steel can be recognized as featureless expanded austenite. This dark zone in the nitrided case is the result of abundant precipitation of CrN, as a consequence of the combination of a high nitriding temperature with long nitriding time. Preferentially, CrN precipitation is manifested in the area close to the surface, because (i) the driving force for CrN development has been highest here, because of the (initially) high nitrogen content and (ii) this part has experienced the longest thermal exposure as growth occurs inwardly. The continuous dark-etched band in the nitrided zone becomes less pronounced with increasing equivalent strain and is replaced by dark regions that appear to coincide with banded features in the deformed structure, indicating that the development of CrN is promoted by features in the deformation structure. At the same time, a remarkable increase in the depth of the nitrided zone is observed (Figure 10(d)).

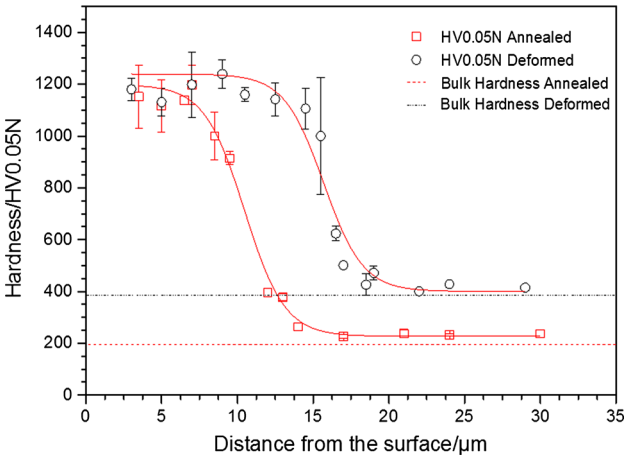

Fig. 9—Hardness depth profiles of AISI 304 in annealed and deformed ($\varepsilon = 0.5$) condition and subsequently nitrided at 703 K (430 °C) for 20 h. Hardness depth profiles were measured with a 5 g load, bulk hardness measurement performed with 200 g load.

X-ray diffractograms of AISI 304 nitrided at 728 K (455 °C) clearly show the presence of CrN and ferrite for all investigated samples, while expanded austenite is no longer the dominant phase (Figure 11). For the annealed sample, the expanded austenite peak originates from the featureless zone deeper in the nitrided case and the position lies close to the original position of austenite because of the low nitrogen content and corresponding low lattice expansion.

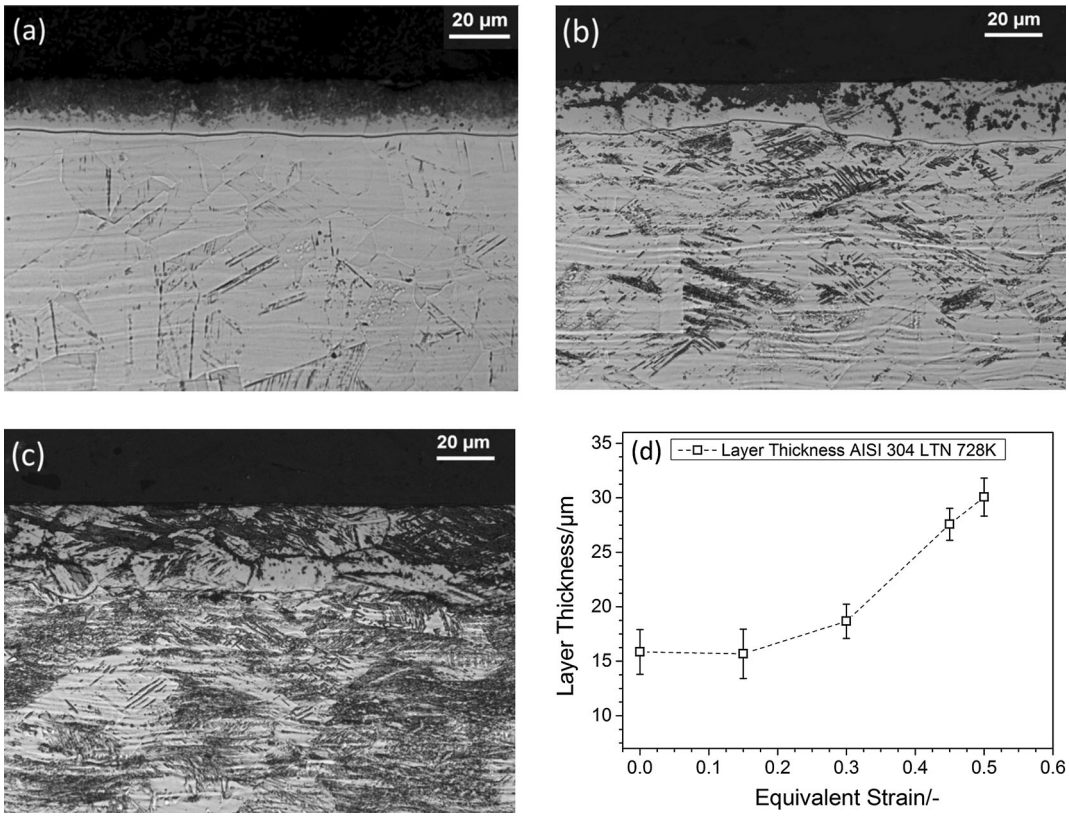

Fig. 10—Micrographs of nitrided AISI 304: (*a*) = Annealed, (*b*): $\varepsilon = 0.30$, (*c*): $\varepsilon = 0.50$, (*d*): depth of the nitrided zone *vs* equivalent strain; Nitriding conditions $T = 728$ K (455 °C), 20 h.

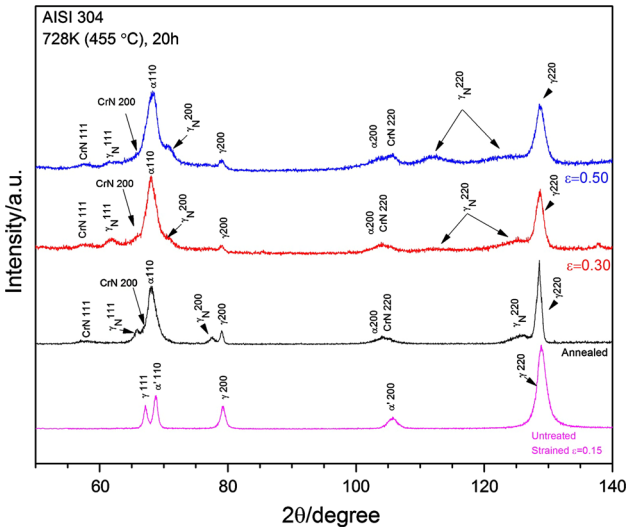

Fig. 11—X-ray diffraction patterns of nitrided AISI 304 [728 K (455 °C), 20 h].

For the deformed samples, it is possible to observe low-intensity expanded austenite peaks together with the characteristic peaks of ferrite and chromium nitrides. These results are consistent with the observations in the corresponding micrographs (Figure 10), where dark-etched regions, related to the presence of CrN, and lighter regions (expanded austenite) are found throughout the thickness of the nitrided case.

Furthermore, as depicted for the $220\gamma_N$ reflections of the AISI 304 tensile strained at $\varepsilon = 0.30$ and $\varepsilon = 0.50$ in Figure 11, expanded austenite is manifested as two peaks. The reflection at lower 2θ is the expanded austenite with the highest nitrogen content, while the reflection at higher 2θ is expanded austenite with relatively low nitrogen content. Expanded austenite with lower nitrogen content is expected in regions (partly) depleted in Cr because of the development of CrN and/or expanded austenite present in the deepest part of the nitrided zone.

2. *EN 1.4369*

a. LTN 703 K (430 °C), 20 hours. Micrographs of EN 1.4369 in the annealed and deformed condition nitrided at 703 K (430 °C) for 20 hours are given in Figure 12. Irrespective of the equivalent strain, the nitrided zone in EN 1.4369 appears virtually unattacked by the etching agent. In the bulk of the sample, banded features inclined about 45 deg to the surface, *i.e.*, approximately aligned with the most stressed sample planes during the plastic deformation, are observed; such bands are unresolved in the expanded austenite zone. Within experimental accuracy, the thickness of the nitrided zone appears independent of the equivalent strain, but a weak trend toward faster growth with increasing degree of deformation can be discerned (Figure 12(d)). Note the thin white zone parallel to and ahead of the line that marks the transition from expanded austenite to the "substrate." This white zone is more pronounced than for the nitrided AISI 304 samples (*cf.* micrographs in Figure 6). Similar features were observed earlier for AISI 316[10] and explained from a small concentration of nitrogen atoms not trapped by chromium atoms (no short-range ordering).[27] In this respect, it is noted that Mn enhances the solubility of N in austenite, thus leading to a clearer zone. Alternatively, this feature could be the result of accumulated carbon atoms pushed ahead of the nitriding front.

The response of the materials deformed through shear and plane strain deformation was similar to the tensile-strained samples at both nitriding temperatures. In contrast to Figure 6 for AISI 304, no significant differences were found in the morphology or thickness of the nitrided case for EN 1.4369. Bragg–Brentano geometry X-ray diffractograms of annealed and tensile-strained EN 1.4369 nitrided at 703 K (430 °C) are collected in Figure 13. Irrespective of the equivalent strain, the only reflections observed are for austenite in the bulk and expanded austenite, consistent with the micrographs in Figures 12(a) through (c). Asymmetric broadening to the high angle side of the 220γ peak is considered to be a consequence of the presence of a low concentration of nitrogen or carbon atoms ahead of the expanded austenite zone (*cf.* the white zone in the micrographs in Figure 12). Grazing incidence X-ray diffractograms show, in addition to (expanded) austenite, the occurrence of reflections of ε-phase in the near-surface region (Figure 14). No indications for the presence of CrN were found. For the $220\gamma_N$ peak, a striking difference is observed between diffracted intensities for the annealed and the deformed state. This indicates a texture difference between the nitrided annealed state and nitrided deformed state. Even though the untreated deformed state also shows a relatively strong 220γ peak as compared with the untreated annealed state (*cf.* Figure 3), the observed 220 intensity difference for the nitrided states appears incommensurate with this initial intensity difference. This result may suggest that the prior deformation texture in the deformed samples affects the composition-induced lattice rotation during nitriding.

The hardness profile in nitrided EN 1.4369 in annealed and strained to $\varepsilon = 0.5$ conditions is presented in Figure 15. Apart from the hardness level in the bulk, the hardness profiles are identical, consistent with earlier observations that the thickness of the nitrided case is independent of the equivalent strain (Figure 12(d)) and that the strain has no influence on the hardness level reached in the nitrided zone. Similar hardness depth profiles were obtained after nitriding of the other strain modes.

b. 743 K (470 °C), 20 hours. Augmenting the nitriding temperature to 743 K (470 °C) shows the appearance of dark-etched areas (Figure 16), most likely associated with decomposition of expanded austenite and the development of CrN. Even under these experimental conditions, the morphology and the thickness of the nitrided case seem to be totally unaffected by the plastic deformation. For the annealed and deformed samples,

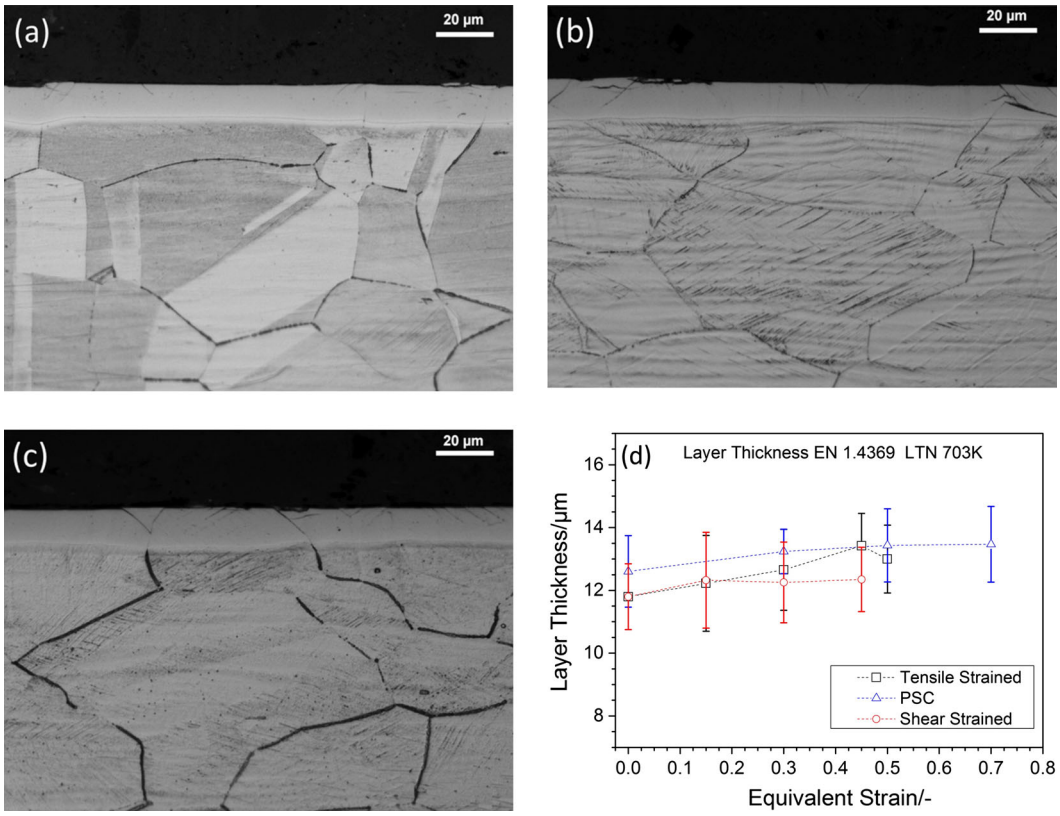

Fig. 12—Micrographs of EN 1.4369 tensile deformed and nitrided: (*a*) =Annealed, (*b*): $\varepsilon = 0.30$, (*c*): $\varepsilon = 0.50$, (*d*) depth of nitrided zone (Nitriding conditions: $T = 703$ K (430 °C), 20 h).

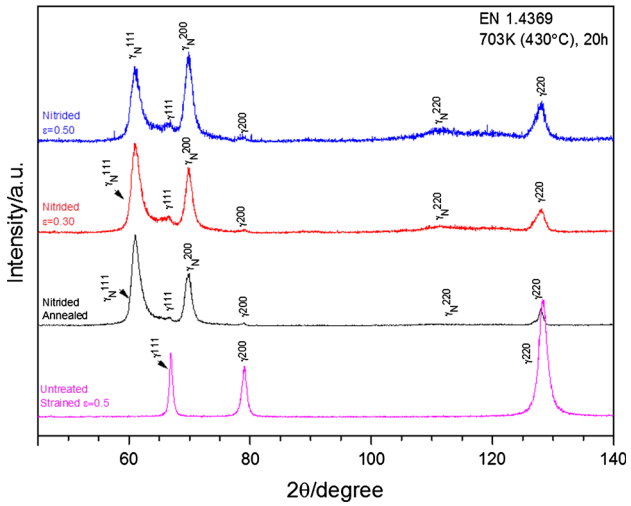

Fig. 13—X-ray diffraction patterns of Nitrided EN 1.4369 [703 K (430 °C), 20 h].

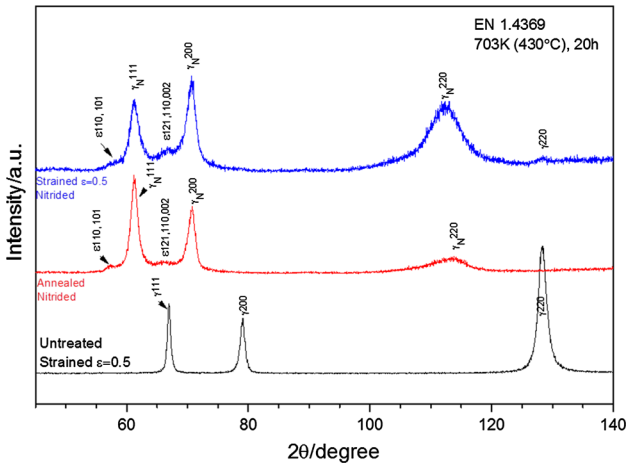

Fig. 14—GI XRD of the EN 1.4369 annealed and tensile strained at a grazing incidence angle of $\alpha = 2.5$.

the nucleation of CrN occurs immediately underneath the surface. Below this area, featureless expanded austenite can be recognized. Nucleation of CrN occurs preferentially in the proximity of the surface for the same reasons ((i) and (ii)) explained for the nitriding at 728 K (455 °C) of the AISI 304. The thickness of the nitrided zone is independent of the equivalent strain, consistent with the observations in Figure 12 at lower nitriding temperature. However, despite the higher processing temperature, the layer thickness of the nitrided case is similar to the one obtained at 703 K (430 °C) (*cf.* Figure 12(d)). This behavior is mainly due to the decomposition of the expanded austenite phase and the formation of CrN, which reduces the diffusive flux of nitrogen into the steel.

Increasing the nitriding temperature to 743 K (470 °C) has a considerable effect on the morphology and composition of the nitrided zone. As compared with nitriding at lower temperature, peaks of expanded austenite and austenite are no longer the dominant phases. XRD investigation shows instead the presence of reflections of CrN and ferrite or expanded ferrite if N is dissolved,** along with expanded austenite (Figure 17) for both the annealed and deformed state. As observed for nitriding this alloy at lower temperature, no clear difference in the phase composition can be observed between the annealed and deformed sample.

The expanded austenite peaks detected are generated by the deeper region of the nitrided case. Their positions lie close to the corresponding austenite peaks because of the low nitrogen content and therefore low lattice expansion. Furthermore, the austenite peaks generated by the substrate are visible in all materials in all processing conditions.

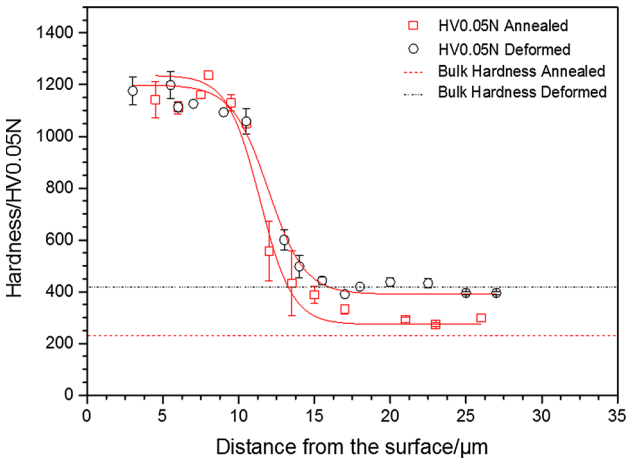

Fig. 15—Hardness depth profile of the EN 1.4369 nitrided at 703 K (430 °C).

IV. DISCUSSION

A. *Mechanical Properties and Microstructure of as-Deformed Material*

The hardness values measured on the samples of AISI 304 and EN 1.4369 (Figure 2) deformed in uniaxial tension are compared with the true (yield) stress values

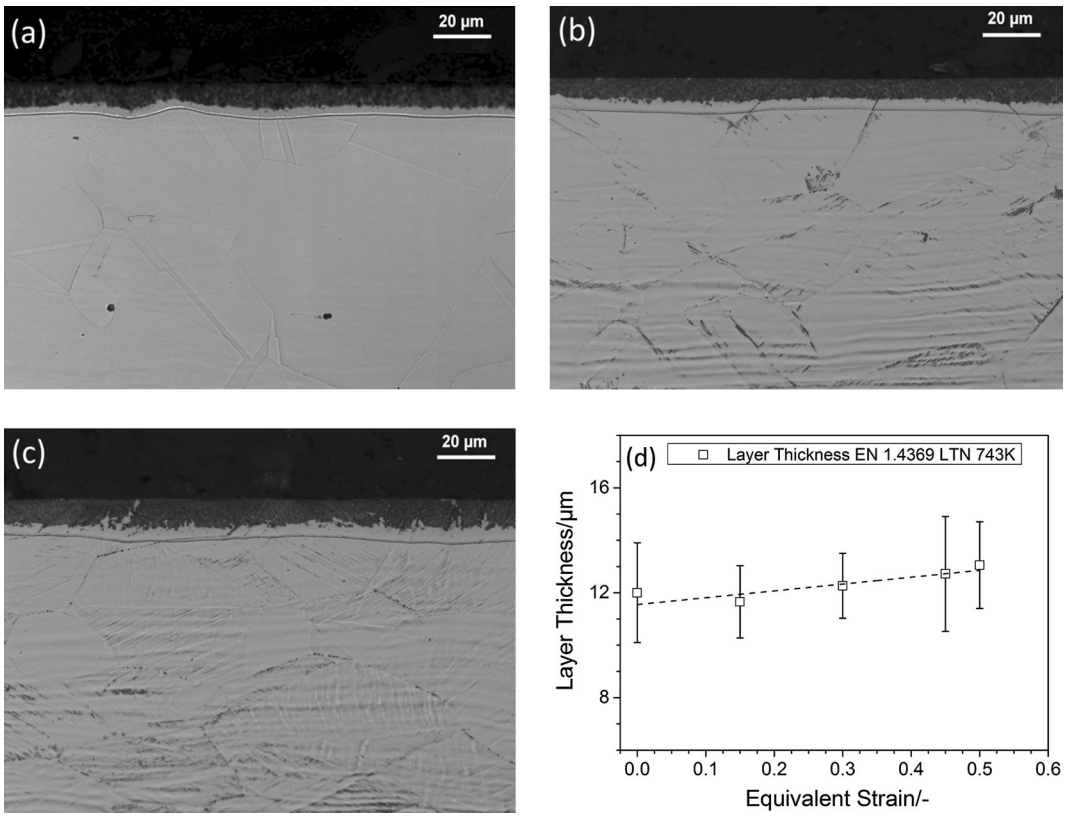

Fig. 16—EN 1.4369 tensile deformed and nitrided: (*a*) = Annealed, (*b*): $\varepsilon = 0.30$, (*c*): $\varepsilon = 0.5$, (*d*): thickness of the expanded austenite zone *vs* equivalent strain [743 K (470 °C), 20 h].

**Since this ferrite is not a result of a martensitic transformation of austenite, but rather a thermally activated decomposition product, it is not referred to as martensite. Nonetheless, it cannot be excluded that nitrogen dissolves into ferrite and leads to a tetragonal distortion of the b.c.c. lattice.

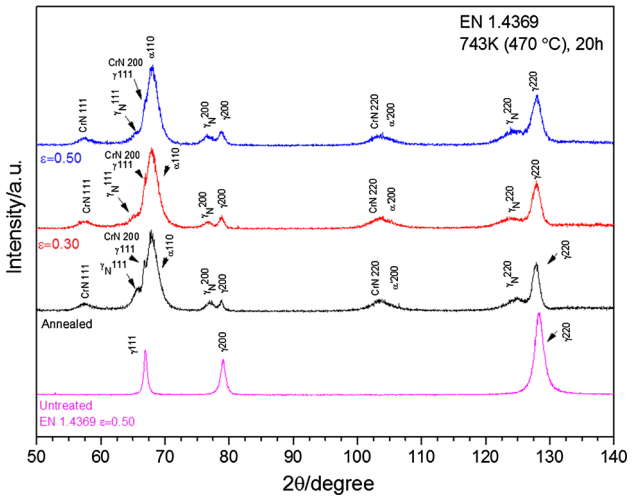

Fig. 17—X-ray diffraction patterns of Nitrided EN 1.4369 [743 K (470 °C), 20 h].

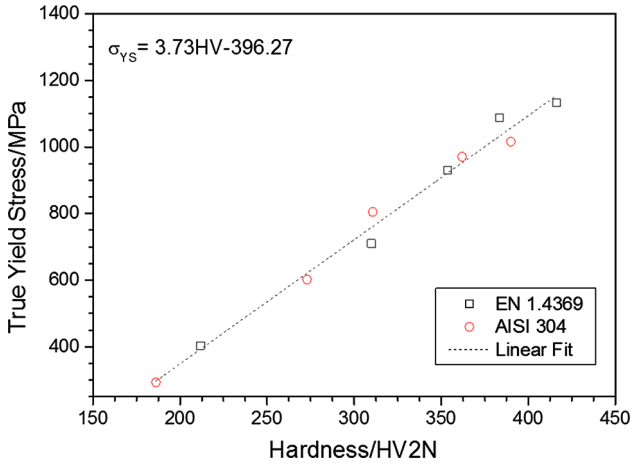

Fig. 18—Yield Strength *vs* bulk Hardness for the EN 1.4369 and AISI 304.

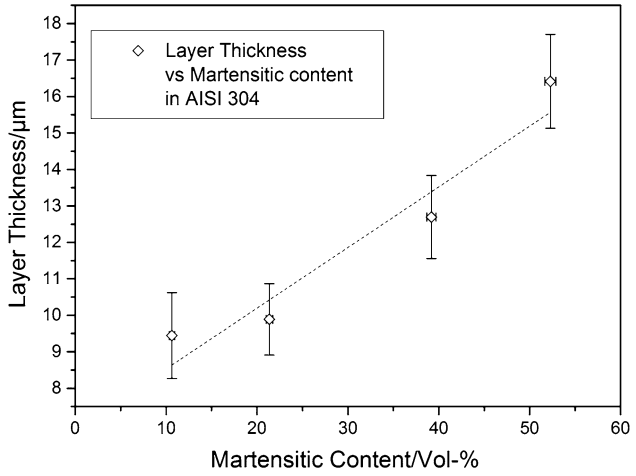

Fig. 19—Expanded austenite thickness evolution as function of the strain-induced martensite content in AISI 304 during low-temperature nitriding (Nitriding conditions: $T = 703$ K (430 °C), 20 h).

(Figure 1) in Figure 18. A linear correlation between true (yield) stress and hardness was found, both being a measure for the resistance against plastic deformation. Apparently, the development of strain-induced martensite in AISI 304 and the presence of nitrogen in EN 1.4369 have comparable or no measurable influence on the resistance against plastic deformation. Extrapolation of the linear regression fit of true stress and hardness data indicates that a hardness of about 1200 HV, as observed in expanded austenite (*cf.* Figures 9 and 15(a)), corresponds to a true (uniaxial) yield stress of about 4 GPa. It is noted that this appreciably high uniaxial tension value is consistent with the occurrence of very large (biaxial) elastic compressive in-plane biaxial residual stress values of several GPa's reported for expanded austenite stabilized by carbon or nitrogen.[8,28]† Nevertheless, huge compressive stress levels in excess of 7 GPa as reported for nitrided AISI 316 cannot be understood and have recently been attributed to the application of inappropriate elastic constants and grain-interaction models.[29]

†In this respect, it is noted that the deformation response upon uniaxial tension and plane stress compression are essentially equivalent.

B. *Effect of Prior Deformation on Nitriding Behavior*

Low-temperature nitriding of austenitic steels in (partly dissociated) NH_3 allowed the development of expanded austenite. The different responses of AISI 304 and EN 1.4369 toward plastic deformation had a decisive influence on the nitriding performance of these alloys. At a relatively low nitriding temperature, prior plastic deformation has no observable effect on the morphology for EN 1.4369 (as investigated with reflected-light microscopy, Figure 12), neither the thickness of the expanded austenite zone nor the hardness. X-ray diffraction suggests that additional plastic deformation (lattice rotation) induced by composition-induced compressive stresses exceeding the yield stress may be affected by prior deformation. For the same nitriding conditions, prior deformation of AISI 304 and the associated development of strain-induced martensite have a clear effect on the morphology and thickness of the nitrided zone, while the hardness appears unaffected. Reflected-light microscopy shows a remarkable increase of the thickness of the nitrided zone (Figure 6). An increase of the thickness of the expanded austenite zone with an increase of the initial volume fraction of strain-induced martensite (Figure 19) is explained as follows. According to growth models that have been derived to describe the growth of a case developing during internal oxidation[30] or internal nitriding,[31] the growth rate is proportional to the product of concentration gradient and (effective) diffusion coefficient and inversely proportional to the amount of nitrogen that is stored in the case on growth. Generally, diffusion of nitrogen atoms in martensite proceeds faster than diffusion of nitrogen in austenite (f.c.c.),[32,33] while

the amount of nitrogen that can be stored in martensite is smaller than in austenite.[3,34] Both these effects would promote faster growth of a martensite case than an austenite case. For the present situation, the developing case should be considered as a dispersion of martensite regions in an austenite matrix. Then, faster diffusion of nitrogen through the martensite regions and less accumulation of nitrogen in these martensite regions both lead to a larger fraction of the flux of nitrogen atoms that enters the sample arriving at the case–core transition and expendable for growth of the case. Consequently, a higher fraction of martensite in the case leads to faster growth.

This explanation applies only for the region in the nitrided zone where the nitrogen content is sufficiently low, where (expanded) martensite is stable. A high nitrogen content may cause a transformation of martensite into austenite because of the strong austenite-forming ability of nitrogen. If such transformation does occur, part of the accelerating effect of martensite on the growth rate of the case is lost.

Grazing incidence XRD investigations confirmed the presence of CrN in AISI 304 with increasing degree of plastic deformation. Since no such CrN development was observed for EN 1.4369, CrN precipitation cannot be the immediate result of energetically favorable nucleation on dislocations in austenite. Rather, the development of CrN is attributed to the presence of strain-induced martensite and the existence of a favorable Baker–Nutting orientation relationship between the b.c.c. lattice of strain-induced martensite and CrN: $\{001\}_{b.c.c.}//\{001\}_{CrN}$ and $\langle 100\rangle_{b.c.c.}//\langle 001\rangle_{CrN}$; existing evidence in the literature that a coherent, *i.e.*, low energy, interface occurs between martensite (b.c.c.) and CrN according to the Baker–Nutting orientation relation has been observed generally for MN (M = Ti, V, Cr, Ta) nitrides in b.c.c. iron.[35] The driving force for CrN formation associated with the presence of expanded martensite is anticipated to be lower than from expanded austenite because the maximum nitrogen content is considerably lower in martensite than in austenite. Then, early nucleation can be explained from a favorable interfacial energy leading to a lower nucleation barrier or from more favorable strain energy in the system. Such development of CrN leads to the consumption of Cr from martensite and will reduce the total amount of nitrogen that can be stored in the martensite region. This contributes to a larger flux of nitrogen in depth and hence a deeper case (see above).

Micro-hardness measurements indicate that the maximum hardness that is achieved after nitriding is, within experimental accuracy, identical for AISI 304 and EN 1.4369, irrespective of the degree of prior deformation or the content of strain-induced martensite. This finding strongly suggests that the dominant strengthening mechanism in expanded austenite is solid-solution strengthening by dissolved nitrogen.

C. *Effect of Temperature on Nitriding Behavior*

At higher nitriding temperatures, *i.e.*, 728 K (455 °C) for AISI 304 and 743 K (470 °C) for EN 1.4369, CrN developed within the process time, irrespective of the deformation state of the sample.

For the EN 1.4369, no effects of the plastic deformation on the morphology and composition of the nitrided layer have been found. In all samples in the annealed and deformed state, the case consists of a continuous band of CrN and ferrite at the surface and expanded austenite underneath. Nitriding at this temperature leads to the formation of expanded austenite that later decomposes into CrN and ferrite after some incubation time.

The driving force for the nucleation of CrN is highest at the surface of the material because of the (initially) high nitrogen content; moreover, this region has experienced the longest thermal exposure, while nitrogen has been present. Therefore, the nucleation of CrN is preferentially observed at and close to the surface of the material.

In this case, it is possible to conclude that the higher dislocation density in the deformed samples does not create more favorable nucleation sites for the decomposition of expanded austenite into CrN and ferrite as compared with the sample in the annealed condition, not even at higher nitriding temperatures.

Hence, in all samples, a continuous band of decomposed expanded austenite has developed. The consequence of the decomposition is a relatively thin case, which is caused by a small diffusive flux of nitrogen atoms from the nitriding atmosphere into the sample. The reason for the small flux of nitrogen atoms is the low solubility of nitrogen in the remaining ferrite, which is depleted from Cr, leading to a shallow nitrogen concentration gradient over the decomposed part of the nitrided case and the relatively long diffusion path for nitrogen atoms through the ferrite labyrinth in the decomposed zone. For AISI 304 nitrided at 728 K (455 °C), ferrite and CrN were present in all samples, irrespective of the processing conditions. Nevertheless, plastic deformation and presence of strain-induced martensite were observed to have a dominating effect on the nitriding behavior. For the annealed sample that is initially in fully austenitic condition, the nitrided layer consists of a homogenous band of decomposed expanded austenite consisting of ferrite and CrN close to the surface and a zone of expanded austenite underneath.

The presence of strain-induced martensite provokes a completely different morphology of the nitrided case. The higher nitriding temperature together with higher martensite content (with relatively low nitrogen solubility) favors relatively fast nitrogen diffusion toward the steel interior. The development of CrN (and ferrite) takes place over the entire case, particularly along features in the deformed structure. The presence of strain-induced martensite is likely to provide favorable sites for the development of CrN (and ferrite), but it appears counterintuitive that only localized CrN development occurs in deformed AISI 304, while annealed AISI 304 shows a continuous zone of decomposed expanded austenite. A possible explanation for this behavior is the combination of a relatively high temperature and the presence of martensite, which facilitate a larger flux of nitrogen through the nitrided zone.

Consequently, the accumulation of nitrogen in expanded austenite (prior to decomposition) is not as pronounced as for a microstructure where no martensite is present. Hence, the driving force for decomposition of expanded austenite is not as high as for expanded austenite forming from an annealed austenite. Furthermore, relatively low nitrogen content in martensite prevents its transformation to austenite. CrN nucleation is promoted by the presence of b.c.c. martensite because of the energetically favorable Baker–Nutting orientation relationship between b.c.c. and NaCl-type CrN.[35] In addition to these effects, the high density of dislocations in the vicinity of the deformation features may provide a means for relatively fast partitioning of the substitutional elements, which is a prerequisite for the nucleation of CrN.

V. CONCLUSIONS

Austenitic stainless steel qualities AISI 304 and EN 1.4369 in annealed and plastically strained conditions were surface hardened by low-temperature nitriding.

On plastic deformation, strain-induced martensite develops in AISI 304, while EN 1.4369 remains austenitic up to investigated maximum equivalent strain of 0.5, irrespective of the degree of deformation or the mode of deformation (tensile, shear, plane strain compression). The stability of austenite against plastic deformation has a significant effect on the nitriding response:

1. strain-induced martensite promotes faster growth of the case depth, while plastic deformation of austenite without martensite formation has no measurable effect on the case depth.
2. strain-induced martensite promotes the development of CrN formation.

It is recognized that in industrial practice the nitriding of components with plastic deformation in the surface region is the rule rather than the exception. As frequently observed in industrial practice, (severe) plastic deformation leads to early development of CrN during nitriding (and, analogously, Cr-carbides during carburizing). Such sensitization is anticipated to impair the anti-corrosion performance of ''stainless'' steel. As demonstrated in the present work, the mechanism leading to premature sensitization at relatively low temperature and relatively short treatment time is the preferred nucleation of CrN in the presence of strain-induced martensite, rather than enhanced nucleation in plastically deformed austenite without strain-induced martensite. Then, the use of austenitic stainless steel with stable austenite suggests itself, as for example, the EN 1.4369 quality investigated in the present work.

ACKNOWLEDGMENTS

For the present research work, the authors gratefully acknowledge the Research Fund for Coal and Steel for the financial support to the PressPerfect project. Furthermore, the authors would like to thank Sandvik Materials Technology for providing part of the materials used during the investigation and M2i-University of Twente for providing the shear-deformed samples.

REFERENCES

1. Z.I. Zhang and T. Bell: *Surf. Eng.*, 1985, vol. 1, pp. 131–36.
2. T. Bell, K. Mao, and Y. Sun: *Surf. Coat. Technol.*, 1998, vols. 108–109, pp. 360–68.
3. J.W. Simmons: *Mater. Sci. Eng. A*, 1996, vol. 207, pp. 159–69.
4. R.P. Reed: *JOM*, 1989, vol. 41, pp. 16–21.
5. D.L. Williamson, O. Ozturk, R. Wei, and P.J. Wilbur: *Surf. Coat. Technol.*, 1994, vol. 65, pp. 15–23.
6. Z. Yu, X. Xu, L. Wang, J. Qiang, and Z. Hei: *Surf. Coat. Technol.*, 2002, vol. 153, pp. 125–30.
7. X. Xu, L. Wang, Z. Yu, J. Qiang, and Z. Hei: *Metall. Mater. Trans. A*, 2000, vol. 31A, pp. 1193–99.
8. H. Dong: *Int. Mater. Rev.*, 2010, vol. 55, pp. 65–98.
9. T.L. Christiansen and M.A.J. Somers: *Int. J. Mater. Res. Former. Zeitschrift Fuer Met.*, 2009, vol. 100, pp. 1361–77.
10. T.L. Christiansen, T.S. Hummelshøj, and M.A.J. Somers: *Surf. Eng.*, 2010, vol. 26, pp. 242–47.
11. T.L. Christiansen and M.A.J. Somers: *Metall. Mater. Trans. A*, 2006, vol. 37A, pp. 675–82.
12. Y. Cao, F. Ernst, and G.M. Michal: *Acta Mater.*, 2003, vol. 51, pp. 4171–81.
13. Y. Sun and T. Bell: *Wear*, 1998, vol. 218, pp. 34–42.
14. C.X. Li and T. Bell: *Corros. Sci.*, 2004, vol. 46, pp. 1527–47.
15. M.K. Lei and X.M. Zhu: *Surf. Coat. Technol.*, 2005, vol. 193, pp. 22–28.
16. W. Liang, X. Bin, Y. Zhiwei, and S. Yaqin: *Surf. Coat. Technol.*, 2000, vol. 130, pp. 304–308.
17. T. Thiriet, T. Czerwiec, D. Hertz, G. Marcos, T. Toll-Duchanoy, S. Migot, B. Brugier, M. Foucault, and T. Belmonte: *Defect Diffus. Forum*, 2012, vols. 323–325, pp. 471–76.
18. M. Chemkhi, D. Retraint, A. Roos, C. Garnier, L. Waltz, C. Demangel, and G. Proust: *Surf. Coat. Technol.*, 2013, vol. 221, pp. 191–95.
19. T. Balusamy, T.S.N. Sankara Narayanan, K. Ravichandran, I.S. Park, and M.H. Lee: *Corros. Sci.*, 2013, vol. 74, pp. 332–44.
20. *Standard Test Methods for Tension Testing of Metallic Materials*, E8M-04: ASTM International, United States, 2013.
21. J. Post: *Report RFSR-CT-2012-00021*, Drachten/Netherlands, 2013, p. D 3.1.
22. G.W. Rowe: *Elements of Metalworking Theory*, Hodder Arnold, London, 1979, p. 144.
23. Th.H. de Keijser, J.I. Langford, E.J. Mittemeijer, and B.P. Vogels: *J. Appl. Crystallogr.*, 1982, vol. 15, pp. 308–14.
24. J.I. Langford: *J. Appl. Crystallogr.*, 1978, vol. 11, pp. 10–14.
25. C. Templier, J.C. Stinville, P. Villechaise, P.O. Renault, G. Abrasonis, J.P. Rivière, A. Martinavičius, and M. Drouet: *Surf. Coat. Technol.*, 2010, vol. 204, pp. 2551–58.
26. J.O. Nilsson, A. Hultin Stigenberg, and P. Liu: *Metall. Mater. Trans. A*, 1994, vol. 25A, pp. 2225–33.
27. T.L. Christiansen, K.V. Dahl, and M.A.J. Somers: *Mater. Sci. Technol.*, 2008, vol. 24, pp. 159–67.
28. T.L. Christiansen and M.A.J. Somers: *Metall. Mater. Trans. A*, 2008, vol. 40A, pp. 1791–98.
29. F.A.P. Fernandes, T.L. Christiansen, and M.A.J. Somers: *Adv. Mater. Res.*, 2014, vol. 996, pp. 155–61.
30. J.L. Meijering: *Acta Metall.*, 1966, vol. 14, pp. 251–58.
31. K.H. Jack: *Acta Crystallogr.*, 1952, vol. 5, pp. 404–11.
32. R. Da Hales and A.C. Hill: *Met. Sci.*, 1977, vol. 11, pp. 241–44.
33. J.R.G. Da Silva and R.B. McLellan: *Mater. Sci. Eng.*, 1976, vol. 26, pp. 83–87.
34. K.H. Jack: *R. Soc.*, 1951, vol. 208, pp. 200–15.
35. M.A.J. Somers, R.M. Lankreijer, and E.J. Mittemeijer: *Philos. Mag. A*, 1989, vol. 59, pp. 353–78.

7 Paper II: Influence of microstructure and process conditions on simultaneous low-temperature surface hardening and bulk precipitation hardening of Nanoflex®

Federico Bottoli, Grethe Winther, Thomas L. Christiansen, Marcel A.J. Somers
Technical University of Denmark, Department of Mechanical Engineering, Produktionstorvet b.425, 2800 Kgs. Lyngby, Denmark

Article published in Metallurgical and Materials Transactions A, Vol. 46, Issue 11, pp. 5201-2516.

Influence of Microstructure and Process Conditions on Simultaneous Low-Temperature Surface Hardening and Bulk Precipitation Hardening of Nanoflex®

FEDERICO BOTTOLI, GRETHE WINTHER, THOMAS L. CHRISTIANSEN, and MARCEL A.J. SOMERS

Precipitation hardening martensitic stainless steel Nanoflex was low-temperature nitrided or nitrocarburized. In these treatments, simultaneous hardening of the bulk, by precipitation hardening, and the surface by dissolving nitrogen/carbon can be obtained because the treatment temperatures and times for these essentially different hardening mechanisms are compatible. The effect of the processing history of the steel on the nitrided/nitrocarburized case was investigated by varying the amounts of austenite and martensite through variation of the degree of plastic deformation by tensile strain, deep cooling, and deliberate manipulation of the austenite stability. The nitrided/nitrocarburized case was investigated with reflected light microscopy, hardness-depth profiling, X-ray diffraction analysis, and glow discharge optical emission spectroscopy. The results demonstrate that a microstructure consisting of martensite results in the deepest nitrided case, while a shallow case develops on a microstructure consisting of austenite. For an initial microstructure consisting of both martensite and austenite a non-uniform case depth is achieved. Simultaneous bulk and surface hardening is only possible for martensite because the precipitation hardening does not occur in an austenite matrix.

DOI: 10.1007/s11661-015-3088-9

I. INTRODUCTION

LOW-TEMPERATURE thermochemical surface engineering of austenitic stainless steels by nitriding and/or carburizing has been widely studied in the past 30 years, because it provides the possibility to improve wear and fatigue performance without impairing the corrosion performance.[1–3] Through the years, plasma-based technologies have been applied for low-temperature nitriding processes and in the last 15 years gaseous processes for nitriding and carburizing of stainless steel were developed, matured, and commercialized. Gaseous processes provide a substantial advantage over plasma and implantation processes, in particular with respect to process control, materials handling, and geometrical constraints.[4]

So far, mainly low-temperature nitriding and carburizing of austenitic stainless steels have been studied, while thermochemical treatment of ferritic, duplex, martensitic, and precipitation hardening stainless steels has not received the same attention. However, a growing interest is recognized in low-temperature surface engineering processes for martensitic and precipitation hardening stainless steels, which have favorable bulk properties as high strength in combination with good corrosion resistance.[5,6] In this respect, it has been demonstrated that precipitation hardening steels can be simultaneously surface and bulk hardened in a single treatment.[7–11]

Among the precipitation hardening stainless steels, Nanoflex®* has been widely investigated and it is applied in several industrial applications because of its interesting mechanical properties.[12–15] Nanoflex's M_s temperature, defined as the temperature at which martensite forms instantaneously during cooling, was reported to be 83 K (−109 °C).[16] However, since Nanoflex® is a metastable precipitation hardening steel, martensite can form isothermally at a temperature appreciably higher than M_s. Depending on the (tailorable) stability of the alloy, the formation of isothermal martensite is observed even at room temperature.[16–20] In general, the stability of Nanoflex at room temperature is a function of various processing parameters, including the annealing conditions, temperature, and the applied mechanical load.[20–22]

It is well documented by transmission electron microscopy that the precipitation hardening effect in Nanoflex derives from the precipitation of Cu-clusters,

*Nanoflex is a registered trademark of Sandvik Materials Technology.

FEDERICO BOTTOLI, Ph.D. Student, GRETHE WINTHER, Associate Professor, THOMAS L. CHRISTIANSEN, Senior Researcher, and MARCEL A.J. SOMERS, Section Head, Professor, Dr.Ir., are with the Department of Mechanical Engineering, Technical University of Denmark, Produktionstorvet b.425, 2800 Kgs, Lyngby, Denmark. Contact e-mail: somers@mek.dtu.dk

Manuscript submitted February 24, 2015.
Article published online August 18, 2015

as well as the ordered intermetallic phases η-$Ni_3(Ti,Al)$ and Ni_3Mo and Fe_2Mo (Laves phase) from the martensite matrix.[23–28] Therefore, depending on the material's initial phase composition, it is possible to achieve excellent properties, such as high bulk hardness and high yield stress, by appropriate aging of the material in the temperature range 673 K and 773 K (400 °C and 500 °C).[25]

Nanoflex's excellent bulk properties can be further improved with respect to wear and corrosion resistance by low-temperature thermochemical surface engineering through the incorporation of N and/or C into the stainless steel matrix leading to the formation of a supersaturated solid solution.[2,4,29,30] The supersaturated solid solution is characterized by a high hardness, excellent wear resistance, and high corrosion and pitting resistance.[6,29,31–34]

The dissolution of N/C into the matrix and the establishment of a composition profile provoke an (constrained) expansion of the crystal lattice that is proportional to the interstitial content. The associated (high) compressive stresses depending on depth are associated with an improvement of the fatigue resistance.[35–38]

In this article, we address low-temperature nitriding and nitrocarburizing of the precipitation hardening Nanoflex. The material was subjected to several annealing and deformation processes before nitriding in order to investigate the sensitivity of the nitriding response to the material in dependence of the initial microstructure.

II. EXPERIMENTAL

A. *Specimen Preparation*

The composition of Nanoflex investigated in this work is given in Table I.

The material was delivered as 220 × 320 × 0.7 mm^3 plates and contained isothermal martensite in the as-received condition. Vibrating sample magnetometry (*cf.* Reference 39 for a description of the quantification method) indicated that the martensite content ranges from 15 to 60 pct, depending on the position on the plate. The Vickers hardness of the as-received material was 268 ± 34 HV_{2N}; supposedly, the large spread in hardness is caused by the variation in martensite content.

Prior to low-temperature surface hardening, the as-received material was subjected to several annealing and deformation treatments of which the details are given below (*cf.* Table II).

- Condition A: the as-received material was tensile strained to equivalent strains of $\varepsilon = 0.05$, $\varepsilon = 0.10$, and $\varepsilon = 0.15$ and successively subjected to low-temperature nitriding at 673 K and 693 K (400 °C and 420 °C) for 20 hours. Also, nitrocarburizing was performed at 693 K (420 °C) for 80 hours in a propene/ammonia atmosphere.
- Condition B: the as-received material was annealed at 1223 K (950 °C) for 1800 seconds (referred to as B1) to obtain *stable* austenite. Hereafter, the material was tensile strained to an equivalent strain of $\varepsilon = 0.25$ (referred to as B2). All the materials in conditions B1–B2 were subjected to low-temperature nitriding at 693 K (420 °C) for 20 hours.
- Condition C: the as-received material was annealed at 1423 K (1150 °C) for 900 seconds to obtain *unstable* austenite (referred to as C1) that quickly transforms into isothermal martensite at room temperature. To avoid isothermal martensite formation, some samples were cooled to 373 K (100 °C) after annealing and immediately transferred to the tensile test facilities where deformation to an equivalent strain of $\varepsilon = 0.25$ (referred to as C2) was applied, while the samples cooled to room temperature. Furthermore, samples in condition C1 were subjected to deep cooling at 233 K (−40 °C) for 24 hours for isothermal transformation to martensite (referred to as C3). All samples in conditions C1–C3 were subjected to low-temperature nitriding at 693 K (420 °C) for 20 hours.

In all cases, annealing, including heating and cooling, was performed in a horizontal tube furnace with a protective argon atmosphere. Cooling was achieved by moving the sample to a cold part of the furnace. Plastic deformation through tensile straining was applied to tensile test specimens with dimensions in accordance with ASTM standards.[40] For all deformed specimens, a strain rate of $6.7 \times 10^{(-3)}$ s^{-1} was applied to a pre-defined equivalent strain level.

Prior to low-temperature nitriding, samples with dimensions 15 × 12.5 mm^2 were ground and polished to a surface finish of 1 μm. The plastic deformation zone induced by the grinding and polishing was removed with electro-polishing in a commercial *Calamo Electrolyte* solution at an applied current density of 25 to 35 A dm^{-2} for 600 seconds.

Low-temperature nitriding or nitrocarburizing was performed in a LAC furnace model PKRC 55/09 retrofitted for gaseous nitrocarburizing. The surface of the material was activated *in situ* by a proprietary procedure. The temperature was monitored for the entire process with a type K (chromel/alumel) thermocouple. The low-temperature surface engineering processes carried out for the different treatments are listed in Table II.

Table I. Chemical Composition of Nanoflex in Wt Pct as Determined and Certified by the Supplier, Sandvik Materials Technology

	C	Si	Mn	Cr	Ni	Mo	Ti	Cu	Al
Nanoflex	0.008	0.26	0.34	11.72	8.8	3.84	0.86	1.88	0.35

Table II. Combinations of Annealing, Deformation, and Low-Temperature Surface Hardening Treatment Applied on Nanoflex (LTN = low-Temperature Nitriding; LTNC = Low-Temperature Nitrocarburizing)

Condition	Type	Initial Condition	Plastic Deformation/Cryogenic Treatment	Thermochemical Treatment	Temperature (K)	Time (h)
A	A1	as received	—	LTN	693 (420 °C)	20
			—	LTNC	693 (420 °C)	80
	A2	as received	plastic deformation (ε = 0.05, 0.10, 0.15)	LTN	693 (420 °C)	20
				LTNC	693 (420 °C)	80
	A3	as received	plastic deformation (ε = 0.15)	LTN	673 (400 °C)	20
B	B1	annealing [1223 K (950 °C), 1800 s]	—	LTN	693 (420 °C)	20
	B2	annealing [1223 K (950 °C), 1800 s]	plastic deformation (ε = 0.25)			
C	C1	annealing [1423 K (1150 °C), 900 s]	—	LTN	693 (420 °C)	20
	C2	annealing [1423 K (1150 °C), 900 s]	plastic deformation (ε = 0.25)			
	C3	annealing [1423 K (1150 °C), 900 s]	cryogenic treatment [233 K (−40 °C), 24 h]			

B. *Microstructure Characterization*

Reflected light microscopy was performed on all samples before and after nitriding. The materials were ground and polished according to standard metallographic techniques and etched with Kalling's Reagent No. 1 for 4 to 10 seconds, depending on the sample condition.

The samples were also subjected to X-ray diffraction analysis with a Bruker D8 AXS X-ray diffractometer equipped with Cr-anode and a Göbel mirror in the incident beam; Bragg-Brentano symmetric geometry was applied. The step size was equal to 0.03 deg 2θ and the counting time was 4 seconds per 2θ step.

The sample bulk and case hardness were determined with microhardness indentation on a Future-Tech FM700 instrument. For the bulk hardness evaluation a load of 2 N was selected; the assessment of the microhardness in the nitrided/nitrocarburized case was carried out by applying a load of 0.05 N.

A composition-depth profile over the nitrided and/or nitrocarburized case was determined with glow discharge optical emission spectroscopy (GD-OES), using a Horiba Jobin Yvon GD profiler 2. The plasma applied for controlled sputtering of the sample surface was 1000 Pa pressure and 40 W. Concentration profiles of substitutionally and interstitially dissolved components were obtained using a selection of stainless steel reference materials and γ'-Fe_4N on pure iron as a reference for nitrogen.

In order to determine the nature of the precipitates formed during annealing at 1223 K (950 °C) for 1800 seconds (referred to as B1), SEM investigation and X-ray diffraction analysis were necessary. SEM investigation was performed on a ground and polished (1 μm) sample using an Inspect S, FEI microscope; an acceleration voltage of 15 keV and a beam spot size of 5 nm were used.

An indication of the elemental composition of the precipitates was revealed with an EDS (Oxford instruments) system attached to the SEM. An acceleration voltage of 15 keV was also utilized for EDS measurements.

X-ray diffraction analysis was performed on precipitate powders extracted by dissolving the metal matrix. Electrochemical dissolution of the matrix was performed in a 5 pct HCl-95 pct ethanol acidic solution. The anode and cathode were, respectively, the sample and a platinum grid surrounding the sample. The dissolution was carried out at a constant potential of 30 V until the complete dissolution on 30 g of Nanoflex in condition B1 was achieved. The powders, collected on a glass plate, were rinsed several times in pure ethanol in order to remove the acidic solution and oxides possibly formed during the process.

For characterization of precipitate powders, the XRD patterns were obtained with a Bruker discover D8 equipped with Cu-anode using Bragg-Brentano geometry. The step size was equal to 0.03 deg 2θ, and the counting time was 20 seconds per 2θ step.

III. RESULTS AND INTERPRETATION

A. *Condition A*

1. *Low-temperature nitriding (LTN) at 693 K (420 °C) for 20 hours*

Due to formation of isothermal martensite during storage, the as-received material had a limited ductility with a maximal equivalent strain of $\varepsilon = 0.15$ by tensile straining. X-ray diffraction phase analysis performed on the as-deformed sample revealed an increase of the fraction of martensite, and a corresponding decrease of the austenite content, with an increase of the equivalent strain (Figure 1).

Evidently, the formation of deformation-induced martensite (Table III) and the increase in dislocation density as consequence of plastic deformation are accompanied with an increase of the microhardness value and a decrease of the variation in microhardness (Figure 2).

The hardness approaches a level of saturation at about 360 HV_{2N} despite a continuous increase in martensite content (*cf.* Table III). Evidently, an increase in martensite content does not contribute to hardness increase for volume fractions above 50 pct of martensite.

Reflected light microscopy investigation of the as-received (A1) and strained conditions (A2) subjected to low-temperature nitriding at 693 K (420 °C) for 20 hours shows how the martensite/retained austenite ratio has a significant influence on the uniformity of the nitrided case (Figure 3).

It is observed that the case that has developed during low-temperature nitriding of the as-received condition A1 Nanoflex steel (Figure 3(a)) is non-uniform in thickness. The dual-phase initial condition leads to the development of both expanded martensite and expanded austenite, as indicated by X-ray diffraction phase analysis (Figure 4). As the degree of plastic deformation and the associated martensite content increase, the nitrided case becomes more uniform and thicker. In particular, the thickness of the case was 11(2) μm for $\varepsilon = 0.05$ deformation, 16(1.5) μm for $\varepsilon = 0.10$ deformation, and 20(3) μm for $\varepsilon = 0.15$ deformation. Along with an increase of the martensite, dark-etched regions appear in the nitrided layer, which indicate the precipitation of CrN along the grain boundaries.[41,42]

The XRD investigation (Figure 4) shows that both expanded austenite and expanded martensite are present. The latter is identified as low-angle shoulders to martensite reflections, while expanded austenite is represented by separate broad peaks at the low-angle side of the austenite peaks.

Evidently, the phase distribution in the nitrided case depends on the phase distribution prior to nitriding. In the as-received samples, peaks of both expanded austenite and expanded martensite are clearly present. With increasing degree of equivalent deformation, expanded austenite vanishes and expanded martensite becomes the only identifiable expanded phase.

No reflections of CrN were observed in the diffractograms. The absence of identifiable CrN peaks, despite minor indications of its presence in reflected light micrographs (Figure 3), is ascribed to the nano-sized diffracting domains and the low volume fraction of CrN as compared to the other phases. Also, the broadened line profiles of martensite in the diffractograms may in some cases (for example the 200 martensite peak) obscure the presence of CrN.

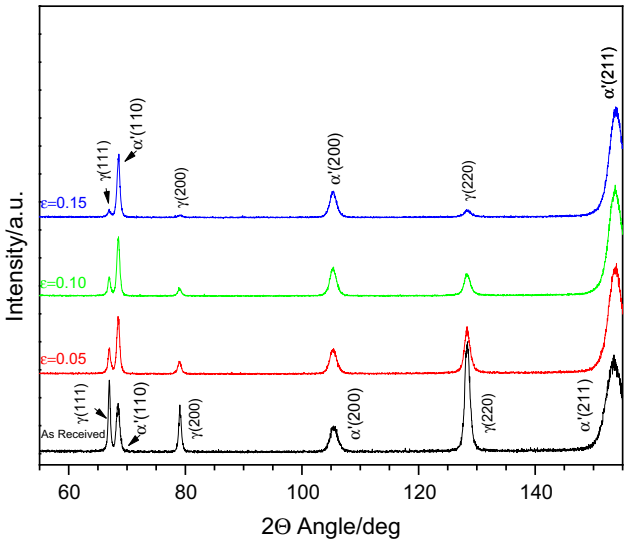

Fig. 1—X-ray diffractograms of the as-received conditions and tensile-strained Nanoflex (samples A1 and A2).

Table III. Volume Fraction of the Martensite Content, Determined with the Rietveld Evaluation Method[55,56] from X-ray Diffractograms

Equivalent Deformation (–)	Martensite Content (Vol Pct)
0.0	40
0.05	56
0.10	66
0.15	79

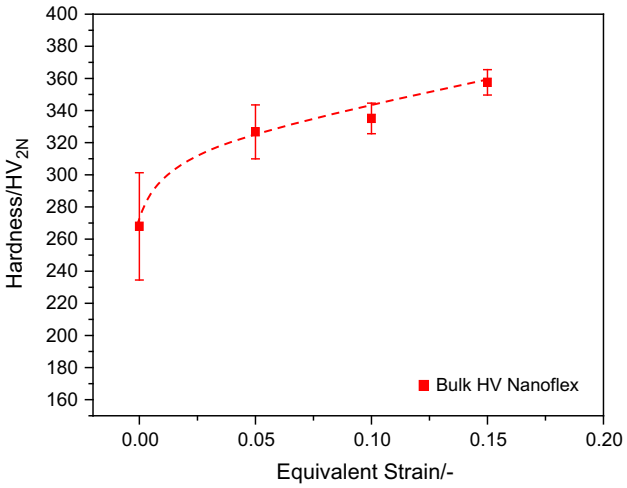

Fig. 2—Hardness *vs* equivalent deformation for Nanoflex.

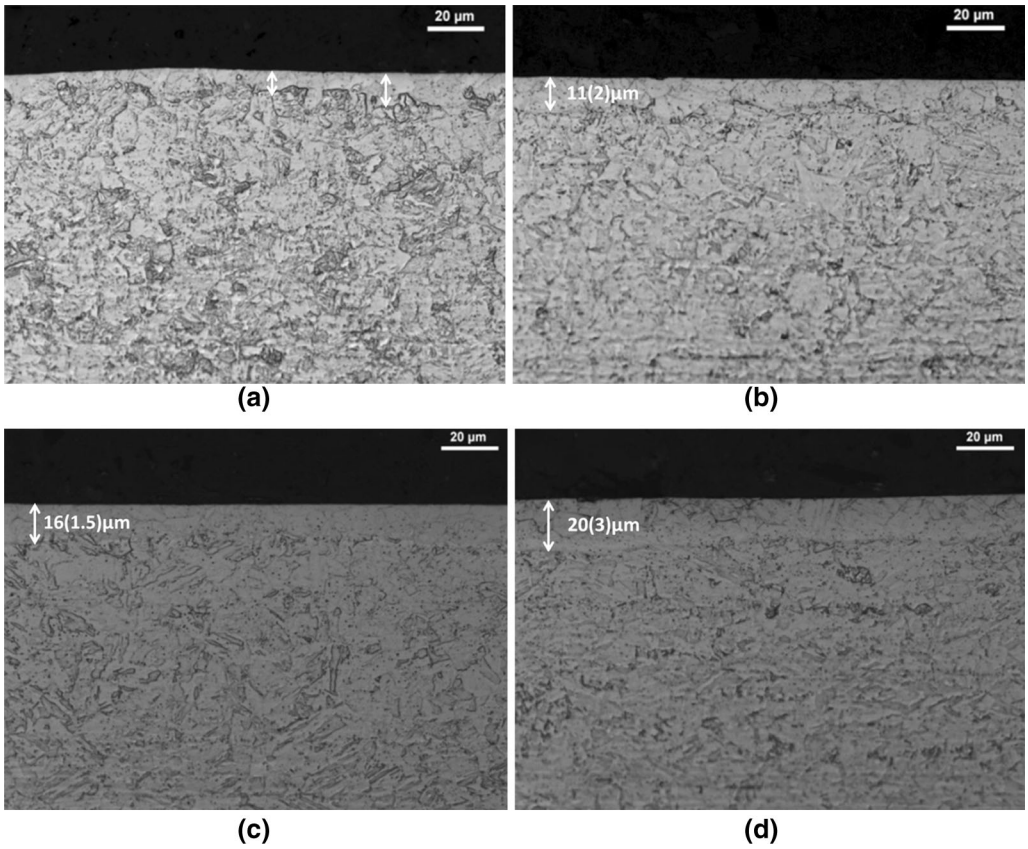

Fig. 3—Nanoflex after tensile deformation and low-temperature nitriding at 693 K (420 °C) for 20 h; (*a*) = As received, (*b*): $\varepsilon = 0.05$, (*c*): $\varepsilon = 0.10$, (*d*): $\varepsilon = 0.15$.

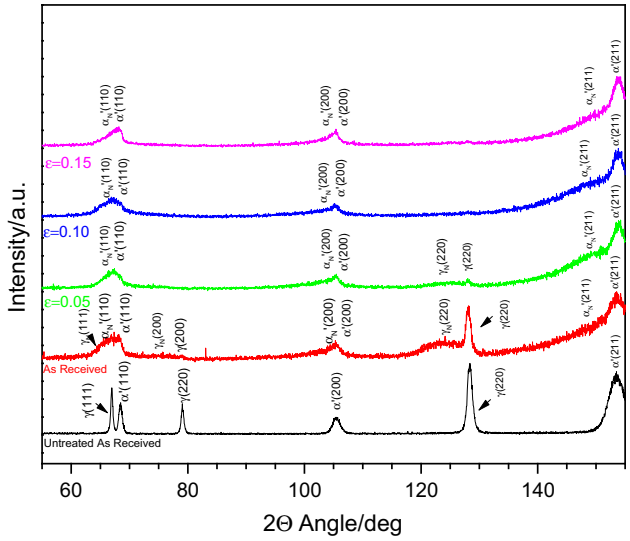

Fig. 4—X-ray diffraction analysis of Sandvik Nanoflex after low-temperature nitriding [693 K (420 °C for 20 h)] of the as-received and tensile-strained conditions. γ and α designate austenite and martensite. γ_N and α'_N are the expanded phases..

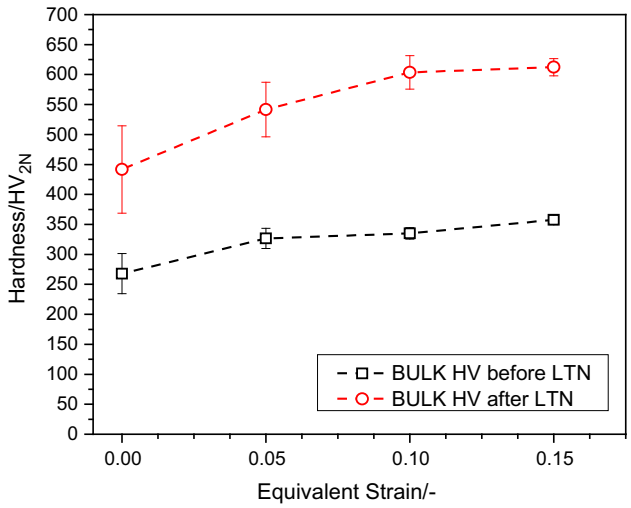

Fig. 5—Bulk hardness of Nanoflex before and after the nitriding treatment at different degrees of plastic deformation.

In the bulk of the treated material, a precipitation hardening effect occurs due to the aging of the martensite.[24,25] Hence, simultaneous surface and bulk hardening is achieved during low-temperature nitriding. As martensite is the precipitation hardenable phase, a more efficient aging effect is observed for a higher martensite content. For higher degrees of plastic deformation, the martensite content is higher and more evenly distributed throughout the sample. Therefore, with increasing equivalent strain, a higher hardness value, a larger increase as compared to the (deformed) as-received state

and a narrower hardness range are found for the bulk hardness (Figure 5).

The hardness profiles over the cases developed during nitriding are given in Figure 6. Consistent with the observation in the micrographs that the depth of the nitrided case increases with equivalent strain and martensite content, the hardness profile over the nitrided case is strongly influenced by the initial phase distribution.

2. *Low-temperature nitriding (LTN) at 673 K (400 °C) for 20 hours*

Encouraged by successful nitriding response of Nanoflex with high martensite contents in Section III–A–1, an additional treatment (A3) was performed on Nanoflex strained at the maximum equivalent strain. The nitriding temperature was reduced to 673 K (400 °C), while nitriding time and ammonia gas flow remained unaltered.

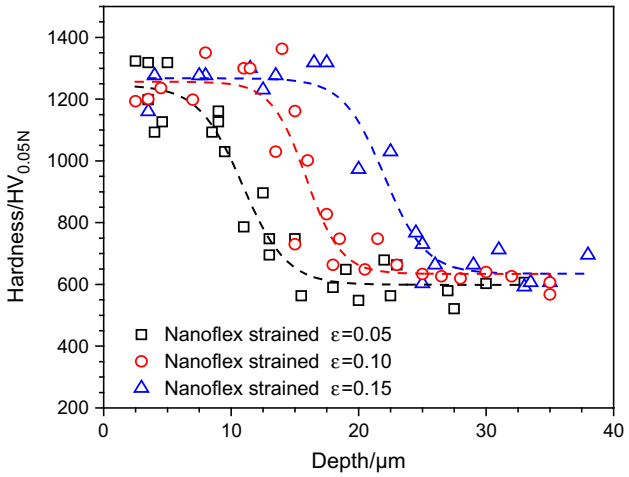

Fig. 6—Hardness-depth profiles of Nanoflex in deformed (ε = 0.05, ε = 0.10 and ε = 0.15) condition and subsequently nitrided at 693 K (420 °C) for 20 h. Hardness-depth profiles were measured with a 0.05 N load.

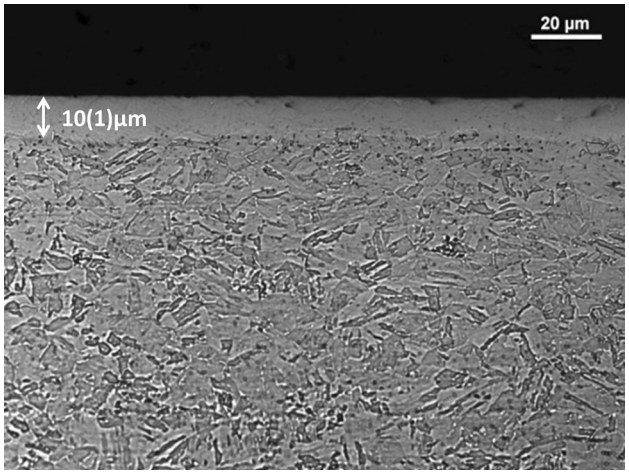

Fig. 7—Nanoflex deformed (ε = 0.15) and nitrided at 673 K (400 °C) for 20 h; Case thickness 10(1) μm.

The micrograph are shown in Figure 7. Despite a significant reduction of the nitriding temperature, a uniform nitrided case developed. No dark-etched regions were found, suggesting a high corrosion potential of the nitrided case due to the absence of CrN precipitates.

Evidently, a reduction of the nitriding temperature from 693 K to 673 K (420 °C to 400 °C) has a strong influence on the thickness and hardness profile of the nitrided case. The nitriding layer produced for this process condition had a thickness of 10(1) μm and a hardness of 1150 $HV_{0.05N}$ (Figure 8) in contrast to 20(3) μm and 1300 $HV_{0.05N}$ for the treatment at 693 K (420 °C). Moreover, a lower bulk hardness of 521(41) HV_{2N} was found, as compared to 612(14) HV_{2N} at 693 K (420 °C). All these effects can be directly ascribed to the temperature reduction, which results in slower diffusion kinetics of nitrogen through the nitrided zone and slower precipitation kinetics of the phases causing bulk hardening [*e.g.*, $Ni_3(Ti,Al)$].[24–28]

3. *Low-temperature nitrocarburizing (LTNC) at 693 K (420 °C) for 80 hours*

Nanoflex in the as-received (A1) and tensile deformed (A2) states were subjected to a low-temperature nitrocarburizing process at 693 K (420 °C) for 80 hours in an ammonia-propene mixture. The reflected light micrographs are depicted in Figure 9.

The uniformity and morphology of the nitrocarburized case are sensitive to the material's phase composition prior to the surface engineering process. The sample in the as-received condition contains a significant amount of retained austenite, leading to a non-uniform case depth during nitrocarburizing. The irregular unetched regions in Figure 9(a) are identified as expanded austenite formed from dissolving nitrogen and carbon into retained austenite. With increasing equivalent strain the martensite content increases, the nitrocarburized case becomes thicker [65(5) μm] and uniform. No significant difference can be discerned

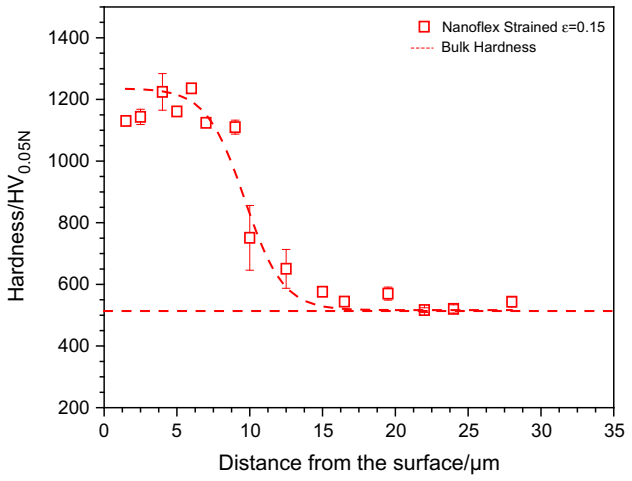

Fig. 8—Hardness profile of Nanoflex tensile deformed (ε = 0.15) and nitrided at 673 K (400 °C) for 20 h.

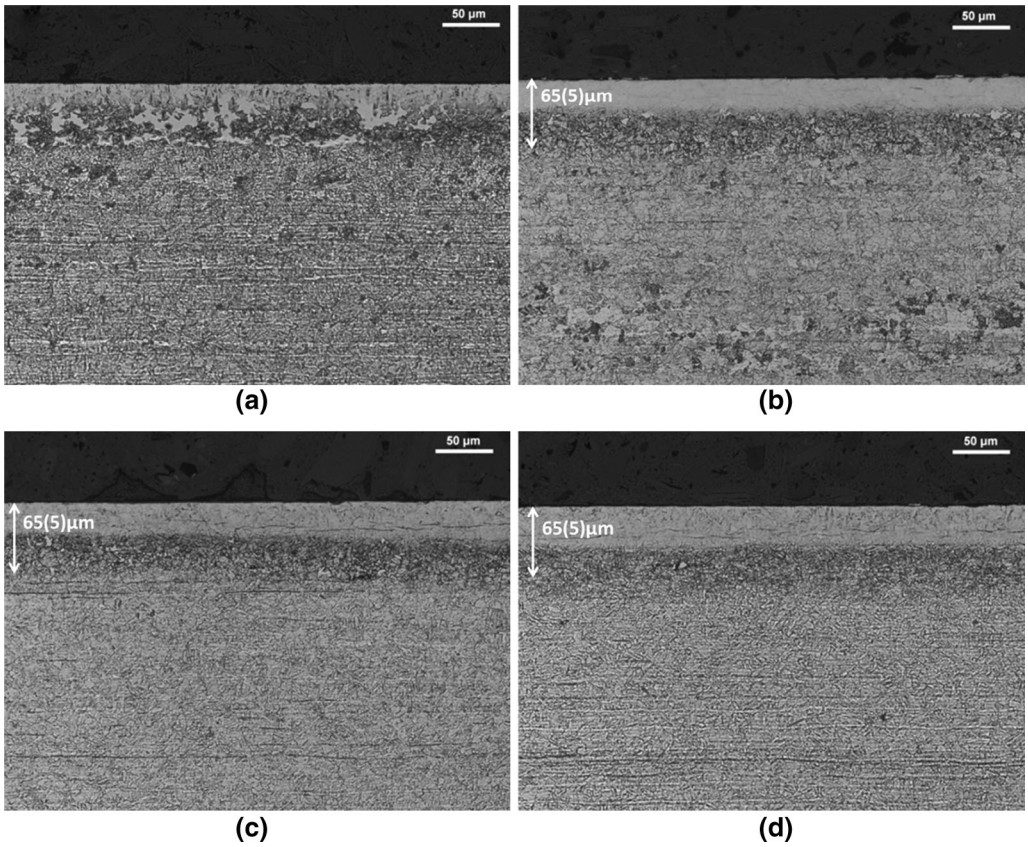

Fig. 9—Nanoflex plastically deformed and nitrocarburized at 693 K (420 °C), 80 h; (*a*) = Annealed, (*b*): $\varepsilon = 0.05$, (*c*): $\varepsilon = 0.10$, (*d*): $\varepsilon = 0.15$; case depth measured for the strained samples (b), (c) and (d) is 65(5) μm.

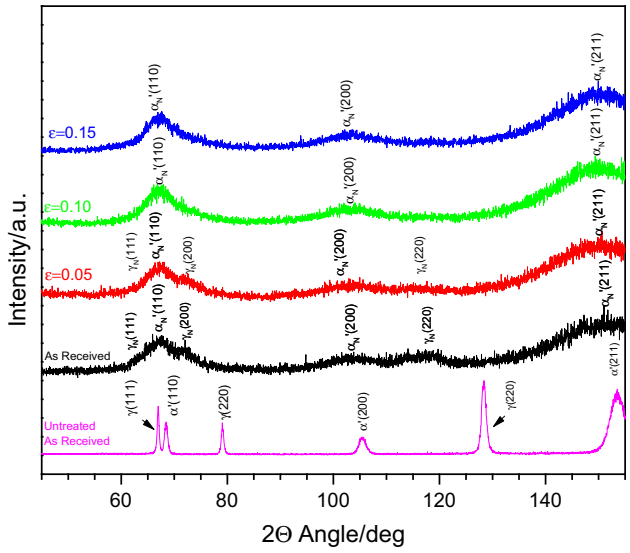

Fig. 10—X-ray diffractograms of Sandvik Nanoflex after nitrocarburizing [693 K (420 °C), 80 h] of the as-received and tensile-deformed conditions strained to the equivalent strains indicated.

between the samples deformed at the three different strain levels.

X-ray diffraction phase analysis shows a dependence of the phase present in the nitrocarburized case on the phase distribution prior to thermochemical treatment (Figure 10).

For the annealed sample, wherein a significant amount of retained austenite is present, nitrocarburizing leads to both expanded austenite and expanded martensite in the outermost region, in accordance with a mixed microstructure in Figure 9(a). For the strained samples, the dominant phase identified is expanded martensite in accordance with a continuous light gray zone in Figures 9(b) through (d). Considering the thickness of the case developed (Figures 9(b) through (d)), the X-ray diffractograms of the strained samples originate from the light gray zone because the dark-etched region lies too deep to be probed by the applied X-radiation.

GD-OES profiles revealed that nitrogen (Figure 11(a)) is predominantly present in the surface-adjacent light gray part of the case, while carbon (Figure 11(b)) is present underneath and bridges the transition to the unaffected core.

The concentration profiles for nitrogen and carbon show a higher interstitial content for the as-received state as compared to the deformed samples. This is ascribed to the higher interstitial solubility in austenite than in martensite and the presence of retained austenite in the as-received and nitrided condition (Figure 11). The case depths for in particular the nitrogen enrichment are largest for the deformed states because the diffusion rate of interstitials is faster in martensite than in austenite.[43,44] See in this respect also Reference 49.

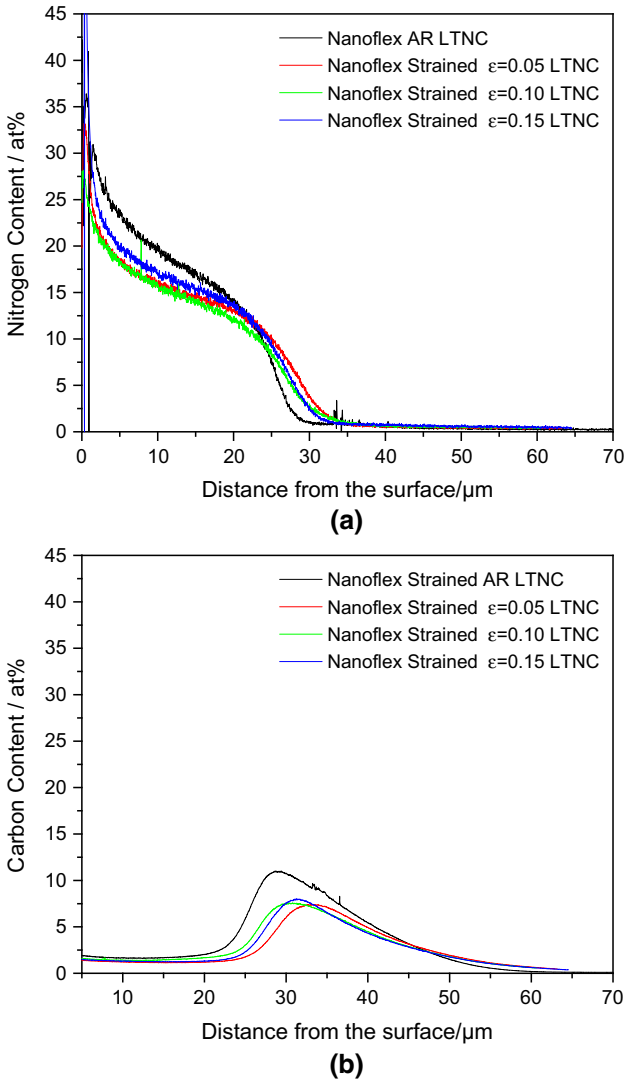

Fig. 11—GD-OES Nitrogen (*a*) and Carbon (*b*) concentration profile for Nanoflex nitrocarburized at 693 K (420 °C), 80 h.

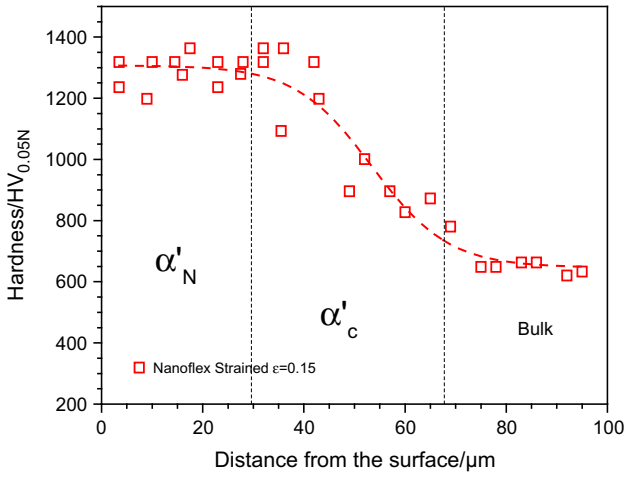

Fig. 12—Hardness profile of Nanoflex tensile deformed (ε = 0.15) and nitrocarburized at 693 K (420 °C), 80 h.

The nitrogen-expanded region has a higher hardness compared to the carbon expanded region (Figure 12). As confirmed from the hardness and GD-OES profiles, the carbon expanded region bridges the hardness decrease from the high hardness value in the nitrogen-expanded part of the case to the softer core: the hardness decreases gradually from 1300 to 600 HV over 30 μm, as compared to the sharp case-core transition obtained on nitriding, where this occurs in a few microns (Figure 6). Note that the case depth achieved after 80 hours of treatment is about 65 μm and the hardness in the bulk is equal to that obtained after 20 hours of nitriding at the same temperature (*cf.* Figure 6), indicating that no significant additional precipitation hardening has occurred.

B. *Treatment B*

1. *Pre-treatment: annealing at 1223 K (950 °C)*

This experimental condition was applied to obtain a more stable austenite phase from the as-received material by annealing at 1223 K (950 °C) for 1800 seconds in argon atmosphere in a horizontal tube furnace (B1).

The stabilizing effect is mainly due to precipitates that are present after the annealing heat treatment. In this respect, ThermoCalc, applying the steel database TCFE version 7.0, predicts driving forces for the formation of Laves phase (Fe_2Mo) and, in particular, chi-phase ($Fe_{36}Cr_{12}Mo_{10}$) at temperatures below 1223 K (950 °C); *cf.* Figure 13. The stability range of these intermetallic compounds is close to the applied annealing temperature of 1223 K (950 °C); incomplete dissolution of these compounds is expected for this treatment. At 1423 K (1150 °C), full dissolution of intermetallic compounds will occur relatively fast, hence resulting in a fully austenitic structure.

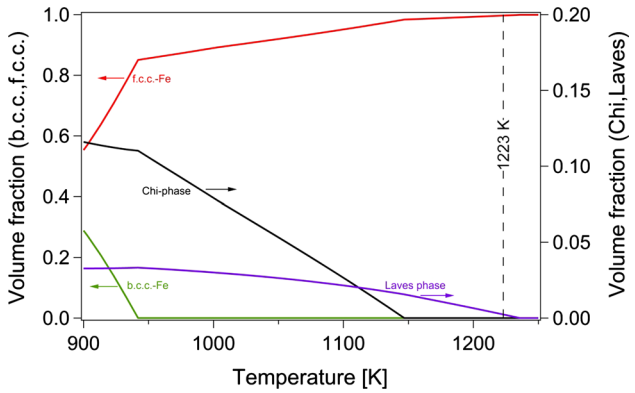

Fig. 13—Equilibrium phase composition of Nanoflex shows that Laves phase and chi-phase are stable phases for relatively high temperatures and develop in the austenite matrix. At the annealing temperature 1223 K (950 °C), a small fraction of Laves phase can develop. The diagram shows that a driving force exists for the development of abundant chi-phase and Laves phase upon heating and during cooling after annealing. Calculations were performed with ThermoCalc using the steel database TCFE *vs* 7.0.

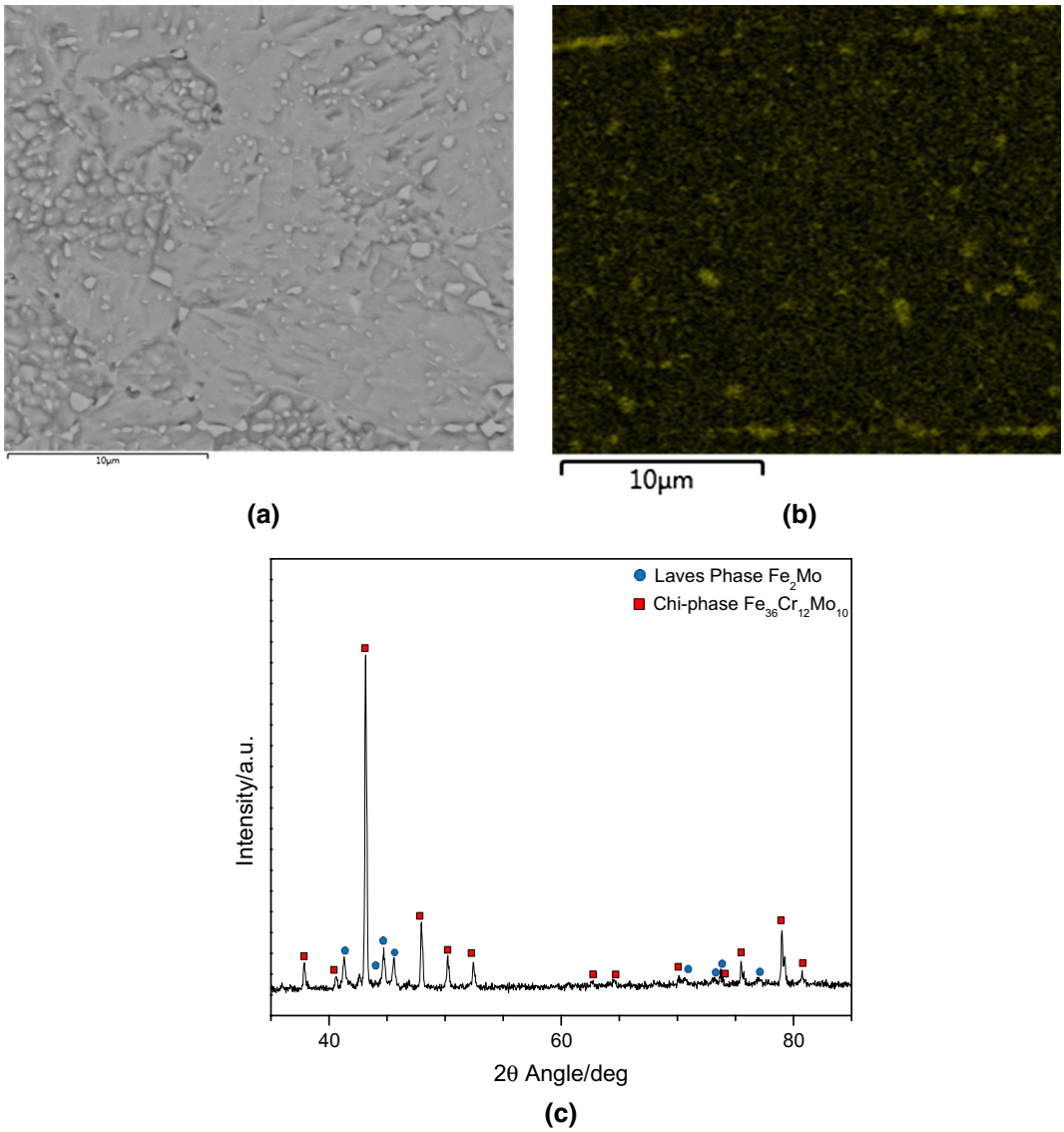

Fig. 14—(*a*) Back-scattered electron micrograph of Nanoflex's microstructure after annealing at 1223 K (950 °C), 1800 s. (*b*): EDS map of Mo L_α radiation showing the presence of Mo enriched areas in the microstructure. (*c*) Phase composition of residue after dissolution of the metallic matrix shows Laves phase and in particular chi-phase.

A back-scattered electron micrograph (Figure 14(a)) and a corresponding map of the distribution of characteristic Mo L_α radiation (Figure 14(b)) show that indeed precipitation has occurred and that the precipitates are enriched in Mo as compared to the surrounding matrix. Dissolution of the metallic matrix and X-ray diffraction phase analysis of the residue shows convincingly that Laves phase and in particular chi-phase were present in the alloy after annealing.

The resulting steel hardness after annealing is 205(5) HV_{2N}. The austenite stability was verified with an attempt to develop isothermal martensite by subjecting a sample to a treatment at 233 K (−40 °C) for 24 hours, as applied commercially to isothermally transform austenite into martensite in Nanoflex. Indeed, no isothermal martensite was formed during the treatment, thereby confirming that the precipitation of Laves and chi-phase, containing ferrite-forming elements, had enhanced the stability of austenite.

2. *Pre-treatment: plastic deformation*

The annealed material was tensile strained to an equivalent deformation level of $\varepsilon = 0.25$ (B2). Reflected light microscopy did not reveal clear changes in the microstructure after straining, but the hardness had increased to 364(7) HV_{2N}.

X-ray diffraction investigation in Bragg-Brentano geometry (Figure 15) shows the deformation had converted most of the austenite into strain-induced martensite; Rietveld refinement[42,43] yielded about 83 pct martensite. Note that the peaks of Laves and chi-phase are very small (*cf.* Figure 14(c)) because of the abundance of the surrounding matrix.

3. *Low-temperature nitriding at 693 K (420 °C) for 20 hours*

Nanoflex in the different conditions (B1, B2) was low-temperature nitrided at 693 K (420 °C) for 20 hours.

For the Nanoflex in the annealed conditions B1 and B2, reflected light microscopy (Figure 16) reveals a uniform nitrided case at the surface. The thickness and the hardness of the nitrided case of B1 are 6(1) μm and 1150 $HV_{0.05N}$, respectively. Compared to the sample in Figure 3(a), this is a relatively shallow case depth. A much deeper case of 25(3) μm and a higher hardness of 1400 $HV_{0.05N}$ are observed for nitrided B2 (Figure 16(b)).

X-ray diffractograms of nitrided B1 and B2 (Figure 17) reveal the presence of expanded austenite peaks with a broad high-angle tail for 111 and 200 in B1 (Figure 17(a)), while nitrided B2 consists of expanded martensite in the analyzed depth range with XRD (Figure 17(b)). The 220 peak for expanded austenite in Figure 17(a) appears to be subdivided in two peaks. No indications of CrN formation are observed in the nitrided B1 and B2 samples. As follows from the XRD investigation, the material transforms almost completely into strain-induced martensite after the plastic straining (*cf*. Figure 15). Low-intensity peaks of retained austenite are still visible. The martensitic microstructure has a completely different response to nitriding compared to the austenitic microstructure.

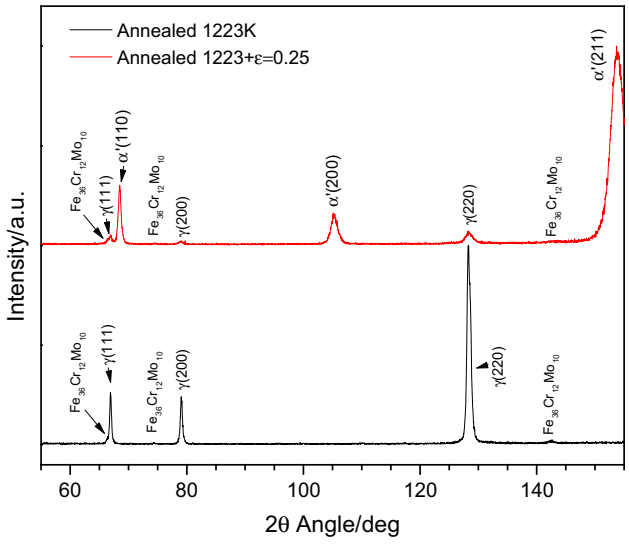

Fig. 15—X-ray diffractograms of annealed [1223 K (950 °C), 1800 s] and subsequently plastically deformed Nanoflex.

For B1, the bulk hardness increased from 203 to 239HV_{2N}. In contrast with the as-received and strained conditions, no pronounced bulk hardening is observed along with surface hardening because the alloy is and remains (mostly) austenitic (Figure 18(b)).

GD-OES profiles measured for the samples B1 and B2 (Figure 18(a)) revealed a significant difference in the nitrogen-depth profiles. Surprisingly, sample B2, which is martensitic, shows a higher nitrogen content compared to the austenitic B1 sample. The higher nitrogen content and the deeper penetration are consistent with the case depths derived from reflected light microscopy (Figure 16). Diffusion of N in martensite proceeds faster than in austenite.[43,44]

Hardness profiles for B1 and B2 samples are compared in Figure 18(b). Sample B1 reaches a maximum hardness of 1150 $HV_{0.05N}$, while sample B2 reaches 1400 $HV_{0.05N}$. The maximum hardness in the martensitic B2 is higher than the hardness achieved in other martensitic samples. This may be a consequence of the high nitrogen content in B2 (Figure 18(a)).

Finally, bulk hardening in martensite of sample B2, simultaneously with surface hardening, leads to a hardness of 652(13) HV_{2N} after nitriding. This hardness is significantly higher than the maximum hardness achieved in the bulk after nitriding of the strained as-received material, which is about 600 HV_{2N}. Undoubtedly, the development of Laves and chi-phase has an influence on the precipitation sequence during bulk hardening, because the Mo depletion of matrix associated with Laves and chi-phase formation implies that no Ni_3Mo and (fine) Fe_2Mo can be expected to precipitate in the bulk during nitriding.

C. *Condition C*

Condition C was included to investigate the response of unstable austenite that has a tendency to transform to

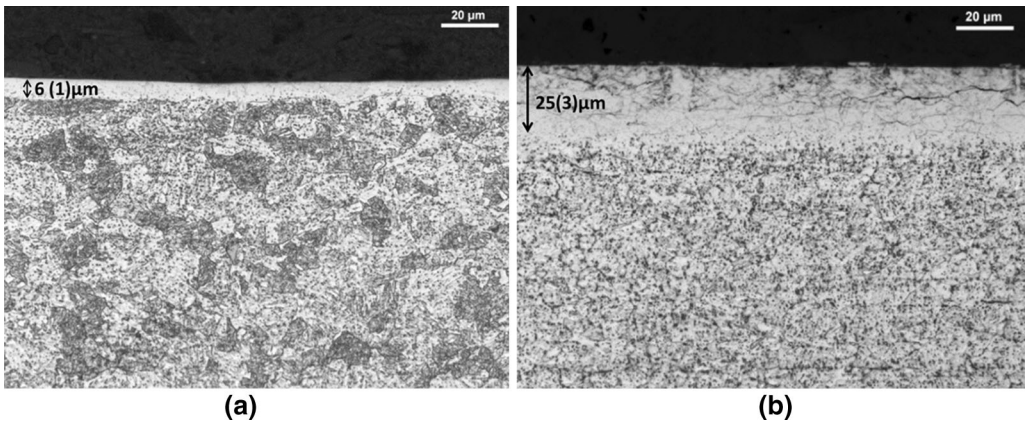

Fig. 16—Optical micrographs of (*a*) Nanoflex annealed (B1), and nitrided [693 K (420 °C) for 20 h]; Case depth 6(1) μm and (*b*) Nanoflex annealed [1223 K (950 °C), 1800 s], deformed (ε = 0.25) and nitrided [693 K (420 °C), 20 h] (B2); Case Depth 25(3) μm.

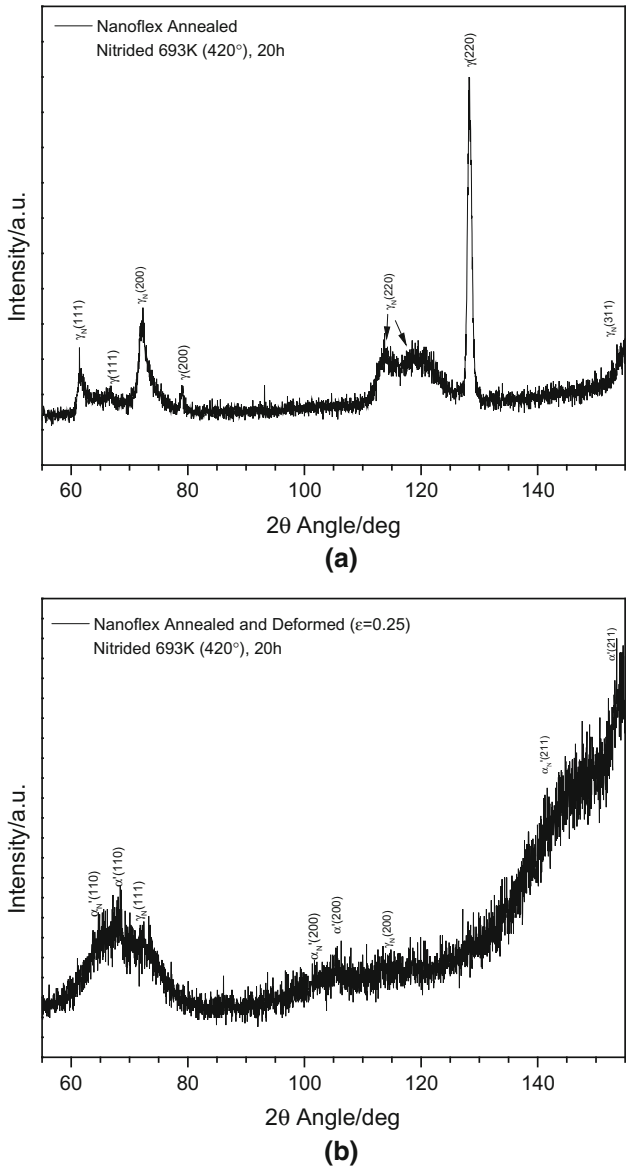

Fig. 17—X-ray diffractograms of (*a*) sample B1 nitrided and (*b*) sample B2, both nitrided at 693 K (420 °C) for 20 h. Nitrided sample B1 shows mainly expanded austenite, while nitrided sample B2 shows predominantly expanded martensite.

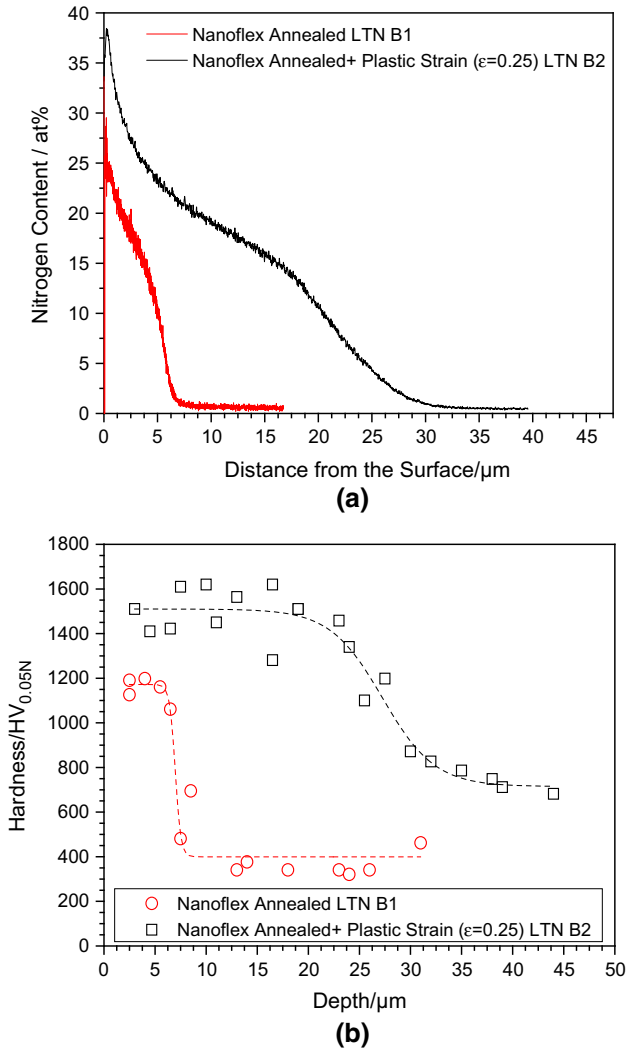

Fig. 18—GD-OES (*a*) and hardness profiles (*b*) after nitriding sample B1 and B2 at 693 K (420 °C) for 20 h.

isothermal martensite at room temperature. Annealing was carried out at 1423 K (1150 °C) for 900 seconds. The microstructure of the material after this treatment (and cross section sample preparation) is given in Figure 19.

Significant grain coarsening is observed as a result of annealing at a high temperature. A large amount of lath martensite has developed as a consequence of isothermal transformation and mechanical grinding/polishing during sample preparation for metallographic analysis (Figure 19).

Sample C1 was selected as the starting condition for two other processes (C2 and C3): tensile straining (ε_{eq} = 0.25) (C2) and a cold treatment [233 K (−40 °C) for 24 hours] (C3). Both these treatments were

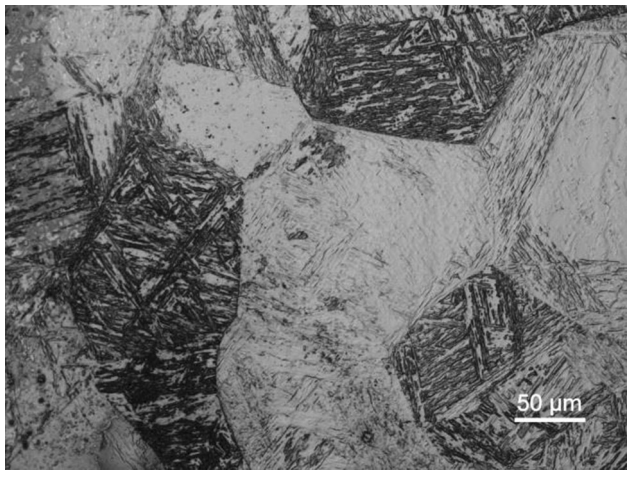

Fig. 19—Microstructure of Nanoflex after annealing at 1423 K (1150 °C), 900 s (C1). Sample preparation at room temperature has led to the formation of lath martensite.

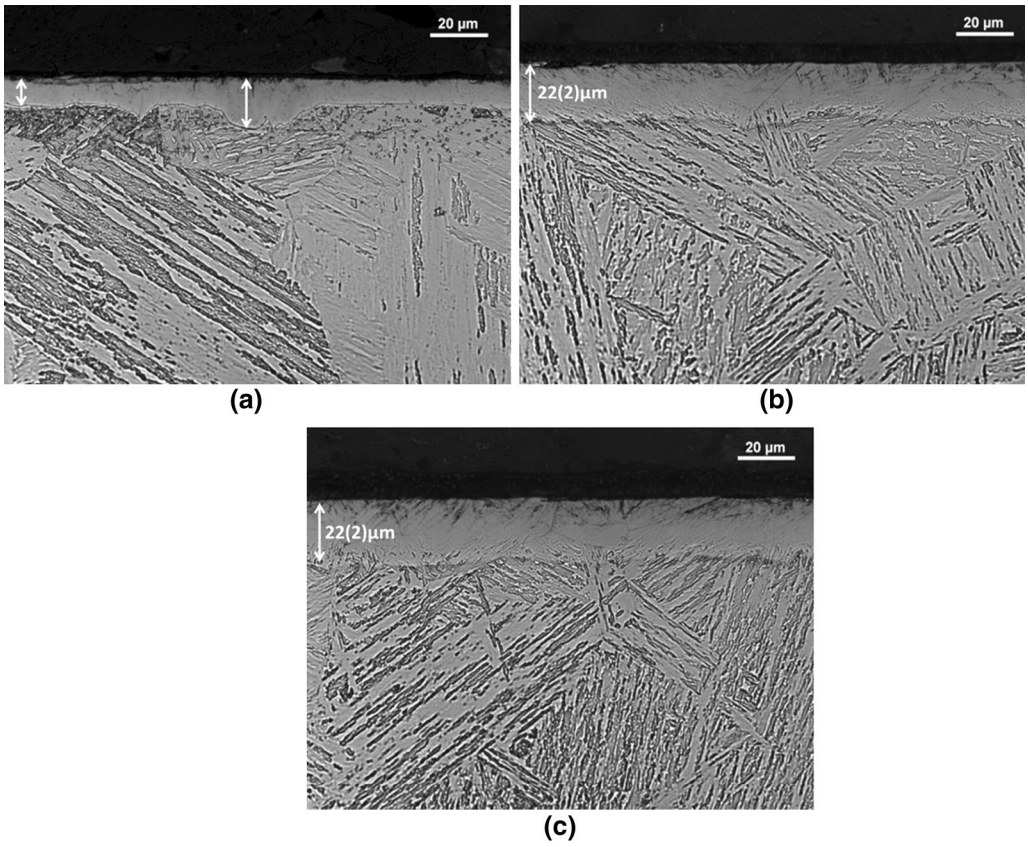

Fig. 20—Reflected light micrographs of (*a*) sample C1, (*b*) sample C2, and (*c*) sample C3 all nitrided at [693 K (420 °C) for 20 h]. The case depths for samples C2 and C3 are identical, *i.e.*, 22(2) μm, while for sample C1 an irregular case depth was obtained.

performed immediately after annealing, to prevent isothermal transformation at room temperature**.

**The amount of isothermal martensite that develops in 1 hour is about 20 pct, while 10 hours is needed to reach 50 pct isothermal transformation.

Samples in conditions C1, C2, and C3 were subjected to low-temperature nitriding at 693 K (420 °C) for 20 hours. It is important to mention that the polishing and electro-polishing operations for sample C1 were carried out before the annealing in order to limit the holding time at room temperature before the low-temperature nitriding process.

The nitriding of annealed sample C1 led to the formation of a non-uniform nitrided case (Figure 20(a)). The case produced has an average thickness of 12(4) μm but shows irregularities, which suggests that the matrix contained both austenite and martensite during nitriding and that partial martensite formation did occur, even though the sample was kept at room temperature for a limited amount of time before being transferred to the furnace for the nitriding process. In this respect, it is noted that the martensitic microstructure visible in Figure 20(a) is likely to have formed after nitriding, either by (continued) isothermal transformation or as a consequence of the deformation introduced on grinding/polishing to reveal the microstructure.

The nitriding response of samples C2 (Figure 20(b)) and C3 (Figure 20(c)) differ significantly from sample C1, because samples C2 and C3 were treated such as to convert austenite into martensite by strain-induced transformation (C2) or by isothermal transformation by deep cooling. The case depths achieved with nitriding of samples C2 and C3 are identical and amount to [22(2) μm]. In the outermost regions of the nitrided cases of samples C2 and C3, dark-etched regions may hint to the local presence of CrN.

X-ray diffraction investigation of Nanoflex in the conditions C1–C3 confirmed the difference in the phase composition of the case in relation to the treatment prior to nitriding (Figure 21). In condition C1, expanded austenite and expanded martensite peaks coexist, while low-temperature nitriding of samples C2 and C3 led to the formation of expanded martensite only, due to the presence of a fully martensitic matrix prior to nitriding. No XRD evidence for the development of CrN was found.

Hardness-depth profiles in Figure 21 show a difference between C1 and C2/C3 that is consistent with the above microscopical and XRD analyses. A more gradual case-core transition is found for sample C1, while a sharper transition is observed for sample C2 and C3. This trend reflects perfectly what is also observed in the micrographs (Figure 20). The coexistence of unstable austenite and isothermal martensite in condition C1 leads to the formation of a non-uniform case, while the

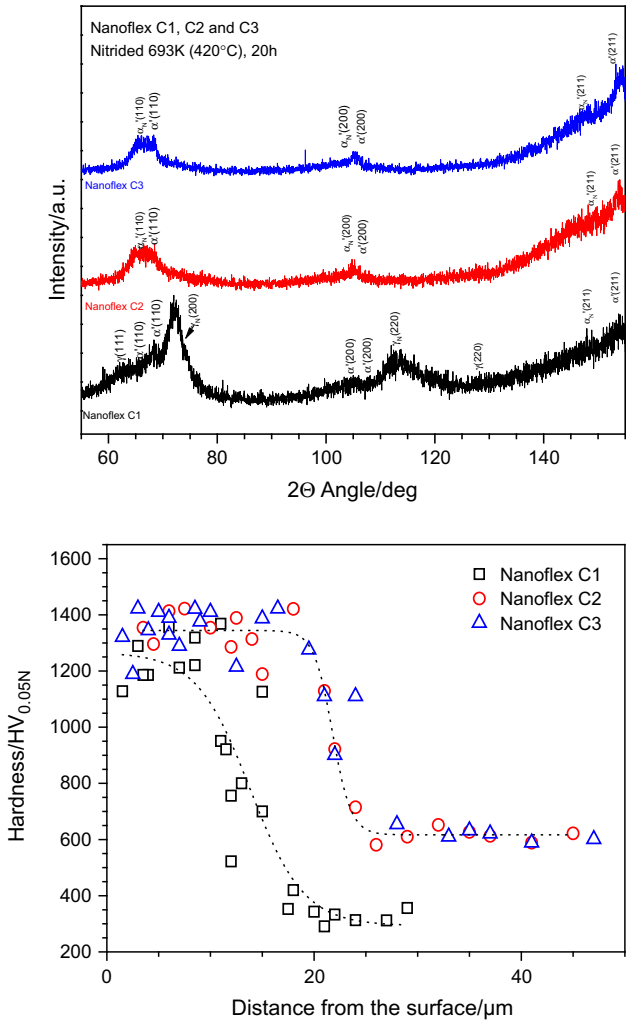

Fig. 21—X-ray diffractogram of Nanoflex annealed [1223 K (950 °C), 1800 s], deformed ($\varepsilon = 0.25$) and nitrided. Hardness-depth profiles of Nanoflex C1, C2, and C3 nitrided at 693 K (420 °C) for 20 h. Hardness-depth profiles were measured with a 0.05 N load.

presence of a fully martensitic matrix (C2–C3) prior to nitriding leads to a deeper case and a sharp case-core transition.

The highest hardness was found for the case of C2/C3, *i.e.*, 1400 $HV_{0.05N}$, albeit only slightly higher than for sample C1.

A major discrepancy is observed between the bulk hardness values for sample C1 as compared to samples C2/C3. For sample C1 the bulk hardness after nitriding was 300(30) HV_{2N}; for samples C2 and C3 hardness values of 595(12) HV_{2N} and 610(11) HV_{2N} were found, respectively. The observed increase in bulk hardness for sample C1, with respect to that of unstrained austenite (Figure 2), is modest and very small as compared to hardness increases in samples C2/C3. Again this indicates that a minor fraction of martensite was present in sample C1 on nitriding.

IV. DISCUSSION

Potentially, simultaneous surface and bulk hardening of precipitation hardening stainless steels available under the tradename Nanoflex is an attractive possibility to tailor materials performance. The present work shows that the outcome of a combined surface and bulk hardening treatment depends strongly on the initial state of the alloy. Surface and bulk hardening abilities will be discussed separately below.

A. *Low-Temperature Surface Hardening of Nanoflex*

In Table IV, a summary of the case thicknesses for all the different experimental condition is given. Starting from a fully austenitic substrate, nitrogen-expanded *austenite* is obtained in the surface region by the ingress of nitrogen during low-temperature nitriding, while nitrogen-expanded *martensite* is formed if the initial state is entirely martensitic. Since the diffusion coefficient of N in austenite is significantly lower than in

Table IV. Thickness of the Case Developed for All the Different Experimental Condition During the Surface Engineering Process (LTN = low-Temperature Nitriding; LTNC = Low-Temperature Nitrocarburizing)

Condition	Initial Condition	Treatment	Layer Thickness
A1	as received	LTN-693 K (420 °C), 20 h	N/A non-uniform
A2	as received + tensile straining	LTN-693 K (420 °C), 20 h	11(2) ($\varepsilon = 0.05$) 16(1.5) ($\varepsilon = 0.10$) 20(3) ($\varepsilon = 0.15$)
A3	as received + tensile straining	LTN-673 K (400 °C), 20 h	10(1) ($\varepsilon = 0.15$)
A1	as received	LTNC-693 K (420 °C), 20 h	N/A non-uniform
A2	as received + tensile straining	LTNC-693 K (420 °C), 20 h	65 (5) ($\varepsilon = 0.05$) 65(5) ($\varepsilon = 0.10$) 65(5) ($\varepsilon = 0.15$)
B1	as received + annealing 1223 K (950 °C), 1800 s	LTN-693 K (420 °C), 20 h	6(1)
B2	as received + annealing 1223 K (950 °C), 1800 s + tensile straining ($\varepsilon = 0.25$)	LTN-693 K (420 °C), 20 h	25(3)
C1	as received + annealing 1423 K (1150 °C), 900 s	LTN-693 K (420 °C), 20 h	12(4)
C2	as received + annealing 1223 K (950 °C), 1800 s + tensile straining ($\varepsilon = 0.25$)	LTN-693 K (420 °C), 20 h	22(2)
C3	as received + annealing 1223 K (950 °C), 1800 s + tensile straining ($\varepsilon = 0.25$) + cold treatment [233 K (−40 °C), 24 h]	LTN-693 K (420 °C), 20 h	22(2)

martensite, and generally, the maximum solubility of nitrogen in austenite is higher than in martensite, implying that a smaller fraction of the inward flux of nitrogen atoms is used for stabilizing martensite than for stabilizing austenite, a thinner nitrided case develops on austenite than on martensite.[45]

In the outermost regions of the expanded martensite case, dark-etched areas were observed, which hint at the development of CrN precipitates at these low process temperatures, while similar indications of CrN formation were not observed in expanded austenite. Usually, CrN is the result of the decomposition of expanded austenite and is promoted by a higher nitrogen content and longer treatment time. The early development of CrN in expanded martensite is explained from the energetically favorable Baker-Nutting orientation relationship between the (expanded) b.c.c. (b.c.t.) lattice and NaCl-type CrN, which lowers the nucleation barrier (see Reference 46 and references therein). These results are consistent with recent observations that the presence of deformation-induced martensite in nitrided AISI 304 promotes CrN formation, while no such CrN formation occurs in expanded austenite.[45] The formation of CrN is expected to lead to locally impaired corrosion resistance as a consequence of Cr-depletion from solid solution.

Previously, it has been reported that the dissolution of nitrogen in martensitic AISI 630 (17.4 PH) leads to a transition of expanded martensite to expanded austenite (and eventually epsilon nitride).[47] A similar transition to expanded austenite was not observed in the present series of experiments, despite a large similarity of the nitriding conditions in Reference 47 and the present work. The observed difference in nitriding performance could be a consequence of two main aspects. The nitriding experiments described in this paper are carried out in an industrial furnace, where a certain, unknown degree of dissociation takes place at the furnace walls, which effectively reduces the nitrogen activity in the gas phase as experienced by the sample. On the other hand, the experiments in References 7 and 47 were performed in a thermobalance, where ammonia dissociation is largely prevented. A higher nitrogen activity in thermobalance experiments promotes the formation of austenite and epsilon phase. Furthermore, the appreciably higher content of ferrite stabilizing elements is present in Nanoflex than in AISI 630, leading to a significant increase of the Cr equivalent from about 12 for AISI 630 to about 21 for Nanoflex. The Ni equivalent in Nanoflex (about 10) is also higher than in AISI 630 (about 7), but not as significant as the Cr equivalent. The Schaeffler diagram would predict that Nanoflex should contain a small amount of ferrite (not martensite) in austenite after cooling to room temperature, while AISI 630 should be fully martensitic. Apparently, the isothermal or strain-induced transformation of austenite into martensite in Nanoflex does not allow the reverse transition into austenite upon nitrogen dissolution.

Comparison of the morphology, thickness, and hardness of the case formed on isothermal martensite and strain-induced martensite showed that identical nitriding performance is achieved, irrespective of the formation mechanism of martensite. This is particularly clear from comparing the nitriding response of samples C2 and C3.

A peculiar observation is the subdivision of, in particular, the 220 expanded austenite peak for nitrided Nanoflex after annealing (Figure 17). A tentative explanation is given here. Upon annealing chi-phase and Laves phase precipitate. The precipitates remove ferrite-forming elements Cr and Mo from solid solution. As the formation of expanded austenite relies on short range ordering of Cr and N atoms (and possibly also on Mo and N atoms), the maximum nitrogen content in the Cr (and/or Mo) depleted regions is reduced as compared to regions where no depletion has occurred.[4,48] Accordingly, the splitting of the 220 γ_N peak could be explained from the presence of regions with low and high Cr (and Mo) contents.

Eventually, when both austenite and martensite are present prior to nitriding, two expanded phases develop. As a consequence of different nitrogen diffusivities in these phases, the case can be inhomogeneous in phase composition and non-uniform in thickness, as most clearly observed in Figure 3(a). The actual variation in thickness is anticipated to depend on the average thickness of the nitrided zone as compared to the size of austenite and martensite regions. When the size of austenite and martensite regions becomes much smaller than the average thickness of the nitrided zone, an effectively uniform case depth can result.

Nitrocarburizing leads to the development of a nitrogen-enriched zone close to the surface and a carbon-enriched zone underneath, as has previously been observed for other austenitic and martensitic stainless steels.[4,49–52] Consequently, the hardness decrease from 1300 $HV_{0.05N}$ in the nitrogen-rich zone to 600 HV_{2N} in the hardened substrate is bridged by the carbon containing region, such that a gradual hardness decrease results, while for nitriding this transition is abrupt. Such a gradual hardness distribution can be considered advantageous for the adherence of the case and for improved fatigue performance, as it would be associated with a gradual transition in residual stress.

B. *Bulk Hardening of Nanoflex*

The precipitation hardening process taking place simultaneously with the surface hardening depends strongly on phases present in the material prior to low-temperature surface hardening. In Nanoflex, precipitation hardening only occurs in martensite.[24–26] Consequently, hardness increase by precipitation is only achieved in martensite regions of the sample; the hardness of austenite in the bulk remains unaffected. The higher the martensite content, the higher is the average hardness (increase) achieved in the matrix (Figure 5). Moreover, an increase of the martensite content leads to less variation in the measured hardness values in the matrix before and after nitriding (Figure 5).

No significant hardness difference was observed between isothermal and strain-induced martensite

(samples C2 and C3). Also, the hardness values obtained in the bulk of C2/C3, *i.e.*, about 600 HV_{2N}, are identical to those of the as-received and tensile strained material (sample A2 $\varepsilon = 0.15$; *cf.* Figure 5). On the other hand, sample B2, containing chi-phase and Laves phase in addition to strain-induced martensite, has a bulk hardness after nitriding that is significantly higher than for C2/C3 and A2 ($\varepsilon = 0.15$). The reason for this difference was not investigated further. It is suggested that the presence of chi-phase, Laves phase and, in particular, the associated Mo depletion of the matrix affects the precipitation sequence in the bulk. Obviously, if most Mo is removed from solid solution by chi-phase formation, hardening can no longer be based on the precipitation of Fe_2Mo and Ni_3Mo. [25,26,53,54]

An interaction of dissolving nitrogen with the strong nitride formers Al and Ti might be anticipated to lead to fast precipitation of AlN and TiN, particularly in the martensitic (b.c.c.) matrix, prior to the formation of expanded phases (*cf.* Reference 50). This was not further investigated in the present work. It is argued that such precipitation is limited to the surface region (and perhaps responsible for darker etching in this regions as observed in samples B2 and C2/C3) and obscured in XRD analyses by expanded phases, while concurrently, $Ni_3(Ti,Al)$ develops in the bulk before nitrogen arrives. A further analysis of these details is considered beyond the scope of the present work.

V. CONCLUSIONS

In this study, bulk and surface hardening processes were successfully combined and the experimental results show how it is possible to tailor the surface and bulk properties by controlling the material's initial microstructure and the surface hardening process parameters.

Prior to nitriding, the as-received material was subjected to different annealing and deformation treatment in order to modify the phase distribution in the material. All the materials were successfully nitrided, but the initial microstructure and phase distribution have a major impact on the morphology, composition, and properties of the case developing during nitriding/nitrocarburizing. Upon low-temperature nitriding and nitrocarburizing, the coexistence of martensite and austenite leads to the formation of an inhomogeneous case of non-uniform thickness due to a large difference in interstitial diffusivity and a difference in solubility of interstitials in austenite and martensite.

For the chosen experimental conditions, the presence of an initially fully austenitic structure leads to the formation of an expanded austenite case of uniform thickness, while the presence of a fully martensitic structure leads to the formation of expanded martensite of uniform thickness. The faster diffusion flux of nitrogen and the lower nitrogen solubility limit in martensite as compared to austenite, leading to the formation of a thicker case on martensite. However, no major difference in the layer morphology and hardness was found between isothermal and strain-induced martensite.

Indications of (unwanted) CrN formation were observed in the outermost region of the expanded austenite, evidenced by dark-etched areas, thus suggesting loss of corrosion resistance.

Precipitation hardening in the bulk occurred simultaneously with the surface hardening process. A higher fraction of martensite (precipitation hardenable phase) results in increased bulk hardness after aging and a reduction in the standard deviation.

ACKNOWLEDGMENTS

For the present research work, the authors gratefully acknowledge the Research Fund for Coal and Steel for the financial support to the PressPerfect project. Furthermore, the authors would like to thank Sandvik Materials Technology for providing the materials used in the experimental activity. Dr. Kristian Vinter Dahl is acknowledged for the ThermoCalc simulations.

REFERENCES

1. B.H. Kolster: *VDI. Ber.*, 1983, vol. 506, p. 107.
2. Y. Sun, X. Li, and T. Bell: *Mater. Sci. Technol.*, 1999, vol. 15, pp. 1171–78.
3. Y. Sun, T. Bell, Z. Kolosvary, and J. Flis: *Met. Sci. Heat Treat.*, 1999, vol. 26, p. 9.
4. T.L. Christiansen and M.A.J. Somers: *Int. J. Mater. Res. Former. Zeitschrift Fuer Met.*, 2009, vol. 100, pp. 1361–77.
5. S.K. Kim, J.S. Yoo, J.M. Priest, and M.P. Fewell: *Surf. Coat. Technol.*, 2003, vols. 163–164, pp. 380–85.
6. A. Leyland, D.B. Lewis, P.R. Stevenson, and A. Matthews: *Surf. Coat. Technol.*, 1993, vol. 62, pp. 608–17.
7. R.B. Frandsen, T.L. Christiansen, and M.A.J. Somers: *Surf. Coat. Technol.*, 2006, vol. 200, pp. 5160–69.
8. M. Esfandiari and H. Dong: *Surf. Coat. Technol.*, 2007, vol. 201, pp. 6189–6196.
9. R.L. Liu and M.F. Yan: *Surf. Coat. Technol.*, 2010, vol. 204, pp. 2251–56.
10. P. Kochmanski and J. Nowacki: *Surf. Coat. Technol.*, 2008, vol. 202, pp. 4834–38.
11. P. Kochmański and J. Nowacki: *Surf. Coat. Technol.*, 2006, vol. 200, pp. 6558–62.
12. J. Post, H. Nolles, K. Datta, and H.J.M. Geijselaers: *Mater. Sci. Eng. A*, 2008, vol. 498, pp. 179–90.
13. J. Post, K. Datta, and J. Huetink: in *Int. Conf. Numer. Methods Ind. Form. Process.*, UT Publications, 2004, pp. 1670–75.
14. J. Post, K. Datta, and J. Beyer: *Mater. Sci. Eng. A*, 2008, vol. 485, pp. 290–98.
15. C. Irander and G. Berglund: *Sandvik Nanoflex®—Designed for Ultimate Performance*, 2006.
16. I. Tamura: *Met. Sci.*, 1982, vol. 16, pp. 245–53.
17. M. Holrnquist, J. Nilsson, and A. Hultin Stigenberg: Scripta Metall*Mater.*, 1995, vol. 33, pp. 1367–73.
18. G.B. Olson and M. Cohen: *Metall. Trans. A*, 1975, vol. 6, pp. 791–95.
19. G.B. Olson and M. Cohen: *J. Less Common Met.*, 1972, vol. 28, pp. 107–18.
20. S.S. Hecker and M.G. Stout: *Metall. Trans. A*, 1982, vol. 13, pp. 619–26.
21. J.A.C. Ramirez, T. Tsuta, Y. Mitani, and K. Osakada: *JSME Int.*, 1992, vol. 35.

22. R.B. Goldfarb and R.P. Reed: *Adv. Cryog. Eng. Mater.*, 1984, vol. 30, pp. 475–82.
23. J. Stickforth: *Technol. Mitt. Krupp*, 1966, vol. 24, pp. 89–102.
24. P. Liu, A. Hultin Stigenberg, and J.O. Nilsson: *Scr. Metall. Mater.*, 1994, vol. 31, pp. 249–54.
25. J.O. Nilsson, A. Hultin Stigenberg, and P. Liu: *Liu. Metall. Mater. Trans. A*, 1994, vol. 25, pp. 2225–33.
26. M. Thuvander, M. Andersson, and K. Stiller: *Mater. Sci. Technol.*, 2012, vol. 28, pp. 695–701.
27. K. Stiller, F. Danoix, and A. Bostel: *Appl. Surf. Sci.*, 1996, vols. 94–95, pp. 326–33.
28. Z. Guo, W. Sha, and E.A. Wilson: *Mater. Sci. Technol.*, 2002, vol. 18, pp. 377–82.
29. Z.I. Zhang and T. Bell: *Surf. Eng.*, 1985, vol. 1, pp. 131–36.
30. D.L. Williamson, O. Ozturk, R. Wei, and P.J. Wilbur: *Surf. Coat. Technol.*, 1994, vol. 65, pp. 15–23.
31. C.X. Li and T. Bell: *Corros. Sci.*, 2004, vol. 46, pp. 1527–47.
32. M.K. Lei and X.M. Zhu: *Surf. Coat. Technol.*, 2005, vol. 193, pp. 22–28.
33. W. Liang, X. Bin, Y. Zhiwei, and S. Yaqin: *Surf. Coat. Technol.*, 2000, vol. 130, pp. 304–8.
34. Y. Sun and T. Bell: *Wear*, 1998, vol. 218, pp. 34–42.
35. T.L. Christiansen and M.A.J. Somers: *Metall. Mater. Trans. A*, 2008, vol. 40, pp. 1791–98.
36. T.L. Christiansen, K.V. Dahl, and M.A.J. Somers: *Mater. Sci. Technol.*, 2008, vol. 24, pp. 159–67.
37. F.A.P. Fernandes, T.L. Christiansen, and M.A.J. Somers: *Adv. Mater. Res.*, 2014, vol. 996, pp. 155–61.
38. T. Bell, J. Lanagan, P.H. Morton, H.W. Bergmann, and A.M. Staines: *Surf. Eng.*, 1986, vol. 2, pp. 133–43.
39. M. Villa, M.F. Hansen, K. Pantleon, and M.A.J. Somers: *Mater. Sci. Technol.*, 2015, vol. 31, pp. 115–22.
40. ASTM International: *Standard Test Methods for Tension Testing of Metallic Materials* [Metric], 2004, p.E 8M-04.
41. P.C. Van Wiggen, H.C.F. Rozendaal, and E.J. Mittemeijer: *J. Mater. Sci.*, 1985, vol. 20, pp. 4561–82.
42. P.M. Hekker, H.C.F. Rozendaal, and E.J. Mittemeijer: *J. Mater. Sci.*, 1985, vol. 20, pp. 718–29.
43. R. Hales and A.C. Hill: *Met. Sci.*, 1977, vol. 11, pp. 241–244.
44. J.R.G. Da Silva and R.B. McLellan: *Mater. Sci. Eng.*, 1976, vol. 26, pp. 83–87.
45. F. Bottoli, G. Winther, T.L. Christiansen, and M.A.J. Somers: *Metall. Mater. Trans. A*, 2015, vol. 46A, pp. 2579–90.
46. M.A.J. Somers, R.M. Lankreijer, and E.J. Mittemeijer: *Philos. Mag. A*, 1989, vol. 59, pp. 353–78.
47. F.A.P. Fernandes, T.L. Christiansen, and M.A.J. Somers: *Proc. 28th Int. Conf. Surf. Modif. Technol.*, Valardocs, Tampere, Finland, 2014, pp. 223–33.
48. J. Oddershede, T.L. Christiansen, K. Ståhl, and M.A.J. Somers: *Scr. Mater.*, 2010, vol. 62, pp. 290–93.
49. H. Dong: *Int. Mater. Rev.*, 2010, vol. 55, pp. 65–98.
50. M. Tsujikawa, N. Yamauchi, N. Ueda, T. Sone, and Y. Hirose: *Surf. Coat. Technol.*, 2005, vol. 193, pp. 309–13.
51. C. Blawert, B.L. Mordike, G.A. Collins, K.T. Short, and Y. Jiraskova: *Surf. Coatings Technol.*, 2000, vols. 128–129, pp. 219–25.
52. M.A.J. Somers and T.L. Christiansen: *J. Phase Equilibria Diffus.*, 2005, vol. 26, pp. 520–28.
53. K. Stiller, F. Danoix, and M. Hättestrand: *Mater. Sci. Eng. A*, 1998, vol. 250, pp. 22–26.
54. M. Andersson, K. Stiller, and M. Hättestrand: *Surf. Interface Anal.*, 2007, vol. 39, pp. 195–200.
55. D.B. Wiles and R.A. Young: *J. Appl. Crystallogr.*, 1981, vol. 14, pp. 149–51.
56. R.J. Hill and C.J. Howard: *Australian Atomic Energy Commission (now ANSTO) Report No. M112*, New South Wales, 1986.

8 Paper III: Low-temperature nitriding of deformed austenitic stainless steels with various nitrogen contents obtained by prior high temperature solution nitriding

Federico Bottoli, Grethe Winther, Thomas L. Christiansen, Kristian Vinter Dahl, Marcel A.J. Somers
Technical University of Denmark, Department of Mechanical Engineering, Produktionstorvet b.425, 2800 Kgs. Lyngby, Denmark

Article submitted to Metallurgical and Materials Transactions A on November 26th, 2015.

Low-temperature nitriding of deformed austenitic stainless steels with various nitrogen contents obtained by prior high temperature solution nitriding

Federico Bottoli, Grethe Winther, Thomas L. Christiansen,
Kristian Vinter Dahl, Marcel A.J. Somers

Technical University of Denmark, Department of Mechanical Engineering,
Produktionstorvet b.425, 2800 Kgs. Lyngby, Denmark

Keywords

High-nitrogen steels, high-temperature solution nitriding, low-temperature nitriding, nitrogen, austenitic stainless steel.

Abstract

In the past decades, high nitrogen steels (HNS) have been regarded as substitutes for conventional austenitic stainless steels because of their superior mechanical and corrosion properties. However, the main limitation to their wider application is their expensive production processes.

As an alternative, high temperature solution nitriding has been applied to produce HNS from three commercially available stainless steel grades (AISI 304L, AISI 316 and EN 1.4369). The nitrogen content in each steel alloy is varied and its influence on the mechanical properties and the stability of the austenite investigated. Both hardness and yield stress increase and the alloys remain ductile. In addition, strain-induced transformation of austenite to martensite is suppressed, which is beneficial for subsequent low temperature nitriding of the surface of deformed alloys. The combination of high and low temperature nitriding results in improved properties of both bulk and surface.

1 Introduction

The increasing demand for high-strength and corrosion-resistant alloys has resulted in the advent of high-nitrogen steels (HNS) as a potential substitute for conventional stainless steels in various engineering applications [1]. Interstitial alloying with nitrogen offers unique advantages over dissolving interstitial elements as boron and carbon, because of the high solid solubility of nitrogen in austenite combined with an effective solid-solution strengthening effect [2–4]. Nitrogen provides a remarkable increase in yield and tensile strength, without sacrificing the toughness [4–7]. Furthermore N dissolved in steel is a strong

austenite stabilizer, which means that lower amounts of expensive austenite formers as nickel are required and the formation of ferrite and/or martensite upon solidification or deformation can be prevented [8].
In addition to a considerable improvement of the mechanical properties, the interstitial dissolution of nitrogen in stainless steel can lead to a significant improvement of the resistance against localized corrosion as crevice and pitting corrosion as it enhances the PREN and MARC numbers importantly [9–12]. Due to the favorable combination of improved mechanical properties and corrosion performance, in the past decades HNS have become an important class of engineering materials. However, despite several advantages, the major obstacle to a wider application of this class of stainless steels is related to their production. The solubility of nitrogen in liquid Fe is only 0.045 wt% at 1600 °C [13]. Consequently, the production of HNS requires high-pressure melting technologies or the utilization of powder metallurgy techniques [9,10]. In contrast to the liquid state, the solubility of nitrogen is higher in the solid state [2]. Hence, rather than dissolving nitrogen in the liquid state or the synthesis of high nitrogen steel powder, gas treatment of the steel component, such as solution nitriding, followed by rapid (gas) quenching to prevent nitride formation [15,16], can be applied to dissolve nitrogen in the matrix. This process can be applied to austenitic stainless steel grades to enhance the austenite stability or to duplex and ferritic stainless steel in order to stabilize the austenitic phase at high temperature.
The excellent bulk properties that can be obtained by solution strengthening can be coupled with outstanding surface properties if the material is subsequently subjected to a low-temperature thermochemical treatment [17–19]. Low-temperature nitriding for instance allows the dissolution of a high amount of nitrogen (up to 38 at%) in the surface zone, leading to the formation of a supersaturated solid solution known as expanded austenite [17] or S-phase [18,19]. The formation of an expanded austenite case results in a significant improvement in the resistance to galling and improves pitting corrosion properties as well as a considerable increase in the wear and fatigue resistance of the component [20–26].
In the present work, high temperature solution nitriding (HTSN) and low temperature nitriding (LTN) are investigated. Both processes entail incorporation of nitrogen in solid solution in stainless steel. Different HTSN treatments were applied onto three commercial alloys (AISI 316, AISI 304L and EN. 1.4369) to study the influence of nitrogen alloying on the mechanical properties and behavior upon tensile deformation.
HTSN treated materials before and after plastic deformation were subsequently low-temperature nitrided and the nitriding response was analyzed to investigate the sensitivity of the low-temperature nitriding treatment for the solution nitrided and deformed structure.

2 Experimental

2.1 Materials

The compositions of the alloys investigated in this study (AISI 316, AISI 304L and EN 1.4369) are given in Table 1. The most important differences between these three commercially available stainless steel grades are the Cr, Ni and Mn contents, which influence the nitrogen solubility and the stability of the austenite phase against martensite formation during plastic straining [5].

The materials were delivered as sheets: AISI 316 and EN 1.4369 as 0.7mm-thick sheets and AISI 304L as 0.45mm-thick sheet. Microstructure analysis revealed a fully austenitic structure for all the three alloys, with hardness and grain sizes as given in Table 2. The microstructure investigations are consistent with an annealed state of the as-received sheet materials. The higher hardness in EN 1.4369 as compared to AISI 316 and AISI 304L, despite the larger grain size, is explained from the solution strengthening induced by the presence of nitrogen as an alloying element.

Table 1: Chemical compositions of AISI 316, AISI 304L and EN 1.4369 in wt% as determined by the suppliers, Lemvigh Muller and Sandvik Materials Technology.

	C	Si	Mn	Cr	Ni	Mo	N
AISI 316	0.07	0.4	1.6	17.0	10.55	2.0	0.05
AISI 304L	0.03	0.32	1.78	18.28	8.08	-	-
EN 1.4369	0.09	0.74	5.92	18.58	7.11	0.18	0.23

Table 2: Hardness and grain size distribution of the as-received stainless steels

	Hardness (HV_{2N})	Grain Size (µm)
AISI 316	176	15(3)
AISI 304L	186	15(1)
EN 1.4369	211	30(5)

Tensile test specimens in accordance with ASTM standard E 8M-04 [27] were cut from the plate material for determination of the mechanical properties and for applying pre-defined levels of tensile straining.

2.2 High-temperature solution nitriding

High-temperature solution nitriding treatment as applied in this work is a commercial process provided by the company Expanite A/S [28,29]. Tensile test specimens of the three selected steel grades were subjected to three different high-temperature solution nitriding treatments. The various steel grades were treated in the same batch. All grades were treated at a solution nitriding temperature of 1423 K (1150°C) in three batches at the N_2 pressures 0.3 bar (HTSN1), 0.6 bar (not investigated in detail in this work) and 0.9 bar (HTSN2). The durations of the treatments were the same and resulted in samples with uniform nitrogen content throughout the sample. A high-pressure gas quench was applied to avoid the formation of nitride precipitates during cooling. The nitrogen contents in the steels after the HTSN treatment were measured with inert gas fusion thermal conductivity detection with a LECO TN500 nitrogen analyzer. Thermodynamic equilibrium calculations related to solution nitriding of the alloys were performed using Thermo-Calc version 4.1 with the Thermo-Calc TCFE7.0 database [30–32].

2.3 Plastic deformation through tensile straining

Tensile test specimens obtained in as-received and solution nitrided conditions were plastically deformed to different equivalent strain levels through tensile straining at a strain rate of $6.67*10^{-3}s^{-1}$. The tensile loading direction was chosen parallel to the rolling direction of the plate.

The materials were tensile strained up to the following equivalent strain levels:

- AISI 316: 0.15, 0.30, 0.42
- AISI 304L: 0.15, 0.30, 0.45.
- EN 1.4369: 0.15, 0.30, 0.50.

The difference in final equivalent strains is related to a difference in ductility among the alloys.

2.4 Low-temperature nitriding

Specimens with dimension 15x12.5mm^2 were cut from the solution nitrided tensile test specimens before and after plastic deformation. These samples were ground and polished, using a final step of 3µm diamond paste and subsequently electro-polished in order to remove the grinding-induced plastic deformation at the surface. Electro-polishing was carried out in a "Struers Polectrol" using "Struers electrolyte A2" with an applied potential of 30V and a current density of 2A/cm^2.

The samples were low temperature nitrided in an industrial LAC annealing furnace model PKRC 55/09 retrofitted for gaseous nitriding under gas circulation. The sample surface was activated in-situ with a proprietary treatment in order to enable the low-temperature surface hardening.

The low-temperature nitriding (LTN) process was performed for all samples at 703K (430 °C) for 20h in a partly dissociated ammonia atmosphere. The process temperature was controlled during the entire processing, including heating, nitriding and cooling, through a type-K thermocouple placed in the proximity to the samples.

2.5 Microstructure characterization

The microstructure of all samples before and after plastic deformation and after low-temperature nitriding was investigated in cross-sections with reflected-light microscopy. The samples were ground, polished and etched with Kalling´s reagent no. 1 for 4-8s, depending on the sample condition. Micrographs were collected using a Neophot 30 operated with a 100x oil immersion planapochromate objective for optimal resolution.

A Future-tech FM700 was used for microhardness indentation; loads of 2N and 0.05N were applied for the assessment of the hardness in the bulk and nitrided zone respectively. The bulk hardness values presented are the average of 25 measurements.

X-ray diffractometry for phase identification was carried out with the Bragg-Brentano symmetric setting and with grazing incidence in a Bruker D8 AXS X-ray diffractometer equipped with Cr-anode and Göbel mirror in the incident beam. The step size was equal to 0.03° 2θ and a counting time of 4s per 2θ step.

Glow discharge emission spectroscopy (GD-OES) was applied for the determination of the surface composition profiles after LTN treatments. The controlled sputtering of the surface was performed with a plasma at 1000Pa and 40W using a Horiba Jobin Yvon GD profiler 2. Quantification of the concentration depth-profiles was achieved using a selection of stainless steel reference materials supplemented with a custom-made γ'-Fe_4N layer on pure iron as the nitrogen reference.

3 Results and interpretation

3.1 Solution nitriding

Calculated cross-sections in the phase diagrams, displaying the γ phase field in the temperature range 1223-1623 K (950 – 1350 °C) vs. the nitrogen content up to 0.8 wt% in the alloys, are shown in Fig. 1a-c together with N_2 isobars that would provide the given nitrogen contents in the steels under equilibrium conditions.

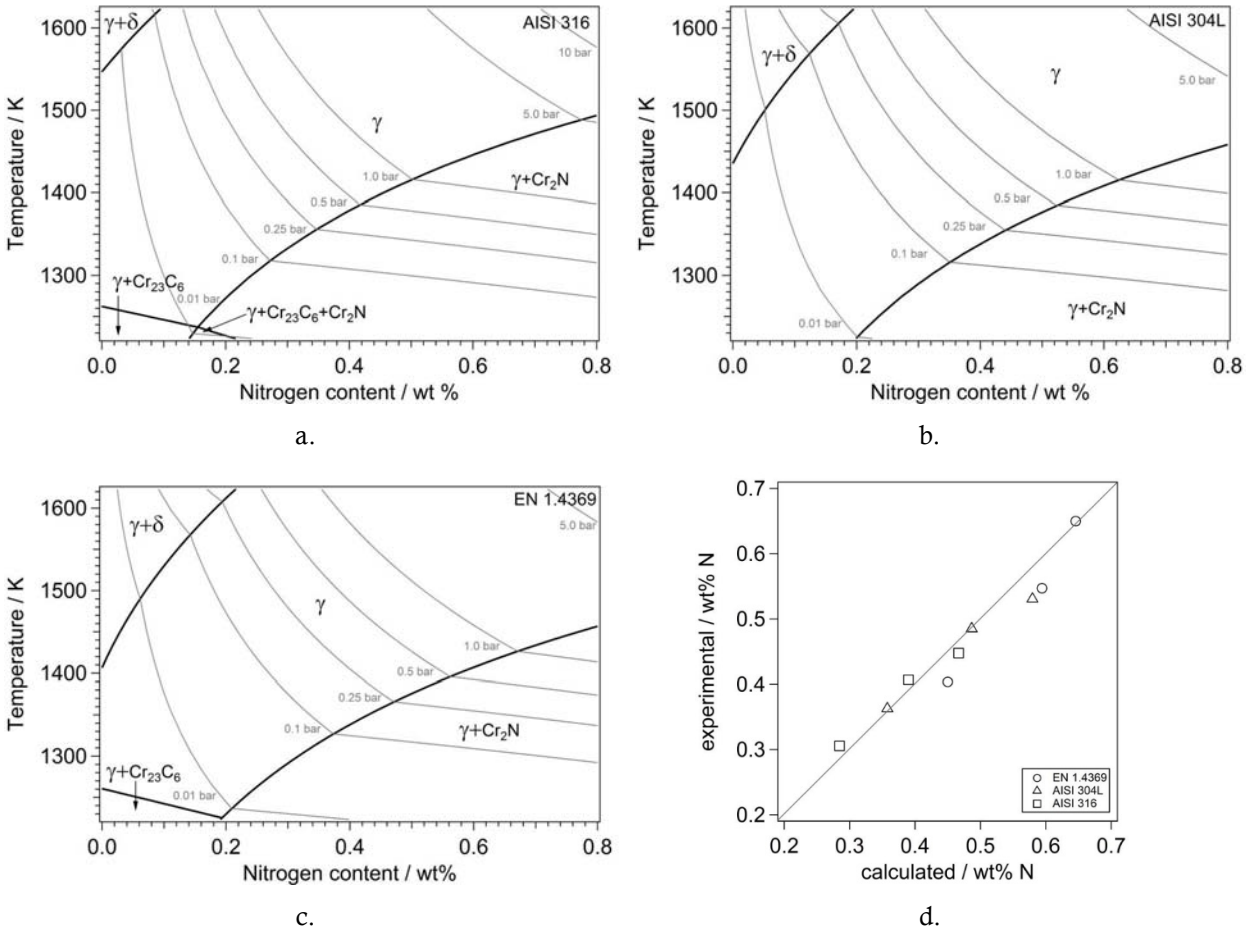

Figure 1: a-c Isopleths in the phase diagram showing the phase stability of austenite in the temperature range 1223-1623K (950-1350 °C) vs. nitrogen content in the solid state. Superimposed on the isopleths, N_2

isobars are given that would provide the equilibrium nitrogen contents. d. comparison of the predicted nitrogen content, as calculated with ThermoCalc, and the experimentally determined nitrogen content in the sample.

Clearly, in principle the nitrogen content in austenite can be adjusted by controlling the N_2 pressure during high-temperature solution nitriding, provided that equilibrium is achieved between nitrogen in the gas and nitrogen dissolved in the solid state. The nitrogen contents and grain sizes after HTSN1 and HTSN2 in the three stainless steels are listed in Table 3. A comparison of nitrogen contents calculated by ThermoCalc with the experimentally determined nitrogen contents is given in Fig.1d for the three steels and all three solution nitriding treatments. For the data in Fig. 1d austenite was the only stable phase. An excellent agreement is achieved between the predicted and experimental nitrogen contents, in correspondence with earlier findings of Frisk [33].

Table 3: Nitrogen content in wt % determined with inert gas fusion thermal conductivity detection **(**LECO TN 500 analyser) and grain grain-size after solid solution treatment

	Nitrogen Content (%wt)		**Grain Size (µm)**	
	HTSN1	**HTSN2**	**HTSN1**	**HTSN2**
AISI 316	0.306(1)	0.448(2)	50(8)	51(7)
AISI 304L	0.363(2)	0.531(1)	75(8)	75(10)
EN 1.4369	0.450(1)	0.646(3)	75(15)	75(10)

Evidently, along with the dissolution of nitrogen in the solid state at 1423 K (1150 °C) substantial grain growth has occurred in the three selected steels (cf. Table 2 and 3). Apparently, the actual grain growth is only determined by the combination of temperature and time, which were the same for the HTSN treatments, and not by the N_2 pressure (or the dissolved nitrogen content in the sample).

3.2 Mechanical properties

The materials in the as-received condition and after the HTSN treatments at 0.3 bar and 0.9 bar N_2 pressure were plastically deformed through tensile straining to different equivalent strain levels. The stress-strain curves obtained in uniaxial tension for the three steel grades are given in Fig. 2a. All curves for AISI 304 and EN 1.4369 are fitted excellently with the Voce equation, which gives the relation between stress, σ, and strain, ε:

$$\sigma(\varepsilon) = \sigma_y + \sigma_{SS}\{1 - e^{-n\varepsilon}\} \quad for\ \varepsilon > 0.02 \qquad \text{Eq. 1}$$

where $\sigma_y$and σ_{SS} are the yield stress and the saturation stress, respectively and n is the work-hardening exponent.

The curves for AISI 316 are also well-fitted by the equation, albeit slightly poorer than for AISI 304 and EN 1.4369. Fig. 2b displays the obtained Voce parameters. The dissolution of nitrogen in austenite gives a significant increase in both the yield stress and saturation stress, while the work-hardening exponent decreases. The Voce parameters for AISI 304 and EN 1.4369 are comparable, while AISI 316 has a higher n-value than the other two alloys. Accordingly, the dissolution of nitrogen not only induces substantial strengthening of the steel, but also changes the work-hardening behaviour. As demonstrated by the insets in Fig. 2a, nitrogen introduces a yield point phenomenon. The experimentally determined upper yield points are consistently higher than the fitted σ_y as shown in Fig. 2b for non-vanishing nitrogen concentrations. For AISI 304L and 316 the yield strength is enhanced more than 100 MPa for HTSN1 and 150 MPa for HTSN2. By contrast, the yield strength of EN 1.4369 after HTSN1 is comparable to the one of the as-received material, despite a considerable increase in nitrogen content (cf. Tables 1 and 3). This will be discussed below.

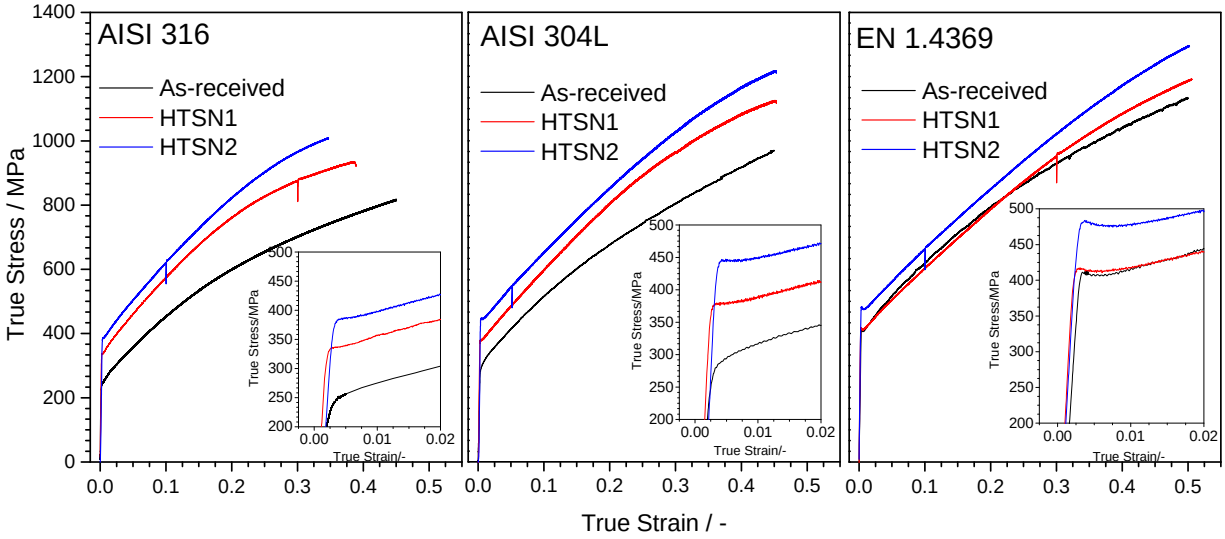

Figure 2a: True stress – true strain curve for AISI 316, AISI 304L and EN 1.4369 in as-received condition and after high-temperature solution nitriding treatment at 0.3 bar (HTSN1) and 0.9 bar (HTSN2) N_2 pressure. Inserts show an enlargement of the transition from elastic to plastic region.

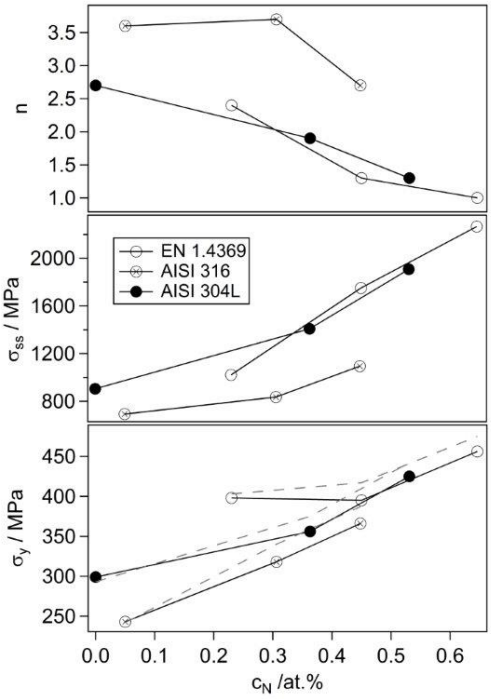

Figure 2b: Parameters obtained by fitting the Voce equation to the stress-strain curves in Fig. 2a. The dashed lines give the upper yield limits as observed in Fig.3b

3.2.1 Hardness

The bulk hardness in the solution-nitrided samples is given as a function of the equivalent deformation in Fig. 3a. In all alloys, the bulk hardness increases with the applied plastic (tensile) strain. For the as-received condition a disproportionately large hardness increase is obtained for the first plastic deformation, while for the solution-nitrided samples the hardness increases linearly with equivalent strain. For each equivalent deformation level, and for all tested materials, higher nitrogen content results in higher bulk hardness. The increase in hardness with the applied equivalent strain is shifted toward higher hardness values as the nitrogen content in the alloy increases.

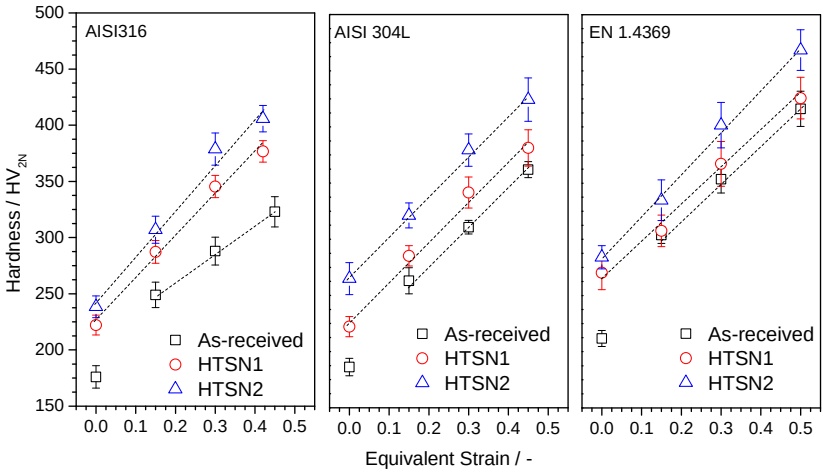

Figure 3a: Hardness in the three selected alloys as a function of the equivalent strain.

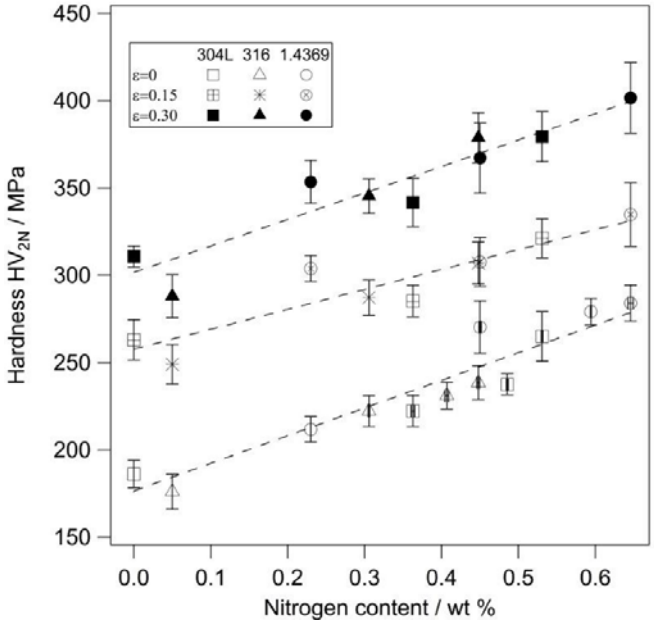

Figure 3b: Hardness increase as a function of the interstitial nitrogen content in the three selected alloys in as-received and HTSN treated conditions, in unstrained and strained conditions to an equivalent strain of 0.15 and 0.30. Note that for the unstrained condition also hardness values for HTSN treatment at 0.6 bar N_2 gas pressure are included.

The hardness as a function of the nitrogen content for equivalent strains: ε=0, ε=0.15 and ε=0.30 is given in Fig.3b. For each steel type and for all solution nitriding treatments, a significant increase of the bulk hardness with dissolved nitrogen content is observed in Fig. 3b. The dashed lines in Fig.3b guide the eye to show that there is a clear dependence of the bulk hardness on the nitrogen content. Clearly, from Figs. 3 it also follows that the hardness increase that is achieved by plastic deformation is larger than the hardness increase obtained by interstitial alloying, irrespective of the nitrogen content.

3.2.2 Phase stability

X-ray diffractograms of the HTSN treated and subsequently deformed steels are given as a function of the equivalent plastic strain for HTSN1 in Fig. 4a and for HTSN2 in Fig. 4b, for the highest equivalent plastic strain applied. All diffractograms given, show that samples remained entirely austenitic on uniaxial tensile deformation. No indications for the development of b.c.c. or h.c.p. martensite were found. In our previous work it was shown that EN.14369 in the as-delivered (annealed) condition remains fully austenitic upon plastic deformation, while AISI 304, with a slightly different composition than the AISI 304L in the present investigation, develops a substantial amount of deformation-induced martensite [34]. Obviously, the stability of austenite against strain-induced martensite formation should be attributed to the presence of nitrogen in solid solution. For the present case the HTSN treated AISI 304L and AISI 316 do not develop strain-induced martensite, indicating that an effective stabilization of austenite can be achieved by introducing nitrogen in the HTSN treatment. Perhaps a lower nitrogen content than dissolved in the current experiments could suffice to prevent strain-induced martensite formation.

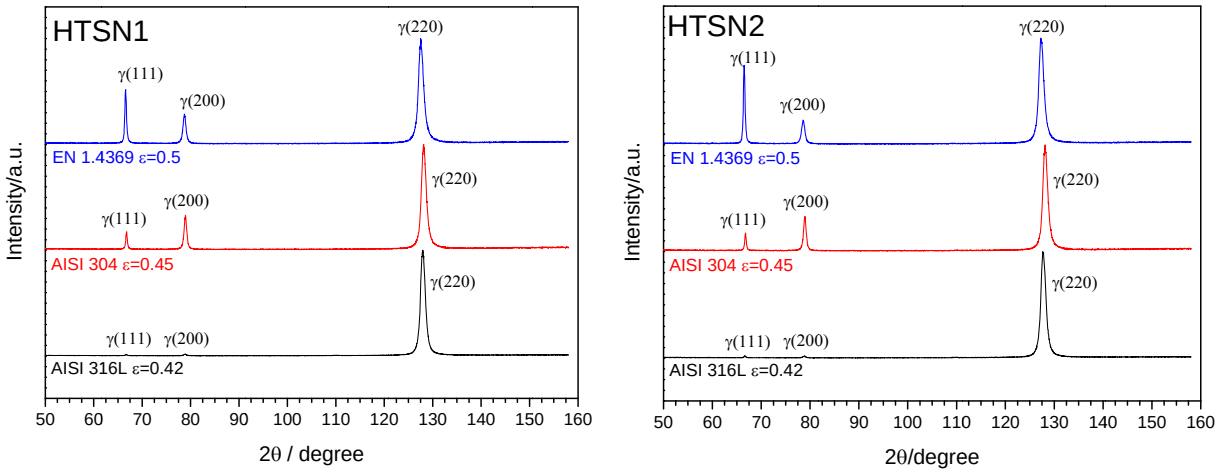

a. b.

Figure 4: X-ray diffractograms after plastic deformation of HTSN1 (a) and HTSN2 (b) treated steels for the highest tensile straining applied to the steels. i.e., ε=0.42 for AISI 316, ε=0.45 for AISI 304L and ε=0.50 for EN 1.4369. No other phases than austenite were identified.

3.3 Low-temperature nitriding

Low-temperature nitriding (LTN) was performed as a finishing treatment for the three selected alloys after the HTSN treatment and plastic deformation. The nitriding responses of HTSN1 and HTSN2 for the three steels are discussed separately below.

3.3.1 Low temperature nitriding after HTSN1

Cross-sectional micrographs of the three alloys after low-temperature nitriding (LTN) at 703K (430 °C) of HTSN1 treated steels with and without additional plastic deformation are given in Figure 5.

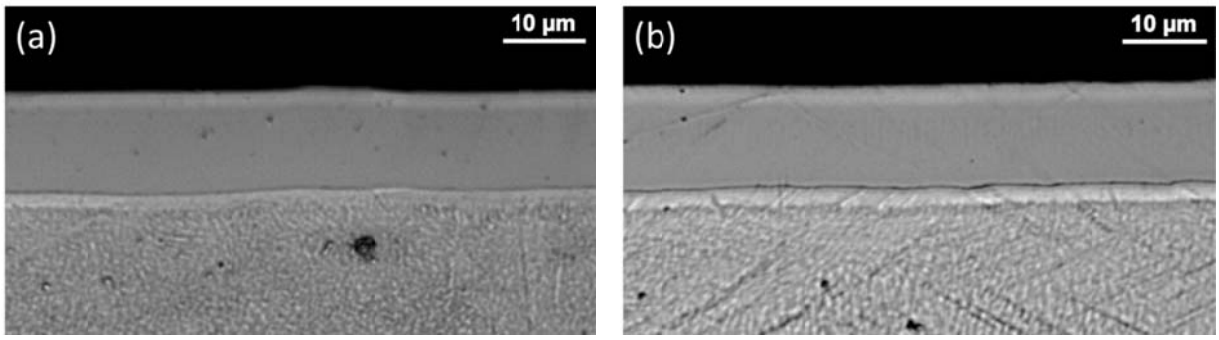

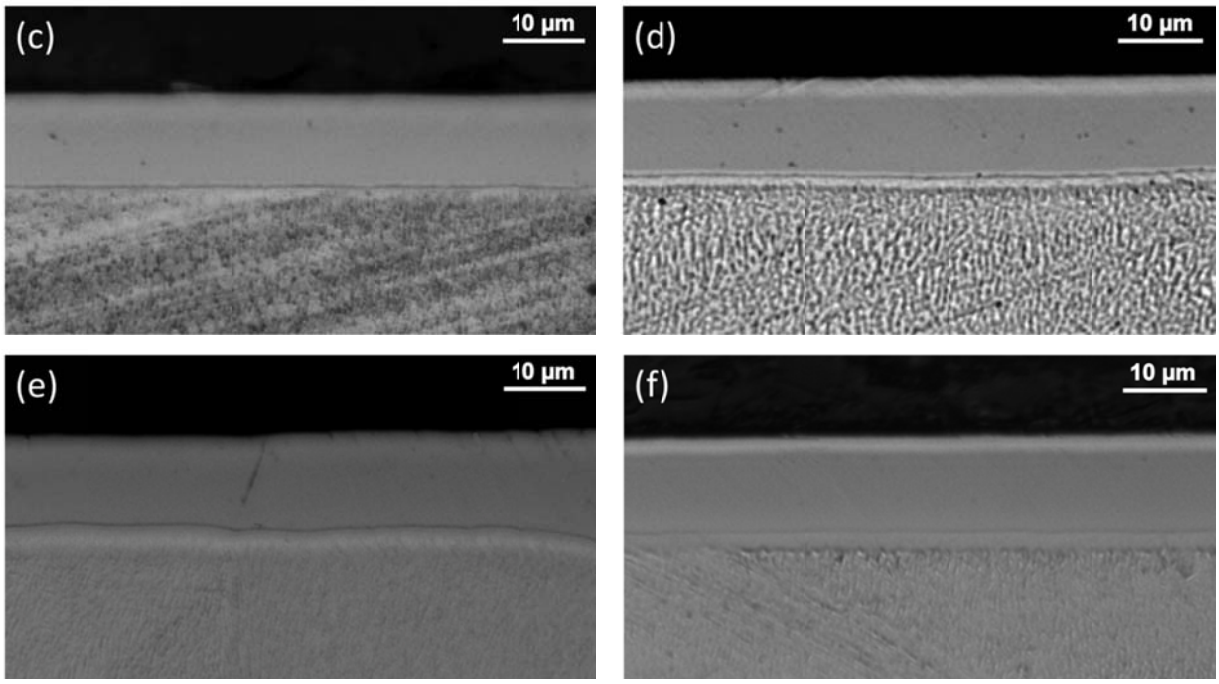

Figure 5: Cross-sectional micrographs of low-temperature nitrided steels: AISI 316 in HTNS (a) and deformed ε=0.42 (b) condition, AISI 304L in HTNS (c) and deformed ε=0.45 (d) condition, and EN 1.4369 in HTNS (e) and deformed ε=0.50 condition (f).

Irrespective of the straining conditions, in all materials the low-temperature nitriding treatment produced a nitrided zone depth of approximately 12µm. The hardness of the layer was 1200$HV_{0.05N}$ throughout the case. Within experimental accuracy the thickness of the nitrided zone appears independent of the alloy composition (including the nitrogen content) and the equivalent strain. The higher corrosion potential for expanded austenite than for the bulk strongly suggests that no development of CrN has occurred by decomposition of expanded austenite (or direct nucleation in strain-induced martensite) under the applied treatment conditions.

In previous experimental activities, it has been demonstrated that plastic deformation for similar applied equivalent strain levels has no influence on the morphology of the nitrided layer for EN 1.4369, while for AISI 304 (without nitrogen), the presence of strain-induced martensite was demonstrated to promote the precipitation of CrN and cause an increase of the case depth [34]. The present results confirm that a fully austenitic structure, even in the deformed condition, provides a reproducible LTN behaviour because no strain-induced martensite is present prior to low-temperature nitriding.

In the micrographs, two features need further explanation: i. a thin relatively bright zone close to the surface and ii. a thin white zone ahead of the expanded austenite front. These features require additional microstructure characterization.

Bragg-Brentano geometry X-ray diffractograms were collected for all the LTN treated steels at the different equivalent deformation levels (ε=0, ε=0.15, ε=0.30 and ε=max). Fig. 6 shows the X-ray diffractograms for the three steels treated according to HTSN1, at the highest equivalent strain level and after LTN.

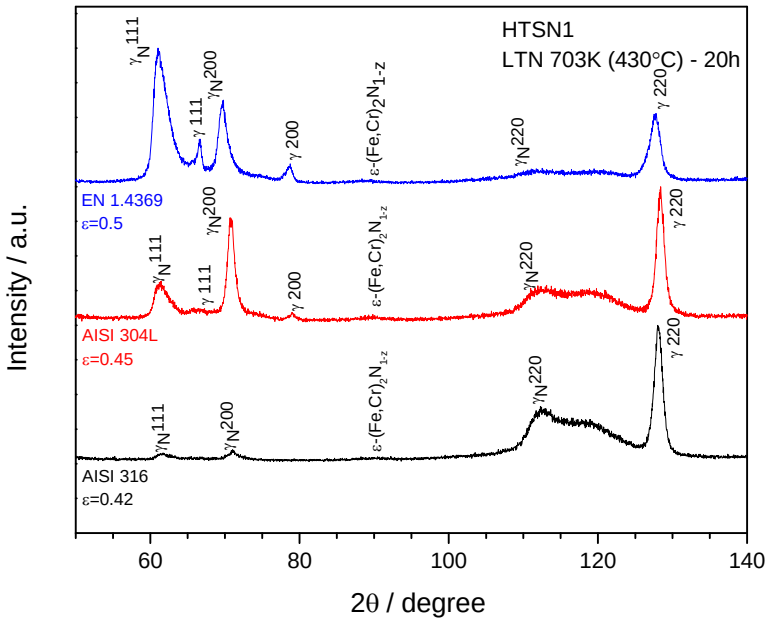

Figure 6: X-ray diffractograms of nitrided steels after HTSN1 and plastic deformation at the highest equivalent strain for the three alloys (Nitriding condition 703K (430 °C), 20h).

In the diffractograms three expanded austenite peaks are prominently present and the corresponding reflections of the austenite, generated from the underlying substrate, are also observed, indicating that the effective information depth of the X-rays is deeper than the case depth. In all cases, the expanded austenite peaks are characterized by asymmetric broadening to the high angle side of the peak. This effect is related to the falling nitrogen concentration over the information depth of the probing X-rays (cf. GDOES profiles in Fig. 7). The behaviour is most pronounced for the 220γ reflection, because the information depth increases with the scattering angle 2θ, and, according to Bragg's law, the lattice spacing range corresponds to a larger 2θ range 220 than for 111 and 200 reflections. No peaks related to the presence of CrN were found, consistent with the reflected light micrographs in Fig.5. Small intensity peaks related to the presence of ε-$(Fe,Cr)_2N_{1-z}$ could be identified. Most likely this hexagonal epsilon nitride (ε-$(Fe,Cr)_2N_{1-z}$) is present at the surface and corresponds to the surface-adjacent white zone in Fig. 5a-f, where the highest nitrogen contents are present. See in this respect also the detailed characterization with grazing incidence XRD on nitrided AISI 630 [35], which shows the presence of ε-phase at the surface in correspondence with a high nitrogen content.

GD-OES depth profiles of nitrogen and carbon for all the alloys (Fig. 7) confirm the presence of very high nitrogen contents in the surface and a carbon accumulation at the case-core transition and close to the surface.

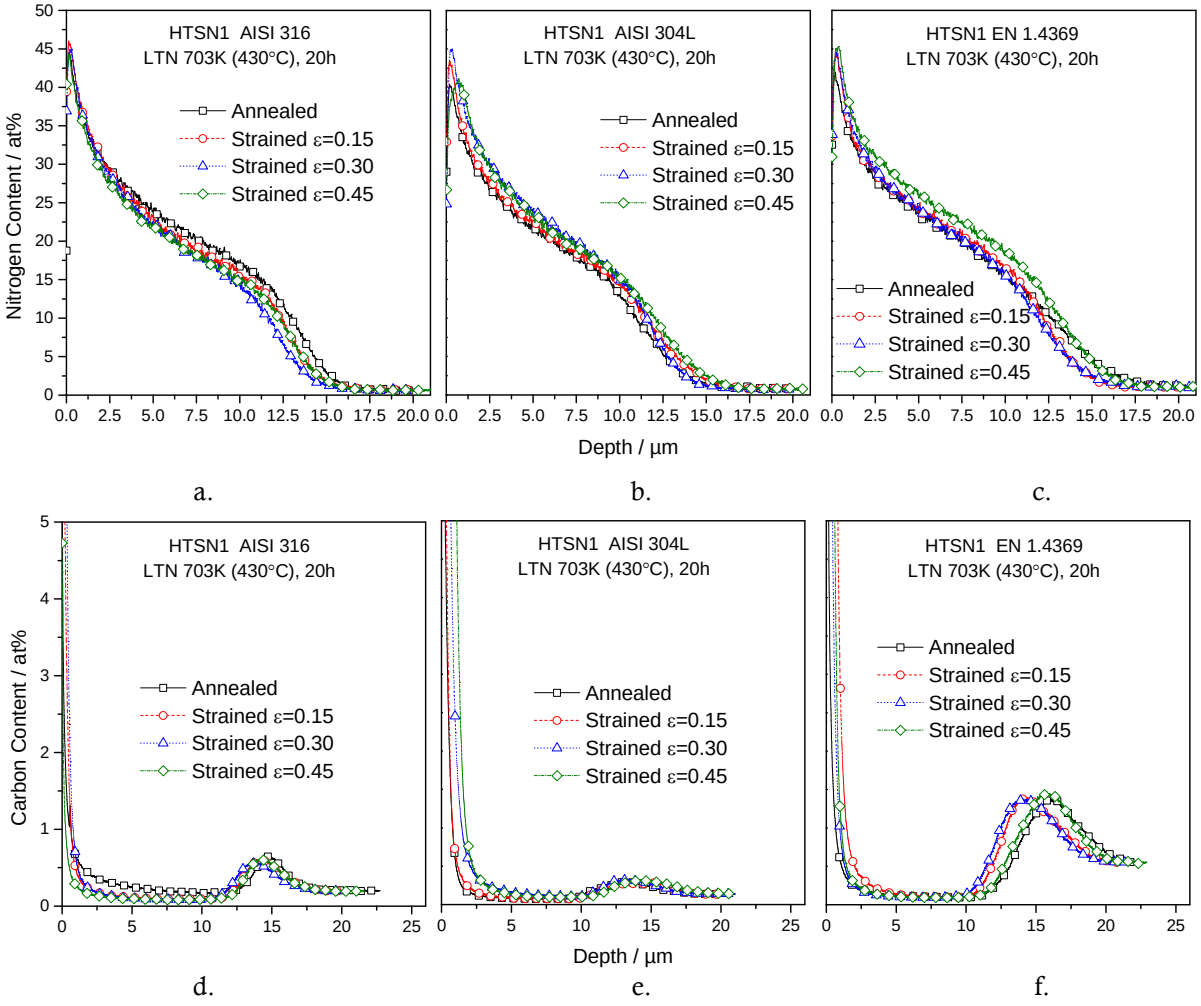

Figure 7: GD-OES profiles of nitrogen and carbon for AISI 316 (a,d), AISI 304L (b,e) and EN 1.4369 (c,f) after HTSN1, deformation and low-temperature nitriding (703K (430 °C), 20h).

Evidently, carbon accumulates ahead of the nitrogen expanded region and reaches up to 1.4 at% for EN 1.4369. All alloys show the same trend, and the accumulation increases with the carbon content originally present in the alloy (cf. Table 1). This is also reflected by an increase of the carbon accumulated with the level of carbon reached at a depth beyond the accumulation, which is clearly highest for EN 1.4369 (Fig. 7f). The occurrence of carbon accumulation underneath the nitrogen-rich zone is generally observed during nitrocarburizing of stainless steel (cf. [19,26,36–39]). In the present case, the carbon accumulation ahead of the nitrogen profile is explained from pushing ahead the carbon already present in the as-received alloys. This happens because iron and chromium atoms prefer a coordination by nitrogen atoms rather than carbon atoms, as reflected by short range ordering of Cr and N atoms in expanded austenite, while such ordering is less pronounced between Cr and C (cf. [40,41]) The carbon present in the first 2 µm of the GD-OES profiles (Fig. 7) could be a consequence of surface contamination that is forward sputtered during GD-OES investigation, as is generally observed. However, since ε-phase can dissolve high quantities of carbon [42–46], the carbon close to the surface could also have been introduced in the LTN treatment,

thus promoting the development of ε-phase in this depth range during the LTN treatment. In this respect it is striking that the depth range of the light bands at the surface of the cases observed in Figs. 5 correlates with the depth range where carbon is present.

Despite only nitriding was applied in this work, this process is highly sensitive to even minor impurity contents of carbon thus carbon absorption could have taken place because of the presence of carbon contamination in the experimental set-up.

3.3.2 Low-temperature nitriding on HTSN2

Reflected-light micrographs of cross sections of the steels after solution nitriding treatment HTSN2, deformation and low-temperature nitriding, are presented in Fig. 8.

In all investigated samples, the LTN treatment of the alloys after HTSN2 and plastic deformation led to the development of a surface region of expanded austenite. For all materials, the expanded austenite case appears featureless after etching, indicating a higher corrosion resistance than the substrate. Again, no significant difference in zone thickness and morphology can be observed between the investigated alloys despite the different chemical compositions of the alloys and the applied equivalent strains. Even for this nitriding condition the hardness of the case was $1200HV_{0.05N}$.

At the outermost surface of expanded austenite, a brighter zone can be identified, which, as pointed out above, is most likely related to the presence of epsilon nitrides (ε-$(Fe,Cr)_2N_{1-z}$) (cf. section 4.1).

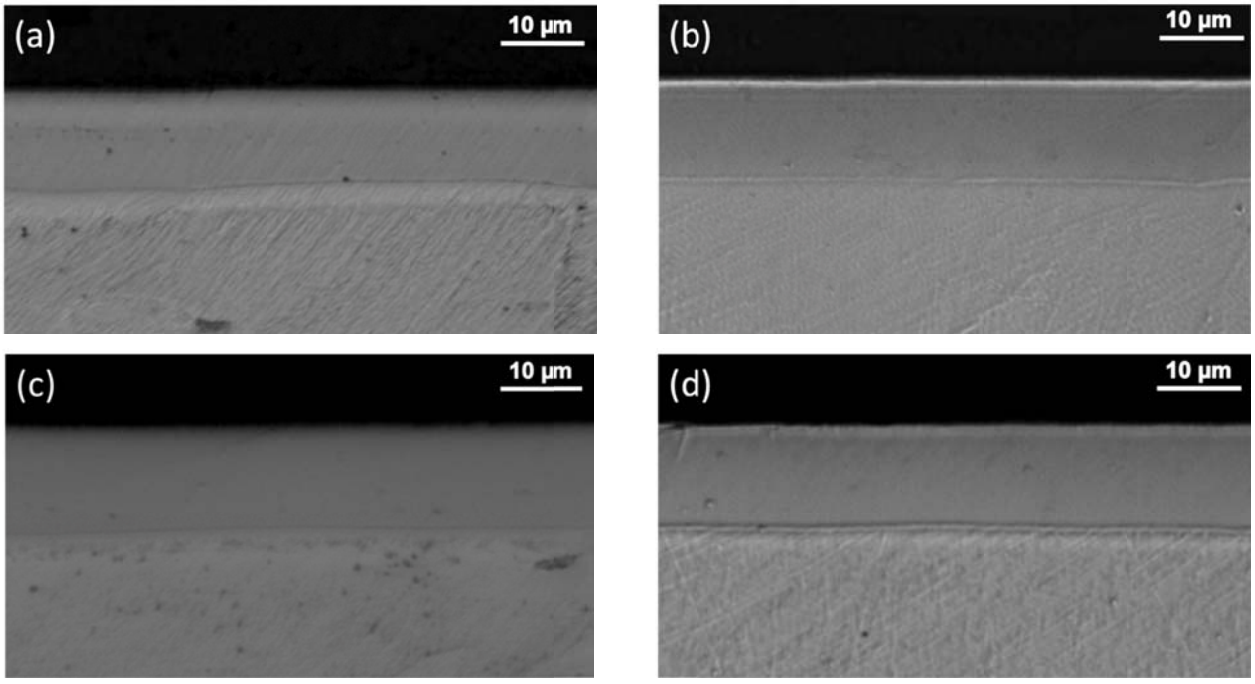

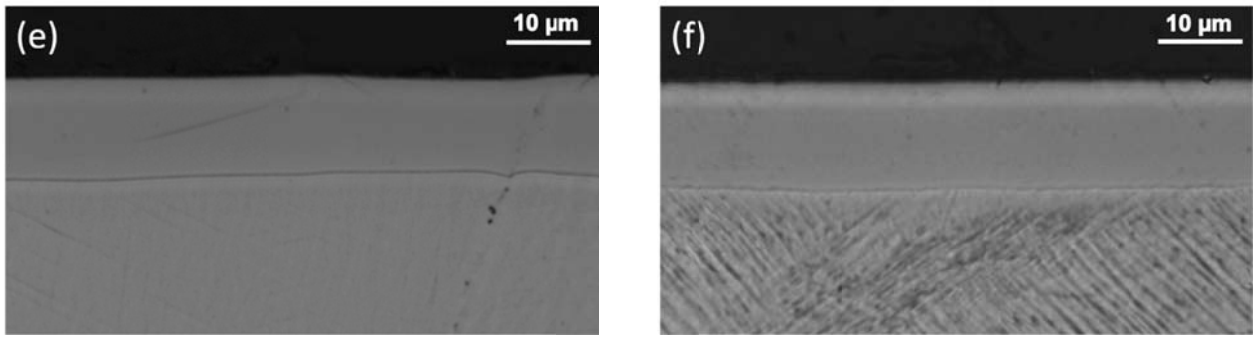

Figure 8: micrographs of low-temperature nitrided steels: AISI 316 HTSN (a) and deformed ε=0.42 (b), AISI 304L HTSN (c) and deformed ε=0.45 (d), EN 1.4369 HTSN (e) and deformed ε=0.50 (f).

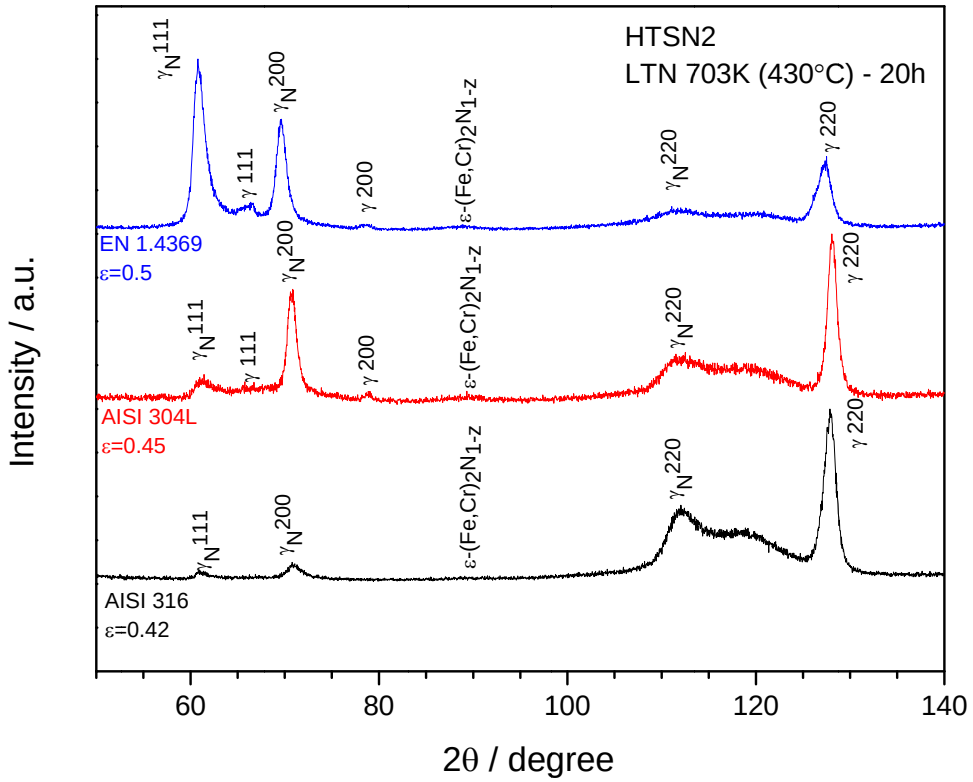

Figure 9: X-ray diffractograms of nitrided materials after HTSN2 and plastic deformation at the highest equivalent strain achieved for the three alloys (Nitriding condition 703K (430 °C), 20h).

XRD investigation in Bragg-Brentano geometry confirmed the formation of expanded austenite after the LTN treatment (Fig. 9). In the diffractograms both peaks of expanded austenite and the underlying austenite substrate can be observed. For all materials, even at the highest applied tensile strain, no evidence for the presence of CrN was identified. However, as for HTSN1 followed by LTN, small intensity peaks related to the epsilon phase (ε-$(Fe,Cr)_2N_{1-z}$) were observed.

GD-OES profiles (Fig. 10) confirm the presence of high amounts of nitrogen in the surface, cf. reflected-light microscopy results in Fig. 8. No pronounced difference between the different alloys at the different tensile strains could be found.

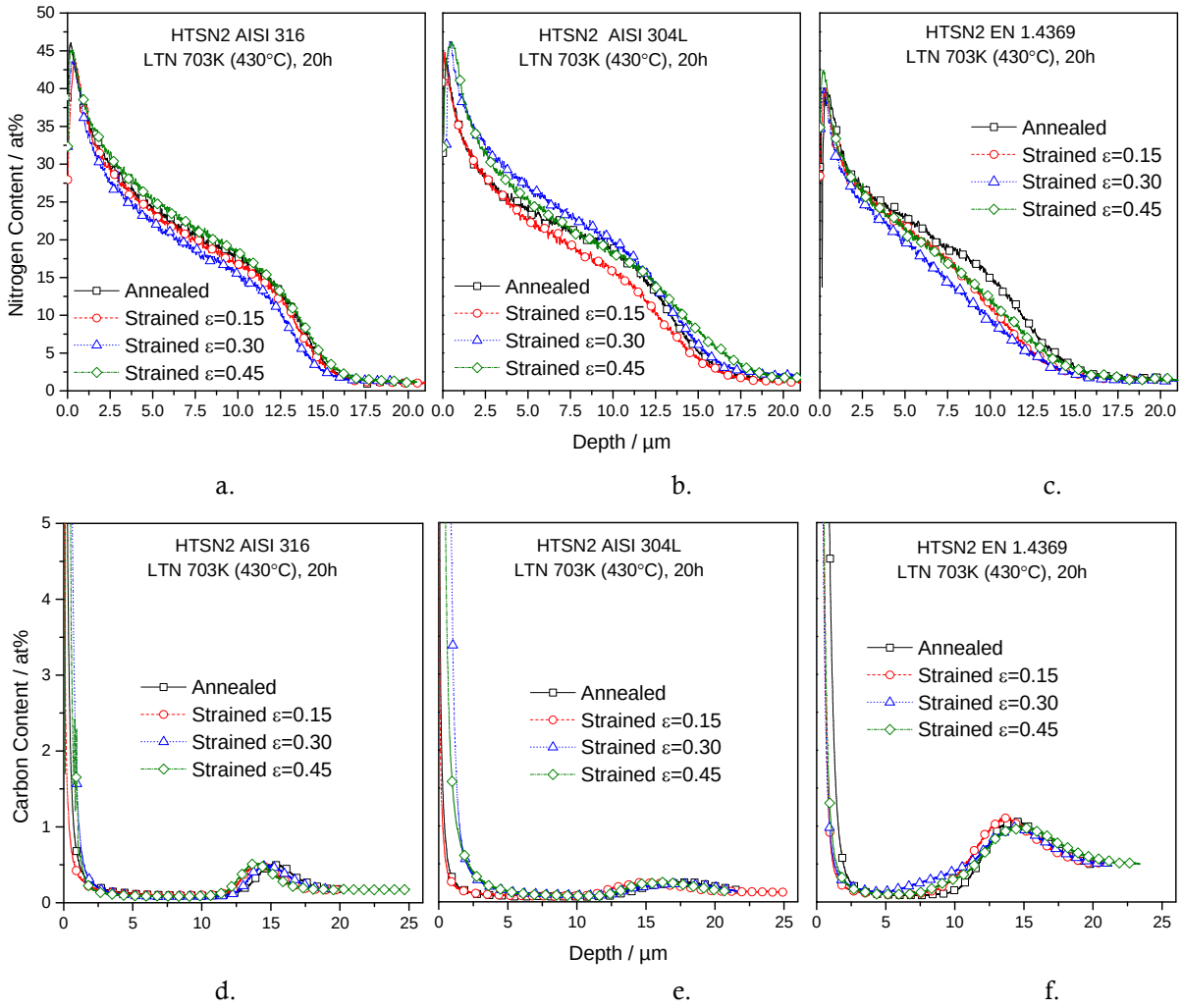

Figure 10: GD-OES profiles of nitrogen and carbon for AISI 316 (a,d), AISI 304L (b,e) and EN 1.4369 (c,f) after HTSN2, deformation and low-temperature nitriding (703K (430 °C), 20h).

4 Discussion

4.1 Nitrogen solubility and effect of nitrogen on mechanical properties

The high-temperature solution nitriding processes performed in the present study allowed the development of high nitrogen steels from conventional, commercial austenitic stainless steels. The nitrogen contents that can be dissolved in equilibrium with a N_2 (partial) pressure depend on the initial chemical composition of the alloys and can be directly related to the presence of different contents of nitride forming and/or

austenite stabilizing substitutional atoms in the selected stainless steel grades. The presence of manganese and chromium, both nitride-forming elements, increases the solubility of nitrogen [5], while an element like Ni, not a nitride former, but an austenite stabilizer, will lower the solubility. Accordingly, the highest nitrogen content was found in the EN 1.4369, which has the highest Mn and Cr content and the lowest Ni content (cf. Fig. 1). A comparison of the predicted and experimental nitrogen solubilities in the three alloys for the applied conditions of high temperature solution nitriding (Fig.1d), shows an excellent agreement.

The addition of nitrogen has a dramatic (beneficial) impact on the mechanical properties of the selected stainless steels, in particular regarding the yield strength and hardness evolution upon straining.

The yield strength and hardness show a linear increase with the nitrogen content, irrespective of the initial chemical composition of the stainless steel grade. This shows that interstitial nitrogen is an effective solid-solution strengthener [5,47]. Solid solution strengthening often follows the square root of the solute concentration. This dependence was not confirmed for the present samples (cf. Fig. 2b). Rather, the approximate linear dependency in Fig. 2b is in agreement with results in the literature for interstitial nitrogen in ferrite [48] and carbon in nickel [49].

Importantly, the present experiments proved the effectiveness of HTSN treatments in obtaining high nitrogen steels from commercially available stainless steel grades, with nitrogen contents beyond those routinely attainable by adding nitrogen to the melt.

The high level of equivalent plastic strain reached for all the alloys confirms that, despite the strengthening effect of the interstitial atoms, the toughness of the stainless steel is not compromised in the investigated range of equivalent straining [5]. The occurrence of a yield drop at the transition from elastic to plastic straining (see inserts in Fig. 2a) is attributed to locking of dislocations by dissolution of interstitials in the dislocation core and/or the surrounding dislocation strain fields [50].

The yield strength is correlated to the hardness [51]. In Fig. 11 the experimentally determined yield stress is given as a function of the hardness for three equivalent strain levels (0, 0.15 and 0.30).

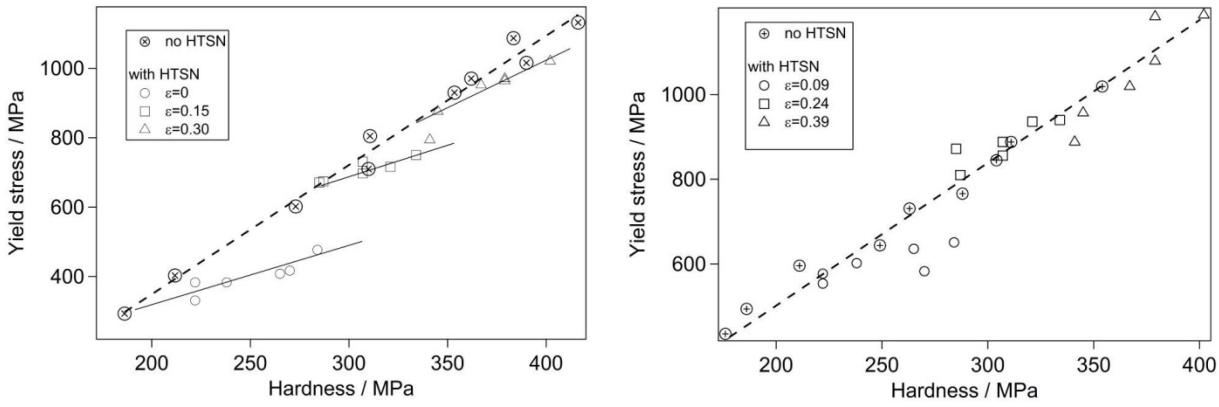

Figure 11: Yield stress for three levels of equivalent strain as a function of the hardness $HV_{2.0N}$. The dashed line indicates the straining/hardening that can be achieved by plastic deformation. a) experimental yield stress for each equivalent strain, b) stress corresponding to a strain 9% larger than the equivalent strain level.

The dashed line in Fig. 11a represents the relation between yield stress and hardness for the case of plastic deformation. This suggests that plastic straining is more effective in enhancing the yield stress than nitrogen dissolution. On the other hand, interstitial alloying is effective in enhancing the hardness. This difference is attributed to the nitrogen-induced changes in the work-hardening (Fig. 2b). As stated by Tabor [52], the representative strain involved in the determination of Vickers hardness by indentation is 8-10%. Accordingly, shifting the stress values in Fig. 11a to the values corresponding to strains of 0.09, 0.24 and 0.39 instead of 0, 0.15 and 0.30 yields a more or less linear relation as illustrated in Fig. 11b.

In addition nitrogen has a large impact on the Hall-Petch slope as determined for a Fe-18Cr-16Ni-10Mn austenitic steel in [53]. The EN 1.4369 alloy is the only one containing significant amounts of nitrogen in the as-received condition where the grain size is smallest. Using Hall-Petch slopes from [53] determined for nitrogen concentrations of 0.17 wt% and 0.54 wt%, which are the ones closest to the 0.23 and 0.45 wt% of the EN 1.4369 in the as-received and HTSN1 conditions, and the corresponding grain sizes (30 and 75 μm) (see Tables 2 and 3) gives a yield stress contribution for the as-received condition that is only about 25 MPa smaller than for the HTSN1 case, which explains the similar yield stress for these two samples. This interpretation is further supported by the hardness data in Fig. 3a which shows a clear difference between the annealed and solution nitrided conditions. The hardness indents are small compared to the grain size and the hardness values are therefore not affected.

The nitrogen dissolved into the three stainless steels by the HTSN treatment contributes to an important stabilization of austenite (cf. Fig. 5), such that the development of strain-induced martensite is effectively hindered in the investigated range of equivalent strains. Even though the present work concerns solution nitriding over the entire sample thickness, such that a uniform nitrogen-concentration profile is obtained over the sample thickness, the results can be transferred to surface engineering of stainless steels where the outer 1-2 mm (or less) is enriched by nitrogen to achieve a stabilization of austenite (or a local conversion of ferrite to austenite), combined with substantial hardening. Such a treatment is industrially applied as a finishing treatment [15,16], but could equally well be followed by additional surface engineering, as shot peening or low-temperature surface hardening by nitriding, carburizing or nitrocarburizing. For shot peening the enhanced austenite stability and higher strain hardening can be exploited, while for low-temperature surface hardening the sensitivity of the process for strain-induced martensite is prevented [[54,55]. The next section describes this aspect for HTSN followed by LTN.

4.2 Low-temperature nitriding

Low-temperature nitriding of the three austenitic stainless steels after HTSN and plastic deformation in partially dissociated ammonia gas atmosphere resulted in the formation of expanded austenite.

In previous research activities, it was shown that the development of strain-induced martensite upon deformation has a detrimental effect on the nitriding behaviour of stainless steels, while the increase in dislocation density in a completely austenitic structure has a negligible influence on the low-temperature treatment [34].

In the present case, all the materials after high temperature solution nitriding and plastic deformation remain austenitic, due to the austenite-stabilizing effect of the dissolved nitrogen.

For the selected experimental conditions, prior plastic deformation has no observable effect on the LTN response, neither on the morphology of the case nor on the nitrogen distribution in the expanded austenite zone. Furthermore, and perhaps most importantly, no indications for the presence of CrN were observed with X-ray diffraction or reflected-light microscopy. Such CrN precipitation, which is generally observed during low temperature nitriding of deformed AISI 316 and AISI 304L, is detrimental for the corrosion resistance of the alloy, because it is associated with local Cr depletion. Absence of dark staining in the micrographs in Figs. 6 and 9 strongly suggests that such Cr depletion has not occurred and that the expanded austenite cases have superior electrochemical properties as compared to the substrate, which is confirmed in a separate study [56].

The present results confirm that nucleation of CrN and associated Cr depletion as observed in deformed stainless steels is not the immediate result of energetically favourable nucleation of CrN on dislocations in austenite, but necessitates the presence of strain-induced martensite (ferrite). An energetically favourable orientation relation between the crystal structures of ferrite and CrN [57–59] is held responsible for this. For all the studied materials, absence of strain-induced martensite effectively prevents the nucleation of CrN in expanded austenite for the investigated processing temperatures.

5 Conclusions

Three different commercially available stainless steels grades (AISI 316, AISI 304L and EN. 1.4369) were subjected to high temperature solution nitriding treatments. The resulting nitrogen contents depend on the composition of the alloys and the applied conditions used in the high temperature solution nitriding process and can be predicted by assuming thermodynamic equilibrium between the various steels and the applied nitrogen pressure. The dissolution of nitrogen in the stainless steel matrix resulted in a significant improvement of, in particular, the hardness, but also the yield stress of the steels, without impairing the toughness. Moreover, the dissolution of nitrogen effectively stabilized the austenitic phase and no strain-induced martensite developed on subsequent deformation.

The homogenous nitrogen-enriched stainless steels obtained by solid solution nitriding, were subjected to plastic deformation and subsequent low-temperature nitriding. The low-temperature nitriding process led to the formation of an expanded austenite case.

The absence of strain-induced martensite has a beneficial influence on the nitriding behavior. The case depth is independent of the steel quality, the degree of deformation and nitrogen content after solid solution nitriding at high temperature. CrN precipitation was avoided, hereby maintaining the stainless properties of the steel.

The combination of the two treatments, solution nitriding and low-temperature nitriding enables to improve the mechanical properties of bulk and surface for the selected commercially available alloys.

Acknowledgements

For the present research work, the authors gratefully acknowledge the Research Fund for Coal and Steel for the financial support to the PressPerfect project. Furthermore the authors would like to thank Sandvik Materials Technology for providing part of the materials used during the investigation. High temperature solution nitriding of the stainless steels was performed by Expanite A/S.

References

[1] M.O. Speidel: *HNS 88 Lille (France)*, The insitute of Metals, London, 1989, p. 92.
[2] K. Frisk M. Kikuchi, M. Kajihara: *HNS 88 Lille (France)*, The insitute of Metals, London, 1989, p. 63.
[3] M.L.G. Byrnes, M. Grujicic, and W.S. Owen: *Acta Metall.*, 1987, vol. 35, pp. 1853–62.
[4] E. Werner: *Mater. Sci. Eng.*, 1988, vol. 101, pp. 93–98.
[5] J.W. Simmons: *Mater. Sci. Eng. A*, 1996, vol. 207, pp. 159–69.
[6] L.Å. Norström: *Met. Sci.*, 1977, vol. 11, pp. 208–12.
[7] Y. Takahashi, K. Yoshida, M. Shimada, and E. Tada: *Adv. Cryog. Eng. Mater.*, 1982, vol. 28, pp. 73–81.
[8] R.P. Reed: *JOM*, 1989, vol. 41, pp. 16–21.
[9] J.R. Kearns and H.E. Deverell: *Mater. Perform.*, 1987, vol. 26, pp. 18–28.
[10] M. Janik-Czachor: *Corrosion*, 1975, vol. 31, pp. 394–98.
[11] J.J. Eckenrod and C.W. Kovach: *Properties of Austenitic Stainless Steels Their Weld Metals*, American Society for Testing and Materials (ASTM), Philadelphia, 1979, pp. 17–41.
[12] M.O. Speidel: *Materwiss. Werksttech.*, 2006, vol. 37, pp. 875–80.
[13] A.H. Satir-Kolorz and H.K. Feichtinger: *Zeitschrift Fuer Met. Res. Adv. Tech.*, 1991, vol. 82, pp. 689–97.
[14] G. Stein and I. Hucklenbroich: *Mater. Manuf. Process.*, 2004, vol. 19, pp. 7–17.
[15] H. Berns: *ISIJ Int.*, 1996, vol. 36, pp. 909–14.
[16] H. Berns and S. Siebert: *ISIJ Int.*, 1996, vol. 36, pp. 927–31.
[17] T.L. Christiansen and M.A.J Somers: *Int. J. Mater. Res. Former. Zeitschrift Fuer Met.*, 2009, vol. 100, pp. 1361–77.
[18] T. Bell: *Key Eng. Mater.*, 2008, vol. 373-374, pp. 289–95.
[19] H. Dong: *Int. Mater. Rev.*, 2010, vol. 55, pp. 65–98.
[20] Z. Yu, X.I. Xu, L. Wang, J. Qiang, and Z. Hei: *Surf. Coatings Technol.,* 2002, vol. 153, pp. 125–30.
[21] M.K. Lei and X.M. Zhu: *Surf. Coatings Technol.*, 2005, vol. 193, pp. 22–28.
[22] Y. Sun and T. Bell: *Wear*, 1998, vol. 218, pp. 34–42.
[23] C.X Li and T. Bell: *Corros. Sci.*, 2004, vol. 46, pp. 1527–47.
[24] Committee of Stainless Steel Producers: *Review of the Wear and Galling Characteristics of Stainless Steels*, American Iron and Steel Institute, Washington, 1978.
[25] M. A.J Somers and T.L. Christiansen: *J. Phase Equilibria Diffus.*, 2005, vol. 26, pp. 520–28.
[26] T. Bell: *Surf. Eng.*, 2002, vol. 18, pp. 415–22.
[27] ASTM International: *Standard Test Methods for Tension Testing of Metallic Materials [Metric]*, United States, 2004, p. E 8M – 04.
[28] T. L. Christiansen, T. S. Hummelshøj, and M.A.J. Somers: WO2012 146254-A1, 2012.
[29] T. L. Christiansen, T. S. Hummelshøj, and M.A.J. Somers: WO2013159781-A1, 2013.
[30] J.O. Andersson, T. Helander, L. Höglund, P. Shi, and B. Sundman: *Calphad*, 2002, vol. 26,

pp. 273–312.
[31] K. Frisk: *Metall. Trans. A*, 1990, vol. 21, pp. 2477–88.
[32] K. Frisk: *Calphad*, 1991, vol. 15, pp. 79–106.
[33] K. Frisk: *Mater. Sci. Forum*, 1999, vol. 318-320, pp. 95–102.
[34] F. Bottoli, G. Winther, T.L. Christiansen, and M.A.J. Somers: *Metall. Mater. Trans. A*, 2015, vol. 46, pp. 2579–90.
[35] F.A.P. Fernandes, T.L. Christiansen, and M.A.J. Somers: *Proc. 28th Int. Conf. Surf. Modif. Technol.*, Valardocs, Tampere, Finland, 2014, pp. 223–33.
[36] C. Blawert, B.L. Mordike, G.A. Collins, K.T. Short, Y. Jiraskova, O. Schneeweiss, and V. Perina: *Surf. Coatings Technol.*, 2000, vol. 128-129, pp. 219–25.
[37] C. Blawert, H. Kalvelage, B.L. Mordike, G.A. Collins, K.T. Short, Y. Jirásková, and O. Schneeweiss: *Surf. Coatings Technol.*, 2001, vol. 136, pp. 181–87.
[38] Z. Cheng, C.X. Li, H. Dong, and T. Bell: *Surf. Coatings Technol.*, 2005, vol. 191, pp. 195–200.
[39] T.L. Christiansen and M.A.J. Somers: *Surf. Interface Anal.*, 2005, vol. 21, pp. 445–55.
[40] J. Oddershede, T.L. Christiansen, K. Ståhl, and M.A J Somers: *Scr. Mater.*, 2010, vol. 62, pp. 290–93.
[41] J. Oddershede, T.L. Christiansen, K. Ståhl, and M.A.J. Somers: *Steel Res. Int.*, 2011, vol. 82, pp. 1248–54.
[42] D.H. Jack and K.H. Jack: *Mater. Sci. Eng.*, 1973, vol. 11, pp. 1–27.
[43] K. H. Jack: *Acta Crystallogr.*, 1952, vol. 5, pp. 404–11.
[44] K. H. Jack: *R. Soc.*, 1948, vol. 195.
[45] K. H. Jack: *Acta Crystallogr.*, 1950, vol. 3, pp. 392–94.
[46] H. Okamoto: *J. Phase Equilibria*, 1992, vol. 13, pp. 543–65.
[47] K.J. Irvine, R. J. Llewellyn, and F. B. Pickering: *JISI*, 1961, vol. 199, p. 153.
[48] Y. Nakada and A.S. Keh: *Acta Metall.*, 1968, vol. 16, pp. 903–14.
[49] Y. Nakada and A.S. Keh: *Metall. Trans.*, 1971, vol. 2, pp. 441–47.
[50] A.H. Cottrell and B.H. Bilby: *Proc. Phys. Soc. Sect. A*, 1948, vol. 62, pp. 49–62.
[51] J.R. Cahoon, W.H. Broughton, and A.R. Kutzak: *Metall. Trans.*, 1971.
[52] D. Tabor: *Proc. R. Soc. A.*, 1948, vol. 192, p. 247.
[53] V.G. Gavriliuk, H. Berns, C. Escher, N.I. Glavatskaya, A. Sozinov, and Yu.N. Petrov: *Mater. Sci. Forum*, 1999, vol. 318-320, pp. 455–60.
[54] B.N. Mordyuk, G.I. Prokopenko, M.A. Vasylyev, and M.O. Lefimov: *Mater. Sci. Eng. A*, 2007, vol. 458, p. 253–61.
[55] T.S. Wang, B. Lu, M. Zhang, R.J. Hou, and F.C. Zhang: *Mater. Sci. Eng. A*, 2007, vol. 458, pp. 249–52.
[56] F. Bottoli, M. S. Jellesen, T.L. Christiansen, G. Winther, and M.A.J. Somers: *Electrochemical characterization and crevice corrosion performance of high temperature solid-solution nitrided and low-temperature nitrided austenitic stainless steel.*, Lyngby, Denmark, 2015
[57] M.A.J. Somers, R.M. Lankreijer, and E.J. Mittemeijer: *Philos. Mag. A*, 1989, vol. 59, pp. 353–78.
[58] P.M. Hekker, H.C.F. Rozendaal, and E. J. Mittemeijer: *J. Mater. Sci.*, 1985, vol. 20, pp. 718–29.
[59] P.C. Van Wiggen, H.C.F. Rozendaal, and E.J. Mittemeijer: *J. Mater. Sci.*, 1985, vol. 20, pp. 4561–82.

9 Paper IV: Electrochemical characterization and crevice corrosion performance of high temperature solid-solution nitrided and low-temperature nitrided austenitic stainless steel

Federico Bottoli, Morten S. Jellesen, Thomas L. Christiansen, Grethe Winther, Marcel A.J. Somers
Technical University of Denmark, Department of Mechanical Engineering, Produktionstorvet b.425, 2800 Kgs. Lyngby, Denmark

Article submitted to Surface and Coatings Technology on the December 4th, 2015

Electrochemical characterization and crevice corrosion performance of high temperature solution-nitrided and low-temperature nitrided austenitic stainless steel

Federico Bottoli, Morten S. Jellesen, Thomas L. Christiansen, Grethe Winther, Marcel A.J. Somers

Technical University of Denmark, Department of Mechanical Engineering,

Produktionstorvet b.425, 2800 Kgs. Lyngby, Denmark

Keywords

High nitrogen steel, low-temperature nitriding, high-temperature solution nitriding, corrosion, pitting, crevice.

Abstract

Three commercially available stainless steels grades (AISI 316, AISI 304L and EN 1.4369) were subjected to high temperature solution nitriding and low-temperature nitriding in order to dissolve nitrogen in the bulk (up to approx. 0.65 wt-%) and at the surface (up to approx. 13 wt-%) respectively. The corrosion properties of the different steels before and after the bulk and surface treatments were studied with potentiodynamic polarization tests in a 0.1 M NaCl solution and crevice corrosion immersion tests in 3 wt-% Fe_3Cl solution.

Nitrogen addition in the bulk proved to have a beneficial effect on the pitting resistance of the alloy although no significant improvement in the crevice corrosion resistance was recorded. The formation of single phase nitrided layer of expanded austenite at the material surface through low-temperature nitriding resulted in considerable improvement of the pitting and crevice corrosion properties of the steels.

1 Introduction

Austenitic stainless steels are well known for their excellent corrosion resistance due to the formation of a dense chromium oxide layer at the surface. This passive film however, is susceptible to local breakdown, especially in chloride containing solutions, thereby causing localized corrosion such as pitting and crevice corrosion [1].

The resistance to localized corrosion in stainless steels can be augmented by the addition of elements such as Cr, Mo and in particular N [1]. For this reason, high nitrogen steels (HNS) have been considered as a substitute for conventional stainless steels for applications where high corrosion resistance is required [2].
Alloying with nitrogen in fact offers several advantages compared to other alloying elements in terms of corrosion and mechanical properties. Nitrogen provides a stabilization of austenite, thereby reducing the amount of expensive nickel required for minimizing the risk of ferrite and/or martensite upon solidification or deformation [3]. Furthermore, nitrogen provides an important increase in the yield and tensile strength, without sacrificing toughness [4–7].
The dissolution of nitrogen in austenitic stainless steels leads to a significant improvement of the crevice and pitting corrosion in aqueous solutions containing chloride ions [8–10]. Several hypotheses have been put forward to explain this behavior: (1) the presence of a high concentration of nitrogen at the steel/passive film surface stabilizing the passive film and suppressing dissolution [11–15]; (2) formation of NH_4^+ ions at the film/solution interface, neutralizing the acidity in the pit and thus promoting repassivation [16,17]; (3) formation of NO_3^- (nitrate) ions would result in improved pitting resistance [18]; (4) the austenite-stabilizing effect of nitrogen [3,4].
Despite the obvious advantages, a major obstacle to large scale application of high nitrogen stainless steels is related to their production. The solubility of nitrogen in liquid stainless steel is limited at atmospheric pressure [19]. Hence, HNS production requires high-pressure melting technologies or the utilization of powder metallurgical production techniques [3,4,20].
On the other side, the solubility of nitrogen in the solid state is appreciably higher than in the liquid state [21]. Accordingly, post-solidification gas treatment, such as solution nitriding followed by rapid (gas) quenching [22,23] can be used to dissolve a controlled amount of nitrogen in existing steel grades. This process can be used on austenitic stainless steel grades, in order to increase the austenite stability and prevent strain-induced martensite formation [24], but also on duplex and ferritic stainless steels in order to transform ferrite and/or stabilize the austenite phase in the nitrogen enriched region [25,26].
Low-temperature surface treatment, such as low-temperature nitriding can be used to improve the surface properties of the material. This thermochemical treatment allows the dissolution of a very high amount of N (up to 38 at-%) into the materials surface, and leads to the formation of a supersaturated solid solution referred to as expanded austenite [27] (or S-Phase [28,29]). The formation of an expanded austenite case during the low-temperature nitriding (LTN) at a temperature where the precipitation of CrN from supersaturated solid solution is avoided, results in a significant improvement of the resistance to galling and improves the pitting corrosion resistance as well as a spectacular increase in the wear and fatigue resistance of the component [30–36].
In the present work, high-temperature solution nitriding (HTSN) and low-temperature nitriding (LTN) are applied to three commercial stainless steel grades in order to dissolve nitrogen in the bulk and the surface, respectively. The nitriding response of the steels was studied with light-optical microscopy and X-ray diffraction. The pitting and crevice corrosion performance resulting after the nitriding treatments were investigated with potentiodynamic measurements, immersion tests and scanning electron microscopy (SEM).

2 Experimental

2.1 Materials

The compositions of the alloys used in this study (AISI 316, AISI 304L and EN 1.4369) are reported Table I.

Table I: Chemical composition AISI 316, AISI 304L and EN 1.4369 in wt-% as provided by the suppliers, Lemvigh Muller and Sandvik Materials Technology.

	C	Si	Mn	Cr	Ni	Mo	N
AISI 316	0.07	0.4	1.6	17.0	10.55	2.0	0.05
AISI 304L	0.03	0.32	1.78	18.28	8.08	-	-
EN 1.4369	0.09	0.74	5.92	18.58	7.11	0.18	0.23

EN 1.4369 was delivered by Sandvik Materials Technology in annealed condition. AISI 316 and AISI 304L were annealed at 1323K (1050 °C) for 300s in a horizontal tube furnace with a protective argon atmosphere. Each steel grade was subjected to four different treatments: three high temperature solution nitriding treatments (HTSN) and one low-temperature nitriding surface treatment (LTN).

2.1.1 High Temperature Solution Nitriding (HTSN)

High temperature gas solution nitriding is a commercial process provided by the company Expanite A/S [37,38]. Three different N_2 partial pressures were applied at 1423K (1150°C) for 4h: 0.3 bar for HTSN1, 0.6 bar for HTSN2 and 0.9 bar HTSN3. Each batch contained the three steel grades. The duration of the treatments resulted in full homogenization and a uniform nitrogen concentration throughout the sample, indicating equilibrium between gas atmosphere and solid state. High pressure gas quench was applied to avoid formation of nitride precipitates during cooling. The nitrogen contents in the steels after treatment, as adjusted by the various applied nitrogen partial pressures, were measured with a LECO TN500 nitrogen analyzer and are given in Table II. The variation in nitrogen concentration for the three different steel grades is due to the different chemical compositions of the starting material [4]. Our previous work has demonstrated that the nitrogen content in the alloys can be predicted accurately by assuming equilibrium between nitrogen in the gas phase during solution nitriding and nitrogen in austenite [24].

Table II: Nitrogen content in wt-% determined with LECO TN 500 analyser after solid solution treatment

	Nitrogen Content (wt-%)		
	HTSN1	**HTSN2**	**HTSN3**
AISI 316	0.306±0.001	0.407±0.002	0.448±0.002
AISI 304L	0.363±0.002	0.485±0.001	0.531±0.001
EN 1.4369	0.450±0.001	0.594±0.001	0.646±0.003

2.1.2 Low-temperature nitriding

Samples with dimensions 5x2cm^2 were obtained from the annealed steel grades. Their surfaces were ground, polished until 3μm finish and subsequently electro-polished in a "Struers Polectrol" apparatus using a "Struers electrolyte A2" with an applied potential of 30V and a current density of 2A/cm^2 to remove any deformation induced by grinding before low temperature nitriding.
Low-temperature nitriding was carried out in a LAC annealing furnace model PKRC 55/09 retrofitted for gaseous nitriding under gas circulation. The sample surface was activated in-situ in order to enable the low-temperature surface hardening. The LTN process was performed for all samples in the same batch at 703K (430 °C) for 20h.

2.2 Electrochemical measurements

Potentiodynamic polarization measurements were performed at room temperature using an ACM potentiostat (GillAC). The surface of the annealed and HTSN treated materials was ground and polished to a mirror like surface before after heat treatment, and prior to electrochemical testing. The surface of the steel sample was ground and polished before low-temperature nitriding and tested in the as-treated condition in order not to alter mechanically the surface after the thermochemical treatment. A flat cell set-up with an exposed area of 0.95 cm^2 of the working electrode (sample) was used for the measurement. An Ag/AgCl electrode and a Pt wire were employed as reference and counter electrode, respectively. The open circuit potential (OCP) was monitored for 30 min prior to conducting each polarization scan. The polarization scans were conducted in naturally aerated 0.1 M NaCl solution of pH 5.2 ± 0.3. The current was measured as a function of the applied potential, which was changed from -0.2 V Ag/AgCl below OCP to +1 V above OCP with a scan rate of 60mV/s. Each scan was repeated at least 6 times to ensure reproducibility.

2.3 Crevice corrosion immersion tests

The crevice corrosion performance of the materials was evaluated by immersion tests according to the ASTM standard G48-11 [39]. A hole of 6 mm was drilled in the centre of 1 mm thick samples with dimensions 5x2cm^2. Two teflon crevice washers were applied on the two parallel flat surfaces of the sample and tightened with bolts. Immersion tests were carried out at room temperature for 168h (1week) in a 3 wt-% Fe_3Cl solution of pH~1. The experiments were repeated twice in order to confirm the reproducibility of the results.

2.4 Microstructure and materials characterization

The microstructures of the samples after HTSN and LTN were investigated in cross-section with reflected light microscopy. The samples were ground, polished and etched for 8s with Kalling´s reagent no. 1.

X-ray diffractometry for phase identification was carried out with the Bragg-Brentano symmetric setting in a Bruker D8 AXS X-ray diffractometer equipped with Cr-anode and Göbel mirror in the incident beam. The step size was 0.03° 2θ and the counting time was 4s per 2θ step.

Microhardness indentation measurements were performed on a Future-Tech FM700 instrument using a load of 0.05 N for the evaluation of the microhardness of the "case".

The surface morphology of the samples after the potentiodynamic polarization measurements was investigated with scanning electron microscopy, using a Jeol JSM-500 microscope at an acceleration voltage of 10 kV.

3 Results

3.1 Characterization of the low-temperature nitrided samples

Low-temperature nitriding was performed on the three selected stainless steel grades in the annealed condition. The optical micrographs in Fig. 1 show that a homogenous pore-free case of expanded austenite has formed during the low-temperature surface treatment. The thickness of the obtained case is 11μm for the three different selected alloys and appears virtually unattacked by the etching agent, suggesting a better corrosion resistance than the underlying substrate. In all cases, the hardness of the layer was measured to be 1200 $HV_{0.05N}$.

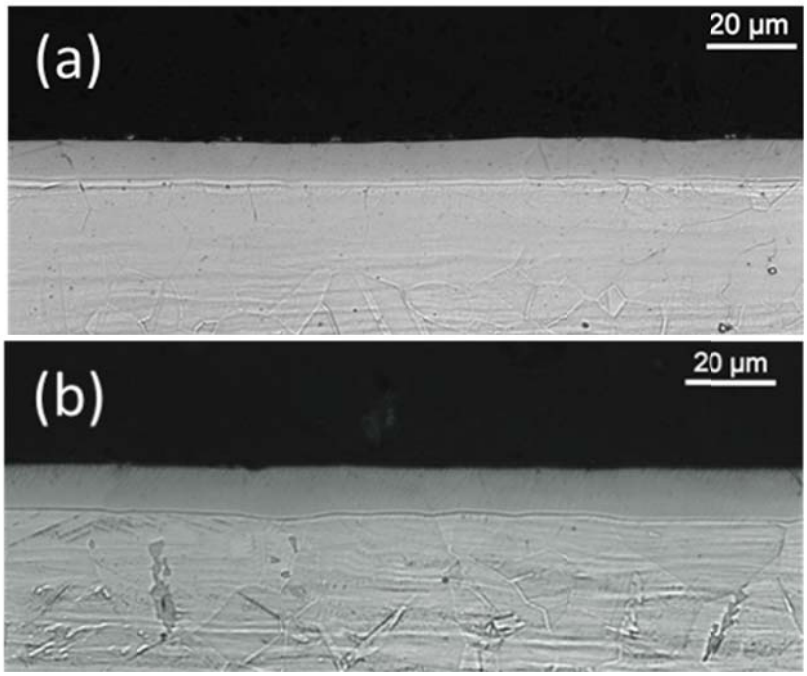

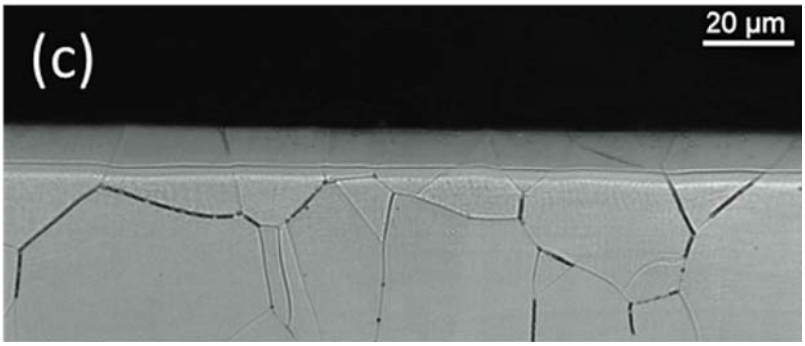

Figure 1: Optical Micrographs on low-temperature nitrided stainless steels: (a) AISI 316, (b) AISI 304L and (c) EN 1.4369 after etching with Kalling´s reagent no. 1 for 8 seconds.

At the case core transition a thin carbon-enriched zone is present for AISI 316 (Fig. 1a) and EN 1.4269 (Fig. 1c), as was verified with GD-OES. This is a consequence of carbon, originally present in these alloys, being pushed ahead of the advancing nitriding front [24].

X-ray diffraction analysis confirms the formation of expanded austenite. In the diffractograms (Fig. 2), the expanded austenite peaks and peaks of the generating austenitic substrate are clearly present for the three treated steels. The expanded austenite peaks are shifted to lower 2θ position as compared to the parent austenitic peaks, because of the (constrained) lattice expansion due to nitrogen dissolution. No evidence for the presence of CrN was found in neither of the samples, thereby confirming that the selected LTN process parameters avoid precipitation of nitrides.

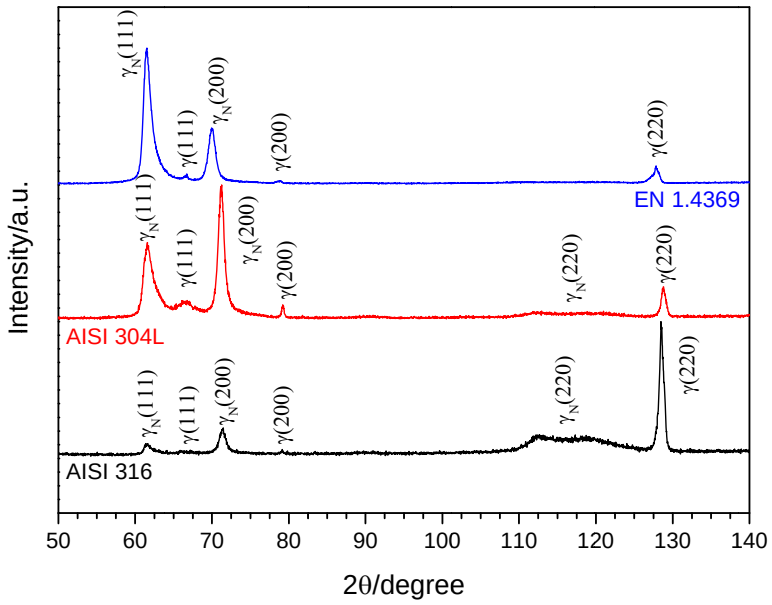

Figure 2: X-ray diffractograms of the materials after LTN process.

3.2 Electrochemical Testing

Polarization curves in 0.1M NaCl solution of the different stainless steel grades subjected to the different treatments (annealed, HTSN and LTN) are given in Fig. 3. In general it is observed that for AISI 316 and

AISI 304L, the absorption of nitrogen in the bulk, through HTSN, or at the material´s surface, LTN, causes a shift of the corrosion potential to a lower or a more negative value.

For EN 1.4369, where nitrogen is already present in the as-received alloy, the corrosion potential, within the experimental accuracy, remains constant.

For the samples AISI 316 and AISI 304L in annealed condition the pitting potential was measured at 650 mV and 400mV, respectively. These curves present a sudden and rapid increase of the anodic current indicating breakdown of the passive film and pit initiation. For the annealed EN 1.4369 the current density increase happens at 250mV but with a less sudden increase as compared to compared to AISI 316 and AISI 304L, indicating that the mechanism for pitting is more directed towards dissolution of inclusions rather than passive film breakdown. EN 1.4369 contains a higher amount of Mn than AISI 316 and AISI 304L, previously reported to have a detrimental effect on the pitting corrosion resistance [40].

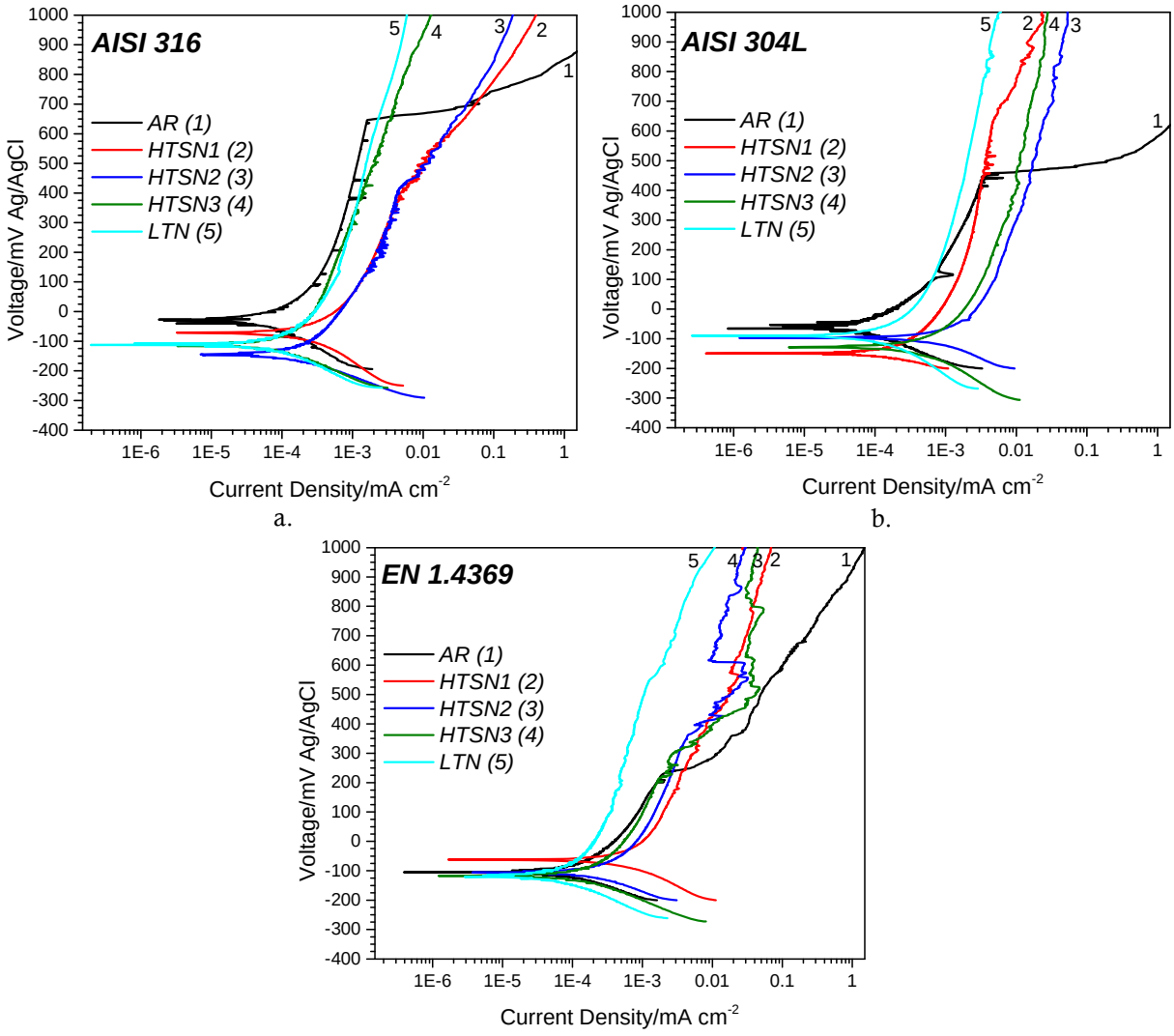

Figure 3: Polarization curves for the AISI 316 (a), AISI 304L (b) and EN 1.4349 in annealed condtion (AR), after HTSN treatment and LTN surface treatment.

The enhanced dissolution of nitrogen in the stainless steel matrix by HTSN results in a significant change in the corrosion behavior of all the materials tested. In the AISI 316 (Fig. 3a), after HTSN treatments, it is not possible to observe a sudden increase in the current density due to the breakdown of the passive film in the potential scan region, up to 1000 mV Ag/AgCl. However, after reaching approximately 150 mV Ag/AgCl, oscillations in the anodic current are observed, which possibly indicate pit initiation and fast re-passivation.

A similar trend is observed for AISI 304L: as the nitrogen content increases, it is no longer possible to identify a potential where passive film breakdown happens, indicating that the amount of nitrogen promotes passivation of the stainless steel.

In the solution nitrided EN 1.4369 samples increased current density is observed at similar potential values as for the annealed material. At potentials above 600 mV Ag/AgCl a reduction of anodic current can be seen, which indicate a decreased dissolution of inclusions. The Pourbaix diagram for Mn [41] shows how an increase of pH increases the passivation region and it is a possibility that the nitriding treatment locally neutralizes the acidity in the pit and thereby decreases the dissolution of Mn enriched inclusions.

In all LTN cases, the current density is similar or lower than untreated stainless steel. No indications of passive film breakdown are observed for any of the LTN treated samples. The polarization curves of the three LTN treated steels show less oscillations than for the HTSN treated samples.

Secondary electron images show the morphology of the surface of the AISI 316 after the potentiodynamic measurements. Microscopic examination of the AISI 316 confirmed passive film breakdown and the presence of large pits (Fig. 4), consistent with the polarization curve AR (1) in Fig. 3a.

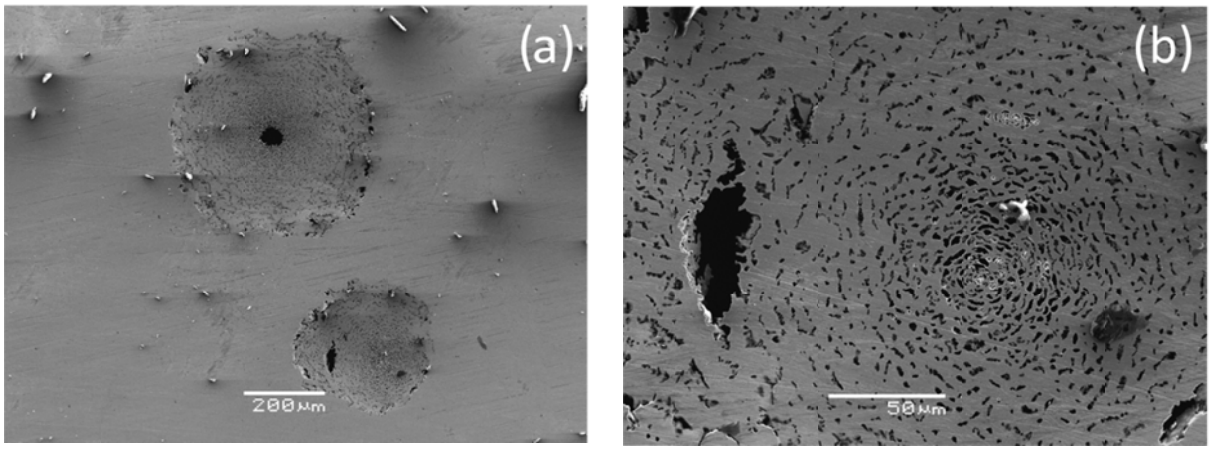

Figure 4: SEM images showing the pits formed in the annealed AISI 316 after the potentiodynamic measurements.

The HTSN treated samples hardly show any evidence of localized corrosion detected by visual inspection. Fig. 5 shows the surface morphology of the AISI 316 samples after HTSN treatment and polarization tests. Scanning electron microscopy investigation shows the presence of small pits, which confirms the hypothesis that pits do form, but their growth appears impaired by the repassivation due to the nitrogen alloying. The pit formation and their subsequent repassivation is consistent with the oscillation in the

anodic current recorded for these samples during the polarization measurements (Fig. 3a for HTSN samples).

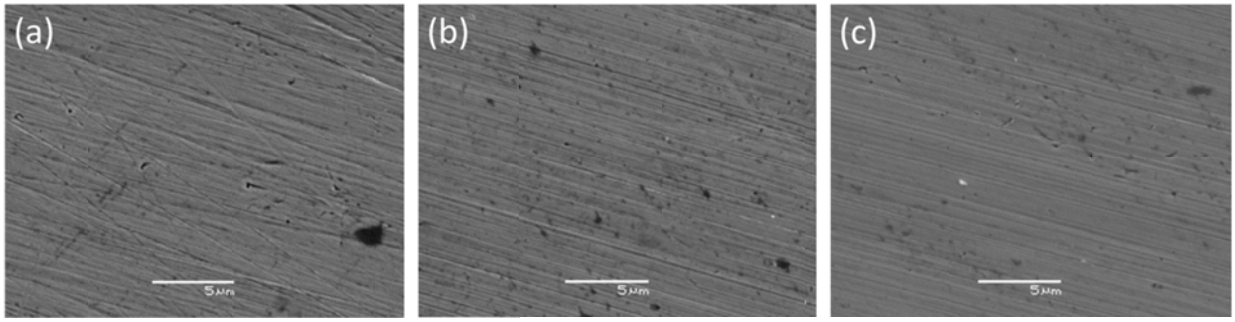

Figure 5: SEM images showing the surface morphology of the AISI 316 HTSN treated samples after the potentiodynamic measurements: (a) HTSN1, (b) HTSN2, (c) HTSN3.

The surface morphology after the potentiodynamic measurements of the AISI 316 low-temperature nitrided is shown in Fig. 6. Naked eye visual inspection did not reveal any large pits and the SEM investigation shows no indication of localized corrosion such as pitting or grain boundary corrosion.

However, it is possible to observe that the surface morphology of the nitrided samples differs greatly from the as-received and HTSN-treated samples (Fig. 6a). The low-temperature nitrided sample has a significantly increased surface roughness; this is a direct consequence of the nitriding process The plastic deformation is evidenced by the slip lines in Fig. 6b and, associated lattice rotation, induced by the enormous composition-induced strains as a consequence of the volume expansion caused by the high amount of dissolved nitrogen [42]. The increase in surface roughness implies that the "exposed" area through which the current density shown in Fig.1 is measured, is larger than the nominal (projected) area used in the calculation of the polarization curves. Hence, taking this effect into account, the current densities for the LTN samples will have an actual lower current density than the nominal values depicted in the polarization curves (Fig. 3).

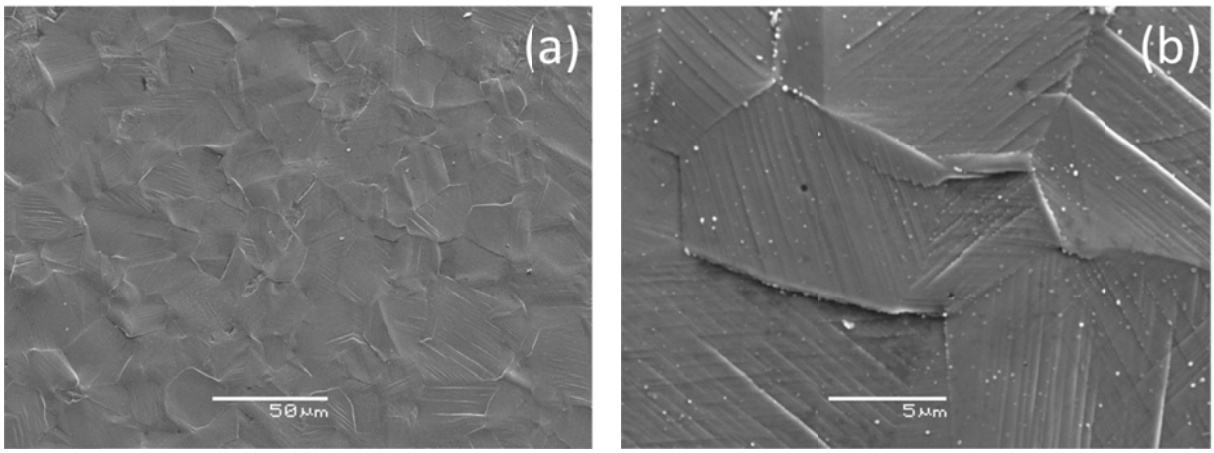

Figure 6: Secondary electron Images of the AISI 316 LTN after the potentiodynamic measurements.

3.3 Crevice Corrosion Performance Testing in Fe_3Cl Solution

Immersion tests of the three different steels in the different processing conditions were performed in a 3 wt-% Fe_3Cl pH≈1 solution. The samples were exposed to the acid environment for 168 hours. In Fig. 7 macroscopic images of the crevice corrosion tested samples are collected.

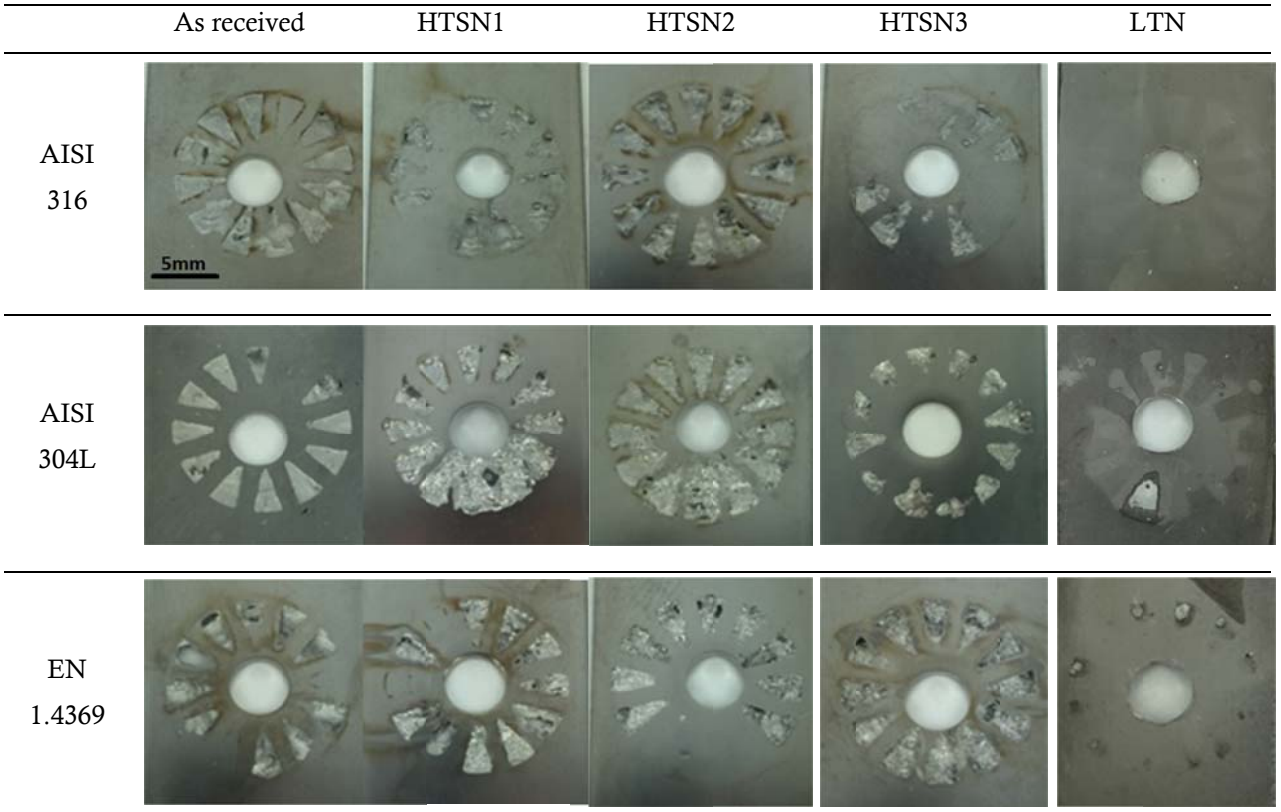

Figure 7: Results of crevice corrosion tests of three stainless steel qualities after various treatments. The tests were performed in a 3 wt-% Fe_3Cl pH≈1 solution for 168 h.

Generally, the steels in annealed and HTSN treated condition show severe crevice corrosion attack. No obvious difference can be discerned between these samples, indicating that, for the severe experimental conditions applied here, it is not possible to conclude whether the HTSN treatment has contributed to an improvement of the crevice corrosion performance. On the other hand, the optical appearance of the low-temperature nitrided samples shows a dramatic improvement of corrosion attack in the crevices between the sample and the teflon washers.

In Fig. 8 the weight loss of the samples after the immersion tests is displayed. Consistent with the images in Fig. 7 no trend is observed in the weight loss of the as-received and HTSN treated samples. The ranking of the three steels remains unaltered by dissolving nitrogen in austenite and within experimental accuracy no reduction in weight loss is observed after HTSN treatment. In contrast, the dissolution of a "colossal" amount of nitrogen (up to 38 at-%[43–45]) into the stainless steel surface by low-temperature nitriding leads to a significant reduction of the weight loss in the crevice corrosion performance test, consistent with the images in Fig.7 and the above mentioned interpretation of the potentiodynamic results in Fig. 3.

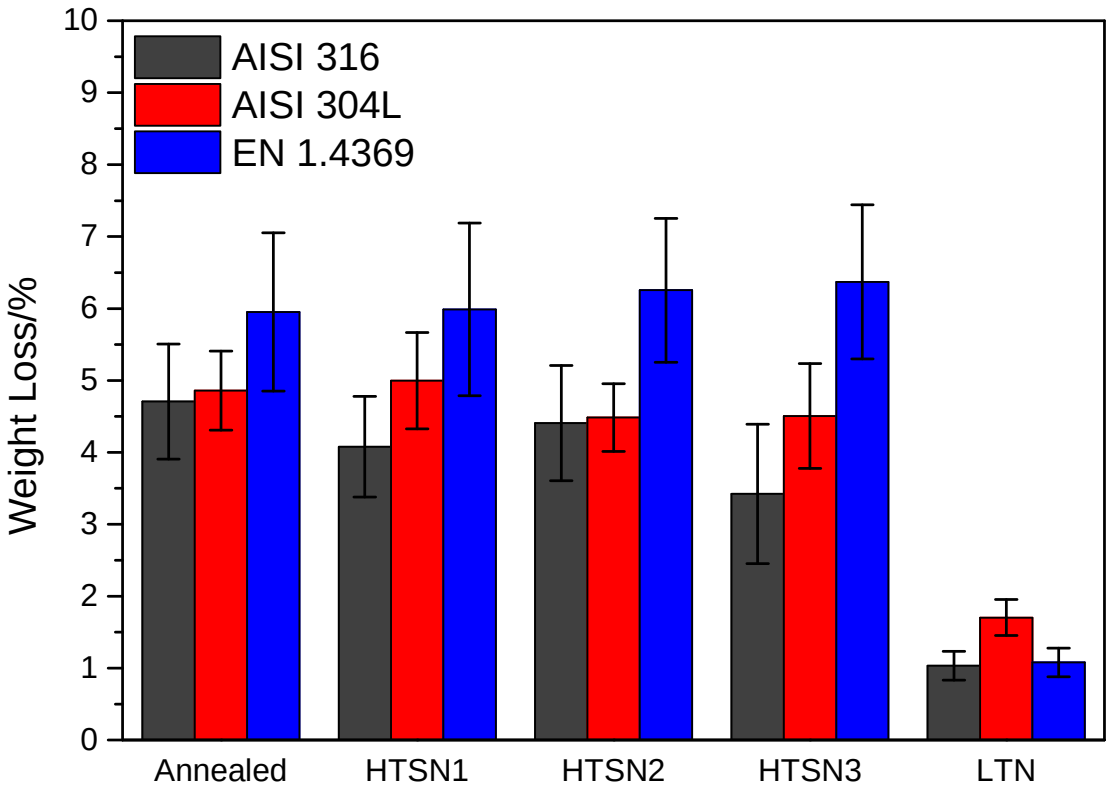

Figure 8: Weight loss after crevice corrosion immersion test for the three investigated stainless steels after different treatments.

4 Discussion

Stainless steels derive their excellent corrosion performance from the presence of a self-healing chromium-based (oxy)hydroxide film at the material´s surface. Nevertheless, stainless steels can suffer from localized corrosion, or pitting, which may well be negligible in terms of weight loss, but often is detrimental. The resistance against localized corrosion can be improved by adding more of the substitutional alloying elements Cr and Mo. In particular the addition of interstitial nitrogen is most efficient in increasing the pitting resistance equivalent number (PREN=%Cr + 3.3(%Mo) + 16(%N)) [46].

In the present experimental activity, three commercially available stainless steel grades were high-temperature solution nitrided and low-temperature nitrided to investigate the pitting and crevice corrosion performance for different nitrogen concentrations in the bulk and at the surface. Compared to the solution nitriding treatment, low-temperature nitriding allows dissolution of up to 38 at-% nitrogen into the material´s surface [43–45]. Assuming that the equation given above is valid also for the very high nitrogen contents, the PREN numbers for the investigated treatments are given in Table III.

Table III: PREN numbers calculated for the investigated HTSN and LTN treatments of the various alloys

	Annealed	**HTSN1**	**HTSN2**	**HTSN3**	**LTN**
AISI 316	24.4	28.5	30.1	30.8	≈180
AISI 304L	18.3	24.1	26.1	26.8	≈180
EN 1.4369	22.8	26.4	28.7	29.5	≈180

For each of the investigated alloys after HTSN, the PREN number increases gradually with the increasing concentration of dissolved nitrogen. On the other hand, due to the colossal amount of nitrogen at the surface after LTN, this value increases dramatically to approx. 180 for all the investigated alloys, since the nitrogen has a much stronger effect (factor 16 in the equation).

The present experimental results confirm an increase of the pitting potential with an increase in nitrogen content, and thus the PREN number. In particular for the low-temperature nitrided material, no evidence of pitting after polarization was found for the investigated potential range.

These results prove that the addition of nitrogen allows an increase of the pitting potential and that it has an important role in repassivation. In this respect the solution nitriding treatment has the most pronounced effect on AISI 304L. The polarization curves in Fig. 3 show that the dissolution of nitrogen in AISI 304L and AISI 316 leads to a more stable passive layer. The solution nitrided samples with lowest nitrogen content for AISI 316 resulted in increased anodic current density (both curves 2 and 3 for a potential beyond 450 mV).

Manganese in stainless steels is proved to have a detrimental effect on the pitting resistance of the alloy [40]. EN 1.4369 in as received condition contained a higher amount of manganese compared to AISI 304L and AISI 316 but contained already a certain amount of N which allows an improvement of the resistance to localized attacks. From the polarization curves of EN 1.4369 in annealed condition it was not possible to observe the characteristic feature for passive film breakdown, as in the other two steel classes, but rather a continuous dissolution which indicates that the mechanism for pitting is more directed towards Mn inclusions dissolution than passive film breakdown. As a consequence of nitrogen addition (HTSN treatment) the increase in current density is observed at similar potential values as for the annealed material but after a certain value of potential the current is reduced indicating a significant decrease in the dissolution rate.

These results are consistent with the several theories showing that nitrogen locally neutralizes the acidity in the pit suppressing its growth and provoking an increase of pH which can lead to an increase the passivation region for Mn [41].

For all steel classes, a high concentration of nitrogen at the material's surface, obtained through the low-temperature nitriding process, do not reveal any sign of pit formation as confirmed also by SEM investigations (Fig.6).

These results are in agreement with what has been found in previous research activities [33,47,48] and are believed to be due to the high concentration of nitrogen at the interface between the passive film and the steel, which suppresses further dissolution of the metal [11–13].

The effect of nitrogen addition on the current density in the anodic region of the polarization curves was widely published in the literature; so far controversial results have been reported since many researchers claim that it provokes a decrease of the current density whereas others claim that it has no or the opposite effect [10,48–54].

In the case examined (Fig. 3) for neither of the investigated alloys it is possible to observe a clear trend of the current density with the increasing nitrogen content.

In general high nitrogen steels exhibit better crevice corrosion performance than stainless steels without nitrogen addition as the weight loss and the number of corrosion spots is markedly reduced [47]. The nitrogen present in solid solution or at the surface is dissolved by the crevice corrosion and contributes significantly to the suppression of the corrosion attack.

The immersion tests carried out in this experimental activity showed that the presence of nitrogen in the bulk after solution nitriding does not provide a significant improvement in the crevice corrosion resistance. However, in the LTN treated materials, a significant delay in the corrosion attack is observed. These results can be explained by the extremely aggressive solution and the long exposure time applied in the experimental campaign. These conditions do not allow a significant improvement in the crevice corrosion performance despite the fact that the polarization curves suggest a difference at least for the AISI 304L and 316. However, the amount of nitrogen in expanded austenite is significantly higher and as such more nitrogen is available for an effective suppression of the corrosion attack.

It is important to mention that these results can be achieved only when nitrogen is present in solid solution and not as CrN precipitates. The precipitation of nitrides would cause a depletion of Cr and N from the matrix, therefore impairing the corrosion resistance of the stainless steel.

5 Conclusion

Three stainless steel grades were subjected to various high-temperature solution nitriding (HTSN) treatments or low-temperature nitriding (LTN).

Depending on the processing conditions, the HTSN process allows a substantial increase of the nitrogen content in the bulk. The presence of nitrogen in the bulk allows a significant improvement of the pitting resistance of the alloy compared to the untreated material. Due to the aggressiveness of the solution used in the crevice corrosion test, no significant improvement as a consequence of nitrogen dissolution could be detected in the HTSN treated materials.

The LTN process leads to the formation of a nitrogen rich case at the material surface. The processing parameters (nitriding temperature and time) allowed the formation of a supersaturated solid solution of nitrogen and no precipitation of CrN. The nitrogen dissolved during the process was significantly higher than what could be obtained with a HTSN process and allowed a dramatic increase in the pitting resistance of the steels.

Crevice corrosion immersion tests of the LTN material showed a reduction of the weight loss as compared to the untreated and HTSN treated materials, despite the harsh environment.

All results indicate that nitrogen has an important effect on the corrosion performance. Future investigations should focus on elucidating the mechanism responsible for the enhanced corrosion performance.

References

[1] L. Shreir, R.A. Jarman, G.T. Burstein, Materials and Corrosion, third ed., Butterworth-Heinemann, Oxford, 1994.

[2] M.O. Speidel, Properties and applications of high nitrogen steels, in: A. Hendry, J. Foct (Eds.), Proceedings International Conference HSN 88 Lille, The insitute of Metals, London, 1989, p. 92.

[3] R. Reed, Nitrogen in austenitic stainless steels, JOM. 41 (1989) 16–21.

[4] J. Simmons, Overview: high-nitrogen alloying of stainless steels, Mater. Sci. Eng. A. 207 (1996) 159–169.

[5] E. Werner, Solid solution and grain size hardening of nitrogen-alloyed austenitic steels, Mater. Sci. Eng. 101 (1988) 93–98.

[6] L.Å. Norström, The influence of nitrogen and grain size on yield strength in Type AISI 316L austenitic stainless steel, Met. Sci. 11 (1977) 208–212.

[7] Y. Takahashi, K. Yoshida, M. Shimada, E. Tada, Mechanical evaluation of nitrogen-strengthened stainless steels at 4K, Adv. Cryog. Eng. Mater. 28 (1982) 73–81.

[8] J.R. Kearns, H.E. Deverell, Use of nitrogen to improve the corrosion resistance of FeCrNiMo alloys for the chemical process industries, Mater. Perform. 26 (1987) 18–28.

[9] M. Janik-Czachor, Effect of nitrogen content in a 18Cr-5Ni-10Mn stainless steel on the pitting susceptibility in chloride solutions, Corrosion. 31 (1975) 394 – 398.

[10] J.J. Eckenrod, C.W. Kovach, Effect of Nitrogen on the Sensitization, Corrosion and Mechanical Properties of 18Cr-8Ni Stainless Steel, in: C.R. Brinkman, H.W. Garvin (Eds.) Properties of Austenitic Stainless Steels and Their Weld Metals, American Society for Testing and Materials (ASTM), Philadelphia, 1979, pp. 17–41.

[11] Y.C.. Lu, R.. Bandy, C.R.. Clayton, R.C. Newman, Surface enrichment of nitrogen during passivation of a highly resistant stainless steel, J. Electrochem. Soc. 130 (1983) 8.

[12] I. Olefjord, L. Wegrelius, Role of nitrogen on the corrosion behavior of austenitic stainless steels, Corros. Sci. 38 (1996) 1203–1220.

[13] C.O.A. Olsson, The influence of nitrogen and molybdenum on passive films formed on the austenoferritic stainless steel 2205 studied by AES and XPS, Corros. Sci. 37 (1995) 467–479.

[14] A. Scrinivasan, B. ReyndersS, H.J. Grabke, Localised corrosion behaviour of high and low nitrogen Cr-Mn steels, Steel Res. 66 (1995) 439–443.

[15] S. Ahila, B. Reynders, H.J. Grabke, The evaluation of the repassivation tendency of Cr-Mn and Cr-Ni steels using scratch technique, Corros. Sci. 38 (1996) 1991–2005.

[16] K. Osozawa, The Effect of Nitrogen on the Corrosion Resistance of Stainless Steels, Japan Soc. Heat Treat. 36 (1985) 206–212.

[17] K. Osozawa, N. Okato, Y. Fukase, K. Yokota, N, Boshoku Gjtutsu (Corros. Eng.). 24 (1975) 1.

[18] H.P. Leckie, H.H. Uhlig, Environmental Factors Affecting the Critical Potential for Pitting in 18–8 Stainless Steel, J. Electrochem. Soc. 113 (1966) 1262.

[19] A.H. Satir-Kolorz, H.K. Feichtinger, On the solubility of nitrogen in liquid iron and steel alloys using elevated pressure, Zeitschrift Fuer Met. Res. Adv. Tech. 82 (1991) 689–697.

[20] G. Stein, I. Hucklenbroich, Manufacturing and Applications of High Nitrogen Steels, Mater.

Manuf. Process. 19 (2004) 7–17.
[21] K.F. M. Kikuchi, M. Kajihara, Solubility of nitrogen in austenitic stainless steels, in: A. Hendry, J. Foct (Eds.), Proceedings International Conference HSN 88 Lille, The insitute of Metals, London, 1989, p. 63.
[22] H. Berns, Manufacture and Application of High Nitrogen Steels, ISIJ Int. 36 (1996) 909–914.
[23] H. Berns, S. Siebert, High Nitrogen Austenitic Cases in Stainless Steels, ISIJ Int. 36 (1996) 927–931.
[24] F. Bottoli, G. Winther, T.L. Christiansen, K. V. Dahl, M.A.J. Somers, Low-temperature nitriding of deformed austenitic stainless steels with various nitrogen contents obtained by prior high temperature solution nitriding, submitted to Metallurgical and Materials Transaction A (2015).
[25] C.M. Garzón, A.P. Tschiptschin, New high temperature gas nitriding cycle that enhances the wear, J. Mater. Sci. 39 (2004) 7101–7105.
[26] A.P. Tschiptschin, Predicting Microstructure Development During High Temperature Nitriding of Martensitic Stainless SteelsUsing Thermodynamic Modeling, Mater. Res. 5 (2002) 257–262.
[27] T.L. Christiansen, M.A.J. Somers, Low-temperature gaseous surface hardening of stainless steel: the current status, Int. J. Mater. Res. Former. Zeitschrift Fuer Met. 100 (2009) 1361–1377.
[28] H. Dong, S-phase surface engineering of Fe-Cr, Co-Cr and Ni-Cr alloys, Int. Mater. Rev. 55 (2010) 65–98.
[29] T. Bell, Current Status of Supersaturated Surface Engineered S-Phase Materials, Key Eng. Mater. 373-374 (2008) 289–295.
[30] Z. Yu, X. Xu, L. Wang, J. Qiang, Z. Hei, Structural characteristics of low-temperature plasma-nitrided layers on AISI 304 stainless steel with an a' -martensite layer, 153 (2002) 125–130.
[31] M.K. Lei, X.M. Zhu, Plasma-based low-energy ion implantation of austenitic stainless steel for improvement in wear and corrosion resistance, Surf. Coatings Technol. 193 (2005) 22–28.
[32] Y. Sun, T. Bell, Sliding wear characteristics of low temperature plasma nitrided 316 austenitic stainless steel, Wear. 218 (1998) 34–42.
[33] C. Li, T. Bell, Corrosion properties of active screen plasma nitrided 316 austenitic stainless steel, Corros. Sci. 46 (2004) 1527–1547.
[34] Committee of Stainless Steel Producers, Review of the Wear and Galling Characteristics of Stainless Steels, American Iron and Steel Institute, Washington, 1978.
[35] M.A.J. Somers, T. Christiansen, Kinetics of Microstructure Evolution during Gaseous Thermochemical Surface Treatment, J. Phase Equilibria Diffus. 26 (2005) 520–528.
[36] T. Bell, Surface engineering of austenitic stainless steel, Surf. Eng. 18 (2002) 415–422.
[37] T.L. Christiansen, T.S. Hummelshøj, M.A.J. Somers, Solution hardening of cold deformed passive alloy workpiece used to form component e.g. lock washer, involves dissolving nitrogen in workpiece and cooling in presence of inert gas which does not contain nitrogen at preset temperature, WO2013159781-A1, 2013.
[38] T.L. Christiansen, T.S. Hummelshøj, M.A.J. Somers, Forming expanded austenite and/or expanded martensite by solution hardening of cold deformed workpiece of passive alloy, WO2012 146254-A1, 2012.
[39] Standard test methods for pitting and crevice corrosion resistance of stainless steels and related alloys by use of ferric Chloride solution, ASTM Int. 03 (2003) 1–10.
[40] A. Pardo, M.C. Merino, A.E. Coy, F. Viejo, R. Arrabal, E. Matykina, Pitting corrosion behaviour of austenitic stainless steels – combining effects of Mn and Mo additions, Corros. Sci. 50 (2008) 1796–1806.
[41] M. Pourbaix, Atlas of electrochemical equilibria in aqueous solutions, Second Ed., National Association of Corrosion Engineers, Houston, Texas, USA, 1974.
[42] C. Templier, J.C. Stinville, P. Villechaise, P.O. Renault, G. Abrasonis, J.P. Rivière, A. Martinavičius, M. Drouet, On lattice plane rotation and crystallographic structure of the expanded

austenite in plasma nitrided AISI 316L steel, Surf. Coatings Technol. 204 (2010) 2551–2558.
[43] T.L. Christiansen, M.A.J. Somers, Low temperature gaseous nitriding and carburising of stainless steel, Surf. Interface Anal. 21 (2005) 445–455.
[44] C. Blawert, H. Kalvelage, B.L. Mordike, G. a. Collins, K.T. Short, Y. Jirásková, et al., Nitrogen and carbon expanded austenite produced by PI3, Surf. Coatings Technol. 136 (2001) 181–187.
[45] Z. Cheng, C.X. Li, H. Dong, T. Bell, Low temperature plasma nitrocarburising of AISI 316 austenitic stainless steel, Surf. Coatings Technol. 191 (2005) 195–200.
[46] I. Olefjord, Surface Composition of Stainless Steels during Anodic Dissolution and Passivation Studied by ESCA, J. Electrochem. Soc. 132 (1985) 2854.
[47] H. Baba, Y. Katada, Effect of nitrogen on crevice corrosion in austenitic stainless steel, Corros. Sci. 48 (2006) 2510–2524.
[48] H. Baba, T. Kodama, Y. Katada, Role of nitrogen on the corrosion behavior of austenitic stainless steels, Corros. Sci. 44 (2002) 2393–2407.
[49] H. Yashiro, D. Hirayasu, N. Kumagai, Effect of Nitrogen Alloying on the Pitting of Type 310 Stainless Steel, ISIJ Int. 42 (2002) 1477–1482.
[50] H. Yashiro, D. Takahashi, N. Kumagai, K. Mabuchi, Effect of Nitrogen and Molybdenum Species on the Pitting of Stainless Steel in High-Temperature Chloride Solutions, Corros. Eng. 47 (1998) 591.
[51] H. Ohno, H. Tanabe, A. Sakai, T. Misawa, Corros. Eng. 47 (1998) 584.
[52] G.C. Palit1, V. Kain, H.S. Gadiyar, Electrochemical Investigations of Pitting Corrosion in Nitrogen-Bearing Type 316LN Stainless Steel, Corrosion. 49 (1993) 977–991.
[53] T. Komori, U. Nakada, Electrochemical Behavior of Nitrogen-Bearing Austenitic Stainless Steels, in: Proceedings 39th Japan Corros. Conf. JSCE, 1992: p. 353.
[54] M. Janik-Czachor, E. Lunarska, Z. Szklarska-Smialowska, Effect of Nitrogen Content in a 18Cr-5Ni-10Mn Stainless Steel on the Pitting Susceptibility in Chloride Solutions, Corrosion. 31 (1975) 394–398.

10 Paper V: Effect of plastic pre-straining on residual stress and composition profiles in low-temperature surface hardened austenitic stainless steel

Federico Bottoli, Grethe Winther, Thomas L. Christiansen, Marcel A.J. Somers

Technical University of Denmark, Department of Mechanical Engineering, Produktionstorvet b.425, 2800 Kgs. Lyngby, Denmark

Article submitted to Metallurgical and Materials Transactions A on November 26th, 2015

Effect of plastic pre-straining on residual stress and composition profiles in low-temperature surface hardened austenitic stainless steel

Federico Bottoli, Grethe Winther, Thomas L. Christiansen, Marcel A.J. Somers

Technical University of Denmark, Department of Mechanical Engineering, Produktionstorvet b.425, 2800 Kgs. Lyngby, Denmark

Keywords

Low-temperature surface hardening, x-ray diffraction, residual stresses, expanded austenite, nitriding, carburizing, nitrocarburizing.

Abstract

The present work deals with the evaluation of the residual-stress profiles in expanded-austenite by applying grazing incidence X-ray diffraction (GI-XRD) combined with successive sub-layer removal. Annealed and deformed (ε_{eq}=0.5) samples of stable stainless steel EN 1.4369 were nitrided or nitrocarburized. The residual stress profiles resulting from the thermochemical low-temperature surface treatment were measured. The results indicate high residual compressive stresses of several GPa's in the nitrided region, while lower compressive stresses are produced in the carburized case. Plastic deformation in the steel prior to thermochemical treatment has a hardly measurable influence on the nitrogen-rich zone, while it has a measurable effect on the stresses and depth in the carbon-rich zone.

1 Introduction

Surface engineering techniques are widely used to modify material surface properties. Through thermal, mechanical and chemical surface treatments, it is possible to tailor the resistance against wear, corrosion and fatigue, and thus enhance the component performance [1]. Most surface engineering techniques are associated with the introduction of residual stress-depth profiles, which can have a detrimental or a favourable effect on the performance of materials and components under certain conditions [2].

Among surface engineering techniques, a growing interest is observed in low-temperature gaseous processes of stainless steels, because, compared to existing treatments, these techniques allow a significant improvement of wear and fatigue resistance, without impairing (but rather improving) the material´s corrosion performance [3–5].

The significant improvement of the material surface properties after low-temperature nitriding, nitrocarburizing or carburizing is due to the dissolution of a colossal amount of nitrogen and/or carbon in the stainless steel matrix, forming a supersaturated solid solution known as expanded austenite [6,7]. The interstitial concentration profile of the dissolved nitrogen and carbon atoms has been reported to lead to the development of enormous compressive residual stresses in the near surface region parallel to the material's surface, from 2-3 GPa after carburising up to 8GPa after nitriding [8–10].

The composition-induced stresses are usually evaluated by angle dispersive diffraction methods using the radiation produced by conventional X-ray tubes. Quantitative assessment of residual stresses in expanded austenite is challenging as the several properties influencing the lattice spacing measured in an X-ray diffraction experiment can change considerably within the depth range probed in an experiment [2]. (Steep) gradients in the local lattice spacing, as a consequence of gradients in composition, stress and stacking fault density can have a significant effect on the result obtained in residual stress determination [2,9–11]. Furthermore, elastic constants [9] and thermal expansion coefficients [12] (and magnetic properties [13]) depend strongly on the interstitial content dissolved in expanded austenite. Extensive research has been carried out with both destructive and non-destructive XRD methods to evaluate the magnitude of the compressive stresses and to take into account the influence of the various parameters [8–11,14,15]

The conventional "$\sin^2\psi$" method, using symmetric Bragg-Brentano geometry, leads to a significant variation of the information depth of the X-rays with tilt angle. This variation leads to the generation of ghost or fictitious stresses that have to be taken into account and corrected for in the data evaluation procedure [11]. Alternatively, the influence of ghost stresses can be reduced by a proper choice of the measurement geometry (not Bragg-Brentano). Recently it was shown for fixed grazing-incidence angles, at the probed depth range is shallow and the resulting information depth can be assumed constant [9,16].

In industrial practice, the presence of residual plastic deformation in the near surface region prior to surface treatment is the rule rather than the exception and may have a strong influence on the low-temperature thermochemical processes [17–19]. In the present study the influence of such residual plastic deformation in the steel on residual-stresses developing in expanded austenite upon nitriding and nitrocarburizing is investigated.

1.1 X-ray diffraction stress analysis

X-ray measurements allow the determination of the stress state in a crystalline phase by measuring the variation of the interplanar spacing in directions along different diffraction vectors with respect to the sample's geometry. X-ray stress evaluation is based on the determination of lattice strains assuming isotropic elasticity theory.

In polycrystalline materials, only the crystallites with their lattice plane normal parallel to the diffraction vector contribute to the diffracted intensity [20]. The contribution of a certain depth under the surface to the diffracted intensity depends on the absorption of incident and diffracted intensity and the path as adjusted by the diffraction geometry [2]. The crystallites closer to the surface have a stronger contribution

while the ones deeper in the material will contribute less to the line profile [2]. Therefore, the lattice spacing determined is the diffracted intensity-weighted d-spacing value, which can be simplified to:

$$d = \frac{\int_0^\infty d(z) \exp\left(-\frac{z}{\tau}\right) dz}{\int_0^\infty \exp\left(-\frac{z}{\tau}\right) dz} \qquad \text{Equation 1}$$

where z is depth and τ is the information depth, which actually is identical to the diffracted intensity-weighted depth. The relationship between the lattice strain in a crystallite with orientation *hkl* and the stress is expressed by:

$$\varepsilon_{\varphi\psi} = \frac{(d_{\varphi\psi}^{hkl} - d_0^{hkl})}{d_0^{hkl}} = ½S_2(hkl)[\sigma_{11}cos^2\varphi sin^2\psi + \sigma_{22}sin^2\varphi sin^2\psi + \sigma_{33}cos^2\psi] + ½S_2(hkl)[\sigma_{12}sin2\varphi sin^2\psi + \sigma_{13}cos\varphi sin2\psi + \sigma_{23}sin\varphi sin2\psi] + S_1(hkl)[\sigma_{11} + \sigma_{22} + \sigma_{33}] \qquad \text{Equation 2}$$

where $d_{\varphi\psi}^{hkl}$ is the lattice spacing for the *hkl* planes in a direction defined by the rotation angle φ and the tilt angle ψ with respect to the frame of reference formed by the principal stresses, d_0^{hkl} is the strain-free lattice spacing, and $½S_2(hkl)$ and $S_1(hkl)$ are the X-ray elastic constants (XECs) for the *hkl* under consideration.
The stress state experienced resulting from a thermochemical treatment can usually be assumed biaxial. Hence, $\sigma_{11} = \sigma_{22} = \sigma_{//}$ and $\sigma_{33}=0$ and Equation 2 can be rewritten as follows:

$$\varepsilon_{\varphi\psi}^{hkl} = \frac{(d_{\varphi\psi}^{hkl} - d_0^{hkl})}{d_0^{hkl}} = ½S_2^{hkl}\sigma_{//}sin^2\psi + 2S_1^{hkl}\sigma_{//} \qquad \text{Equation 3}$$

Equating Equation 3 to zero and rearranging the terms, allows finding the strain free spacing d_0^{hkl} probed for the strain free direction $\psi_{\varepsilon=0}$:

$$sin^2\psi_{\varepsilon=0} = \frac{-2S_1^{hkl}}{½S_2^{hkl}} \qquad \text{Equation 4}$$

The conventional "$\sin^2\psi$" method, using symmetric Bragg-Brentano geometry, is characterized by a significant variation of the information depth with the tilt angle, such that the depth range analysed is reduced with increasing tilt angle. Consequently, if a lattice spacing-depth profile occurs as a consequence of a composition and/or a stress profile, the conventional "$\sin^2\psi$" method combines experimental lattice spacings obtained for different information depths in one determination of the stress, thereby introducing artefacts leading to fictitious stress values, so-called ghost stresses, in addition to the actual stress value.
Conversely, asymmetric geometry (grazing incidence mode) allows a small fixed (or tilt dependent) incidence angle, limiting the probed depth range to a shallow region in the proximity of the surface. By the application of a fixed grazing incidence, the information depth varies to a limited extent, while by tailored variation of the incidence angle with the tilt angle a constant information depth can be achieved [21,22].

On applying grazing incidence mode, it has to be taken into account that the lattice spacing is probed in a direction that is tilted with respect to the surface normal, even for no actual rotation. The effective tilt angle ψ is given by:

$$cos\psi = cos\chi \cos(\theta - \alpha) \qquad \text{Equation 5}$$

where χ is the tilt angle in the laboratory frame of reference. Hence, asymmetric geometry set-up does not require correction procedures, which would have been the case for measurement in symmetric geometry mode, where gradients may strongly affect the obtained lattice spacings.

1.2 X-Ray elastic constants

For any practical applications, the knowledge of the X-ray elastic constant is a necessary prerequisite for the determination of the stress-state of the material. The diffraction elastic constant can be obtained from single-crystal elastic constants through the use of grain interaction models (GIM).

Several grain interaction models have been proposed in literature [21] . The Voigt [23] and Reuss [24] grain interaction models are considered the two extreme models. The Voigt GIM assumes that the strain distribution is homogenous in the specimen, while the Reuss GIM assumes that the stress tensor is equal for all crystallites. The two extreme cases of GIM in polycrystals were proven by Hill to set the upper and lower bounds for the mechanical elastic constants. The Neerfeld-Hill model [25,26] suggests that the arithmetic average of the Voigt and Reuss models is in better agreement with experimental data.

The Vook-Witt and the inverse Vook-Witt models [27] include extreme grain interaction assumptions along the two considered principal directions. For special conditions at the free surface the Vook-Witt model assumes equal strains in the surface plane and zero stress perpendicular to the surface; the inverse Vook-Witt model assumes equal strain perpendicular to the surface and equal stresses in the surface plane.

Eventually, in the Eshelby-Kröner model [28,29] the crystallites surrounding an individual crystallite are conceived as an elastically homogenous matrix with averaged elastic properties of the entire polycrystal.

The determination of the single-crystal elastic constant is therefore an essential prerequisite for the calculation of X-ray elastic constants for polycrystals, irrespective of the GIM adopted.

So far, single crystal elastic constants have not been determined for expanded austenite; therefore, the elastic constants reported for stainless steel Fe-12%Cr-12%Ni are often used [9,10,15]. However it has been shown that the presence and the amount of interstitial atoms in solid solution has an enormous influence on the X-ray elastic constant, and in particular that the ratio E_{200}/E_{111} grows substantially with the growing content of dissolved atoms [9]. Furthermore, recent work on the magnetic properties of nitrogen stabilized expanded austenite [13], shows that depending on the nitrogen content and the temperature, expanded austenite is paramagnetic or ferromagnetic and has a Curie temperature in-between the nitriding temperature and room temperature. As magnetic and elastic properties are coupled it is anticipated that also the elastic properties of nitrogen stabilized expanded austenite are different at nitriding and room temperature.

In the present work, the X-ray elastic constants of paramagnetic Fe-12%Cr-12%Ni and ferromagnetic γ'-Fe_4N (Table 1) were calculated, using the Reuss GIM. These values were used for the evaluation of

residual stresses in expanded austenite which are expected to be representative for a low (paramagnetic) and intermediate to high (ferromagnetic) interstitial content. Changing the crystal structure from γ–Fe and γ'-Fe_4N a reversal of the elastic anisotropy occurs [23]; a similar reversal was observed for expanded austenite with low and high interstitial content [9,30].
The motivation for adopting the Reuss GIM was the good correspondence of the obtained stress profiles for the 111 and 200 family planes in previous work [9].

Table 1: X-ray elastic constants for Fe-12%Cr-12%Ni and for γ'-Fe_4N for the {111} and {200} family planes calculated with the Reuss grain interaction models [9]. The X-ray elastic constant for γ'-Fe_4N were calculated for crystallographically and elastically isotropic polycrystals [21] using s_{11}= 4.36 MPa^{-1}, s_{22}=1.33 MPa^{-1} and s_{44}=21.75 MPa^{-1} as single crystal elastic constants for γ'-Fe_4N [31].The values are given in 10^{-6} MPa^{-1}.

Reuss GIM				
	Fe-12%Cr-12%Ni		**γ'-Fe_4N**	
	XEC		**XEC**	
	111	200	111	200
S_1^{hkl}	-0.7	-4.3	-3.06	-1.33
½S_2^{hkl}	4.3	15	10.9	5.68

2 Experimental

2.1 Materials preparation

The stainless steel EN 1.4369 with chemical composition Fe-0.09C-0.23N-0.74Si-0.18Mo-5.92Mn-18.58Cr-7.11NI (wt%) was investigated in this experimental activity. The supplier provided the material in annealed condition as 0.7mm thick plates. Tensile test specimens were cut out from the plate material in accordance to the ASTM standard E 8M-0419. The tensile loading direction was chosen parallel to the rolling direction of the plate. Tensile straining was applied at a strain rate of 6.67x10^{-3} s^{-1} to an equivalent strain of ε_{eq}=0.5.
Specimens with dimensions 15x12.5x0.7mm^3 were obtained from the annealed and deformed material. The flat surface of the specimens was ground and polished to a final step of 3µm diamond paste and afterwards electro-polished in order to remove the plastic deformation zone introduced by grinding. The electro-polishing was carried out for 20s in a "Struers Electrolyte A2" solution with an applied potential and current density of 30V and 2A/cm^2, respectively.

2.2 Low-temperature thermochemical processes

Samples in annealed and deformed state were subjected to three different treatments: nitriding and nitrocarburizing.

The low-temperature nitriding and nitrocarburizing processes were performed in a LAC annealing furnace model PKRC 55/09 retrofitted for gaseous nitriding/nitrocarburizing. The samples were suspended on a type K (chromel/alumel) thermocouple to monitor the temperature during the entire nitriding cycle, including heating and cooling. To enable low-temperature surface hardening, the sample surface was activated in-situ by a proprietary procedure.

The nitriding process was carried out in a pure ammonia atmosphere at 703K (430°C) for 20h while the nitrocarburizing was carried out in an ammonia/propane gas mixture at 693K (420°C) for 20h.

Attempts to carburize EN 1.4369 did not succeed for the annealed, despite various procedures of surface activation. It is anticipated that the presence of nitrogen in the as-received condition of this alloy is responsible for this inability to dissolve carbon. For this reason carburized samples are not included in this investigation.

2.3 Microstructural characterization

The microstructures of all samples before and after low-temperature thermochemical processes were investigated in cross section with reflected-light microscopy. The samples were ground, polished and etched with Kalling's reagent no.1 for 5-8 s. Micro-hardness indentation measurements to obtain the hardness profile over the "case" were performed on a Future-Tech FM700 instrument using a load of 0.05 N.

Glow discharge optical emission spectroscopy (GD-OES) was applied for the determination of the surface composition profiles after the low-temperature thermochemical treatments. Controlled sputtering of the surface during GD-OES was performed with a plasma at 1000Pa and 40W using a Horiba Jobin Yvon GD profiler 2.

Concentration profiles of substitutionally and interstitially dissolved components were obtained using a selection of stainless steel reference materials and γ'-Fe_4N on pure iron as a nitrogen reference.

2.4 X-ray diffraction stress depth profiling

X-ray diffraction analysis was performed with a Bruker AXS D8 diffractometer equipped with Cr-tube source with a characteristic wavelength of 2.2897 Å. A voltage of 40kV and a current of 40mA were used for the measurements. The lattice spacing profiling for residual stress analysis over the thickness of the hardened surface was determined in grazing incidence geometry using point focus configuration and a vanadium window to remove Cr K_β.

The measurements were performed in a range 55°-85° 2θ. This range was selected to include the 111 and 200 reflections of austenite and expanded austenite. The step size was 0.05° 2θ and the counting time was 6s per 2θ step. The grazing incidence angle was kept fixed at α=2° for all the tilting angles χ. Line profiles were obtained for 5 values of χ angle (0°, 25°, 38°, 49°, 60°).

Although it is considered good practice to use high 2θ angles for the evaluation of residual stresses the 220 and 311 reflections were too weak and broad to guarantee an accurate evaluation of the stress profiles. The possible instrumental influence of applying reflections in the low 2θ range was determined: stress-free stainless steel powder was measured resulting in "stress-values" less than 100MPa. This contribution is negligible as compared to the stress values to be determined in the present case.

Keeping a small fixed grazing incidence angle can limit the probed volume to a shallow surface region. However, even for fixed grazing incidence angles, the information depth changes with ψ angle. This small variation in the penetration depth, which is from 0.18 to 0.35μm in the investigated 2θ range, is responsible for the generation of substantial ghost stresses especially in the near surface region area, where a very steep gradient in the lattice parameter is present because of the steep nitrogen concentration profile.

After each measurement, a thin sublayer of approximately 1.5μm of expanded austenite was removed by gentle polishing with 3μm diamond paste. The sublayer removal procedure was performed on each of the analysed samples until the material substrate was reached (no 2θ shift of the substrate reflection was recorded). The weight loss after every polishing step was measured to accurately monitor the sublayer removal.

2.5 Stress analysis data analysis

The 111 and 200 X-ray line profile of each sample collected at the different depths were fitted to determine the centroid peak position of the Bragg peak. From the centroid it was possible to calculate the as-measured lattice spacing core, the centroid peak position contained contributions from γ_N and γ_C, γ_N and γ and from γ_C and γ, respectively. Away from these transition regions the centroid position can be exclusively attributed to γ_N, γ_C or γ. The $\sin^2\psi$ plots for the 111 and 200 reflections values $\langle d_{\varphi\psi}^{hkl} \rangle$ for the 111 and 200 reflections. In the transition regions from γ_N to γ_C, γ_N to γ and from γ_C to the γ were constructed by fitting straight lines through the as-determined lattice spacing, $\langle d_{\varphi\psi}^{hkl} \rangle$ vs. the corresponding $\sin^2\psi$ value. The slope $\Delta\langle d_{\varphi\psi}^{hkl} \rangle / \Delta sin^2\psi$ and intercept $\langle d_{\psi=0}^{hkl} \rangle$ were determined.

3 Results

3.1 Low-temperature nitriding

EN 1.4369 in annealed and deformed condition was subjected to low-temperature gas nitriding at 703K (430°) for 20h in pure ammonia. Reflected light microscopy (Fig.1) reveals the morphology of the case produced during the process. In both conditions a uniform layer of expanded austenite with a thickness of 10(1) µm is found in the outermost surface.

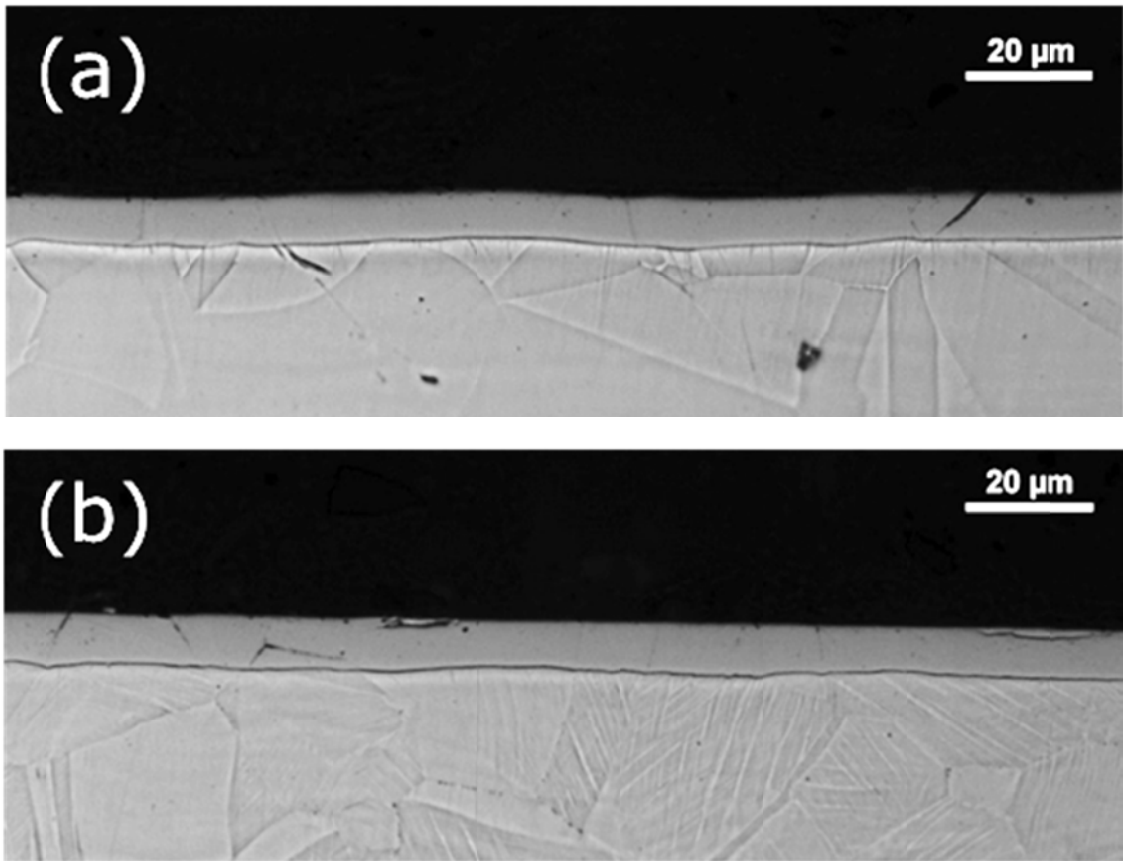

Figure 1: Reflected light micrographs of the annealed (a) and deformed ε=0.5 (b) EN 1.4369 LTN at 703K (430°) for 20h.

XRD phase analysis in Bragg-Brentano geometry confirms the formation of expanded austenite during the low-temperature gaseous process (Fig. 2). In the 2θ range investigated it is possible to identify the expanded austenite and the austenite peaks. The peaks of the expanded austenite are shifted to lower 2θ compared to the parent austenite phase, because of the lattice expansion provoked by the nitrogen dissolution. As observed in the micrographs, no significant difference in the degree of expansion of austenite can be observed in the X-ray diffractograms of the annealed and deformed sample, consistent with previous work, which indicated that EN 1.4369 consists of stable austenite [17].

The GD-OES profiles in Fig. 3 confirm the presence of a nitrogen-rich zone in proximity of the surface. The atomic concentration of nitrogen at the surface is close to about 40% and decreases steeply

approaching the composition of the parent austenite at about 11 µm. A trend is observed that the nitrogen depth profile reaches deeper for the strained condition than for the annealed condition (Fig. 3).

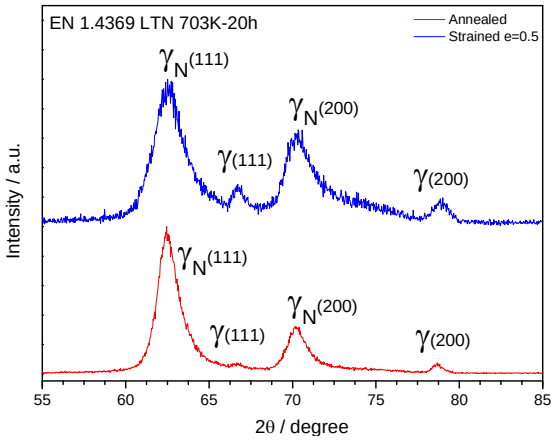

Figure 2: X-ray diffractograms of EN 1.4369 after LTN (703K (430 °C), 20h) of as-received and tensile-strained conditions.

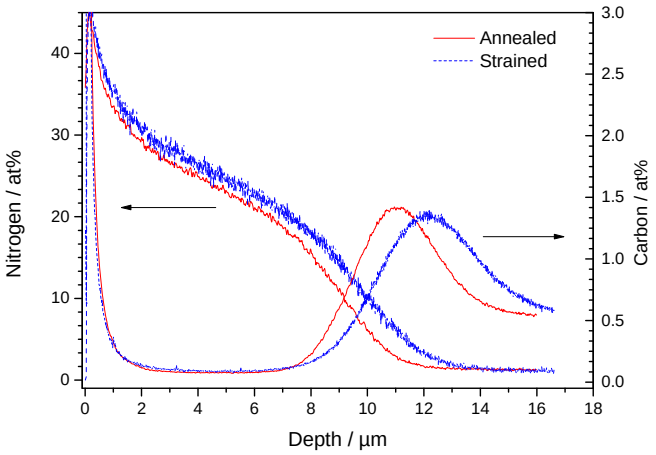

Figure 3: GD-OES nitrogen and carbon concentration profiles for EN 1.4369 after LTN (703K (430 °C), 20h) of as-received and tensile-strained conditions.

For the evaluation of the residual stresses in the materials, the lattice spacing values $\langle d_{\varphi\psi}^{hkl} \rangle$ were measured for the 111 and 200 reflections and from these the $\sin^2\psi$ plots were calculated.

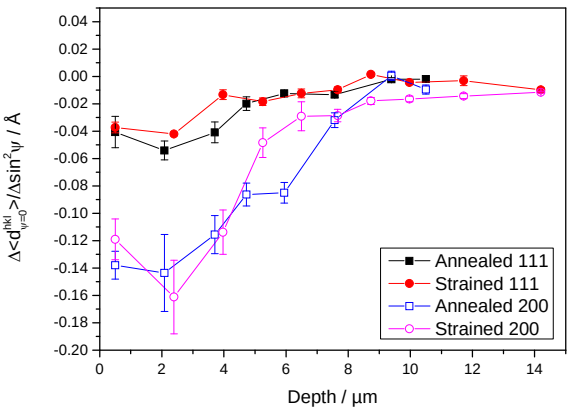

Figure 4a: $\Delta\langle d_{\varphi=0}^{hkl} \rangle / \Delta sin^2\psi$ slopes obtained from the measurement at different depth after successive layer removal for the annealed and deformed samples.

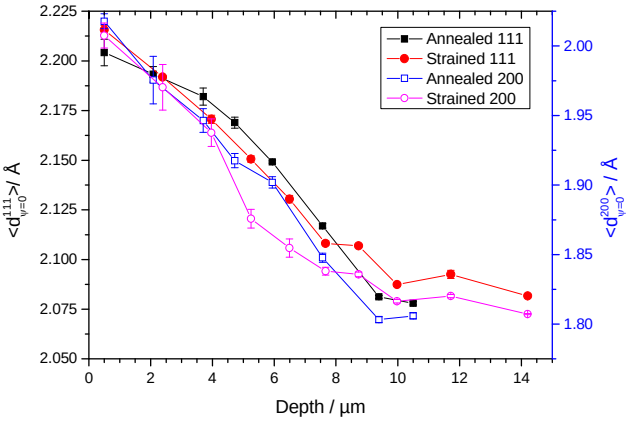

Figure 4b: $\langle d_{\varphi=0}^{hkl} \rangle$ intercept obtained from the measurement at different depth after successive layer removal for the annealed and deformed samples.

In Fig. 4a the slopes for the 111 and 200 peaks for both the annealed and strained conditions are given. The values of the slopes are more negative at the surface, indicating high compressive stresses in these regions, and they increase smoothly to less negative values (lower compressive stresses) on approaching the parent austenite. Eventually they stabilize to slightly negative values after 10µm. It is noted that more negative values of the slopes are found for the 200 reflection than for the 111 reflection, suggesting that 200 is more sensitive for applied stress than 111.

The calculated intercept values (Fig. 4b) decrease smoothly throughout the layer thickness and reach a plateau for depths after 10µm. These observations are in agreement with the micrographs in Fig. 1 and the composition profiles in Fig.3. Evidently, within experimental accuracy no difference can be discerned between the annealed and deformed cases. Apparently, the presence of plastic deformation prior to low-temperature nitriding does not have a measurable influence on the compressive stresses induced by gaseous nitriding. Furthermore, the slightly deeper nitriding front as suggested by the GD-OES profiles in Fig. 3 were not confirmed by the stress measurements, most likely as a consequence of the experimental accuracy (see error bars in Figs. 4).

3.2 Low-temperature nitrocarburizing

EN 1.4369 in annealed and deformed condition was subjected to low-temperature gas nitriding at 693K (420°) for 20h in a controlled ammonia/propene atmosphere. For both samples the nitrogen expanded austenite is lying closest to the surface, while the carbon expanded region is located underneath. Even for low-temperature nitrocarburizing no significant difference can be discerned between the annealed and deformed sample in the reflected light microscopy analysis (Fig. 5).

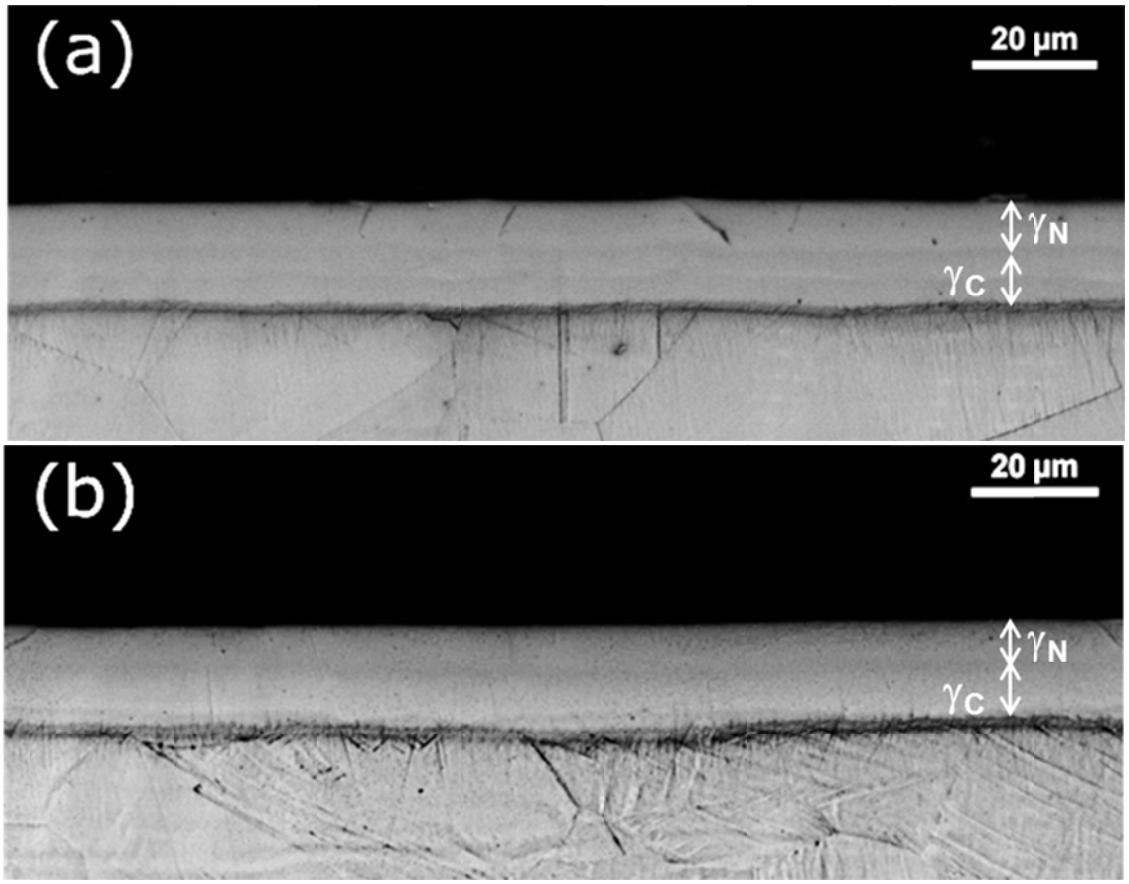

Figure 5: Reflected light micrographs of the annealed (a) and deformed ε=0.5 (b) EN 1.4369 LTNC at 693K (420°) for 20h.

X–ray diffraction analysis (Fig. 6) confirms the formation of separate zones with nitrogen and carbon expanded austenite in both samples. In this case, reflections from the substrate are no longer visible due to a thicker case and the limited depth probed by the applied X-radiation.

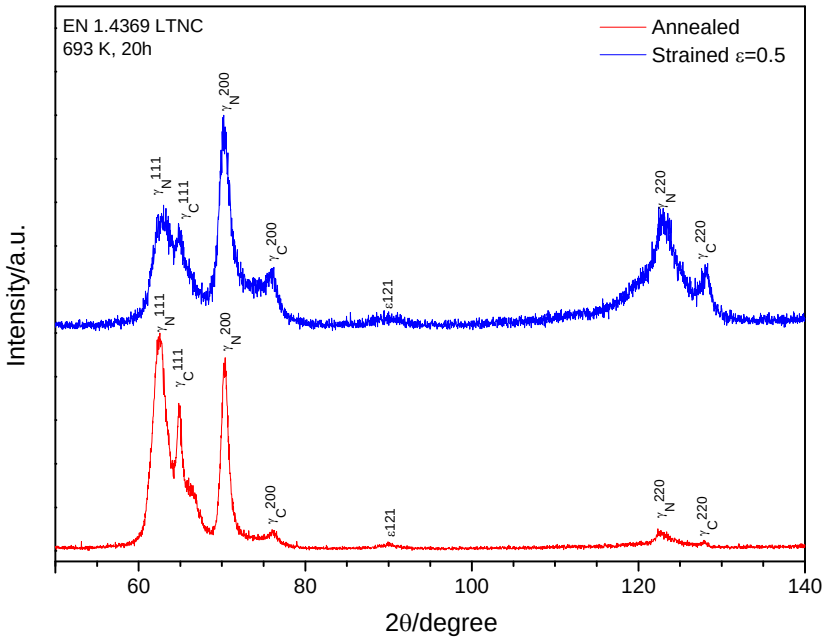

Figure 6: X-ray diffractograms of EN 1.4369 after LTNC (693K (420 °C), 20h) of as-received and tensile-strained conditions.

The GD-OES and hardness profiles for the annealed and deformed state are given in Figs. 7-8. The GD-OES measurement confirms the transition from a separate nitrogen-rich to a separate carbon-rich zone (Fig. 7). As for the nitrided samples a trend is observed that the nitrogen stabilized expanded austenite reaches slightly deeper for the strained sample than for the annealed sample. This trend is more pronounced for the carbon stabilized expanded zone; for the strained sample the carburized part reaches more than 3 µm deeper than for the annealed sample.

The total interstitial content as determined by GD-OES is compared to the hardness profiles over the case in Fig. 8. Clearly, the hardness scales with the total interstitial content until a level of 1200 HV is reached. This is particularly clear for the strained sample where the discontinuous decrease in interstitial content on entering the carbon-rich zone is associated by a discontinuous decrease in micro-hardness.

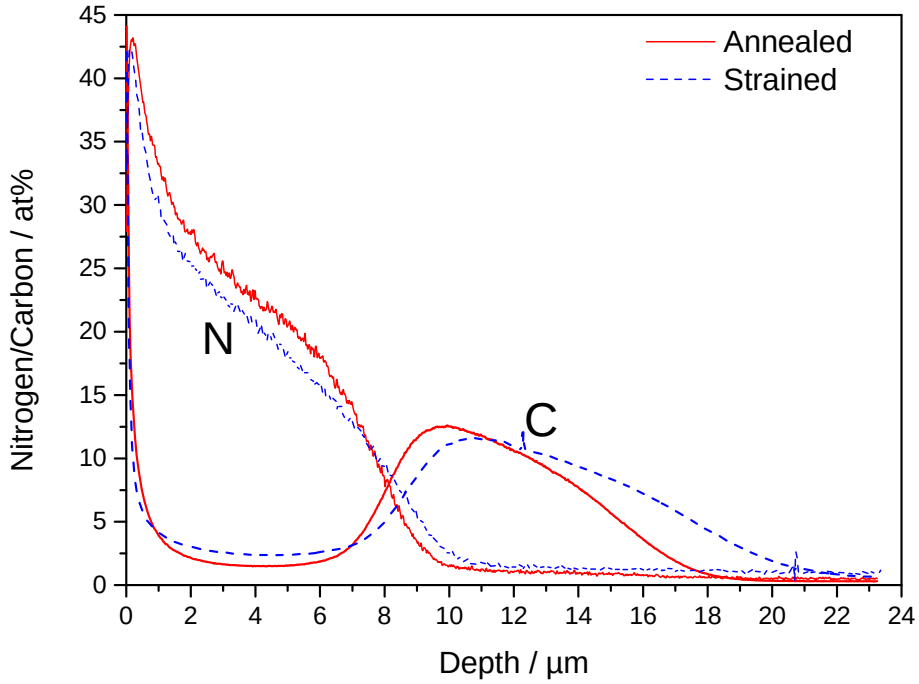

Figure 7: GD-OES profiles of nitrogen and carbon for EN 1.4369 annealed or deformed and subsequently nitrocarburized at 693K (420°C), 20h.

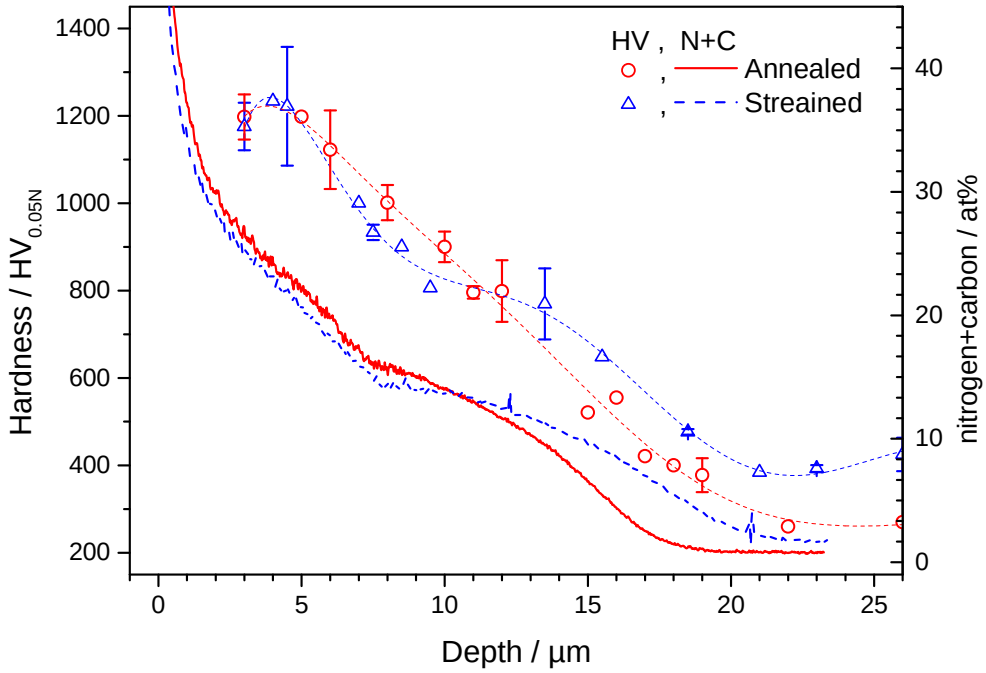

Figure 8: Hardness profile and GD-OES profile of total interstitial content in the EN 1.4369 annealed and tensile deformed (ε=0.5) samples nitrocarburized at 693K (420°C), 20h.

For both conditions, the hardness in the nitrogen-rich region is significantly higher than in the carbon-rich region. The hardness profiles show that the carbon-stabilized expanded phase bridges the hardness

difference between the nitrogen expanded part of the case to the core and therefore a smooth decrease in hardness to the bulk hardness value is obtained over several microns. This differs considerably from what is obtained during low-temperature nitriding, where the case-to-core transition occurs within few microns and a sharp hardness transition is measured [5].

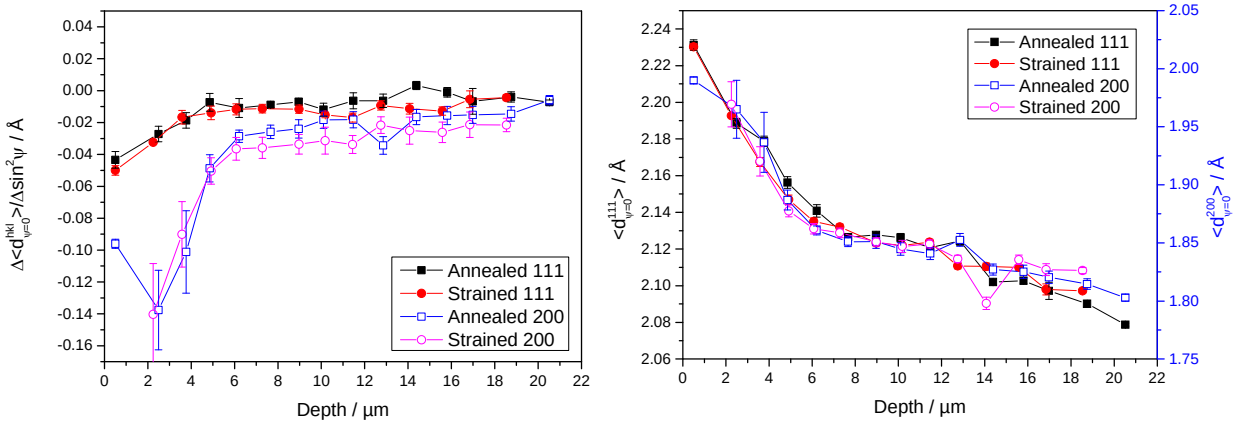

a. b.

Figure 9: Slopes, $\Delta\langle d^{hkl}_{\varphi=0}\rangle/\Delta sin^2\psi$, (a.) and intercepts, $\langle d^{hkl}_{\varphi=0}\rangle$, (b.) of the $sin^2\psi$ plots for nitrocarburized EN 1.4369 in annealed in strained condition and derived from 111 and 200 line profiles.

From the $\sin^2\psi$ plots the slopes and intercepts were obtained (see Fig. 9a and 9b, respectively). For both conditions (annealed and deformed samples), more negative values of the slope are found in the nitrided region; subsequently the slopes increase rapidly deeper in the case, indicating a considerable reduction of the compressive stresses. Eventually, in carbon stabilized expanded austenite at depths of more than about 8 µm, the slopes increase slightly but steadily until levelling off at a slightly negative value in proximity of the bulk.

The trends of the slopes of the 111 and 200 reflections in the nitrogen expanded region of the annealed and deformed sample are similar (Fig. 9a), but a consistent difference can be observed in the carbon-rich expanded austenite zone. In this region the values of the slopes are always more negative for the strained than for the annealed condition, indicating that larger compressive stresses are present in pre-strained carbon expanded austenite.

The intercepts of the $\sin^2\psi$ plots decrease continuously (Fig. 9b) with increasing depth. Clearly a steeper decrease in intercept is found in the nitrogen-rich than the carbon-rich region, consistent with the change in total interstitial content and hardness in Fig. 8.

4 Discussion

4.1 Stress profiles and stress-free lattice parameters

The Reuss GIM was applied for the evaluation of the strain-free lattice parameters and the stress profiles for the annealed and strained materials after the surface engineering processes (LTN, LTNC). The X-ray elastic constant of austenite and γ'-Fe_4N were used for the calculation (cf. section 1.2). The measured lattice spacings were used for the evaluation of the strain-free lattice parameters using the relations $\langle a^{111} \rangle = \langle d^{111}_{\psi=0} \rangle \cdot \sqrt{3}$ and $\langle a^{200} \rangle = \langle d^{111}_{\psi=0} \rangle \cdot 2$.

The strain-free direction is a function of the X-ray elastic constant (Eq. 4). Nevertheless the strain-free lattice parameters profiles obtained for the 111 and 200 reflections are in good agreement with each other irrespective of the chosen X-ray elastic constants. In Fig. 10 the average of the strain-free lattice parameters derived from 111 and 200 reflections is given for the investigated samples, using the XECs for austenite (Fig. 10a) and Fe_4N (Fig. 10b).

As seen in the figures, the two sets of XECs give almost the same results. The difference between the strain-free lattice parameters obtained from 111 and 200 is less than 1% of the average in all cases.

As follows from Fig.10, the dependence of the strain-free lattice parameter on depth is analogous for nitrided and nitrocarburized samples in the nitrogen-rich part, while a marked difference is obtained in the carbon-rich part. Here the strain-free lattice parameter does not decrease as steeply as in the nitrogen-rich part and a deeper case is obtained, consistent with the GD-OES profiles in Figs. 3 and 7 and the micrographs in Fig. 1 and 5.

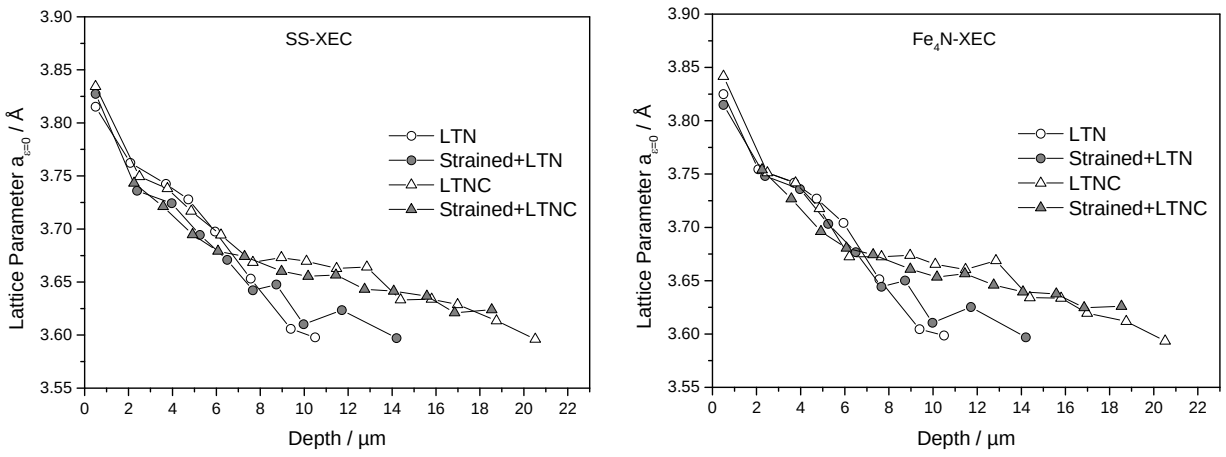

a. b.

Figure 10: Dependence of strain-free lattice parameter, $a_{\varepsilon=0}$, on depth for all investigated samples calculated using the stainless steel XEC (SS-XEC) (a.) and Fe_4N XEC (b.). In both cases, the lattice parameter is the average of those derived from 111 and 200 reflections for interpolation in the strain-free direction of the $\sin^2\psi$ relations.

The slopes obtained from the $\sin^2\psi$ plots were used for the calculation of the stress profiles for the various process conditions (Fig. 11). In contrast with the strain-free lattice parameter, not surprisingly, a significant influence is observed of the X-ray elastic constants on the measured stress profiles over the depth.

The profiles measured using the Reuss GIM and the XECs for stainless steel show a fair correspondence for the 111 and 200 reflections (Fig. 11a). High compressive residual stresses result in the nitrogen-rich region of the case as the result of a high amount of nitrogen content. In the carbon-rich regions lower compressive stresses are obtained, consistent with a lower amount of dissolved interstitials. The decline of compressive stress with the increasing depth is steep in the nitrogen-expanded region, while for the carbon-expanded region a more gradual decrease is observed along the case. These observations reflect what has been observed in the GDOES and hardness profiles (cf. Fig. 3, 7 and 8).

Close to the case-core transition positive values of stress are obtained. Notwithstanding the fact that a positive stress has to be expected in the unaffected core to compensate for the large compressive stresses in the case, tensile stresses can equally well be conceived as merely an effect of the measurement and data evaluation procedures. In this region, the calculated values are significantly influenced by using the centroid position for the line profile evaluation, loss of linearity of the experimental d_ψ-$\sin^2\psi$ dependence and, for the steep gradients, ghost stress effects. Therefore, it is not possible to conclude whether the obtained values are actual tensile stresses or just an artefact of the applied measurement and data evaluation procedures.

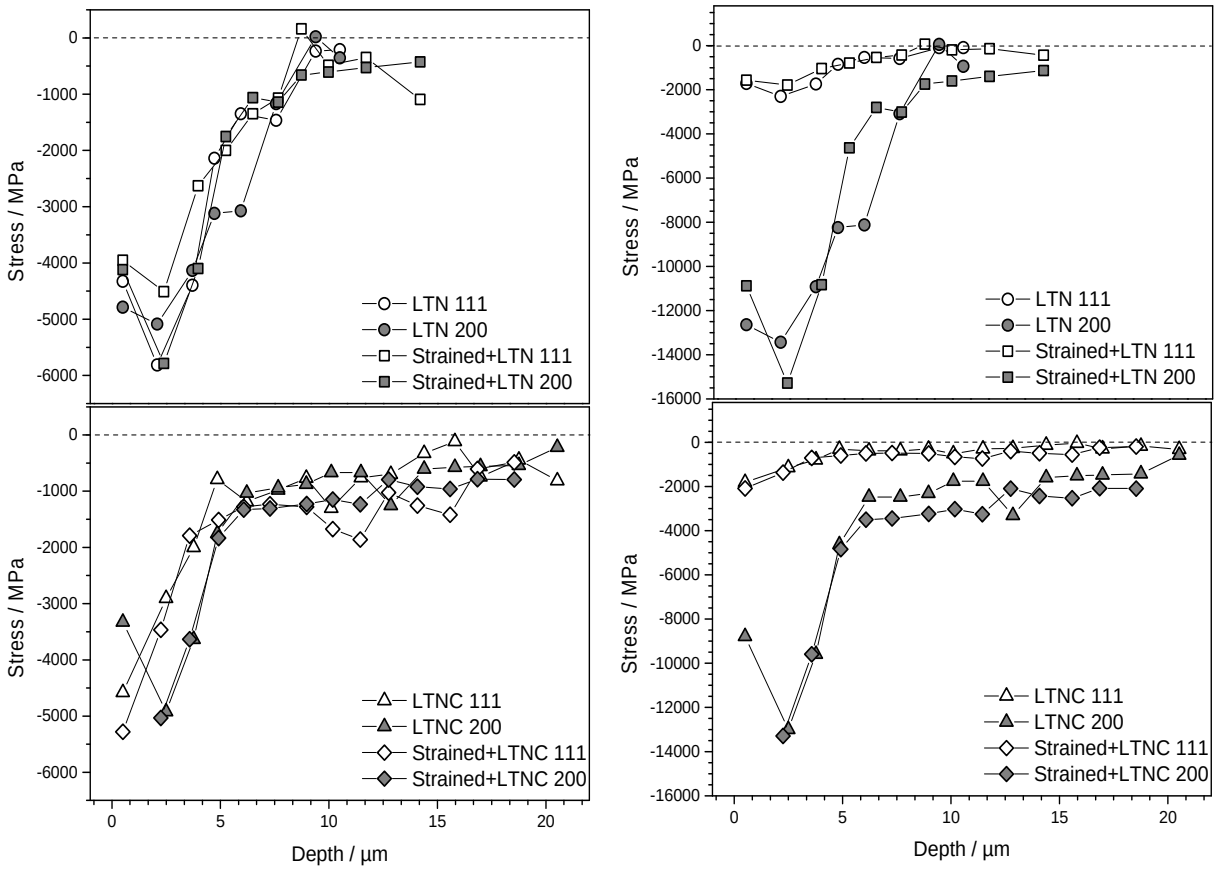

Figure 11: Stress-depth distributions obtained from the slope in d_ψ-$\sin^2\psi$ dependencies (Fig. 4a), applying X-ray elastic constants for stainless steel (a.) and γ'-Fe_4N (b.), adopting the Reuss grain interaction model.

Applying the XECs of γ'-Fe_4N, a major discrepancy between the stress values obtained from the probed reflections was found for the Reuss GIM (Fig. 11b). Obviously, the stress values calculated for the 200 reflection are unrealistically high; values of compressive stress up to 15.5GPa in the case formed upon low-temperature surface treatment cannot be subtended by this material.

This major discrepancy suggests that the X-ray elastic constants for iron-nitride, in combination with the Reuss GIM, are not suitable for the evaluation of the residual stresses in expanded austenite, despite the similarity in the crystal structures of γ_N and γ'-Fe_4N. A slightly better correspondence between 111 and 200 with elastic constants as for γ'-Fe_4N is anticipated for the Voigt GIM. Then, the difference as observed in Fig. 4a will be reproduced, because the XECs for 111 and 200 are identical for the case of the Voigt GIM.

It has been shown in previous research activities that the X-ray elastic constants for expanded austenite depend strongly on the nitrogen content [9]. In particular the $½S_2^{111}/½S_2^{200}$ ratio increases strongly with the nitrogen content. Consequently, despite a fair agreement of the stress profiles calculated with the γ–Fe XEC with the Reuss GIM, the present results can, at best, be used for a qualitative estimation of the stress distribution, but cannot be exploited for the calculation of the real profile distribution in expanded austenite.

4.2 Influence of plastic deformation on stress in expanded austenite

It is evident from the present results that, ahead of the nitriding front, within carbon expanded austenite residual stress changes gradually, and as such bridges the large difference in lattice parameter between nitrogen-stabilized and austenite. Qualitatively, the compressive residual stress level in carbon expanded austenite (Fig. 11) is higher in the strained sample than in the annealed sample. Apparently, for nitrogen expanded austenite no such difference in residual stress level between strain and annealed sample condition prior to nitriding/nitrocarburizing was observed. Different responses for nitrogen and carbon expanded austenite can be explained as follows.

On LTN, nitrogen dissolution results in the introduction of huge lattice strains corresponding to very large compressive stresses. Only part of the lattice expansion can be accommodated elastically. Along with an increase in interstitial content the (expanded) austenite is strengthened. Above a certain interstitial content the additional lattice strain corresponds to a residual stress increase that exceeds the additional yield strength. Such plastic deformation has been observed for nitriding in the form of a nitrogen dissolution-induced lattice rotation, depending on the initial grain orientation [30,32,33]. The crystal rotation effect produced upon nitriding has many similarities [30] with the grain-orientation dependent lattice rotations of individual bulk grains measured in monotonic tensile tests in a number of materials [34–36]. These rotations are further traced to activation of specific grain orientation dependent slip system combinations [30,37,38].

For carburizing such plastic accommodation has so far not been reported. Recent attempts to predict nitrogen profiles and stress profiles during nitriding incorporate crystal plasticity and strengthening, leading to realistic nitrogen-concentration profiles and stress-depth distributions [39].

In the materials tested in this experimental activity, the amounts of nitrogen dissolved during nitriding/nitrocarburizing are far beyond the level above which plastic deformation is introduced in expanded austenite and also larger than the amount estimated to correspond to an apparent plastic strain exceeding 0.2 [30]. This means that the additional deformation introduced during nitrogen expanded austenite formation can be higher than the level of plastic deformation introduced during pre-straining. Assuming that the effect of plastic deformation prior to nitriding/nitrocarburizing on the GD-OES profiles in Fig. 3 and Fig. 7 is the result of faster interstitial (pipe) diffusion as a consequence of the high dislocation density, it can be understood that a possible effect of prior plastic deformation on the nitrogen-depth profile is obscured by the additional excessive plastic deformation introduced by the high nitrogen content itself. Only the region below the critical nitrogen content where plasticity is introduced, which is close to the case-core transition [40], or the transition to carbon expanded austenite experience no additional plastic deformation from the LTN or LTNC treatment. Consequently, the effect of pre-straining is most clearly observed here.

5 Conclusion

The influence of residual plastic deformation on the residual stress state created as a consequence of low-temperature nitriding and/or nitrocarburizing was evaluated with grazing incidence X-ray diffraction.

The results obtained with the applied evaluation procedure and data analysis confirm that the prior plastic deformation has a negligible influence in the nitrogen enriched region of the nitrided and nitro-carburized layer. This effect is related to the additional plastic deformation induced as a consequence of the dissolution of colossal amounts of nitrogen which hinders the effect of residual plastic deformation prior to low-temperature thermochemical process.

On the other hand, carbon dissolution does not induce plastic deformation in the austenitic substrate because of the lower lattice expansion, thus the effect of pre-straining and the associated dislocation density affects the residual stress state in the material.

The evaluation of the residual stress state was carried out using the Reuss grain interaction model and two different sets of x-ray elastic constants, austenite and γ'-Fe_4N. Despite the similarities between the crystal structure of γ'-Fe_4N and expanded austenite a major discrepancy was found between the residual stress state resulting from the different reflections, indicating that the method is not reliable for the correct evaluation of the magnitude of the residual stresses.

The use of austenite XEC and Reuss GIM provides a fair agreement of the residual stress profiles found for the different reflections and therefore could be used for a quantitate estimation of the stresses in the nitrided/nitrocarburized case. However this method cannot be used for a correct estimation of the absolute magnitude of the residual stresses because of the high sensitivity of the XECs to nitrogen concentration.

In conclusion, for the correct estimation of the amount of residual stresses created as a consequence of thermochemical surface treatment it is necessary to determine the XEC for different interstitial concentrations.

Acknowledgements

For the present research work, the authors would like to express their gratitude to the Research Fund for Coal and Steel for the financial support to the PressPerfect project. Furthermore the authors would like to thank Sandvik Materials Technology for providing the material used during the investigation.

References

[1] J.S. Burnell and P.K. Datta: *Surface Engineering Casebook*, 1st ed., Woodhead Publishing Ltd, Cambridge, 1996.

[2] V. Hauk: *Structural and Residual Stress Analysis by Nondestructive Methods*, Elsevier, 1997.

[3] T. Bell: *Key Eng. Mater.*, 2008, vol. 373-374, pp. 289–95.

[4] H. Dong: *Int. Mater. Rev.*, 2010, vol. 55, pp. 65–98.

[5] T.L. Christiansen and M.A.J. Somers: *Int. J. Mater. Res. Former. Zeitschrift Fuer Met.*, 2009, vol. 100, pp. 1361–77.

[6] T.L. Christiansen and M.A.J. Somers: *Scr. Mater.*, 2004, vol. 50, pp. 35–37.

[7] T.L. Christiansen, M.A.J. Somers, and A Sample Preparation: *Metall. Mater. Trans. A*, 2006, vol. 37, pp. 675–82.

[8] T.L. Christiansen, T S Hummelshøj, and M.A.J. Somers: *Surf. Eng.*, 2010, vol. 26, pp. 242–47.

[9] F.A.P. Fernandes, T.L. Christiansen, G. Winther, and M.A.J. Somers: *Acta Mater.*, 2015, vol. 94, pp. 271–80.

[10] S. Jegou, T.L. Christiansen, M. Klaus, C. Genzel, and M.A.J. Somers: *Thin Solid Films*, 2013, vol. 530, pp. 71–76.

[11] T.L. Christiansen and M.A.J Somers: *Mater. Sci. Eng. A*, 2006, vol. 424, pp. 181–89.

[12] B. Brink, K. Ståhl, T.L. Christiansen, and M.A.J. Somers: *J. Appl. Crystallogr.*, 2014, vol. 47, pp. 819–26.

[13] B. Brink, K. Ståhl, T.L. Christiansen, C. Frandsen, M.F. Hansen, and M.A.J. Somers: C*omposition-dependent variation of magnetic properties and interstitial ordering in homogeneous expanded austenite*, DTU-Technical university of Denmark, Lyngby, Denamrk, unpublished research, 2015.

[14] T.L. Christiansen and M.A.J. Somers: *Mater. Sci. Forum*, 2004, vol. 443-444, pp. 91–94.

[15] T.L. Christiansen and M.A.J. Somers: *Metall. Mater. Trans. A*, 2008, vol. 40, pp. 1791–98.

[16] M.A.J Somers and E.J Mittemeijer: *Metall. Trans. A*, 1990, Vol. 21A, pp. 189-204.

[17] F. Bottoli, G. Winther, T.L. Christiansen, and M.A.J. Somers: *Metall. Mater. Trans. A*, 2015, vol. 46, pp. 2579–90.

[18] F. Bottoli, G. Winther, T.L. Christiansen, and M.A.J. Somers: *Metall. Mater. Trans. A*, 2015, vol. 46, pp. 5201–16.

[19] F. Bottoli, G. Winther, T.L. Christiansen, K. V. Dahl, and M.A.J. Somers: *Low-temperature nitriding of deformed austenitic stainless steels with various nitrogen contents obtained by prior high temperature solution nitriding.*, DTU-Technical university of Denmark, Lyngby, Denamrk, unpublished research, 2015.

[20] B.E. Warren: *X-Ray Diffraction*, Courier Dover Publications, New York, USA, 1969.

[21] U. Welzel, J. Ligot, P. Lamparter, A.C. Vermeulen, and E.J. Mittemeijer: *J. Appl. Crystallogr.*, 2005, vol. 38, pp. 1–29.

[22] A. Kumar, U. Welzel, and E.J. Mittemeijer: *J. Appl. Crystallogr.*, 2006, vol. 39, pp. 633–46.

[23] W. Voigt: *Lehrbuch Der Kristallphysik*, Teubner, Leipzig, 1910.

[24] A. Reuss: *Z. Angew. Math, Mech.*, 1929, vol. 9, p. 49.

[25] H. Neerfeld: *Mitt. K. Wilh.Inst. Eisenforschg.*, 1942, vol. 24, pp. 61–70.

[26] R. Hill: *Proc.Phys. Soc. London*, 1952, vol. 65, pp. 349–54.

[27] R.W. Wook and F. Witt: *J. Appl. Phys.*, 1965, vol. 7, pp. 2169–71.

[28] E. Kröner: *Z. Phys.*, 1958, vol. 151, pp. 504–18.

[29] J.D. Eshelby: *Proc. R. Soc. A.*, 1957, vol. 241, pp. 376–96.

[30] J.C. Stinville, J. Cormier, C. Templier, and P. Villechaise: *Acta Mater.*, 2015, vol. 83, pp. 10–16.

[31] T. Takahashi, J. Burghaus, D. Music, R. Dronskowski, and J.M. Schneider: *Acta Mater.*, 2012, vol. 60, pp. 2054–60.

[32] J.C. Stinville, P. Villechaise, C. Templier, J.P. Rivière, and M. Drouet: *Acta Mater.*, 2010, vol. 58, pp. 2814–21.
[33] C. Templier, J.C. Stinville, P. Villechaise, P.O. Renault, G. Abrasonis, J.P. Rivière, a. Martinavičius, and M. Drouet: *Surf. Coatings Technol.*, 2010, vol. 204, pp. 2551–58.
[34] G. Winther, L. Margulies, S. Schmidt, and H.F. Poulsen: *Acta Mater.*, 2004, vol. 52, pp. 2863–72.
[35] H.F. Poulsen, L. Margulies, S. Schmidt, and G. Winther: *Acta Mater.*, 2003, vol. 51, pp. 3821–30.
[36] R. Pokharel, J. Lind, A.K. Kanjarla, R.A. Lebensohn, S.F. Li, P. Kenesei, R.M. Suter, and A.D. Rollett: *Annu. Rev. Condens. Matter Phys.*, 2014, vol. 5, pp. 317–46.
[37] J. Oddershede, J.P. Wright, A. Beaudoin, and G. Winther: *Acta Mater.*, 2015, vol. 85, pp. 301–13.
[38] G. Winther: *Acta Mater.*, 2008, vol. 56, pp. 1919–32.
[39] F.N. Jespersen, J.H. Hattel, and Marcel A.J. Somers: *Proceedings ASM Heat Treat. 2015*, Detroit, 2015, p. in press.
[40] F.N. Jespersen, J.H. Hattel, and Marcel A.J. Somers: *Model. Simul. Mater. Sci. Eng.*, 2015, in press.

11 Conclusions and future work

The topic of this thesis is the study of the influence of the material's initial phase composition and the presence of plastic deformation on the properties and performance of the surface layers obtained through low-temperature thermochemical processes. In this respect, various stainless steel alloys with different initial phase composition and different degree of plastic deformation were subjected to low-temperature surface treatment.

Through the results obtained during the experimental activity it was possible to conclude that:

- The plastic deformation level and straining mode has a negligible influence on the properties and morphology of the layer created as a consequence of low-temperature thermochemical processing if the material maintains a fully austenite matrix upon straining. No precipitation of chromium nitrides and no significant variation of the layer thickness were found after low–temperature processes for plastically deformed austenite structures compared to the annealed materials.

- The presence of isothermal and strain-induced martensite promotes the nucleation of chromium nitrides in the expanded case as premature sensitization at relatively low temperatures and relatively short treatment time occurs upon low-temperature surface treatment. Furthermore the presence of martensite promotes faster growth of the case compared to a fully austenitic matrix for equivalent processing conditions.

- The formation of expanded austenite results in high compressive residual stresses at the materials surface. In the case of low-temperature nitriding the compressive stresses are largest at the surface and decrease steeply deeper in the case. The steep stress gradient generated in this zone can be directly related to the large compositional gradients. The influence of plastic deformation prior to nitriding was measured to be negligible and, if present, obscured by the high additional plastic deformation induced by the nitrogen incorporation itself.

- The carbon expanded austenite zone in the nitrocarburized case is characterized by lower compressive residual stresses compared to the nitrogen enriched zone. The compressive residual stresses in carbon expanded austenite change gradually and as such bridge the large difference in lattice parameter between nitrogen-stabilized austenite and the parent austenite. In this case it was possible to observe that plastic deformation prior to low-temperature thermochemical processing affects the stress distribution and the depth of the carbon enriched zone.

- Nitrogen alloying of various stainless steel grades obtained through high temperature solution nitriding allowed the formation of "High-Nitrogen Steels" and led to a considerable improvement of the mechanical properties, i.e. hardness and yield strength in annealed and deformed condition.

Furthermore the presence of high nitrogen contents in solid solutionn in the bulk led to stabilization of the austenite phase even for deformed structures, for which no strain induced martensite could be detected. The absence of strain induced martensite has a beneficial effect for the low-temperature nitriding processing as no CrN precipitation and no variation of the nitrided case thickness could be observed. Hence, high temperature solution nitriding leads to reproducible and predictable performance during subsequent low-temperature nitriding.

- Dissolution of nitrogen in the bulk or at the materials surface through high temperature solution nitriding and low-temperature nitriding respectively allows a significant improvement of the pitting corrosion resistance for several stainless steel grades. In particular, an expanded austenite zone is characterized by an outstanding resistance to localized corrosion as demonstrated by enhanced (or absence of a) pitting potential and dramatically slower dissolution during crevice corrosion performance tests.

The results obtained in this project met the objective of the "PressPerfect" project and enabled a deeper understating of the material's behaviour and performance after the finishing operations of industrial components.
In particular, through correct material´s selection and through the use of a combination of thermal treatments and processing routes it is possible to tailor the response to low-temperature thermochemical process in order to have the desired bulk and surface properties in the final product.
From an application point of view it is encouraging that a wide range of prior forming operations are not detrimental to the properties and morphology of the surface created by low-temperature thermochemical processing as long as stable austenite is maintained in the material´s substrate.
Strain-induced martensite formation has been successfully suppressed by high temperature solution nitriding as an initial processing step, and proved to be also highly beneficial for the mechanical and corrosion properties of the bulk.
Based on the encouraging results obtained in this Ph.D. thesis, it is believed that more research is required to optimize the high-temperature solution nitriding in order to determine the minimum nitrogen content necessary to stabilize the austenite during forming operations of various stainless steel alloys, thus preventing strain-induced martensite formation.
Furthermore it would be of great industrial interest to verify whether these processes can be applied on thick stainless steels components in order to prevent strain-induced martensite formation only at the material´s surface. This way high-temperature solution nitriding would be a viable method for treatments of components which are subsequently deformed and surface treated through low-temperature thermochemical processes.

DTU Mechanical Engineering
Section of Materials and Surface Engineering
Technical University of Denmark

Produktionstorvet, Bld. 425
DK-2800 Kgs. Lyngby
Denmark
Phone (+45) 4525 2205
Fax (+45) 4593 6213
www.mek.dtu.dk
ISBN: 978-87-7475-445-9